

Hafnium Metal-Organic Frameworks: Formation Routes and Defect Engineering

Francesca Catherine Noriko Firth

Yusuf Hamied Department of Chemistry

Selwyn College

University of Cambridge

This thesis is submitted for the degree of

Doctor of Philosophy

September 2021

Declaration

This thesis is the result of my own work and includes nothing which is the outcome of work done in collaboration except as specified in the text.

This thesis is not substantially the same as any work that has already been submitted before, or is concurrently being submitted, for any degree, diploma or other qualification at the University of Cambridge or any other University or similar institution. It does not exceed the prescribed 60,000 word limit for the Degree Committee for the Faculty of Physics and Chemistry.

Hafnium Metal-Organic Frameworks: Formation Routes and Defect Engineering

Francesca Catherine Noriko Firth

Abstract

Metal-organic frameworks (MOFs) consist of metal nodes or clusters linked by multidentate organic ligands. By altering the identity of these components, the properties of the MOF can be tuned. Furthermore, combining the versatility of MOFs with the considerable potential of low-dimensional materials like nanosheets or nanowires gives a wide range of functionalities for real-world applications. The deliberate introduction of defects into a MOF, or 'defect engineering', is a particularly significant method of modifying its properties. The UiO family of MOFs, comprising hafnium or zirconium clusters and bidentate linkers, is especially promising due to its stability and its ability to incorporate defects.

This thesis explores the effect of controlling the synthesis conditions on the type and distribution of defects in UiO family MOFs, using a range of characterisation techniques including powder X-ray diffraction to identify and understand resultant structural changes, among them the formation of phases with a different hafnium metal cluster. Based on this understanding of defect engineering, synthetic conditions needed to create new related UiO phases are identified and successfully used, enabling the creation of UiO family MOF nanomaterials.

The nuclearity and topology of the metal cluster are key to the formation of different MOF phases. This thesis uses *in situ* X-ray pair distribution function analysis to identify critical hafnium cluster intermediates in the early, pre-crystalline stages of solution formation of UiO family MOFs, and to compare these MOF reaction solutions to reactions forming only the metal clusters. Using solution nuclear magnetic resonance spectroscopy, this work then further explores the interactions in these reaction solutions, both in the solvent and between the solvent molecules and metal clusters, and investigates the effect of changing the composition of the solvent on the formation and behaviour of the hafnium clusters. These insights into the processes occurring during MOF reactions are key to the future of rational design of MOF syntheses.

Acknowledgements

My thanks first and foremost go to my supervisor Professor Clare Grey. Without her encouragement, support, and compassion, this thesis would not exist. She is the most brilliant and inspiring scientist I have had the honour of meeting, but far more important is her skill as a mentor in the example she sets of wisdom, commitment, and integrity.

I thank Dr Matthew Cliffe, who has advised, challenged and encouraged me throughout my research. I am most grateful for his valuable guidance.

Thank you to the members of the Grey Group, for their enthusiasm and engagement, for friendship and support, for all the moments of fun. It has been a pleasure and privilege to work alongside them all. Thank you also to the members of the Cliffe Group and Nottingham Nanocarbon Group.

To all of my collaborators: in particular I would like to acknowledge Diana Vulpe, Marta Aragonés-Anglada, Dr Peyman Moghadam and Dr David Fairen-Jimenez, for performing gas sorption measurements; Professor Ben Slater, for DFT optimisation of crystal structures; Dr Sean Collins and Dr Duncan Johnstone, for scanning transmission electron microscopy; Dr Michael Gaultois and Dr Yue Wu, for being part of an excellent round-the-clock session collecting XPDF data; Dr Dean Keeble and Dr Maria Diaz-Lopez, for their expertise at Beamline I15-1, Diamond Light Source; Dr Matthew Dunstan and Dr Erlendur Jónsson, for assistance with Python scripts; Dr Joshua Stratford, for sharing, explaining, and troubleshooting DiffPy scripts; Duncan Howe, for his assistance, suggestions and advice regarding solution NMR; Didi Rinkel, for solution NMR experiments and valuable discussions; Dr Chris O'Keefe, for advice on NMR experiments and data processing. I would also like to thank Dr Andrew Morris, Euan Bassey and Michael Jones for interesting discussions.

I would like to thank all those without whom research would not run smoothly: Sharon Connor in particular, and all the staff of the Yusuf Hamied Department of Chemistry. I thank the Engineering and Physical Sciences Research Council (EPSRC) for funding.

I would like to thank Selwyn College, which has been home for the past eight years and which has opened up so many opportunities. To Dr Daniel Beauregard and Dr James Keeler;

to all the members of Selwyn College Chapel; to Gina Vivian-Neal; to the porters and to all the staff: thank you.

Thank you to my friends new and old, especially those who have given me so much support over the last few years: each of my friends has been a source of joy.

I thank my family, especially my parents, for their constant love, support and faith.

Thank you to all those who have in any way encouraged and enabled me to indulge my curiosity about the world, and to explore in particular this little niche of science. I am deeply grateful.

A.M.D.G.

Michaelmas 2021

Contents

Abstract.....	vi
Acknowledgements.....	viii
Contents.....	x
List of Abbreviations and Terminology.....	xiv
Chapter 1. Introduction.....	1
1.1 Metal-Organic Frameworks.....	1
1.1.1 MOF syntheses.....	5
1.2 Defects.....	7
1.2.1 Types of Defects.....	7
1.2.2 Defects and Defect Engineering in MOFs.....	9
1.3 Zirconium MOFs and Other Metal Analogues.....	11
1.3.1 UiO-66 and Isorecticular MOFs.....	12
1.3.2 Defect Ordering in UiO family MOFs.....	13
1.3.3 The Discovery of nano-reo UiO-66(Hf).....	15
1.3.4 The Discovery of hcp and hxl UiO-67(Hf).....	20
1.4 Hafnium and Zirconium Clusters.....	24
1.4.1 Zirconium and Hafnium Solution Chemistry.....	25
1.4.2 Solvent Interactions in Synthesis Mixtures.....	27
1.5 Studying the Formation of MOFs.....	32
1.6 Characterisation Techniques.....	33
1.6.1 X-ray Scattering.....	33
1.6.2 Powder X-ray Diffraction.....	36
1.6.3 X-ray Pair Distribution Function.....	40
1.6.4 Nuclear Magnetic Resonance.....	45

1.6.5 Thermogravimetric Analysis.....	54
1.7 Motivation and Aims.....	58
Chapter 2. Defect-Engineering in the Synthesis of UiO Family MOFs: New Phases and Defect Structures	61
2.1 Experimental Methods	64
2.1.1 Synthesis.....	64
2.1.2 Post-synthetic Treatment	65
2.1.3 Characterisation	66
2.2 Results and Discussion.....	68
2.2.1 The Role of Formic Acid and Water on UiO-67(Hf) Phases.....	68
2.2.2 The Effect of Water on UiO-66(Zr/Hf) (F ₄ BDC).....	72
2.2.3 Synthesis of hcp UiO-66(Hf).....	76
2.2.4 Investigation of Defect Concentrations in hcp UiO-66(Hf) Phases <i>via</i> TGA and ¹ H NMR Studies.....	81
2.2.5 Adsorption Isotherm Measurements of hcp UiO-66(Hf).....	86
2.2.6 Post-synthetic Treatment	88
2.3 Conclusions.....	98
Chapter 3. Formation Routes of UiO Family Hafnium Metal-Organic Frameworks and Clusters in Solution using <i>in situ</i> X-ray Pair Distribution Function Analysis.....	103
3.1 Experimental Methods	107
3.1.1 Synthesis.....	107
3.1.2 X-ray Pair Distribution Function Measurements	107
3.1.3 Powder X-ray Diffraction.....	108
3.1.4 Analysis	108
3.2 Results.....	110
3.2.1 Cluster Models.....	110

3.2.2 Refinement against hcp UiO-66(Hf)	114
3.2.3 Behaviour of HfCl ₄ in Water	115
3.2.4 Behaviour of HfCl ₄ in DMF : Formic Acid : Water Solvent.....	117
3.2.5 Behaviour of HfCl ₄ in DMF : Formic Acid : Water Solvent at Raised Temperatures	122
3.3 Discussion	134
3.3.1 The Role of Acid	134
3.3.2 The Role of Water.....	135
3.3.3 The Role of Temperature.....	136
3.3.4 Framework Growth and Temperature.....	137
3.3.5 Summary	139
3.4 Conclusions.....	140
Chapter 4. Studying Solution Interactions in Reaction Mixtures of Hafnium Clusters.....	143
4.1 Experimental Methods	148
4.1.1 Synthesis.....	148
4.1.2 Solution NMR.....	148
4.1.3 X-ray Pair Distribution Function Measurements	149
4.1.4 X-ray Pair Distribution Function Analysis	149
4.2 Results.....	150
4.2.1 Initial Hafnium-free Solutions.....	150
4.2.2 Unheated Hafnium-containing Solutions.....	155
4.2.3 Reactions at 150°C.....	171
4.3 Discussion	180
4.4 Conclusions.....	183
Chapter 5. Varied Reaction Conditions of UiO Family Cluster Precursor Solutions.....	185
5.1 Experimental Methods	187

5.2 Results.....	188
5.2.1 Reactions with Different Solvent Compositions.....	188
5.2.2 Aged Solutions	197
5.3 Discussion	208
5.4 Conclusions.....	211
Chapter 6. Conclusions and Future Work.....	215
Bibliography	225
Appendices	277
Appendix A: Calculation used for TGA curves of hcp UiO-66.....	277
Appendix B: <i>in situ</i> hydrothermal cell for XPDF measurements	279
Appendix C: selective one-dimensional NOESY spectra	280
Appendix D: ¹³ C NMR of DFW 65:25:10 solutions.....	281

List of Abbreviations and Terminology

AcOH	acetic acid
BET	Brunauer-Emmett-Teller (type of isotherm)
BDC	benzene-1,4-dicarboxylate, the dianion of benzene-1,4-dicarboxylic acid (H ₂ BDC; also known as terephthalic acid)
BPDC	biphenyl-4,4'-dicarboxylate, the dianion of biphenyl-4,4'-dicarboxylic acid (H ₂ BPDC)
DMF	<i>N,N</i> -dimethylformamide
F ₄ BDC	2,3,5,6-tetrafluoro-1,4-benzenedicarboxylate, the dianion of 2,3,5,6-tetrafluoro-1,4-benzenedicarboxylic acid (H ₂ F ₄ BDC, also known as tetrafluoroterephthalic acid)
FcOH	formic acid (FcO: formate anion)
fcu	face-centred cubic topology
hcp	hexagonal close-packed topology
hns	hexagonal nano-sheet topology, similar to a single layer of hxl
hxl	2D hexagonal close-packed layer topology
isorecticular	see 'reticular chemistry' below; structures with the same topology but e.g. different size of components, such as different linker lengths in a MOF
modulator	an acid added to a MOF (solvothermal) synthesis, originally to control its growth and morphology; now commonly used to create defects in the framework
modulated synthesis	a method of synthesising MOFs, usually solvothermally, incorporating a modulator into the reaction mixture
MOF	metal-organic framework
NMR	Nuclear Magnetic Resonance
NOE	nuclear Overhauser effect
Pawley refinement	a method of analysing diffraction data, in which crystal symmetry and unit cell parameters are compared against the data (for example, to determine whether the experimentally-obtained Bragg peaks are

	plausible for a crystal structure of a given symmetry and unit cell dimensions) and refined using least-squares analysis
PDF	Pair Distribution Function
PXRD	Powder X-Ray Diffraction
PyDC	2,5-pyridinedicarboxylate, the dianion of 2,5-pyridinedicarboxylic acid (H ₂ PyDC)
Q	scattering vector, $Q = \frac{4\pi \sin \theta}{\lambda} = \frac{2\pi}{d}$
reo	an eight-connected primitive cubic topology, in which new vertices are placed in the middle of each edge and then connected to form octahedra around the original vertices; the name is derived from the O net in the ReO ₃ structure ^{1,2}
reticular chemistry	the method of assessing and comparing materials by deconstructing and classifying their structures into periodic nets
reticular (MOF) synthesis	the method of designing the synthesis of MOFs with desired structures by selecting linkers and clusters based on their topologies and connectivities
Rietveld refinement	a method of analysing diffraction data, in which a model crystal structure, including symmetry, unit cell parameters, atomic positions and occupancies, is compared against the data using least-squares analysis
SEM	Scanning Electron Microscopy
solvothermal	a method of synthesis in solvent at elevated temperatures, sometimes in a pressurised vessel (e.g. autoclave/Parr reactor)
TGA	Thermogravimetric Analysis
topology	the property of a geometric object which allows its structure (and spatial relationships of its components) to be defined, unaffected by e.g. change in size
turbostratic	a type of disorder in a crystal structure, where planes are no longer in the expected consistent stacking sequence and instead are displaced or rotated around the normal to the plane

UiO	abbreviated name for the isoreticular family of MOFs first made in the University of Oslo; the original UiO MOFs comprised zirconium (oxo)(hydroxo) clusters and linear dicarboxylate linkers such as terephthalate
-----	---

Chapter 1. Introduction

1.1 Metal-Organic Frameworks

Metal-organic frameworks (MOFs) consist of metal nodes or clusters linked by multidentate organic ligands in one or more dimensions [Figure 1.1].^{3,4} As such, MOFs are a type of coordination network, which is a subset of coordination polymer.^{5,6} The study of MOFs is therefore encompassed by the august field of coordination chemistry, which can be traced back to the synthesis of Prussian Blue (a ferrocyanide coordination compound) in the early 1700s.³ MOFs, however, are a relatively recent discovery, with the first material named a ‘metal-organic framework’ reported in 1995,⁷ although the field has since expanded rapidly to reach over 70,000 entries in the Cambridge Structural Database by 2016 (shortly before the start of research for this thesis) and over 90,000 by 2020.^{8,9}

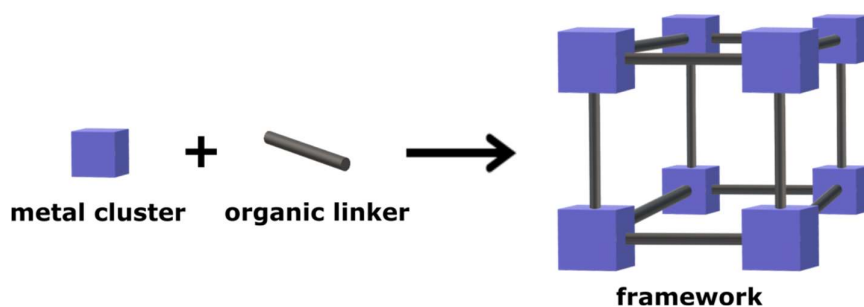


Figure 1.1. Schematic of how a MOF is built from a combination of metal clusters and organic linkers; this diagram shows cubic clusters, which can be coordinated by six linear bidentate linkers.

These materials, therefore, have great diversity. This is due to the huge library of different possible candidates for the type (or even multiple types) of metal or linker. Altering the identity of these components, for example *via* substitution of the metal centres or introduction of functional groups on the linker,^{10,11} can change the properties of the MOF such as reactivity, surface area or topology.^{12–15} One of the most prominent and in some way[†] defining properties of MOFs is their porosity^{4,9,16–18} due to the creation of pores encompassed by the linkers and clusters. The identity—in particular, geometry—of the linkers and

[†] *Permanent* porosity was originally used to define MOFs but the definition has been subsequently altered to include materials with the *potential* for void space⁵ which allows for the inclusion of e.g. ‘breathing’ MOFs.^{404–406}

clusters affects the porosity of the framework which in turn influences the ability of the MOF to host guests for storage or reaction inside the pores.^{19,20}

As a result of the defined geometries of the linkers and clusters and the resultant ordering of the extended structure of the framework, the majority of reported MOFs are crystalline (that is, with long-range order derived from repetitive translation of a meaningful structural unit) to the extent that many definitions of MOFs include crystallinity as a necessary property, alongside porosity.^{4,20} This definition is increasingly being challenged in recent years by the advent of the study of amorphous and glassy MOFs;²¹⁻²³ the predominance of reports of crystalline MOFs may in part be due to their relative ease of study and structural characterisation *via* single-crystal or powder X-ray diffraction, which is not the case for amorphous and glassy MOFs.²² However, the relationship between the geometry of the MOF components and their recurring coordination motifs, and the topology of the MOF framework, allows the huge library of MOFs to be assessed and compared *via* deconstructing and classifying their structures into periodic nets or 'reticular structures'.^{1,3,24-27} Each topology is assigned a symbol as part of a systematic nomenclature, recorded and defined in the Reticular Chemistry Structure Resource (RCSR) database;² this nomenclature is used throughout this work.

MOFs are of great interest for a wide variety of applications, including energy storage and carbon capture,^{28,29} due to their outstanding chemical tunability as a result of the wide variety of available linkers and metal clusters.¹⁹ As with many other materials, interest is increasing in the possibility of making nano or low-dimensional structures derived from MOFs.³⁰⁻³² While MOFs inherently have high *internal*-surface-area-to-volume ratios due to their internal porosity,²⁰ low-dimensional materials such as 'two-dimensional' nanosheets³³ and 'one-dimensional' nanowires³⁴ have high *external*-surface-area-to-volume ratios (that is, high aspect ratios), which enable strong interactions with other surfaces and large quantities of functionalising or adsorbing molecules.^{10,31} Combining this advantage of low-dimensional materials with the versatility and tunability of MOFs gives a wide range of prospective applications such as conductive metal-complex wires³⁵ and semipermeable membranes for molecular sieving, sensing, proton exchange,³⁶⁻⁴⁰ and battery separators^{11,41}. However, the library of these MOF-based nanomaterials is very small compared to that of existing three-

dimensional MOFs, and current routes to produce them have severe limitations, such as, in the case of vapour deposition of MOF thin-films, poor control of location and distribution of atoms and hence a decrease in crystallinity.^{30,42,43} Expanding the range of low-dimensional MOFs and improving their synthesis are therefore key goals in order to harness their potential.

However, in order to exploit fully the potential of MOFs for real-world applications one of the most pressing concerns in the field is the need for *rational design* of MOFs; that is, working towards the design of syntheses to obtain MOFs with specific desired properties and hence pre-selected structures.⁴⁴⁻⁴⁷

This reverse-engineering of MOFs can be approached *via* reticular synthesis,^{17,20} in which linkers and clusters can be selected based on their topologies and predicted coordination geometries to create the resultant structure.^{3,17,48} A trigonal planar linker with three coordinating sites, combined with a metal cluster with three coordination sites, will produce an entirely different MOF from a non-linear bidentate linker and a dimeric cluster, which is again different from the combination of a linear bidentate ligand and a hexanuclear cluster.^{19,24,49-51} By considering the relationship between the geometries of the clusters and linkers, and the resultant framework, reticular synthesis can be applied both to the creation of frameworks based on the same cluster and similar linker topology as existing MOFs (to make 'isorecticular' series) and to the design of new MOFs. In many isorecticular series of MOFs the properties of the material are altered by using a functionalised linker.^{52,53} new MOF structures, and hence different porosities, can be obtained by using a linker with different geometry and/or denticity.^{45,54}

While the geometry of the linker is indeed important in determining the structure of a MOF, the shape and identity of the metal cluster are also crucial.^{55,56} Multinuclear metal clusters (also called 'secondary building units')⁵⁵ bring increased architectural stability, originating from strong cluster-linker bonds and cluster rigidity, to the resultant framework (as compared to mononuclear metal nodes), resulting in more stable porosity as well as a well-defined directionality which is key to the *rational design* approach.^{57,58} The emphasis of the reticular synthesis method on identifying the contributions of the metal cluster to the resultant framework structure is a crucial foundation of this thesis.

One method to obtain MOFs with new properties, such as for sorption or catalytic applications, is to create new metal clusters with different geometries and coordination behaviours. Different metals tend to form clusters with different nuclearities, i.e., how many metal units are in each cluster; this can range from two, in copper or zinc paddlewheel units, to higher nuclearities in titanium and zirconium clusters.^{59,60} Clusters with higher nuclearity are often more highly connected and therefore more stable.⁶¹ Metals with higher charge density, such as Zr(IV), are often more strongly bound (or coordinated) to the donor atoms, for example the oxygens of a carboxylate group, and hence show lower linker lability;⁶¹ dissociation is less favoured. Clusters may also not have all of their coordination sites taken up by intercluster structural linkers. These undercoordinated open metal sites on the cluster can be sites for catalysis, for the coordination of other reactive species⁶²⁻⁶⁵ or for adsorption of guests.^{51,66}

By understanding the inorganic component, therefore, control can be obtained over both the nuclearity of the cluster⁶⁷ and the connectivity of the MOF⁶⁸, which allows the MOF structure and properties to be changed dramatically.⁵⁶ Although some cluster structural motifs recur frequently,⁴⁴ the identity of the metal cluster is not always easy to predict. MOFs generally form *via* self-assembly; that is, a process in which an initial system of disordered components spontaneously forms an organised structure as a result of specific, local interactions between the components.⁶⁹ The reaction from metal and ligand precursors through to the final MOF framework is frequently a 'black box' process,^{46†} in which the resultant MOF is determined by the manner in which the metal clusters form and coordinate together with the linkers. One method of obtaining some control over the cluster species, and hence over the framework which forms, is by 'seeding' the MOF reaction with a pre-synthesised molecular cluster species,^{70,71} with the aim of the cluster-terminating ligands exchanging for intercluster linkers and hence forming a framework. However, the presence of other species, such as solvent, may still affect both the exchange and coordination processes,⁷² and the stability of the clusters, and result in a MOF structure different from that desired.

† A 'black box' process is one which is viewed in terms of its inputs and outputs, where the internal workings are not known (or are not available for inspection).

1.1.1 MOF syntheses

The nature of the metal clusters in a MOF is dependent on both the metal itself and on the identity and concentration of other species present¹⁸ (this will be discussed in more detail later in this Chapter) and hence the synthesis conditions and reagents will greatly affect the outcome;³ many MOFs have been reported to form only through one synthesis method or in a very specific set of conditions. Reported MOF syntheses have a range of different conditions, including temperature and presence and type of solvent. Furthermore, each method has both advantages and limitations. It is therefore important to identify the most suitable option when attempting to design a synthesis.

Among the earliest methods of MOF synthesis, in keeping with techniques used to obtain molecular crystals of other materials, are low- or room-temperature syntheses.¹⁹ In these processes, the MOF was obtained from the solvent through direct precipitation, evaporation, or recrystallisation. In contrast, many techniques used presently involve elevated temperatures to overcome both kinetic and thermodynamic limitations. Solvothermal synthesis, one of the most widely-used methods, involves heating the MOF reagents in solution in a closed vessel above the boiling point of the solvent.¹⁹ Lower heating temperatures, and hence lower pressures, can also be used. These conventional heated reactions, however, often have high energy and time costs. Microwave heating is promising as an alternative, as it frequently requires shorter reaction times as well as enabling greater control of the reaction *via* the possibility of selecting the heating power to target locations and timepoints in the reaction;^{73,74} electrochemical synthesis can also offer similar real-time selectivity.^{75,76} Moving away from reactions in traditional solvents, employing ionic liquids can alter the interactions between the solvent and the MOF precursors, including the potential for structure templation.^{77,78} Gelation and sol-gel⁷⁹ techniques can be used to synthesise both amorphous MOFs, which retain the local structure but not the long-range order of crystalline MOFs, and monolithic MOFs, which are MOF structures, not necessarily crystalline, of macroscopic size and continuous morphology.⁸⁰ For reactions where the presence of solvent is undesirable, either due to unwanted interactions or for environmental concerns, mechanochemical techniques can be used, in which direct absorption of mechanical energy enables the breaking and formation of bonds.⁸¹⁻⁸³ Finally, recent developments suggest that even all-gas-phase reactions may have potential for atomically

precise syntheses of MOFs;⁸⁴ however, current understanding of the processes occurring during the synthesis, and control over the structure of the resultant materials, are limited.^{84,85}

When attempting to determine those reagents and conditions which are most likely to form the desired MOF structure, techniques such as high-throughput screening, which allow rapid and efficient investigation of a wide reaction space, are extremely valuable.⁸⁶⁻⁸⁸

However, these techniques are currently not suitable for use in all reaction conditions; therefore, a fundamental understanding of the processes and interactions occurring during MOF syntheses is needed, as these insights may be applicable to a broad range of synthesis methods as well as providing clues for the synthesis of previously-unrealised MOFs.

Gaining this understanding, and hence obtaining control over the synthesis, are extremely important objectives in the journey towards full *rational design* of MOFs and their constituent metal clusters.

1.2 Defects

The above discussion of the relationship between designing the structure of MOFs and obtaining desired properties did not address one extremely important factor: the presence of defects in a MOF structure. The introduction of defects is a particularly significant method of modifying the properties of materials,^{89,90} as seen in the alteration of the conductivity upon doping silicon,⁹¹ changing the strength or magnetic properties of steels by adding impurities or dislocations,⁹² or the incorporation of vacancies into solid electrolytes *via* solid-state synthesis.^{93,94} MOFs are no exception in this respect: the presence of defects in a metal-organic framework has long been known to alter its properties,⁹⁵ from pore surface area— affecting gas sorption ability—to changing mechanical strength and introducing new reactive properties, such as the enhancement of catalytic activity.^{96–98} Obtaining control over the type, location and concentration of defects in MOFs is therefore of interest in order to study and harness them.^{99–101} However, this first requires an understanding of the various types of defects possible, as well as the ways in which they are introduced.

1.2.1 Types of Defects

Perfect, long-range order in a material is the exception rather than the rule. Defects occur naturally in growing crystals as a perfect crystal is entropically disfavoured. Defects may be categorised by their dimensionality and by their length scale [Figure 1.2].¹⁰²

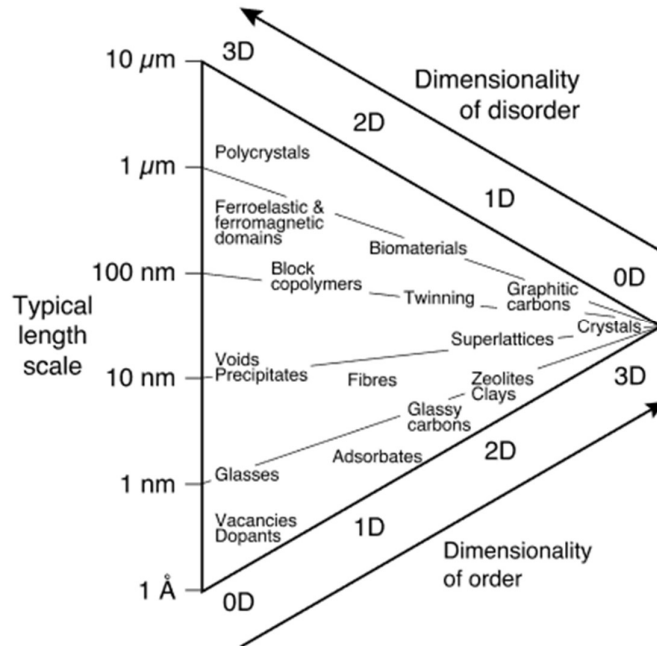


Figure 1.2. Reproduced from Ref. 102. Original caption: Typical length scales and dimensionality of disorder in some classes of materials. The disorder in most materials is usually defined relative to a lattice. Glasses are an exception, where short range order is determined by nearest neighbour bond distances and interbond angles. Medium range order in glasses refers to residual correlations between atom positions on lengthscales between 0.5 and 3 nm.

In crystal structures, zero-dimensional defects may be categorised as ‘point’ defects, while one- and two-dimensional defects are ‘line’ and ‘plane’ defects respectively. Point defects can include vacancies (in which atoms or individual components are missing from their normal sites), interstitials (in which components are inserted into normally-unoccupied sites) and substitutionals (in which a component is replaced by a different component). These defects can also be combined, as in the case of Schottky defects (where, in an ionic crystal, both an anion and a cation are missing) and Frenkel defects (where an ion moves from its usual lattice site into an interstitial site).¹⁰³ Line defects, meanwhile, can include both edge dislocations (in which an extra half-plane or row is inserted into the lattice midway, causing nearby planes to distort) and screw dislocations (in which the lattice is ‘cut’ partway along a plane and then slipped across by one lattice vector, i.e., each component is in an identical lattice site, one across from its original position). Plane defects can include grain boundaries, where two different crystallites join together, and crystal stacking faults and boundaries. For example, a crystal structure with the ordering of planes ABCABCABC could have a stacking fault (ABCABABC) or a twin boundary (mirror plane; ABCABCACBA). In

some crystal structures, including perovskites, shear planes are also possible; while the crystal usually consists of corner-sharing coordination polyhedra, a shear plane can cause these polyhedra to become edge-sharing or face-sharing instead [Figure 1.3].¹⁰⁴

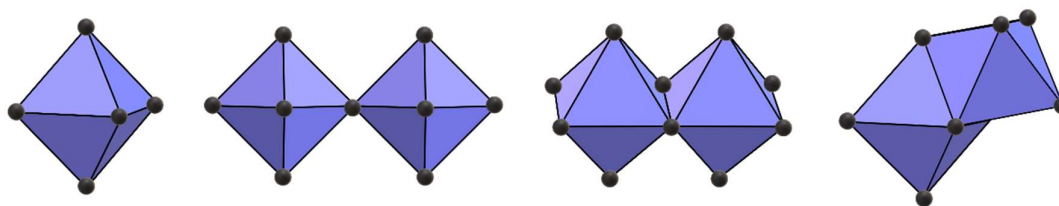


Figure 1.3. Schematic of coordination polyhedra in e.g. a perovskite. l-r: single coordination polyhedron; corner-sharing; edge-sharing; face-sharing.

1.2.2 Defects and Defect Engineering in MOFs

Defects in MOFs can display dimensionalities similar to those seen more generally in crystalline materials, from point defects such as missing clusters or linkers, through line defects such as edge or screw dislocations, to planar defects such as stacking faults. All of these introduce new reactivities or change physical properties such as morphology or topology.^{12,15,99,100,105,106}

While defects are inherent to MOF materials and therefore arise during synthesis and/or further treatment, the understanding that defects affect the properties of a MOF has led to the rise of the field of ‘defect engineering’ in which defects are deliberately introduced with the aim of altering specific properties of the framework.^{97,99,107,108} This may be done either directly during synthesis or *via* postsynthetic treatment, with varying amounts of control over the defects produced, in many cases without losing the overall ordered, crystalline structure of the MOF.¹⁰⁹

Postsynthetic treatment can include mechanical treatment, postsynthetic washing, acid treatment¹¹⁰ to remove linkers *via* hydrolysis of cluster-linker bonds, or ligand-exchange^{111–113} to introduce new functionalities. MOFs can be synthesised with more than one kind of linker, or with mixed-metal clusters;^{99,114,115} these can be distributed randomly throughout the framework, or display local cooperative ordering effects.¹¹⁶ Alongside these ‘substitutional’ defects, ‘vacancy’ defects can include missing-linker defects, which can be created through either synthesis or postsynthetic treatment,¹¹⁷ to give cluster-surface reactive groups such as sulfates, functionalised organic ligands and hydroxide/water groups,^{101,118–125}

which can themselves be further reacted to create additional functionalities and reactivities.¹²⁶ During synthesis, some degree of control over the amount of defects is enabled both by changing the concentration of the linker-replacing species and by changing other synthesis properties such as temperature.^{98,119} Missing-linker defects can also be introduced through techniques such as modulated synthesis, in which a monocarboxylic acid is used to replace linkers.^{13,14,99,105,107,127,128}

Modulated Synthesis

Missing-linker defects require compensating 'capping' ligands at coordination sites on the metal cluster left vacant by the absence of linkers; these capping ligands are usually derived from other species (such as solvent or counterions) present during the synthesis.^{12,53,129} Defects can therefore be deliberately introduced *via* the inclusion of these species in the reaction mixture.^{130–135} In 'modulated' synthesis a monocarboxylic acid modulator is included in the synthesis, which not only affects the pH of the reaction but also gives a ready source of monocarboxylate groups. Modulated synthesis was originally devised as a method of controlling the morphology and polydispersity of MOF crystals by slowing the speed of crystallisation^{98,99,136} and *via* capping coordination sites on the faces of the MOF crystal.^{14,137,138} However, the monocarboxylate anions also compete with the MOF linkers to coordinate to the clusters, effectively decreasing the metal-linker ratio and becoming incorporated into the crystal structure in place of the linker; this results in missing-linker defects.^{53,105,128,129,137–141} By altering the identity and concentration of the modulator included in the synthesis the concentration of linker vacancies in a MOF can be tuned systematically.^{15,98,142}

While no means an exhaustive list, this brief discussion of the types of defects in MOFs and the ways they can be introduced into the framework shows just how rich the possibilities are when seeking to tune the properties of a MOF by the deliberate inclusion of defects, or 'defect engineering'. Since defects alter the properties of the framework, obtaining control over the type, location and concentration of defects will in turn allow control over the properties of the MOF.^{12,15,99,100,105} However, many MOFs are unstable to the inclusion of high quantities of defects, especially missing-linker defects, for example as a result of low intercluster connectivity (resulting in framework collapse). Therefore, when pursuing an

exploration of the deliberate creation and effect of defects, a MOF candidate must be chosen which is able to incorporate these defects without significant loss of stability.^{141,143} Zirconium MOFs, and their hafnium analogues, are the subject of much investigation into their ability to incorporate defects; one such MOF candidate is UiO-66, alongside its isorecticular family.

1.3 Zirconium MOFs and Other Metal Analogues

The discovery of zirconium MOFs opened up a wealth of possibilities for new structures and for structural modification.⁶⁸ These MOFs comprise some of the most well-known and frequently-studied materials in the field.^{61,68,144} In these MOFs, zirconium is found in the Zr(IV) oxidation state, giving it a high charge density and hence affinity for coordination by ligands with oxygen atoms. This leads to the formation of metal-oxo and -hydroxo clusters which are the basis for the high stability of the resultant frameworks.

By far the most common zirconium cluster observed in MOFs is hexanuclear, with metal centres bridged (or capped) by oxo and hydroxo ligands resulting in a $[\text{Zr}_6(\mu_3\text{-O})_4(\mu_3\text{-OH})_4]^{12+}$ cluster. This cluster was first observed coordinated by 12 linear dicarboxylate linkers in the archetypal UiO-66 MOF, which is discussed in more detail below.⁵⁰ While this M_6 cluster can be fully coordinated by 12 bidentate linkers, the coordination of additional site-terminating species, alongside a range of linker geometries, can result in MOFs with different connectivities and hence different topologies; some examples are given in Table 1.I below.

Table 1.I. Some of the well-known MOFs containing the hexanuclear $[\text{Zr}_6(\mu_3\text{-O})_4(\mu_3\text{-OH})_4]^{12+}$ cluster.

MOF identifier	Number of cluster sites coordinated by linker	Geometry of linker	Reference
UiO-66	12	Linear dicarboxylate	Cavka <i>et al.</i> ⁵⁰
MOF-801-841	6,8,10 or 12	various	Yaghi <i>et al.</i> ¹⁴⁵
PCN series	12	Elongated linear dicarboxylate or tetratopic porphyrinic	Zhou <i>et al.</i> ^{146,147}
NU-1000	8	Tetratopic	Farha, Hupp <i>et al.</i> ¹⁴⁸
DUT-67	8	Bent dicarboxylate	Kaskel <i>et al.</i> ¹⁴⁹

Zirconium MOFs have also been reported with cluster species other than the classic hexanuclear cluster discussed above, with new and exciting properties such as catalytic activity different from that displayed by the hexanuclear cluster.¹⁵⁰ Some of these MOF clusters contain this hexanuclear structure as a subunit, with similar motifs as found in the condensation of perovskite coordination polyhedra discussed earlier. These include infinite chains, found in CAU-22 in the form of edge-sharing hexanuclear clusters *via* two bridging -OH groups (Stock *et al.*),¹⁵¹ and in CAU-27 in the form of coordination-polyhedron-sharing clusters (Stock *et al.*).¹⁵² Moving away from the Zr₆ cluster motif, zirconium MOFs can also contain clusters with a simpler structure, such as the infinite one-dimensional chains of zirconium atoms bridged by μ₃-O similar to the structure of monoclinic ZrO₂, found in MIL-140 (Serre *et al.*),¹⁵³ or even more simply, edge-sharing ZrO₈ polyhedra, found in MIL-153 and MIL-163 (Devic *et al.*).^{154,155}

Inspired by the success of these MOF syntheses with zirconium (IV) clusters, the use of other tetravalent metals in MOFs has been explored due to their similar potential for forming stable metal-oxo clusters. Several of the resulting MOFs also contain hexanuclear clusters isostructural to the classic [Zr₆(μ₃-O)₄(μ₃-OH)₄]¹²⁺ cluster, with metals such as cerium¹⁵⁶ and uranium,^{157,158} as well as hafnium,^{159,160} cerium^{161,162} and thorium¹⁶³ analogues of UiO-66.

1.3.1 UiO-66 and Isoreticular MOFs

First reported in 2008 by Cavka *et al.*, the UiO family of MOFs (named after the University of Oslo where it was first made) is today considered one of the most-studied, 'benchmark' MOFs.¹⁴⁴ The UiO family, of which UiO-66 is the most well-known, is made from zirconium clusters and linear dicarboxylate linkers.⁵⁰ UiO-66 denotes the framework made with terephthalate (BDC) linkers (one phenyl ring) while in UiO-67 the linkers are made with the longer biphenyldicarboxylate (BPDC, two phenyl rings); functionalised versions of these linkers can also be used to produce more members of this iso-reticular series. As mentioned above, UiO family MOFs have also been synthesised with metals other than zirconium; hafnium analogues¹⁶⁴ are the particular focus of this thesis.

In almost all reported members of this archetypal UiO family, the framework combines these clusters and linkers to give a face-centred cubic (**fcu**) topology. In this structure each hexanuclear M₆(μ₃-O)₄(μ₃-OH)₄ metal cluster is strongly coordinated by 12 carboxylate

groups [Figure 1.4]. This makes these frameworks—compared to other MOFs—both particularly thermally stable (decomposing about 540°C) and chemically resistant to water and other solvents.^{50,61,165} As well as stability this family of MOFs possesses catalytic activity and gas sorption capabilities^{166–168} and the use of organic linkers with different functionalities can give access to new or improved properties such as increased CO₂ adsorption.^{52,169,170} This also makes the UiO family of particular interest for real-world applications including sorption, catalysis, sensors and energy storage materials.^{29,30,38,98,164,169,171,172}

The UiO family is commonly synthesised solvothermally, although mechanochemical and electrochemical methods have also been investigated.^{83,173,174}

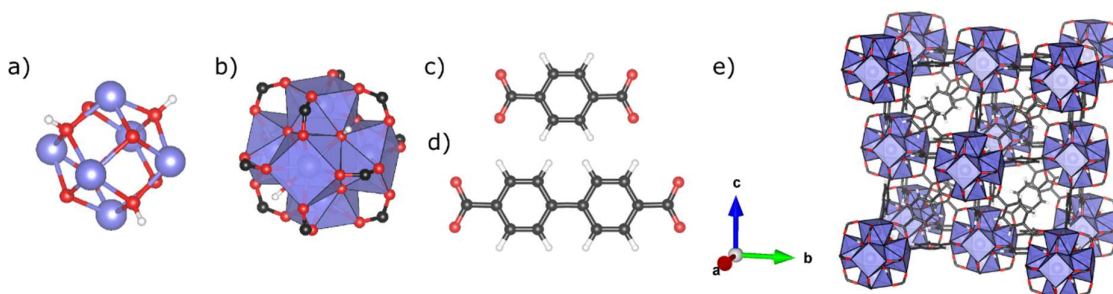


Figure 1.4. Building blocks of UiO family MOFs: a) $M_6O_4(OH)_4$ cluster, where $M = \text{Hf}, \text{Zr}$, showing the capping $\mu_3\text{-O}$ and $\mu_3\text{-OH}$ anions on the M_6 octahedron; b) polyhedral representation of the cluster, with coordinating $-\text{CO}_2$ groups; c) BDC (linker for UiO-66); d) BPDC (linker for UiO-67); e) UiO-66 fcu structure (crystal file from Ref. 165). Colour scheme: M, blue; O, red; C, black; H, white.

1.3.2 Defect Ordering in UiO family MOFs

Zirconium and hafnium MOFs, including the UiO family, exhibit the potential for a wide range of defect chemistry. UiO-66 is viewed as one of the ‘model systems’ for studying defective MOFs and for using defect-engineering to tailor properties,^{97,101,107,144} as it commonly incorporates both linker and cluster vacancies^{99,122,141} and the framework remains stable despite the presence of these defects due to the strong metal-linker coordination and high connectivity of the framework.¹⁵⁴

One of the most common routes to creating defects in UiO-66 is modulated synthesis. While this is expected to produce missing-linker defects¹⁰⁷ and can be used to tailor the properties of the MOF,⁹⁷ recent studies on modulated synthesis of UiO family MOFs have revealed some especially exciting and novel behaviour with great potential for the future of defect

engineering: defect ordering. Owing to the influence of this research on the work presented in this thesis, these defect-ordering studies are discussed in some detail below.

1.3.3 The Discovery of nano-reo UiO-66(Hf)

For a more in-depth discussion of the defect-mediated structures in this section, see:

M. J. Cliffe, W. Wan, X. Zou, P. A. Chater, A. K. Kleppe, M. G. Tucker, H. Wilhelm, N. P. Funnell, F.-X. Coudert and A. L. Goodwin, *Nat. Commun.*, 2014, **5**, 4176. [Ref. 141]

D. N. Johnstone, F. C. N. Firth, C. P. Grey, P. A. Midgley, M. J. Cliffe and S. M. Collins, *J. Am. Chem. Soc.*, 2020, **142**, 13081–13089. [Ref. 175]

Modulated synthesis, as discussed above, involves the inclusion of a monocarboxylic acid in the MOF solvothermal reaction mixture. Modulated synthesis of UiO family MOFs in particular was found to cause the inclusion of up to high levels of missing-linker defects, where the modulator carboxylate anion terminates the vacant cluster coordination sites.^{98,170} Moreover, the concentration of these defects could be tuned systematically in relation to the amount of modulator in the synthesis.¹⁵

In almost all cases these point defects appeared to be randomly distributed through the MOF structure. However, when formic acid (HCOOH) was used as a modulator, Cliffe *et al.*¹⁴¹ noticed that the powder X-ray diffraction pattern of UiO-66(Hf) showed not only the Bragg peaks consistent with the expected crystalline **fcu** framework but also diffuse scattering in the form of weak, broad peaks in locations forbidden for the **fcu** structure. Instead, the locations of this diffuse scattering were consistent with a locally primitive cubic structure [Figure 1.5].¹⁴¹ Further investigation revealed that these two structures could be found within the same MOF crystallites—that is, that the inclusion of formic acid was *not* forming two distinct, separate phases. Increasing the amount of formic acid increased the intensity of these diffuse peaks, suggesting that formic acid was directly responsible for the structural changes indicated [Figure 1.5].

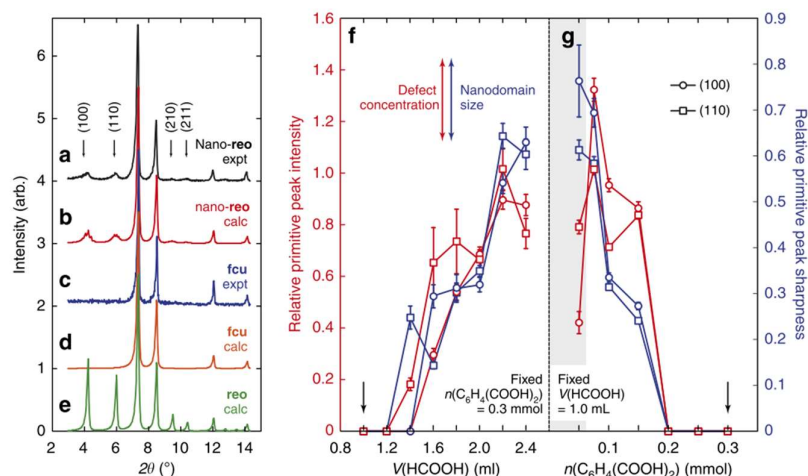


Figure 1.5. The effect of formic acid on UiO-66(Hf). Figure and caption reprinted by permission from Springer Nature: Nat. Commun., ‘Correlated defect nanoregions in a metal-organic framework’, M. J. Cliffe *et al.*, 2014. (Ref. 141). (a) The experimental low-angle X-ray diffraction pattern of UiO-66(Hf), measured over the angular range 3–15° ($\lambda=1.541 \text{ \AA}$), consists of a sharp Bragg scattering component with reflections obeying the conditions expected for the face-centred-cubic lattice and a less-intense diffuse scattering component centred on ‘forbidden’ reflection positions associated with a primitive cubic superstructure. The four most intense diffuse scattering peaks are highlighted by arrows. (b) The corresponding diffraction pattern calculated from the **re** defect nanoregion model described in the text: the intensities and peak widths of both Bragg and diffuse scattering contributions are quantitatively accounted for by this model. The experimental (c) and calculated (d) diffraction patterns for a defect-free **fcu** framework, showing the absence of diffuse scattering features. (e) A long-range-ordered **re** model gives rise to superlattice peaks in the same positions as those observed in (a), but simultaneously overestimates peak intensities and underestimates peak widths. Instead, the relative intensities and widths of the diffuse superlattice reflections measure defect concentration and domain size, respectively. (f) Increasing modulator (formic acid) concentration for fixed linker concentration during synthesis results in a higher concentration of **re** nanoregions of increasing domain size, as does (g) decreasing linker concentration for fixed modulator concentration. Points of identical composition are indicated by arrows; the shaded region in g corresponds to compositions for which additional phases are present. For all data points in g and h, the solvothermal reaction conditions used were as follows: 48 h, 120 °C, 4ml DMF, 0.3 mmol HfCl₄; HCOOH and C₆H₄(COOH)₂ concentrations as indicated in the plots. Relative primitive peak sharpness values (blue data points) were determined as the ratio of peak widths $\sigma(111)/\sigma(100)$ and $\sigma(111)/\sigma(110)$ extracted from Pawley profile fitting; relative primitive peak intensities (red data points) were determined as the ratio of observed primitive peak intensity to the extrapolated value at maximum defect concentration. The error bars represent standard uncertainties in the mean values.

Cliffe *et al.* determined that the structural change caused was the creation of missing-cluster defects owing to the correlation of missing-linker defects (which can be compared to the missing-cation-and-missing-anion Schottky defects mentioned earlier in this Chapter). These cluster vacancies were found to be introduced along $\langle 100 \rangle$ directions in the **fcu** matrix and could be modelled with the eight-connected **re** (primitive cubic) topology within the host, twelve-connected, **fcu** framework [Figure 1.6].¹⁴¹

However, this local defect-correlation-induced defectivity was not the only novel discovery with this MOF. These missing-cluster defects were *themselves* correlated, creating

nanodomains of this **reo** structure within the **fcu** matrix: nano-**reo** UiO-66(Hf). Far from the dominant understanding that defects in MOFs are randomly distributed, this modulated synthesis of UiO-66(Hf) with formic acid in fact produced two kinds of defect ordering, both local and more extended; the size of the nano-domains of the **reo** structure could be further tuned through adjusting the concentration of formic acid.^{141§}

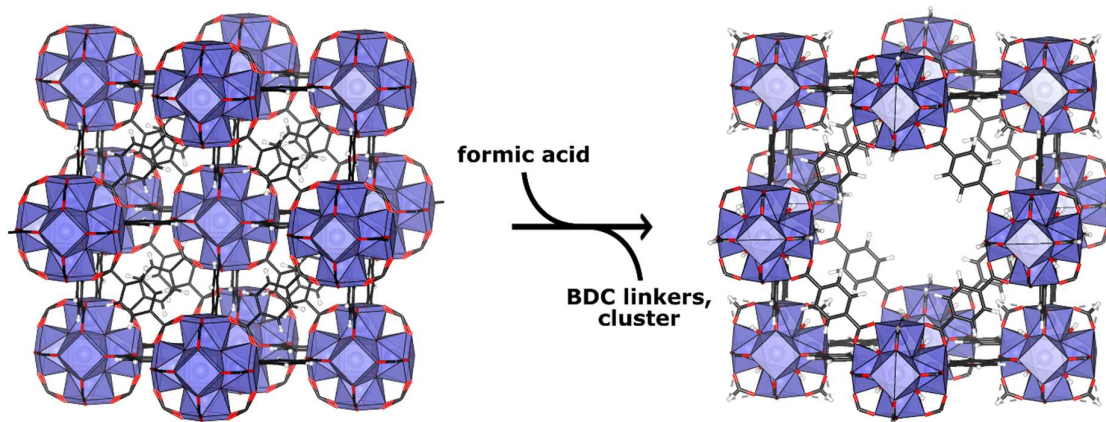


Figure 1.6. Single unit cells of the structures of **fcu** UiO-66 (left) and **reo** UiO-66 (right), viewed down [100], showing the missing cluster due to correlated loss of linkers in {100}-type planes, and thus the change in symmetry from face-centred cubic to primitive. Crystal files from Refs. 165 and 141.

This discovery inspired further work. The ability of defects to order, while observed in other materials such as transition-metal oxides,^{176,177} had not until this point been observed for MOFs. Furthermore, it was unknown precisely how these UiO-66(Hf) defect nano-domains were situated within the **fcu** matrix, including their relative orientations. A powerful technique used to observe individual defects in real space such as missing linkers in UiO family MOFs is high-resolution transmission electron microscopy (HRTEM); while the ability to directly view defects in MOFs is powerful, this technique however does not provide information on the ordering of defects resulting in new MOF phases, nor on relative orientations of different structures within the MOF.¹⁷⁸ Furthermore, this technique requires high energies which can damage samples. Electron diffraction, on the other hand, can be

§ Complete defect ordering in UiO-66(Hf), however, is prevented by the concomitant formation of a $\text{Hf}_6\text{O}_4(\text{OH})_4(\text{FCO})_{12}$ (FCO = formate anion) hafnium formate layered framework as modulator concentration increases.^{141,341}

used with lower energies, and provides information about the distribution and correlation of defects and resulting changes to the crystal structure of the MOF.¹⁷⁹ Building on these techniques, using four-dimensional scanning transmission electron microscopy in combination with powder X-ray diffraction on samples of nano-**reo** UiO-66(Hf) with different defectivities (created by varying the ratio of metal salt to linker, with modulating formic acid) Johnstone *et al.*¹⁷⁵ therefore investigated the defect domain size and ordering within nano-**reo** UiO-66(Hf).¹⁷⁵

Refinement of powder X-ray diffraction data on the different samples and comparison of the **reo**-characteristic (110) reflection to the **fcu**-characteristic (111) reflection showed that as the defectivity increased the domain size of the **reo** nano-regions also increased [Table 1.II]. Using a combination of direct-imaging and scanning electron diffraction, regions of the UiO-66(Hf) crystallites producing **fcu**- and **reo**-characteristic diffraction patterns were then mapped.¹⁷⁵ This revealed even greater correlation between the defect structures than had previously been observed. In the case of the more defective samples, the defect nanodomains could clearly be seen to have a coherent interface with the **fcu** matrix; moreover, the domains were ordered in a rectangular lamellar structure which was further preferentially ordered perpendicular to the crystallite facets [Figure 1.7].¹⁷⁵ The size and morphology of these domains could be adjusted along with the defectivity by tuning the synthesis.

Table 1.II. Parameters derived from PXRD and Pawley refinement on samples of nano-**reo** UiO-66(Hf). Data obtained by author and published in Ref. 175.

HfCl ₄ : H ₂ BDC molar ratio	reo domain size / nm	PXRD reflection ratio of reo (110) to fcu (111)
6:5	51.6(1.3)	0.1325(28)
1:1	47.4(1.4)	0.10081(22)
3:4	31(5)	0.040(5)
3:5	5.5(4)	0.12(3)

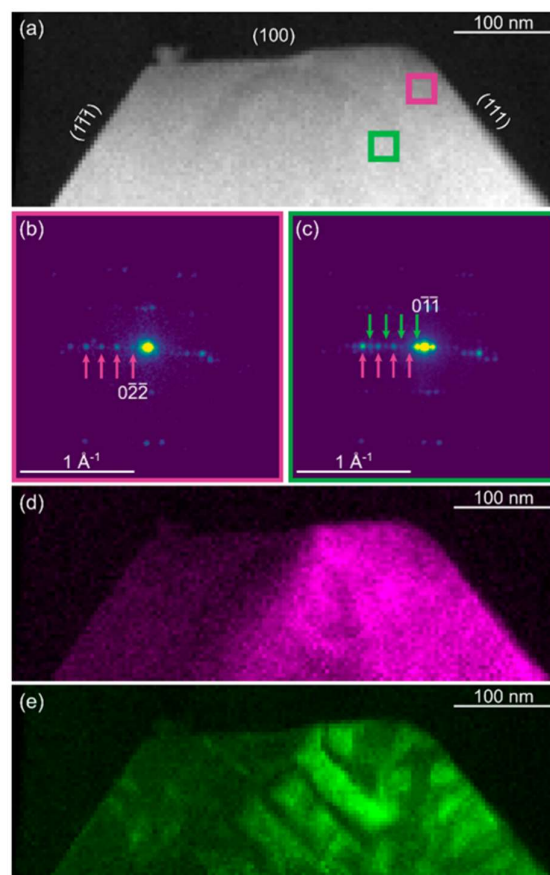


Figure 1.7. Analysis of ordering of defect nanodomains in nano-**reo** UiO-66(Hf). Reproduced with permission from ACS, 'Direct Imaging of Correlated Defect Nanodomains in a Metal–Organic Framework', Johnstone et al., 2020 (Ref. 175). Original caption: SED analysis of defect nanodomains in a 6(Hf):5(BDC) UiO-66(Hf) particle with high defect density. (a) ADF-STEM image indicating regions where integrated electron diffraction patterns (b, c) were selected. (b) Diffraction pattern from the magenta region, marked in a, containing only parent reflections indicating the **fcu** phase. (c) Diffraction pattern from the green region, marked in a, containing both parent and superlattice reflections indicating the **reo** phase. (d) VDF image formed using integration windows centered on the parent reflections, marked in b). (e) VDF image formed using integration windows centered on superlattice reflections, marked in c, to directly image **reo** defect nanodomains.

Not only did this study of nano-**reo** UiO-66(Hf) reveal previously unknown defect structuring formed through modulated synthesis, it also revealed clues about the formation mechanism of these MOFs. The lamellar structure, perpendicular to the crystallite growth front, suggests a diffusion-limited growth process in which local, short-range fluctuations in the concentration of modulating ligands at the growth front of the crystallites determine whether the **fcu** or **reo** structure forms, and that the two domains grow together in tandem. The formation of the **fcu** structure, for example, will take up terephthalate (BDC) linkers from the solution leading to a short-range excess of formate anions and eventually to an outcompetition of BDC by formate, causing the **reo** structure to grow nearby. Furthermore,

the domains of **fcu** and **reo** have an interface along {211}-type crystallographic planes which pass through the metal clusters and the cluster-ligand coordination sites, again suggesting that the concomitant growth of these defect structures is due to competitive coordination of the BDC linkers and formate ligands.¹⁷⁵

1.3.4 The Discovery of **hcp** and **hxl** UiO-67(Hf)

For a more in-depth discussion of the defect-mediated structures in this section, see:

M. J. Cliffe, E. Castillo-Martínez, Y. Wu, J. Lee, A. C. Forse, F. C. N. Firth, P. Z. Moghadam, D. Fairen-Jimenez, M. W. Gaultois, J. A. Hill, O. V. Magdysyuk, B. Slater, A. L. Goodwin and C. P. Grey, J. Am. Chem. Soc., 2017, 139, 5397–5404. [Ref. 12]

The studies in the section above focussed on UiO-66, but the extension of work to other members of the isorecticular family is important to provide increased understanding of the processes of defect formation in these Hf MOFs. In particular, the role of formic acid as modulator appears key to the formation of the defect-ordered nano-**reo** phase of UiO-66(Hf). This therefore inspired further investigation by Cliffe *et al.* into the effect of formic acid as a modulator in the synthesis of UiO-67(Hf),¹² which is isorecticular to UiO-66 but with a longer bidentate dicarboxylate linker derived from biphenyldicarboxylic acid (H₂BPDC). In **fcu** UiO-67, with the longer BPDC linker, linker vacancies are less stable and have not been detected to any appreciable degree; this framework therefore has the potential for different behaviour compared with UiO-66, in which linker vacancies can occur to high concentrations.^{180–182}

In the formic-acid-modulated synthesis of UiO-67(Hf) the nano-**reo** phase was not seen. Instead, the powder X-ray diffraction pattern indicated the presence of an ordered, single phase bulk crystalline material not observed previously. While the pattern had some reflections in similar locations to those seen for **fcu** UiO-67(Hf), indicating the structure was related, structure solution in fact indicated that a new, three-dimensional, hexagonal MOF had formed, with Hf₁₂ clusters rather than the Hf₆ clusters found in the **fcu** MOF.¹² The topology of this new MOF structure was determined to match the **hcp** net. Although not immediately obvious, this **hcp** UiO-67(Hf) framework can be related to the **fcu** framework by once again considering the inclusion of missing-linker defects in tandem with the discussion of plane defects earlier in this Chapter.

If the missing-linker defects order within some of the (111) planes of the parent **fcu** structure, i.e., between the close-packed planes (with stacking sequence ABCABC), a shear can occur resulting in the stacking sequence ABBAABBA [Figure 1.8]. The M_6 clusters, with coordination sites left vacant by the missing linkers, can then ‘condense’ together *via* the formation of μ_2 -OH bridges, in a manner similar to the face-sharing condensation of perovskites caused by shear, to give M_{12} ‘double’ clusters [Figure 1.8]. Rather than as nano-domains, this new defect-mediated MOF, **hcp** UiO-67(Hf) is obtained as an ordered single phase bulk material, with 18-coordinate $[[M_6(\mu_3-O)_4(\mu_3-OH)_4]_2(\mu_2-OH)_6]^{18+}$ clusters (as compared to the $[M_6(\mu_3-O)_4(\mu_3-OH)_4]^{12+}$ clusters which are 12-coordinate in the **fcu** MOF and 8-coordinate in the nano-**reo** domains).¹²

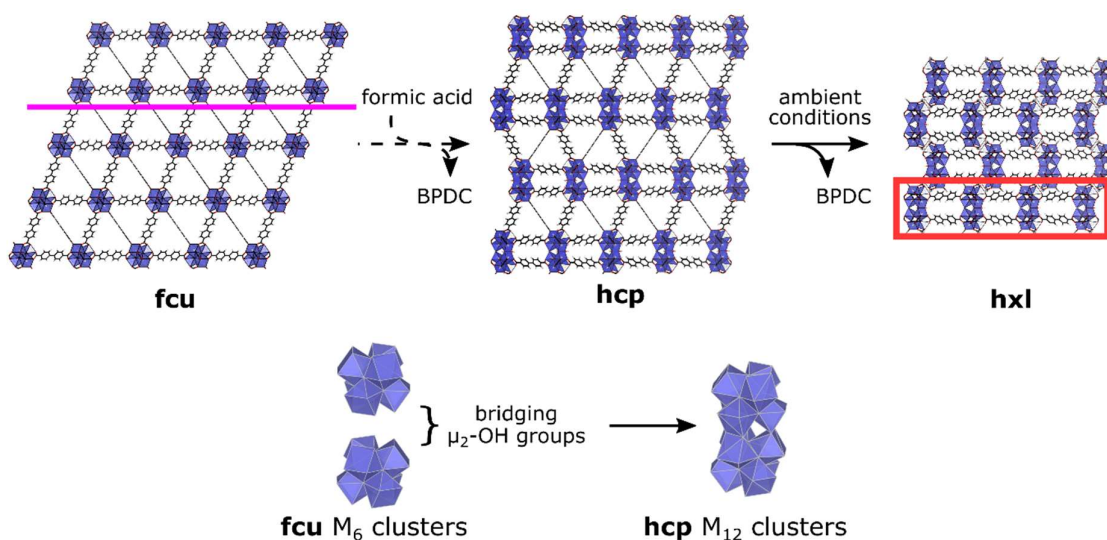


Figure 1.8. Derivation of phases of UiO-67 and the associated metal cluster condensation. The **fcu** phase (left) is viewed along the $[10\bar{1}]$ direction, highlighting the ABCABC stacking sequence of single clusters. The (111) plane, in which linkers are lost to form the **hcp** phase, is shown in pink. The **hcp** phase (centre) is viewed along the $[100]$ direction. This loses connectivity in the (001) planes to give the **hxl** phase (right), which can be delaminated to give **hns** nanosheets (red box). Dashed arrows show the differences in the synthesis conditions used to prepare different phases; solid arrows show post-synthetic treatments. The cluster condensation from two M_6 ‘single’ clusters in the **fcu** phase to one M_{12} ‘double’ cluster in the **hcp** phase is shown in polyhedral representation underneath. Crystal files from Refs. 165 and 12.

The structural relationship between the **fcu** and **hcp** frameworks can also be visualised by distorting the cubic structure along the $[111]$ direction so that the (111) plane of the **fcu** structure corresponds to the (001) plane of the **hcp**. This relationship explains the similarity in the powder X-ray diffraction (PXRD) patterns as the **fcu** (111) reflection, corresponding to the close-packed plane, is replaced by reflections corresponding to the (002), (100) and (101) pseudo-close-packed planes in the **hcp** structure, with the **fcu** (111) and **hcp** (101) reflections

in the same location, but with the **hcp** (002) and (100) reflections in particular enabling differentiation between the two phases.

This new **hcp** UiO-67(Hf) displays structural directionality in the framework; the *ab*-planes have twice as many linkers compared with those in the inter-plane, *c*-direction. Due to the resulting anisotropic stability of the framework (the *c*-direction linkers are no longer chemically identical to those in the *ab*-plane) Cliffe *et al.*¹² observed that selective topotactic delamination of the **hcp** material under gentle conditions produced a crystalline layered **hxl** structure *via* the—reversible—loss of further *c*-direction linkers; conceptually similar loss of metal-oxo coordination bonds has subsequently been observed to cause reversible structural transformations in other MOF materials.¹⁸³ Under more forcing conditions (such as sonication or grinding) the **hxl** material can be cleaved to give two-dimensional nanosheets, hereafter named **hns** UiO-67(Hf) [Figure 1.8].^{12,167,184}

Therefore, while modulated synthesis of UiO-67 using formic acid can be visualised as creating linker vacancies, these are compensated by an even greater defect-ordering process than that seen in the formation of nano-**reo** UiO-66, resulting in an even more significant change in the topology with the formation of the bulk hexagonal structure **hcp** UiO-67. This is one of the first examples of the synthesis of entire higher-dimensional defect-mediated structures. Furthermore, this study shows that by harnessing correlated defects it is possible to obtain previously inaccessible MOF topologies, such as nanosheets, with new and distinct properties.¹²

Just as for nano-**reo** UiO-66(Hf) the discovery of this second new defect-engineered phase of UiO family MOF provides insights into the reactions taking place during the synthesis. The **hcp** phase requires higher temperatures to form (consistent with other higher-nuclearity Hf and Zr MOFs)¹⁵³ than does the **fcu**; at intermediate temperatures a poorly-crystalline material formed. The reaction was also found to be slower with formic acid than for a synthesis containing hydrochloric acid, at least in part due to solubility issues; this, however, could have an effect on the resultant structure. The formation of **hcp** UiO-67(Hf) also appears to take place in stages; initially, a noncrystalline, inorganic aggregate forms, and then (following the time when the **fcu** framework would start to form) the **hcp** framework grows, with a rate suggesting that its precursor is in large excess.¹²

This observation once again indicates that the formation routes of the MOF, in particular the pre-crystallisation and early-crystallisation stages, are critical in determining the phase or structure which results. Studying these formation routes and the solution behaviour of MOF clusters and precursors in reaction conditions is, therefore, key to developing an understanding of the role of defect-engineering in the synthesis of new MOF phases and hence to the potential of new *rational design* of syntheses for still-unrealised MOFs.

1.4 Hafnium and Zirconium Clusters

Zirconium and hafnium are particularly favourable for the design of new MOF structures: in contrast to copper, for example, which often forms dinuclear ‘paddlewheel’ units¹⁸⁵, there is a rich variety of known zirconium and hafnium clusters from which MOFs could potentially be made, with a wide range of nuclearities, geometries and coordination densities.^{59,68,152,186,187} There are over 1300 structures containing between 3 and 21 Zr or Hf ions in their molecular formula—forming either molecular clusters or being part of an extended framework (including MOFs) —in the CCDC (Cambridge Crystallographic Database) alone.^{188*} Even accounting for the diversity of ligand species, a wide variety of Zr and Hf metal-oxide inorganic substructures or ‘core’ clusters (derived by removing peripheral ligands) is still observed. Understanding the nature of these clusters is crucial as the MOF cluster has a significant role in determining the resultant structure as well as potentially providing reactive sites which alter the properties of the MOF.^{62,64,189}

Although the most common cluster motif in Zr and Hf MOFs (e.g. in the UiO family⁵⁰) is the $M_6(\mu_3-O)_4(\mu_3-OH)_4$ cluster based on Zr_6O_8 octahedra,^{12,152,190} these ‘core’ clusters range from small, low-nuclearity molecular clusters through to large structures such as infinite polymeric chains,^{151,153,154,191,192} increasingly resembling the structure of high temperature, tetragonal ZrO_2 as nuclearity increases.¹⁹³ Just as in other extended metal oxide structures these metal (hydr)oxide clusters can share vertices,¹⁵² edges,^{12,61} faces and coordination-polyhedra (see Figure 1.3).^{152,194–196}

Hydrothermal—or, to generalise, solvothermal—synthesis has been used from the earliest syntheses of zirconium and hafnium MOFs and has become one of the most common synthesis methods.⁷ From the work on defect-ordering in UiO family MOFs discussed above it is clear that understanding the solution behaviour of the metal clusters in solution, and therefore the processes which occur in the MOF solvothermal syntheses, is key to understanding the resultant MOF phases.

* Cambridge Crystallographic Database, search performed July 2020

1.4.1 Zirconium and Hafnium Solution Chemistry

The behaviour of zirconium and hafnium ions in solution is quite complex and the structures of the metal complexes formed with solvent or other species have not been unambiguously determined: the solubility and structures observed are strongly dependent not only on the pH of the solution, as zirconium complexes are susceptible to hydrolysis,¹⁹⁷ but also on the presence of species such as coordinating ligands. While this section focusses on zirconium species, the behaviour and measurable properties of zirconium and hafnium clusters are very similar, as both are group IV metals with near-identical radii.^{61,172,182,198}

The choice of solvent affects the formation of the metal clusters in solution, the degree of Zr or Hf cluster aggregation being greatly affected in particular by the presence of water in the synthesis. In aqueous, and especially aqueous acidic conditions, the distorted-square-planar tetrameric species $[M_4(OH)_8 \cdot 16H_2O]^{8+}$ is dominant.^{196,197,199–203} This cluster is surrounded by a structured coordination sphere of water molecules^{130,204} similar to other nanoparticles in solution.²⁰⁵ This water coordination sphere is potentially the source of further hydroxide bridges between metal centres in condensation of the clusters.^{130,204,206–208}

The degree of hydrolysis, and subsequent aggregation, can be modulated by the use of additional reagents²⁰⁷ such as acid²⁰⁹ (which, as discussed earlier in the Chapter, in some MOF syntheses is required to form the crystalline framework^{74,210} and in others is used to control particle morphology^{48,190,210,211}). When the pH of the solution is altered a number of other species involving Zr^{4+} can exist in aqueous solutions: the metal ions have high charge density, arising from their +4 oxidation state, and so favour hard donor atoms, such as oxygen, to which they coordinate strongly. Zirconium (IV) and hafnium (IV) both have a small ionic radius but high charge density; therefore hydroxyl bridges and oxo- and hydroxo- capped clusters are predominant in the known Zr and Hf species; these range from hydroxides and water-coordinated complexes, through trimers and tetramers, to polymers with hydroxo bridges and oxo linkers.^{130,132,212} At low pH, mononuclear $Zr(OH)^{3+}$ is found at low $[Zr]$, and $Zr_2(OH)_6^{2+}$, $Zr_3(OH)_4^{8+}$ and $Zr_4(OH)_8^{8+}$ at higher $[Zr]$. At higher pH (>3) a greater range of mononuclear species is observed, such as $Zr(OH)_2^{2+}$, $Zr(OH)_3^+$ and $Zr(OH)_4$.¹⁹⁷

The presence of other acids or ligands (such as those necessary for MOF synthesis) will affect the nature of the complexed species, including triggering the formation of higher-

nuclearity clusters.^{130–134,213} The oxo- and hydroxo-groups coordinate more strongly than carboxylate anions, supporting the formation of the μ_3 -O and μ_3 -OH capped M_6 metal cluster seen in UiO-66.²¹⁴ Carboxylates, and other ligands coordinating through oxygen, are still frequently observed as cluster-terminating ligands^{215,216} as can be seen in the hydroxide/carboxylate mixed-ligand frameworks of some defective UiO family MOFs.^{132,135} As noted above, and in other recent work, formic acid in particular has been found to affect both the coordination and the nuclearity of the clusters from which hafnium MOFs form.^{12,141,160}

The inclusion of more than one species of carboxylic acid also affects the identity and stability of the metal complex formed. Carboxylic acids, including the monocarboxylic acids often chosen as 'modulators' in MOF syntheses, can possess a wide range of metal-ligand binding strengths as different carboxylic acids have different coordination strengths.^{130,135} A judicious choice of carboxylic acid can therefore 'block' coordination sites on a cluster to further nucleophilic attack, preventing cluster aggregation in the case of water/hydroxides or the formation of multi-cluster framework species in the case of linker coordination.^{130,135,217}

The degree of cluster aggregation is also directly affected by the temperature and duration of the synthesis. On heating acidic zirconium solutions, for example during a solvothermal synthesis, the metal ions first form complexes involving Zr^{4+} bridged by hydroxyl bridges, assumed to originate from the water molecules in the first coordination sphere.¹³⁰ At higher temperatures further dissociation can occur to give oxo- compounds, the formation of which is difficult to reverse.¹³⁰ The conversion of bridging OH groups from $Zr-(OH)_2-Zr$ to $Zr-O-Zr$ can lead to aggregation to form first the octameric $Zr_8(OH)_{20}^{12+}$ and then the 10-mer or even gel-like two-dimensional tetrameric sheets.^{133,218} This complex formation can lead to precipitation of sparingly soluble salts of indefinite composition, which helps to explain the observed formation of inorganic noncrystalline aggregates as precursors during the synthesis of MOFs.^{12,219} Like heating, ageing the reaction mixture can increase the amount of bridging μ_2 -OH between metal centres and also encourages their conversion to μ_3 -O and μ_3 -OH groups.^{130,190,201,218} Ageing therefore favours the formation of higher-nuclearity Zr or Hf clusters.²²⁰

The solutions containing these metal complexes therefore represent a highly complicated system, the exact nature of the clusters depending on many factors including concentration, pH, solvent, temperature and the composition of the reaction mixture (such as the inclusion of additional species alongside the metal salt and linker). Altering any of these parameters will directly influence the cluster formation and, in the case of MOF synthesis, ultimately help to determine the identity of the MOF that is formed. While it is clear that water and modulating ligands are critical to the identity and stability of the resultant metal clusters (from ligand-terminated molecular clusters²⁰¹ through to MOFs^{130–134,221}), the exact interplay of these factors, especially in multi-species reaction mixtures, is not well understood. As discussed below, even a frequently-used solvent can display great complexity and thus even small changes can greatly affect the cluster formation.

1.4.2 Solvent Interactions in Synthesis Mixtures

DMF, formic acid and water in MOF synthesis

Across the wider literature a variety of solvents and conditions have been used in the synthesis of zirconium MOFs and their related analogues with other metals; among these, syntheses using *N,N*-dimethylformaldehyde (DMF) and water as solvents are particularly popular.¹⁵⁶ DMF has been used from the very first syntheses of UiO family MOFs,⁵⁰ while water also features prominently in the search for more environmentally-friendly reaction solvents.^{151,222,223} However, the use of these solvents has been found to greatly affect the resultant structure of the MOF and its constituent clusters. Modulating acid is also often used in these syntheses; as highlighted earlier in this Chapter, formic acid in particular has been found to have a significant effect on the MOF phase.^{12,141} Water, DMF and formic acid can all be found within the MOF structure, for example as terminating ligands on the metal clusters,^{148,149} as well as determining the phase of the MOF which forms^{151,163,224} including *via* the creation of clusters of different nuclearity.^{12,151} In order to further explore the role of these solvent species in the formation of MOFs, this work predominantly uses solvents which comprise some ratio of *N,N*-dimethylformaldehyde (DMF), formic acid, and water.

Hf-free solutions

While DMF, formic acid and water as separate components are all standard and frequently-used solvents, when mixed they do not behave in a straightforward manner—even without

the addition of the metal salt used to make metal clusters, or the linkers which combine with the clusters to give MOF frameworks. The interactions within the solvent must be understood before the effect on any additional components (such as metal clusters) can be explored.

Alongside weaker transient van der Waals forces and dipole-dipole interactions, all three of the solvent components are capable of hydrogen-bonding but with different strengths: ^{225,226} hydrogen bonds can be as short as 1.9 Å (as in water and some other O-H—O systems)^{227–229} or as long as 4 Å (as in some C-H—O systems).^{228,230} In pure DMF, hydrogen-bonds can be formed between molecules in dimers with a variety of potential configurations; the dominant configurations involve hydrogen-bonds between the carbonyl oxygen (the strongest hydrogen-bond acceptor) on one molecule and a proton from each of the methyl groups (despite being weak donors) in the second molecule, giving a total of four hydrogen-bonds per dimer with C-H—O bond lengths of 3.2–3.5 Å.²²⁵ Spatial correlations up to ~16 Å—three solvation shells—are also noted.²²⁸

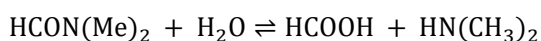
Water is well-known to have strong intermolecular hydrogen-bonds, leading to a variety of dynamic structures.^{231–233} In DMF-water mixtures the hydrogen-bonding between water molecules is dominant and even enhanced by the presence of low concentrations of DMF, resulting in water-rich and DMF-rich regions, but at higher concentrations of DMF the water structuring breaks down and more hydrogen-bonding to DMF occurs.^{230,234–236} The preferred orientations of these hydrogen-bonding networks include the oxygen atom in a water molecule facing the DMF methyl groups (with 0.25–0.45 hydrogen bonds per oxygen at high [DMF] and a C—O distance of ~3.7 Å) and the carbonyl oxygen in the DMF molecule facing one of the water protons (with ~0.4 hydrogen bonds per oxygen and an O—O distance of ~2.9 Å).²³⁰

When formic acid is considered these interactions become much more complex. Carboxylic acids have the propensity to form dimers *via* hydrogen-bonding between the two COOH groups. Liquid formic acid can also include hydrogen-bonds between the carbonyl oxygen and the formate proton; a combination of these two bonding modes (to increase the overall number and strength of bonds) can result in the formation of chain-like hydrogen-bonded structures with further formic acid molecules.^{237,238} When water is also involved, studies

suggest a variety of possible hydrogen-bonding modes, most commonly with between one and two water molecules and one formic acid per hydrogen-bonding 'unit', with both the formic acid CH and COOH protons involved.²³⁹ The acid carbonyl oxygen is the strongest donor but both the acid carbonyl oxygen and the acid COOH proton engage in strong bonds with the water molecules; in the mixture of formic acid and water, the amount of acid-acid correlation decreases as the amount of water increases (although the acid-acid bonds are less disrupted than is observed for other carboxylic acids) but overall there is an increase in coordination number of both species.²⁴⁰

A mixture of DMF, formic acid, and water therefore is likely to contain some level of local dynamic heterogeneity owing to the differences in the range of hydrogen-bonding strengths between molecules. Furthermore, hydrogen-bonding reduces the speed of proton exchange, compared to the fast exchange seen in non-hydrogen-bonded acid-water systems, meaning that species in these systems will likely have complicated exchange processes.²⁴¹

MOF syntheses frequently use elevated temperatures and so the effect of temperature on the reaction solvent should also be considered. It is known that the lifetime of hydrogen bonds decreases as temperature increases.²⁴² In these systems water-DMF hydrogen bonds are affected more than water-water bonds, implying that the microheterogeneity of these systems is likely to increase at higher temperatures.²⁴³ Furthermore, DMF is known to decompose at high temperatures to form CO and HNMe₂;²⁴⁴ however, when heated in the presence of water DMF can instead hydrolyse to give formic acid and dimethylamine (DMA):²⁴⁵



The effect of this reaction is extremely important: DMA is more basic than formic acid is acidic, resulting in an overall basic solution; the higher the temperature, the further the equilibrium shifts to the right, and so the more basic the solution (up to a pH of ~11 if formic acid is not added).²⁴⁵ Therefore, the temperature of pH-sensitive reactions using DMF as solvent (either non-dry, or with added water) needs to be carefully considered in order to understand its effect on the reaction.

When an acid is also added to the solution this will again affect the proton concentration (pH is difficult to define in non-aqueous solutions): not only will the DMA become protonated, but an increase in acid solubility at higher temperatures will work to counteract

the decrease in proton concentration from the greater hydrolysis of DMF resulting in a less basic solution. While many acids could be used to change the acidity of the solution without further significant interactions, the choice made in syntheses in this work to use formic acid results in a more complex situation as the addition of formic acid affects the above equilibrium process and disfavours the decomposition of DMF. Formic acid also has the potential to decompose at elevated temperatures, forming either CO₂ and H₂ or CO and H₂O, depending on the pathway^{246–248} (influenced by temperature and other reagents; the former pathway is potentially favoured by the presence of water and DMF).^{249,250} Thus temperature will again influence the solvent composition and acidity, although at the temperatures used in this work the equilibrium positions of the decomposition of DMF and of formic acid are likely to remain close to the starting materials.

The hydrogen-bonding and structuring of the solvent will also be altered by the decomposition reaction. The pH/proton concentration and coordination chemistry of these common MOF reaction solvents, are therefore not fixed throughout a reaction, nor (as is evident from several studies^{251–253}) do the choice of temperature and acid modulator and the addition of water only affect the MOF formation directly.

Hf-containing solutions

The presence of metal salts and clusters will also (chemical reactions aside) affect the solvent structuring. As well as the effects on proton lability and solution pH due to Lewis acidity, nanoparticles in solution often have coordination or solvation shells.²⁰⁵ While it is known that the distorted square-planar tetramer cluster [M₄(OH)₈·16H₂O]⁸⁺ in water displays solvent structuring^{130,204} it is extremely important to consider the possibility, and effects, of solvent structuring in more complex mixtures. Previous studies have suggested that ionic solutes in formic acid/water mixtures have a first solvation shell preferentially populated by water and a second shell populated by formic acid, resulting in a slightly reduced solute diffusion coefficient.²⁵⁴ This could potentially also be the case for solutes such as MOF-related metal clusters in solutions of DMF, formic acid and water; any preferential solvent structuring around clusters will likely create further microheterogeneities, as well as affecting the interactions between clusters, and therefore influence the reactions of these species.

As mentioned in the previous section, the solvent systems only become more complex when heat is applied, and this is no less true for solutions containing the metal salt and cluster precursors. As well as any kinetic and thermodynamic effects of elevated temperature, for example on the preferred aggregation of cluster species,^{220,255,256} changes in acidity of the solution will affect the protonation of the clusters—and, in full MOF reactions, the protonation of the organic linkers—and therefore their ability to coordinate or aggregate. Alteration of the composition of the solvent, due either to incorporation into forming metal clusters or to decomposition, will affect the hydrogen-bonding and coordination shells around the clusters and hence the interactions between clusters and (if present) the linkers required to form MOFs. As mentioned earlier, fluctuations in the local concentration of formic acid and water have also been hypothesised to play a key role in the defect structuring of the MOF framework nano-**reo** UiO-66(Hf) *via* the competitive formation of the **reo** or the **fcu** structure depending on the solvent interactions;¹⁷⁵ even the use of hydrochloric acid as modulator has been shown to affect the synthesis of UiO-66 due to oscillatory fluctuations in the concentration of autocatalytic H⁺ driving the coordination network condensation.²⁵⁷

Alongside understanding the nature of the metal clusters, therefore, it is essential to examine the interactions in the reaction solvent in order to determine the effect of different conditions on the synthesis products.

1.5 Studying the Formation of MOFs

In order to understand, and therefore control, how MOFs form, they must be studied at all stages, from their precursors through to the final structures. MOF self-assembly, as stated earlier in this Chapter, is in many cases a 'black box' in which little is known about intermediates in the synthesis; however, an improved understanding of the evolution of MOFs in synthesis can drive strategies for the development of new MOF materials.^{78,258} The importance of *in situ* (including *in-operando*) techniques is well-established and a range of complementary techniques have already been applied to the precursors, syntheses, and formation routes of other materials such as metal oxides^{259–264} and zeolites.^{79,265,266} In the relatively young field of MOFs, however, while these techniques are familiar when applied to already-synthesised MOF materials,²⁶⁷ for example in determining changes in (crystal) structures during heating,^{268,269} or for gas sorption measurements,^{270,271} only recently has their use before and during MOF syntheses come to prominence.^{219,267,272,273} These investigations of syntheses are perhaps most frequently focussed on crystallisation processes and kinetics^{19,274–277} but *in situ* measurements can also reveal clues about atomic-scale structural evolution and local transitions,²⁶⁸ amorphous and disordered phases, and solvation structures and solution processes²⁷⁸ all of which are key to understanding the formation of MOFs.

Similarly, *in situ* work on the synthesis of UiO family MOFs has mainly investigated the crystallisation kinetics of UiO-66(Zr).^{74,279,280} There are, indeed, *ex situ* studies investigating the formation of MOF-related clusters and precursors,²⁵² and one *in situ* study has shown that in the solvothermal synthesis of UiO family MOFs, the M_6 clusters form in solution with the organic linkers subsequently coordinating to them to nucleate and grow the 3D framework.¹² However, thus far the formation of UiO family MOFs prior to crystallisation is relatively underexplored – in particular, the behaviour of the reaction mixture including metal cluster precursors and solvent. This Chapter has indicated that the nature of the Hf and Zr clusters is integral to the formation of the MOF; the role played by the synthesis conditions in determining the nuclearity and topology of the metal clusters, and hence the formation of the MOF, must therefore be investigated.

1.6 Characterisation Techniques

Many characterisation techniques can be used to understand the structure and behaviour of MOFs including their reactions and stages in their synthesis. This section introduces the main techniques used and their suitability in characterising the materials explored in this thesis; more complete and rigorous theory may be found elsewhere.

1.6.1 X-ray Scattering

X-ray scattering techniques are some of the most powerful and most widely-used methods used to explore the structures of both crystalline and non-crystalline materials.^{281–283} The electrons in an atom scatter X-ray radiation; each type of atom will scatter a beam of X-rays approximately proportionally to the number of its electrons. The scattering from multiple atoms, and from different kinds of atoms, within a material will therefore result in interference between the scattered beams. The structural relationship between atoms (including planes of atoms, in crystalline materials) affects this interference; thus, by detecting and analysing the scattered radiation from a sample, information can be obtained about the structure of the material.

This thesis uses two such techniques, powder X-ray diffraction (PXRD)—particularly useful in the study of crystalline materials—and X-ray pair distribution function (XPDF) analysis—which provides information about both long- and short-range structure and ordering within a material. Both of these techniques have the ability to measure structures at longer lengthscales (to the order of nanometres), such as those seen in MOFs and related metal clusters, unlike other common techniques such as extended X-ray absorption fine structure (EXAFS) or nuclear magnetic resonance (NMR).

Theory of X-ray Scattering

A more complete and rigorous introduction to X-ray scattering can be found in Refs. 284–286.

A beam of X-rays of wavelength λ moving in the direction \mathbf{r}_i can be modelled by the complex plane wave equation

$$\psi(\mathbf{r}_i) = \psi_0 e^{i\mathbf{k}\cdot\mathbf{r}_i} \quad (1)$$

where $k = \frac{2\pi}{\lambda}$ and ψ is the wavefunction.

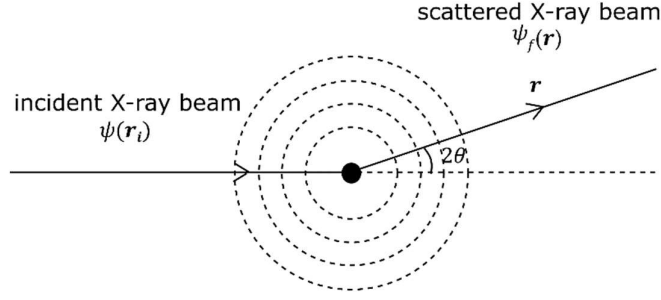


Figure 1.9. Schematic of an X-ray beam being scattered by an atom (viewing a 2D cross-section). The atom scatters X-rays in a sphere around it.

If this X-ray beam interacts elastically with an atom (assuming the energy of the X-rays to be such that no energy is absorbed from or given out to the X-ray beam by the atom), then the X-rays will be scattered as a spherical wave but with the same energy; for a given displacement vector \mathbf{r} the scattered wave will have a parallel wavevector \mathbf{k}_f [Figure 1.9] such that

$$\psi_f = f \psi_0 e^{i\mathbf{k}_f \cdot \mathbf{r}}. \quad (2)$$

where f is the form factor, which determines how much the atom scatters.

If the beam of X-rays interacts instead with more than one atom, and assuming that the scattering barely affects the incident beam, then the contribution of the j th atom, at position \mathbf{R}_j , to the scattered wave will be given by

$$[\delta\psi_f]_j = \psi_0 f_j e^{i\mathbf{k}_i \cdot \mathbf{R}_j} \left(\frac{e^{i\mathbf{k}_f \cdot (\mathbf{r} - \mathbf{R}_j)}}{|\mathbf{r} - \mathbf{R}_j|} \right) \quad (3)$$

which can be written as

$$[\delta\psi_f]_j = \psi_0 f_j e^{i\mathbf{k}_f \cdot \mathbf{r}} \left(\frac{e^{i\mathbf{Q} \cdot \mathbf{R}_j}}{|\mathbf{r} - \mathbf{R}_j|} \right) \quad (4)$$

where the scattering vector $\mathbf{Q} = \mathbf{k}_i - \mathbf{k}_f$ and the phase difference between the waves is given by $\mathbf{Q} \cdot \mathbf{R}_j$. Therefore the net scattered wave will be given by

$$\psi_f = \psi_0 e^{i\mathbf{k}_f \cdot \mathbf{r}} \sum_{j=1}^N f_j \left(\frac{e^{i\mathbf{Q} \cdot \mathbf{R}_j}}{|\mathbf{r} - \mathbf{R}_j|} \right) \quad (5)$$

Returning to the form factor, this is the Fourier transform of the electron density around the atom and so will be related to the atomic number and shape of the atom, and can be quantified by a function $f_j(Q) = \iiint \beta_j(\mathbf{R}) (e^{i\mathbf{Q}\cdot\mathbf{R}}) d^3\mathbf{R}$ where β_j is the 'scattering length density (SLD) function' of atom j . In X-ray scattering, this is proportional to the electron density.

If the distance from the sample to the detector is large then in Eqn. 5 $|\mathbf{r} - \mathbf{R}_j| \approx |\mathbf{r}| = r$ and so the equation of the net scattered wave can be rewritten as the structure factor

$$F(\mathbf{Q}) = \psi_0 e^{ik_f r} \sum_{j=1}^N f_j(Q) \left(\frac{e^{i\mathbf{Q}\cdot\mathbf{R}_j}}{r} \right). \quad (6)$$

which is proportional to the differential cross-section, that is, a measure of the amount of scattering at each direction. The differential cross-section is the number of counts (e.g. X-ray photons) per unit solid angle divided by the number of incident counts per unit area of the beam), and is proportional to

$$\left| \sum_{j=1}^N f_j(Q) (e^{i\mathbf{Q}\cdot\mathbf{R}_j}) \right|^2. \quad (7)$$

However, detectors cannot directly measure $F(\mathbf{Q})$, only the amplitude

$$I(\mathbf{Q}) = |F(\mathbf{Q})|^2 = \frac{|\psi_0|^2}{r^2} \left| \sum_{j=1}^N f_j(Q) (e^{i\mathbf{Q}\cdot\mathbf{R}_j}) \right|^2. \quad (8)$$

For each unit area δA of the detector, which subtends a solid angle $\frac{\delta A}{r^2}$ of the scattered radiation, there will be a scattering rate $|F(\mathbf{Q})|^2 \delta A$. Thus the amplitude measured by the detector per unit area can be simplified as

$$I(\mathbf{Q}) = cst. \times \left| \sum_{j=1}^N f_j(Q) (e^{i\mathbf{Q}\cdot\mathbf{R}_j}) \right|^2 \quad (9)$$

1.6.2 Powder X-ray Diffraction

Powder X-ray Diffraction (PXRD) is a powerful technique for characterising crystalline materials and is often applied in the study of crystalline MOFs. Different crystal structures produce different PXRD patterns, allowing them to be distinguished; refinement techniques allow comparison and adjustment of model structures against experimental datasets.

Alongside this, different peak shapes and peak widths can provide information about the particle size, disorder, strain, and other properties of the material.

Theory of Bragg scattering from crystalline materials

A more rigorous introduction to Bragg diffraction can be found in Refs. 285,286.

In a perfect crystalline material atoms are arranged in a periodically-repeating lattice with a unit cell defined by the vectors $(\mathbf{a}, \mathbf{b}, \mathbf{c})$ with angles between them (α, β, γ) ; that is, for a scatterer (atom) at location \mathbf{R}_j there will be an identical scatterer at each point translated by integer multiples of \mathbf{a} , \mathbf{b} , and \mathbf{c} . The SLD function is therefore

$$\beta(\mathbf{R}_j) = \beta(\mathbf{R}_j + n_1\mathbf{a} + n_2\mathbf{b} + n_3\mathbf{c}) \quad (10)$$

where all n are integers. It can be seen that the intensity measured by a detector, $I(\mathbf{Q}) = |F(\mathbf{Q})|^2$, is therefore related to the square of $e^{i\mathbf{Q}\cdot\mathbf{R}_j} = e^{i\mathbf{Q}\cdot(n_1\mathbf{a} + n_2\mathbf{b} + n_3\mathbf{c})}$ and thus will only be non-zero if the scattering is constructive, that is, if $\mathbf{Q}\cdot(n_1\mathbf{a} + n_2\mathbf{b} + n_3\mathbf{c}) = 2\pi n$. This is true for $\mathbf{Q} = h\mathbf{a}^* + k\mathbf{b}^* + l\mathbf{c}^*$ where h, k and l are integers and \mathbf{a}^* , \mathbf{b}^* and \mathbf{c}^* are vectors in reciprocal space (where $\mathbf{a}^* = \frac{2\pi\mathbf{b}\times\mathbf{c}}{\mathbf{a}\cdot(\mathbf{b}\times\mathbf{c})}$ etc. and so $\mathbf{a}^* \cdot \mathbf{a} = 2\pi$, $\mathbf{b}^* \cdot \mathbf{b} = 2\pi$ and $\mathbf{c}^* \cdot \mathbf{c} = 2\pi$). This means that scattering from a perfect crystalline sample is only non-zero for specific values of \mathbf{Q} ; these points of scattered intensity are called Bragg peaks. Giving the position \mathbf{R}_j of an atom as $x_j\mathbf{a} + y_j\mathbf{b} + z_j\mathbf{c}$, the structure factor $F(\mathbf{Q})$ can then be written as

$$F(hkl) = \sum_{j=1}^N f_j(Q) \exp[i(hx_j + ky_j + lz_j)]. \quad (11)$$

The indices h, k and l can be used to specify planes within a crystallographic unit cell which intersect the axes of the cell at \mathbf{a}/h , \mathbf{b}/k and \mathbf{c}/l . These planes are therefore defined according to their Miller indices (hkl) .

Scattering from a crystal can be considered in relation to these planes. When an incident X-ray beam of wavevector \mathbf{k}_i and wavelength λ is elastically scattered at angle θ by identical atoms in two lattice planes with spacing d_{hkl} , one 'ray' will travel further than the other and so, once scattered, they will have two different phases. The change of phase between the two 'rays' is given by the path length difference $2(d_{hkl} \sin \theta)$ [Figure 1.10].

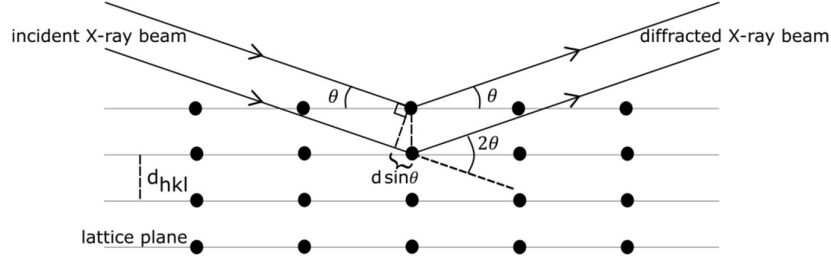


Figure 1.10. Schematic diagram of X-ray diffraction from atoms in (hkl) planes of a simple two-dimensional lattice.

Constructive interference between the two scattered rays will occur only when the change of phase is a multiple of λ . These conditions are given by Bragg's law,

$$n\lambda = 2d_{hkl} \sin \theta. \quad (12)$$

This can also be understood in terms of the scattering vector; for $\mathbf{Q} = \mathbf{k}_i - \mathbf{k}_f$ then the angle between \mathbf{k}_i and \mathbf{k}_f is given by 2θ . For wavevectors with magnitude $\frac{2\pi}{\lambda}$ then the change of phase is given by $\mathbf{k}_i \cdot \mathbf{k}_f = \left(\frac{2\pi}{\lambda}\right)^2 \cos 2\theta$. To obtain the relationship in terms of \mathbf{Q} ,

$$|\mathbf{Q}|^2 = (\mathbf{k}_i - \mathbf{k}_f)^2 = k_i^2 + k_f^2 - 2\mathbf{k}_i \cdot \mathbf{k}_f \quad (13)$$

As k_i and k_f are both equal to $\frac{2\pi}{\lambda}$, this simplifies to

$$|\mathbf{Q}|^2 = 2 \left(\frac{2\pi}{\lambda}\right)^2 - 2 \left(\frac{2\pi}{\lambda}\right)^2 \cos 2\theta = 8 \left(\frac{\pi}{\lambda}\right)^2 (1 - \cos 2\theta) \quad (14)$$

giving

$$|\mathbf{Q}| = Q = \frac{4\pi \sin \theta}{\lambda}. \quad (15)$$

Bragg peaks occur when $\mathbf{Q} = h\mathbf{a}^* + k\mathbf{b}^* + l\mathbf{c}^*$ following the requirement $\mathbf{Q} \cdot (n_1\mathbf{a} + n_2\mathbf{b} + n_3\mathbf{c}) = 2\pi n$ (see above). This can be evaluated in one dimension as $(\mathbf{Q}) \cdot (n\mathbf{a}) = 2\pi n$. Since in one dimension scalar values can be used, and given a spacing between crystallographic

planes d , $Q(nd) = 2\pi n$ and so the value of Q for which Bragg scattering is observed from these planes is given by

$$Q = \frac{2\pi}{d}. \quad (16)$$

Measurement

Using monochromatic (single, constant wavelength) X-rays, and measuring the intensity of scattering over a range of values of θ , the diffraction data can be plotted in terms of intensity versus 2θ or versus Q . Q has the advantage of being independent of radiation wavelength and thus can be used to compare data from different instruments.²⁸⁴ As mentioned above, coherent, constructive scattering will only occur when the change of phase is a multiple of λ , which translates to specific values of θ and of Q . Therefore the plot will show peaks of intensity at these values (Bragg peaks, as mentioned above). The locations of the Bragg peaks reveal information about the symmetry and lattice plane spacing in the sample; the intensity is related to the SLD function and therefore to the type of atoms in that lattice plane.

Practical Considerations

Metal-organic frameworks usually have long-range order i.e., are crystalline and so X-ray diffraction is a particularly useful technique for their characterisation and structure solution. However, many samples of MOF are microcrystalline (i.e., insufficiently large for single-crystal diffraction) and so powder X-ray diffraction techniques must be used.²⁸³ These microcrystalline samples are mostly randomly oriented (crystallites with morphologies such as needles or plates may have some degree of orientation relative to each other; this can affect the resultant peak shapes in the diffraction pattern and hence can be accounted for with a peak shape parameter during refinement). In order to account for these multiple orientations, the powder sample is often rotated under the beam to ensure the orientations of the crystallites can be averaged out, thereby reducing the effects of orientational artefacts such as sample texture. A monochromatic X-ray beam will give 'cones' of diffracted radiation from the rotating sample; by rotating both the radiation source and the detector around an arc of fixed radius (Bragg-Brentano geometry), the intensity of diffracted radiation at a given angle can be measured. This gives a one-dimensional plot of intensity *vs* 2θ (or Q) which can be interpreted as discussed above.

Refinement

An understanding of the likely structure of a sample (i.e., the size and symmetry of the unit cell) may be used to determine whether the Bragg peaks in an experimentally-observed pattern can be indexed (i.e., assigned Miller indices) in a way which is consistent with those expected from that structure. This is the principle behind Pawley refinement,²⁸⁷ the dominant method of analysing powder X-ray diffraction data used in this thesis. In this process, each peak in the pattern is fitted using parameters describing instrumental zero error, peak position, peak width, peak shape and peak intensity. All of these parameters are refinable (i.e., the peak intensity is not calculated from a proposed structure, unlike in Rietveld refinement; the intensity of each peak is a separate parameter). Constraints are applied to peak positions using a proposed size and symmetry of the crystal structure unit cell to obtain the Miller indices (hkl) of crystallographic planes; these peak positions can be used to refine the cell parameters.

If a crystal structure is known, including atomic positions, the intensities of Bragg peaks can be calculated *via* $F(hkl)$ values. These intensities are not refined but instead are used to optimise the atomic positions, allowing the theoretical structure to be refined until it agrees with the experimental data (the principle behind Rietveld refinement^{288,289}). Comparisons using Pawley and Rietveld methods may be performed using least-squares refinement, where at each step i , $R = \sum_i w_i (Y_{i,obs} - Y_{i,calc})^2$ is minimised ($Y_{i,obs}$ is the experimental value, $Y_{i,calc}$ is the calculated value, and w_i is a weighting based on the size of the values). Structure solution from diffraction data is not carried out in this thesis and so will not be discussed further.

Powder X-ray Diffraction and Defective Materials

Since Bragg diffraction requires crystalline materials with long-range order, materials with deviations from this long-range order are more challenging to characterise. Particles of small size cause peak broadening, which can be modelled during refinement but may obscure features in the pattern.

Turbostratic disorder (i.e., loss of order in one crystallographic direction, such as when the stacking sequence between planes, or distances between planes, in one direction, are not consistent) causes peak absences and asymmetric broadening dependent on (hkl).²⁹⁰ For a

sample with randomly rotated or translated **ab** planes, the *d*-spacing in the **c** direction will not be affected and so (00*l*) Bragg peaks will remain unaffected; however, lattice planes with dependency on **a**, **b** and **c** will no longer have any kind of order and so will not produce coherent scattering, resulting in absent (*hkl*) peaks. Lattice planes perpendicular to the **ab** planes will have a range of *d*-spacings up to the maximum of the original non-disordered spacing; given $Q = \frac{2\pi}{d}$, this will result in an asymmetric broadening of (*hk0*) peaks towards high-*Q*. For a sample with disorder in the *spacing* between planes in the **c** direction, this disorder will affect the spacing of any lattice planes other than those normal to the **c** direction and so any peaks dependent on *l*, including both (00*l*) and (*hkl*) peaks, will be lost. (*hk0*) peaks will, however, remain sharp (although given the likelihood of some turbostratic disorder, they may likely become broadened).

High levels of defect ordering may produce a different characteristic powder X-ray diffraction pattern, as discussed earlier in this Chapter in the case of the nano-**reo** phase of UiO-66(Hf); for example, defect correlation which leads to a change in symmetry will result in different Bragg peaks. Defects which are not ordered may also affect the peak shapes, broadening, and intensities but it can be difficult to determine the nature or concentration of these defects using X-ray diffraction data alone and so other complementary characterisation techniques are necessary for a full understanding of these materials.⁹⁸

1.6.3 X-ray Pair Distribution Function

While PXRD is useful in understanding the structures of crystalline MOFs, Bragg diffraction cannot be used to study non-crystalline species such as MOF-related molecular clusters. Additionally, due to the similarities between the PXRD patterns of some MOF structures (including the **fcu** and **hcp** UiO family MOFs),^{12,251} it is not always immediately obvious that a MOF structure with a different cluster has formed; a separate method, which gives insight into the local structure of the MOF, is required.

Studies on Zr and Hf clusters to track or solve their structures are not straightforward (especially *in situ* studies of solvothermal syntheses). Solution NMR is extremely challenging as the key nuclei (¹⁷O, ⁹¹Zr, ¹⁷⁷Hf and ¹⁷⁹Hf, in the absence of organic linker species^{291,292}) all either have large quadrupolar moments (e.g. $Q(^{177}\text{Hf}) = 3.4 \text{ b}$ and $Q(^{179}\text{Hf}) = 3.8 \text{ b}$),²⁹³ have low gyromagnetic ratios (e.g. $\gamma(^{179}\text{Hf}) = -0.682 \times 10^7 \text{ rad/Ts}$), or are of very low abundance (e.g.

$^{17}\text{O} = 0.038\%$). While techniques such as extended X-ray absorption fine structure (EXAFS) methods can identify Zr and Hf species in solution, and are sensitive to species with low abundance, this technique is limited to smaller molecular clusters due to multiple scattering events reducing the sensitivity required to observe longer-range coordination.²⁰¹

X-ray pair distribution function (XPDF) measurements can acquire structural information on non-crystalline species and are particularly sensitive to heavier elements such as Zr and Hf owing to their high electron density. When applied to MOFs, XPDF measurements can be used to understand the local structure of disordered and non-crystalline MOFs and their clusters and precursors,²⁷³ and to investigate the interactions between clusters and coordinating molecules.²⁶⁷ Previous work has demonstrated that *ex situ* XPDF measurements are sensitive to the identity of the cluster in UiO family MOFs and can clearly distinguish between isolated Zr atoms, Zr_6 clusters, and Zr_{12} clusters.¹² *Ex situ* XPDF measurements can detect and differentiate between tetramer and single cluster species in room temperature solutions related to UiO family MOF syntheses.²⁹⁴ *In situ* techniques, including XPDF, are well-regarded in enabling investigation of the formation of MOFs and related inorganic materials,^{267,273,295,296} having been successfully used to track the size of interlinked cluster aggregates forming MOF crystallites in solvothermal UiO-66 syntheses,²⁹⁴ as well as of metal oxido nanoclusters.^{260,261,263,297}

Theory of X-ray Pair Distribution Function Analysis

A more complete introduction to Pair Distribution Function Analysis can be found in Refs. 284,298–302.

Pair distribution function analysis resembles X-ray diffraction analysis insofar as it involves the Fourier transform of scattering data. However, unlike X-ray diffraction analysis, XPDF uses total scattering data (which may include the Bragg scattering data). Furthermore, as XPDF is often used to consider the local structure i.e., small interatomic distances, the Fourier transform process means that data must be collected to higher Q values than for PXRD.

In order to understand the pair distribution function the scattering length density (SLD) function, β_j , must be revisited. As stated in Eqn. 9 the scattered intensity, $I(\mathbf{Q})$, is

proportional to the differential scattering cross-section, which is given by

$$|\sum_{j=1}^N f_j(Q) (e^{i\mathbf{Q}\cdot\mathbf{R}_j})|^2$$

where the atomic scattering form factor is $f_j(Q) = \iiint \beta_j(\mathbf{R}) (e^{i\mathbf{Q}\cdot\mathbf{R}}) d^3\mathbf{R}$.

This means that the differential scattering cross-section can be written as proportional to $|\iiint \beta(\mathbf{R}) (e^{i\mathbf{Q}\cdot\mathbf{R}}) d^3\mathbf{R}|^2$. This is related to the auto-correlation function of $\beta(\mathbf{R})$, which is a convolution of the electron density in the structure with its inverse, and which provides information on the distance distribution of structures within $\beta(\mathbf{R})$. The auto-correlation function can be written as $\iiint \beta(\mathbf{R}')^* \beta(\mathbf{R}' + \mathbf{R}) d^3\mathbf{R}'$. For non-crystalline structures this function is spherically symmetric.

By considering the integral of the auto-correlation function over all space for a given separation r between atoms, and assuming atoms have a uniform SLD, then the number of atoms of type l at a separation r from an atom k in spherical shell of thickness dr is given by $n_{kl}(r) = 4\pi r^2 \rho_l g_{kl}(r) dr$, where ρ_l is the number density of atoms of type l ($\rho_l = c_l \rho_0$ where c_l is the atomic concentration and ρ_0 the average number density of atoms in the sample). The overall PDF, $g(r)$, is the sum of all the separate PDFs $g_{kl}(r)$ weighted by the scattering power of the atoms:

$$g(r) = \sum_{k,l=1} c_k c_l f_k(Q) f_l(Q) [g_{kl}(r) - 1] . \quad (17)$$

In order to calculate the pair distribution function, therefore, the atomic composition of the sample must be known.

The overall PDF can also be obtained by an inverse Fourier transform from the differential scattering cross-section and hence from the scattering intensity $I(\mathbf{Q})$. From Eqn. 9, the scattering from a sample is measured as $I(\mathbf{Q})$. Applying corrections and normalisation (see below), the total scattering function $S(\mathbf{Q})$ is obtained as

$$S(\mathbf{Q}) = 1 + \frac{I(\mathbf{Q}) - \sum c_i |f_i(Q)|^2}{|\sum c_i f_i(Q)|^2} . \quad (18)$$

The total scattering function can then be transformed to the reduced total scattering structure factor $F(\mathbf{Q}) = \mathbf{Q}(S(\mathbf{Q}) - 1)$ which is Fourier transformed to give the pair distribution function $g(r)$. $g(r)$ is often normalised further to result in $\frac{g(r)}{|\sum c_i f_i(Q)|^2} = g'(r) - 1$.

Thus, a measurement of the scattering intensity of a sample can be used to acquire data showing the likelihood of finding two atoms within a sample at every separation distance, even to small interatomic distances, and thus the real-space local structure of the sample (whether crystalline or not).

In this thesis the pair distribution function is given as the reduced atomic pair distribution function, $G(r) = 4\pi r \rho_0 [g'(r) - 1]$, which is weighted so that features at high r are more visible. This is equivalent to the function with notation $D(r)$ used by programmes such as RMCProfile (which are not used in this thesis).^{303,304}

Processing and Refinement of the Scattering Data

The experimental data, recorded in the format (2θ , intensity), must be converted to the pair distribution function $g(r)$; this is done in several steps. The experimental data are processed to remove noise and small-angle scattering using selected minimum and maximum Q values and the Q limit of meaningful measurement from the instrument (see Figure 1.11 and Ref. 305]. Prior to the Fourier transform, the Q -spacing must be set such that $\Delta Q \leq \frac{\pi}{r_{\max}}$ where r_{\max} is the limit of visible structural features, in order to provide good resolution of the final PDF. The data must also be corrected for e.g. instrument background and sample container background.³⁰⁶ Additionally, the X-ray form factors die off rapidly as Q increases; omitting a correction for this would lead to a slow modulation in $S(Q)$ over Q and hence sharp peaks in the Fourier transform. The composition of the sample must therefore be known (or closely estimated) in order to apply a correction and normalisation. Correction must also be made for multiple or incoherent scattering and Compton scattering,^{307,308} and is done *via* application of a polynomial smoothing function, r_{poly} . The data can then be converted to $F(Q)$ and Fourier transformed to produce the pair distribution function.

The steps performed by the software PDFgetX3³⁰⁵ used in this thesis are shown in Figure 1.11 a). PDFgetX3 allows 'ad hoc corrections for experimental aberrations' to be made;²⁹⁸ parameters such as the background scaling, and values for Q_{\min} , Q_{\max} and r_{poly} can be varied with a live graphical output [Figure 1.11 b)], enabling the best data to be obtained.

```

a) In [2]: pdfgetter.describe()
0 TransformTwoThetaToQA
  convert x data from twotheta to Q in 1/Å
1 TransformQGridRegular
  Remove the data outside the (qmin, qmaxinst) range
2 TransformBackground
  subtract background intensity
3 TransformXrayASFnormChris
  scale and normalize intensities by x-ray scattering factors
4 TransformSQnormRPoly
  Normalize S(Q) by fitting a polynomial
5 TransformSQToFQ
  Convert S(Q) to F(Q).
6 TransformFQgrid
  Resample F(Q) to a regular grid suitable for FFT
7 TransformFQToGr
  Convert F(Q) to G(r).

```

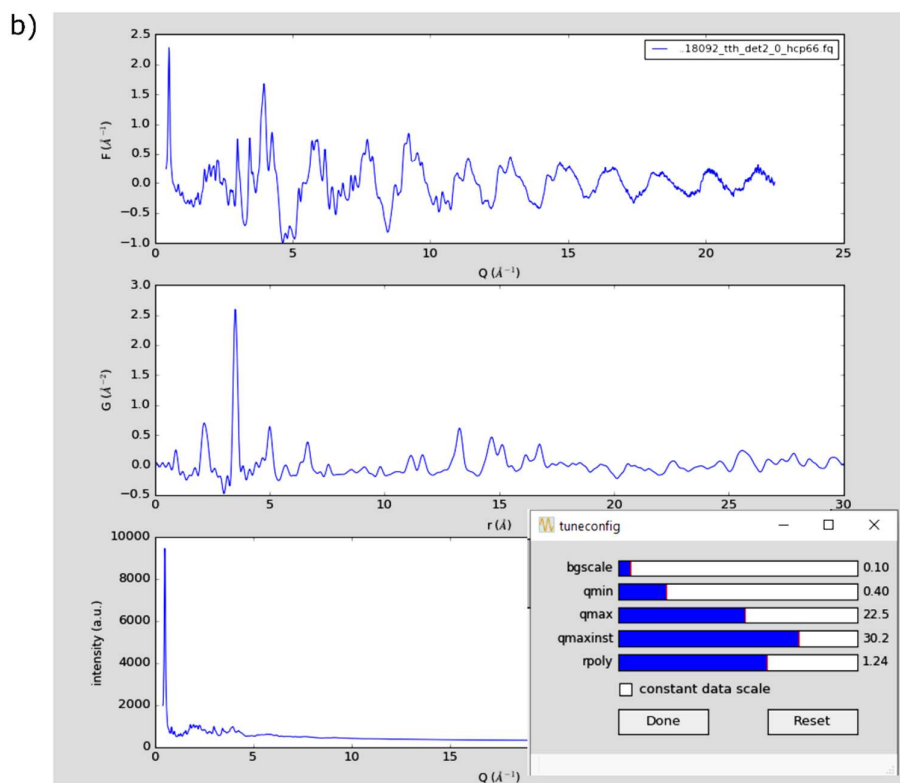


Figure 1.11. a) Screenshot of the process used by the programme PDFgetX3;³⁰⁵ b) screenshot of the live graphical output, with slider bars to vary the parameters for background scaling, Q_{min} , Q_{max} , Q_{max} instr. and r_{poly} .

Unlike for neutron scattering, the absolute intensities of $G(r)$ are less significant for X-ray data (due to the normalisation) and so are not always shown in this thesis.

In a similar manner to the analysis of PXR data a proposed model structure can also be compared against XPDF data. In this thesis the package DiffPy-CMI³⁰⁹ is used, allowing individual non-periodic non-interacting cluster species to be input as model structures. Crystal structures can also be input as models alongside the non-crystalline species.

Parameters can be input and refined (some of them beyond the scope of this thesis), including the particle diameter and shape, isotropic atomic displacement parameters, and atomic-motion-derived contributions to peak broadening. In this way the calculated pattern produced by a proposed structure, or combination of structures, can be compared to the experimental data using least-squares refinement.

1.6.4 Nuclear Magnetic Resonance

Scattering techniques, while powerful, by no means produce complete understanding of the structure and interactions in a material. Powder X-ray diffraction (PXRD), while one of the methods most commonly used in the characterisation of MOFs, relies on the material having a crystalline structure and so does not provide structural data on non-crystalline, or pre-crystallisation, species. X-ray pair distribution function (XPDF) analysis, meanwhile, provides information about interatomic distances, at both short and long lengthscales, even in non-crystalline materials.

Nuclear magnetic resonance (NMR) spectroscopy, however, does have particular strengths: it can be used to probe the interactions and dynamics within a system in ways beyond the reach of scattering techniques. Included in the information about the chemical environment of a nucleus, NMR can reveal details not only about the physical proximity of two nuclei through space, like XPDF, but also through-bond connectivities.³¹⁰ Unlike XPDF and PXRD, NMR enables information to be collected about nuclei of each chemical element present separately (providing they have an NMR-active nuclide) which can help to deconvolute the exact structure and interactions in a system. While NMR data can be acquired on heavier elements such as the Hf and Zr used in the UiO family MOFs described in this work, it can (in contrast to X-ray scattering techniques, which are insensitive to lighter elements as these have lower electron density) also be used to gain information on lighter nuclei such as ^1H and ^{13}C . Hence, a combination of PXRD, XPDF and NMR is particularly valuable for the materials studied in this work as it allows investigation of both crystalline and non-crystalline systems, and of both heavier elements such as the hafnium metal clusters and lighter species such as organic molecules or water. This spans the range of materials and systems found in this work, from full, crystalline MOF frameworks through to their cluster precursors in solution.

NMR has frequently been applied to both MOFs and metal coordination complexes in order to understand their structure and behaviour. Frequently, this technique is used on solutions of digested MOFs to understand the ligand composition and defect concentration (the metal clusters of the MOF are precipitated out upon digestion, while the ligands remain in solution).^{15,63,105,251} For intact MOF and zeolite structures solid-state NMR allows identification of the organic ligands while attached to the metal clusters³¹¹⁻³¹³ as well as, in the case of metal-oxo, -hydroxo and -hydride clusters, the environments of the protons and oxides connecting the metal centres.^{292,314,315} NMR has also been used to probe the environments of guest molecules; that is, whether they are coordinated to a cluster or contained within a pore, and the geometry and chemical environment of the pores.^{66,316}

Although NMR on pre-prepared samples is a well-established method of analysis, the use of NMR to probe the formation of MOFs is less widely used. *In situ* techniques are valuable in understanding the reactions and crystallisation of organic molecules in solution and of inorganic and metal-containing materials both in liquid and solid state.³¹⁷⁻³²⁰ However, the power of these techniques to help understand the changes occurring in *in situ* MOF reactions, including combined liquid and solid-state measurements ('CLASSIC' NMR³²¹) to explore the reaction from the solution phase through to crystallisation, is only beginning to be unlocked.²⁷⁸ In particular, the species involved in the synthesis of hafnium and zirconium UiO family MOFs have not been well explored.

NMR investigation of these Hf- and Zr- oxo-hydroxo clusters is often not straightforward. ^{177/179}Hf and ⁹¹Zr have large quadrupolar moments and/or low gyromagnetic ratios³¹⁰ and ¹⁷O is both quadrupolar and has very low natural abundance, limiting sensitivity and resolution and hence making these nuclides challenging for NMR studies.³²² Furthermore, in the dynamic exchange found in these solutions (especially water-containing solutions), often the dominant signal is derived from the solvent, rather than from the metal clusters themselves, which also makes ¹⁷O enrichment unfavourable (expensive, and would enhance both the cluster oxygen environments and the solvent).³²³ Interestingly, even ¹H NMR can prove challenging when performed on Zr clusters due to very high shifts and line broadening.³¹⁵ Those studies which perform ¹H and ¹³C NMR often include cluster-surface ligands with

multiple methyl groups, helping to improve sensitivity to the presence of the ligands and clusters.³²⁴⁻³²⁶

The bulk of NMR performed on Hf and Zr MOFs (including the UiO family studied in this work) typically focusses on the ligand composition and connectivity of the metal clusters *via* ¹H NMR of a digested sample,^{15,327} or ¹H, ¹³C and/or ¹⁷O NMR on a full MOF framework.^{63,66,124,323} Although the importance of the surface chemistry of metal clusters, particularly when solvated, is well known, the body of work investigating Hf and Zr metal clusters, especially in solution,³²⁸ is not as extensive as, for example, work on aluminium clusters³²⁹ or polyoxoanions of Group 5 and Group 6 oxides.⁶⁴

Many of the Hf or Zr species studied are not found in the synthesis of UiO family MOFs and their precursors;²⁵¹ for example zirconium chlorides with interstitial hydrogens.^{315,330} Clusters similar to those found in UiO family MOFs have been explored using techniques such as X-ray diffraction and EXAFS^{70,213,215,331} as well as NMR, but not in conditions similar to those used in the synthesis of **hcp** and **hxl** UiO frameworks. Most notably, these conditions explored are without any significant presence of water,^{213,216,325,332} in contrast to the conditions in which the aforementioned UiO frameworks are synthesised. One exception is the tetrameric species $[\text{Zr}_4(\text{OH})_8(\text{H}_2\text{O})_{16}]^{8+}$, known to exist as the dominant species in aqueous zirconium solutions,^{196,200} which has been characterised in aqueous conditions using ¹H and ¹⁷O NMR.²⁹² This showed for the first time some of the protons on the zirconium-terminating water molecules, separately from the 'bulk' water peak. The terminal water molecules were differentiated into two types, inert (i.e., visible on the NMR timescale) and labile, while the bridging hydroxides were not seen, potentially due to fast proton exchange: the strength of the Zr-O bonds results in these complexes being highly acidic (more so than for the same concentration of HCl) and the inert protons were visible only due to their unusually long lifetimes (~0.1 s, compared to ~10⁻⁴ s for protons on inorganic complexes containing other metals).²⁹² In more dilute solutions, the proton exchange becomes even faster. These NMR experiments provide a clue as to the difficulty of observing protons of this type on other clusters.

Understanding the behaviour of MOF clusters in their reaction solutions is extremely important in understanding their synthesis. While metal-sensitive techniques such as XPDF

provide valuable information on the core structure of the cluster, the insights gained through solution NMR enable a more well-rounded understanding of the system as a whole, and particularly of the solvent interactions which are so crucial in the formation of these clusters and their related MOF frameworks.^{175,255}

Theory of NMR spectroscopy

A more rigorous introduction to NMR spectroscopy can be found in Refs. 333–335.

Nuclear magnetic resonance spectroscopy, as the name implies, utilises a fundamental property of the atomic nucleus. Nuclei have an intrinsic angular momentum called spin, denoted by quantum number I , which is determined by the number of protons and neutrons in the nucleus. The nuclide primarily considered in this thesis, ^1H , has spin $I = \frac{1}{2}$, thus this discussion will focus only on spin- $\frac{1}{2}$ nuclides. The nuclear spin results in a nuclear magnetic moment, $\boldsymbol{\mu} = \frac{\gamma I h}{2\pi}$, where γ is the gyromagnetic ratio (a given constant for each particular nuclide) and h is Planck's constant.

In the presence of an external magnetic field \mathbf{B}_0 , the orientation of the nuclear magnetic moment is quantised. Allowed orientations are given by the nuclear magnetic quantum number, $m_I = -I, -I + 1, \dots, I - 1$, i.e., $2I+1$ different orientations. The nuclear spins precess about an axis parallel to the external magnetic field at the Larmor frequency [Figure 1.12 a)],

$$\omega_0 = -\gamma B_0. \quad (19)$$

The quantisation of nuclear spin gives rise to distinct spin states with energies given by

$$E = -\frac{\gamma h}{2\pi} m_I B_0. \quad (20)$$

For spin- $\frac{1}{2}$ nuclides such as ^1H , there are two spin states, α (spins aligned parallel to \mathbf{B}_0 ; lower energy) and β (spins aligned antiparallel to \mathbf{B}_0 ; higher energy). The energy difference between these two spin states is given by

$$\Delta E = \frac{\gamma h B_0}{2\pi}. \quad (21)$$

If both states were equally populated there would be no net magnetic moment. However, at thermal equilibrium, the relative populations of the α and β states are given by the Boltzmann distribution: the lower energy state α is slightly more populated than the β state.

This results in a net magnetisation, M_0 , which is parallel to the external magnetic field B_0 [Figure 1.12 b)].

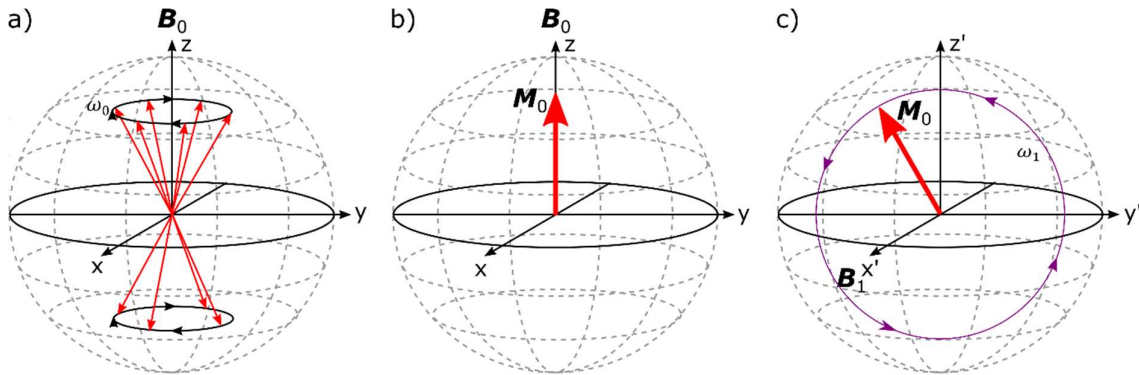


Figure 1.12. Diagrams showing the magnetisation of a sample in three dimensions: a) individual spins precessing at ω_0 around the z-axis with applied field B_0 viewed in the laboratory frame; b) the net magnetisation M_0 aligned along the z-axis, parallel to B_0 ; c) the net magnetisation upon application of an RF pulse, viewed in the rotating frame.

In an NMR experiment, a sample is placed inside a coil, in a probe inside the strong external magnetic field B_0 . If an alternating current is passed through the coil with radiofrequency (RF) ω_{RF} , this produces an oscillating magnetic field B_1 which is perpendicular to B_0 . This additional applied magnetic field will affect the bulk nuclear magnetisation of the sample, M_0 .

If the frame of reference, rather than being stationary ('laboratory frame'), is modelled as rotating about B_0 with frequency ω_{RF} ('rotating frame') then the effect of this applied field B_1 on the magnetisation can be more easily understood. If $\omega_{RF} = \omega_0$, the spins appear to be stationary in the 'rotating frame' and so B_0 is effectively zero and B_1 is stationary. The spins, and therefore the net magnetisation M_0 , will now precess about B_1 with frequency $\omega_1 = \gamma B_1$ [Figure 1.12 c)].

This RF 'irradiation' is typically applied as a pulse with a finite duration τ : this causes M_0 to rotate a set amount towards the $x'y'$ (transverse) plane [Figure 1.13 a)]. The angle (in degrees) by which it is rotated is given by

$$\theta = \gamma B_1 \tau . \quad (22)$$

Once the RF pulse is switched off and the receiver is turned on, the additional applied field B_1 is no longer present. Returning to the 'laboratory frame', the spins are affected by the strong external field and so will begin to precess in the xy plane about B_0 . This precession of

the magnetisation induces a current in the receiver coil which is detected by the NMR spectrometer. This signal is called the free induction decay (FID); it does not persist indefinitely as the magnetisation will start to relax back to its equilibrium state along the z -axis parallel to \mathbf{B}_0 . This relaxation occurs *via* two processes: spin-lattice relaxation, which is the relaxation of the longitudinal (z) component due to interaction with the surrounding molecular lattice (or surroundings in general) [Figure 1.13 b)], and spin-spin relaxation, which is relaxation in the transverse (xy) plane due to interchange of energies between nuclear spins (so that some precess faster than ω_0 and some slower) [Figure 1.13 c)].

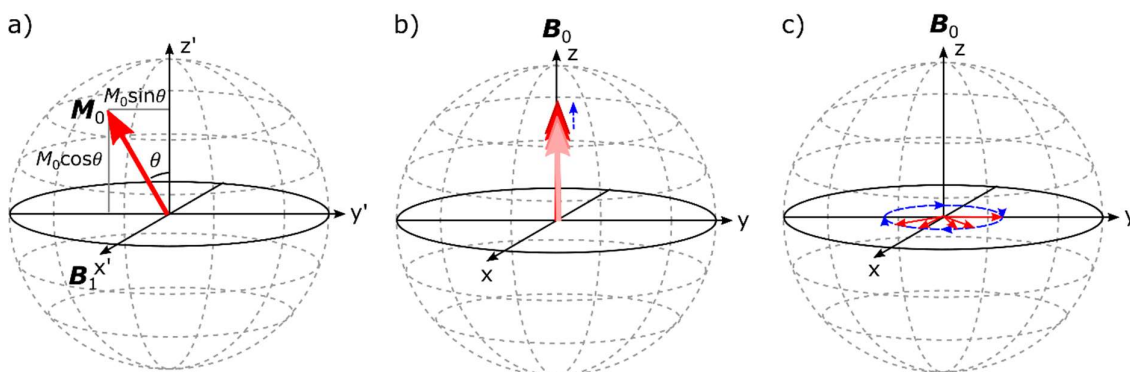


Figure 1.13. Diagrams showing a) the rotation of the magnetisation from an RF pulse, viewed in the rotating frame; b) the relaxation of the net magnetisation in the longitudinal (z) direction; c) the relaxation in the transverse (xy) plane, with the individual components precessing at different speeds so they fan out.

Before any other pulse can be applied, the magnetisation needs to be fully relaxed back to equilibrium. Both relaxation processes cause an exponential decay over time (a factor of $\exp(-\frac{t}{T})$) of the signal observed: the spin-lattice exponential decay is described by the time constant T_1 and the spin-spin decay is described by T_2 . After times of approximately $5T_1$ or $5T_2$ the magnetization is effectively relaxed completely back to its pre-perturbation state (99.33% relaxed) and thus another pulse can be applied. This pulse-acquire sequence is repeated several times and the resulting signals averaged to improve signal-to-noise ratios.

So far, only a system of isolated spins has been considered. However, molecules do not consist of bare nuclei; instead, they are surrounded by electrons. The exact electron density around a nucleus is determined by the chemical environment and is different for each chemically-distinct nucleus. The movement of the electrons is an electric current; the strong applied external field \mathbf{B}_0 induces circulation of the electrons which generates a local magnetic field at the nucleus. This local magnetic field can either be parallel to \mathbf{B}_0 , in which

case the field experienced by the nuclei is augmented and the nuclei are said to be 'deshielded', or it can oppose B_0 , in which case the field experienced by the nuclei is slightly reduced and the nuclei are 'shielded'; this interaction is known as 'chemical shielding'. Thus, the precession frequency will be different for each chemically distinct nucleus.

The frequency of precession of spins in each chemical environment induces an oscillating current in the receiving coil and hence each distinct chemical environment has a contribution to the time-domain FID. Fourier transforming the FID generates a frequency-domain spectrum with peaks at frequencies corresponding to each chemical environment. This spectrum can be used to determine the identity of the components and to provide information about their local chemical environment.

Two-Dimensional Experiments

The previous section described a very simple NMR experiment, producing a one-dimensional spectrum. However, it does not provide information about, for example, interactions such as exchange between chemical environments, through-bond J -couplings,³¹¹ or of through-space internuclear correlations.³³⁶ More information can be acquired from a system by applying a series of RF pulses, with different durations, spacings and phases. This is called a 'pulse sequence'.

There is a variety of pulse sequences which can be used to generate spectra not in one frequency dimension but two, i.e., the intensity of the signal is a function of two frequencies. Therefore, information can be acquired about the relationship or correlation between two different chemical environments.

To do this, the pulse sequence needs at least two pulses (or sets of pulses) [Figure 1.14]. The first pulse (or set of pulses) excites the spins in the sample to create transverse magnetisation (known as the 'preparation' period). The magnetisation then evolves (i.e., precesses at frequencies determined by the chemical shieldings and J -couplings) for a time period t_1 . A second pulse (or set of pulses) is then applied and magnetisation is transferred between nuclei (called 'mixing'). The FID is then acquired for a time t_2 .

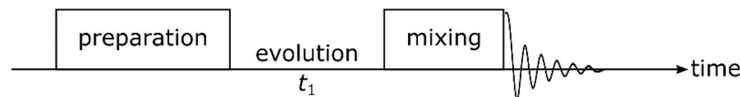


Figure 1.14. Schematic of a two-dimensional NMR pulse programme. The RF pulses are indicated by boxes and the FID by an exponentially-decaying wave. The size and separation of the boxes are arbitrary.

The two-dimensional spectrum is acquired by repeating the pulse programme and detecting during time t_2 for a set of different (incremented) values of t_1 . Since the FID is a function of two time variables, it must be Fourier transformed twice to give the 2D spectrum. A two-dimensional plot then gives peaks, the coordinates of which in each dimension provide information about the environments which are correlated.

One of the most widely-used two-dimensional experiments is EXSY (Exchange Spectroscopy). This follows a pulse sequence, shown in Figure 1.15, in which all pulses are 90° and applied along the x' -axis of the rotating frame. Consider a system of two spins, 1 and 2: the pulse sequence will be followed by considering the effect of the pulses of spin 1. The first pulse rotates the magnetisation of spin 1 by 90° , onto $-y'$. The spins are then allowed to evolve for time t_1 , so that the magnetisation precesses in the xy -plane of the 'laboratory frame' (i.e., it has a component proportional to $-\cos \omega_1 t_1$ in y and $\sin \omega_1 t_1$ in x , where ω_1 is the frequency of precession of spin 1). The second 90° pulse then rotates the y' -component onto the z' axis and leaves the x' -component unaffected. This generates magnetisation in z' which is 'labelled' with the frequency ω_1 .

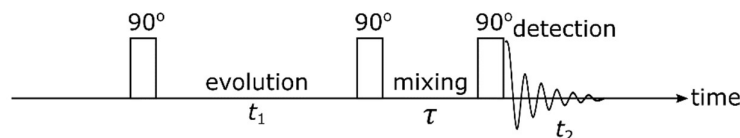


Figure 1.15. Schematic of the pulse sequence used in EXSY experiments.

During the mixing time, τ , spin 1 may undergo exchange (the extent of which is determined by the kinetics of the exchange) with spin 2. If this occurs, then spin 2 will have magnetisation proportional to $-\cos \omega_1 t_1$, which means it is now 'labelled' with the frequency of precession of spin 1. Some proportion of spin 1 will not exchange. A final 90° pulse then rotates the z' -components back onto the y' -axis and then the spins evolve over a time t_2 and the FID detected.

The FID will have both a component from the non-exchanged proportion of spin 1 and a component from the spin 2 which did exchange, which has an amplitude modulated by

$\cos \omega_1 t_1$. This means the Fourier transform of this 1D 'slice' will have two peaks, one for the non-exchanged spin 1 at coordinates (indirect dimension, direct dimension) = (ω_1, ω_1) , and one for the spin 2 which had magnetisation transferred from spin 1 at coordinates (ω_1, ω_2) where ω_2 is the frequency of precession of spin 2. Incrementing over time t_1 produces a two-dimensional spectrum, with peaks on the diagonal corresponding to the spins which did not exchange, and cross-peaks corresponding to exchange.

Thus in an EXSY-type experiment, observing cross-peaks in the spectrum indicates environments which are undergoing chemical exchange with each other—such as solvent molecules, or ligands on the surface of a cluster.

This EXSY experiment is identical to the NOESY (Nuclear Overhauser Effect Spectroscopy) experiment. However, in a NOESY spectrum, exchange of magnetisation can occur by cross-relaxation of spins close together in space (related to the Nuclear Overhauser Effect or NOE). This also results in cross-peaks; depending on the size and hence tumbling speed of the molecules in solution, the cross-peaks will be either positive (slow tumbling; large molecules; negative NOE) or negative (fast tumbling; small molecules; positive NOE) relative to the peaks on the diagonal.

In a NOESY-type experiment, positive cross-peaks could be due either to chemical exchange or to cross-relaxation where the molecules are large. An experiment called ROESY, or Rotating frame NOE Spectroscopy, is complementary to NOESY and can be used to distinguish between cross-peaks coming from exchange and from NOEs: in a ROESY-type experiment, peaks resulting from NOE will be negative relative to positive peaks on the diagonal and those resulting from exchange will be positive.

Applying a variety of both one-dimensional and two-dimensional experiments can, therefore, provide a wealth of information about a system beyond that obtained using X-ray scattering techniques. One-dimensional ^1H NMR, for example, can identify the different environments in a solution of metal clusters, both from the solvent and from any cluster-surface ligands. Meanwhile, two-dimensional NOESY can be used to examine the interactions between these environments, such as through-space interactions even between different molecules and chemical exchange occurring both within the solvent and between the solvent and the clusters. ROESY experiments can be used to differentiate between these

processes and to support conclusions about the processes and through-space structuring present in multi-component systems such as the reaction solutions explored in this work.

1.6.5 Thermogravimetric Analysis

More information on thermogravimetric analysis of MOFs can be found in Refs. 15,337,338.

In contrast to the techniques discussed thus far thermogravimetric analysis (TGA) alone does not give direct information about either the ordered/long-range or the local structure of a material. Thermogravimetric analysis, in which a sample is heated in a crucible and the mass changes compared to that of an empty crucible over the temperature range, enables the investigation of the temperature stability of a material under different atmospheres such as air or nitrogen. When combined with heat flow analysis (differential scanning calorimetry), which measures the energy absorbed or released by a sample during the heating process, this can be used to provide information about phase changes such as melting, or kinetic phenomena such as glass transitions, in a material.

Thermogravimetric analysis can be performed in an inert or oxidising/reactive gas atmosphere. If a TGA is performed under air, and the mass of the final product of the oxidation is known, analysis of the resultant mass-temperature curve can be used, not only to determine the temperatures at which thermal decomposition events occur, but also to calculate the composition of the original material. 'Steps' in the TGA curve indicate mass losses; the fractional or percentage mass change in each step, when combined with understanding of the structure of the material, can therefore indicate the loss or combustion of different molecules in the material. In MOFs mass losses can be due to losses of guests in the pores or to different stages of framework decomposition; the final product is often the oxide of the metal forming the MOF clusters³³⁹—in UiO family MOFs, the final product of the oxidation of the hafnium analogue is HfO₂.

This understanding can be used to help determine the number of defects in a MOF sample. If a mass loss step is, for example, known to involve the loss of all linker species in a framework and conversion to the metal oxide, discrepancies between the expected mass fraction of linkers and the experimentally-observed fraction indicate the presence of defects.³⁴⁰ Additional analysis of the TGA curve may then be used to determine the mass

fraction of other molecules in the material and hence the proportion and nature of missing-linker-compensating species.

The loss of a dicarboxylate linker from between two clusters in UiO family MOFs requires the presence of compensating 'capping' molecules at both coordination sites in order to charge-balance the clusters. These capping molecules are usually derived from other species present during the synthesis such as modulating acid, water, or hydroxide.^{12,140,141} Each linker is bound to each cluster in a bidentate manner; that is, bridging between two metal atoms, with two separate M-O bonds [Figure 1.16]. A similar bonding mode is observed in most cases for monocarboxylates, i.e., two monocarboxylate anions derived from (for example) the modulating acid would be required to compensate for one dicarboxylate linker (although in some cases the carboxylate group can 'bridge' between metal clusters *via* one monodentate M-O bond to each cluster).³⁴¹ Similarly, in order to compensate for the loss of one carboxylate group per cluster, one hydroxide group and one water molecule are required for both charge and coordination-number balance; a second, hydrogen-bonded, water molecule has been determined to add stability to this configuration [Figure 1.16].³⁴² Thus two hydroxides and four water molecules could compensate for a linker vacancy in UiO family MOFs.

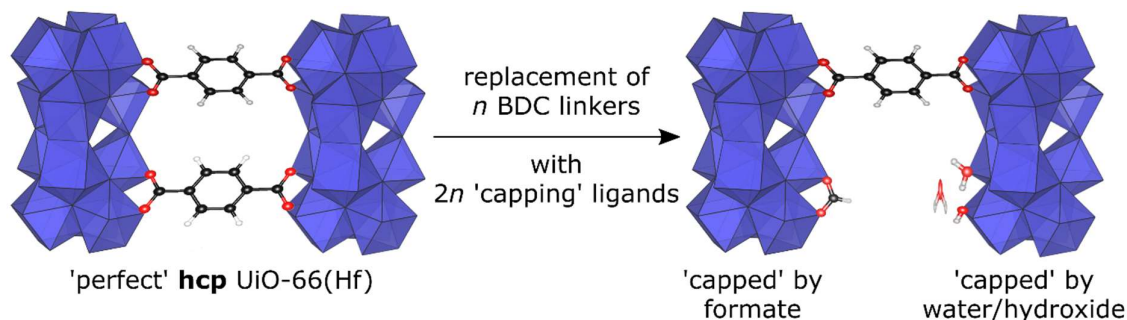


Figure 1.16. Schematic showing the replacement of dicarboxylate linkers by capping molecules in hcp UiO-66. For clarity the M_{12} double clusters are shown in the polyhedral representation and only one terephthalate linker per double cluster is shown. The linker-compensating molecules shown are a formate anion (left) and a combination of a hydroxide anion and two water molecules (right).

As long as these defect-compensating molecules are quite small (i.e., with less mass than the missing linker), the replacement of dicarboxylate linkers with capping molecules results in the mass of the framework being lower than would be expected for a perfect framework. This means that, as long as the identity of the capping molecules is known, by calculating the mass fractions at different stages of the framework decomposition the ratio of capping

molecules to linkers can be determined and therefore the concentration of missing-linker defects in the sample can be estimated.

In the thermal decomposition of UiO family MOFs several key mass loss steps are observed. Initial mass losses below 150°C are due to the loss of solvent molecules,³³⁷ likely including hydrogen-bonded water molecules.³⁴² After this loss the MOF sample will consist of the metal clusters with linkers and cluster-capping (missing-linker-compensating) ligands in a ratio dependent upon the synthesis and activation conditions.

The second significant mass loss occurs between 250 and 300°C, corresponding to the dehydroxylation—in the hafnium analogue—of the $\text{Hf}_6\text{O}_4(\text{OH})_4$ cluster to Hf_6O_6 .^{50,169,337} In defective UiO-66 materials where formate molecules have replaced some linkers, formate ligands are lost over a similar temperature range.^{15,165} Metal-bound water molecules are also lost during this stage (which can lead to coordinative unsaturation of metal sites).^{210,342} During dehydroxylation and loss of formate the metal clusters must remain charge-balanced; in samples which are not completely activated, or in which hydrogen-bonded water molecules are present, it is likely that the formate molecules are replaced by hydroxide because of high levels of water in the pores. For the **hcp** model an additional assumption is that the six bridging μ_2 -OH forming the 'belt' between the two halves of the M_{12} cluster are not lost in the dehydroxylation step.

The largest step in the TGA curve, at around 520-540°C, corresponds to the decomposition of the remaining framework and the formation of HfO_2 . In this work, the decomposition temperature T_{decomp} is calculated as the temperature at which the rate of mass loss (dm/dT) is greatest. As noted above, a smaller-than-expected final mass loss is likely to be due to a deficiency of linkers in the sample and their vacancy-compensating small ligands.^{138,165,337,343} For a single variety of compensating ligands (i.e., one species of monocarboxylate anion, or the hydroxide-water model only) it is straightforward to calculate the composition of the original framework from the size of this mass loss step: for example, if n linkers are replaced by $2n$ capping molecules, then there is only one unknown quantity and therefore the TGA measurement alone will suffice. If two or more types of compensating ligands are present, including hydroxide-water, there are now two or more unknown quantities and so additional information on the ratio of the ligand species, such as solution NMR on a

digested MOF sample to determine the ratio of any organic ligands present, is required alongside the TGA in order to calculate the defectivity of the MOF [see Figure 2.18, Figure 2.19, Figure 2.20].

1.7 Motivation and Aims

MOFs are particularly promising for real-world applications such as catalysis or sorption, due to the wide range of metals and ligands from which those with the potential to form a MOF with desired properties may be chosen.^{11,167,344} Alongside these synthesis routes the deliberate introduction of defects into the MOF—defect engineering—is becoming increasingly recognised as an important technique for tailoring existing MOF properties as well as introducing new reactivities and functionalities.^{97,99,165,345}

The future of MOF design lies in the rational synthesis of new desired MOF structures with a range of connectivities and different linkers, and subsequently different physical/chemical properties and topologies. Being able to design a synthesis and reproduce results reliably is a key step towards harnessing MOFs for real-world applications. However, the factors determining control over the degree and correlation of defects are not well understood. Defects in MOFs, including in UiO family MOFs, are often assumed to be randomly distributed; however, recent work has shown that under certain synthetic conditions defects in UiO family MOFs can correlate, leading to the formation of new defect-mediated MOF topologies [Figure 1.17] with different properties from the parent non-defective UiO frameworks.^{12,141} In particular, the **hcp** UiO-67(Hf) framework contains a different metal cluster nuclearity and topology. This discovery demonstrated that control over the synthesis conditions—in particular, modulated solvothermal synthesis—could be used to change not just the concentration of point defects in a framework but the entire structure of a MOF. These studies indicate that the UiO family of Hf MOFs is ripe for further study in order to seek greater understanding of defect-mediated MOF structures.

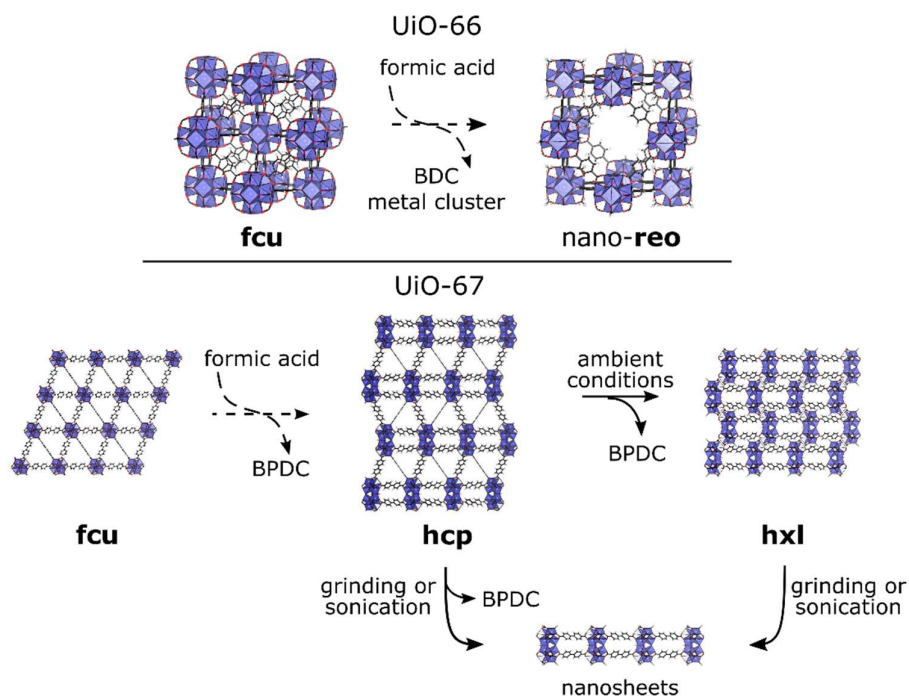


Figure 1.17. Reported phases of UiO-66 (top; formed with terephthalate ('BDC') linkers) and UiO-67 (bottom; formed with biphenyldicarboxylate ('BPDC') linkers). Dashed arrows show the differences in the synthesis conditions required in order to obtain different phases; solid arrows show postsynthetic treatments. Structural models derived from crystallographic information files reported in Refs. 12,141,165.

The defect-engineering studies discussed earlier also revealed clues as to the formation routes of these hafnium MOFs and to the importance of understanding the formation routes and solution chemistries of the MOFs and their precursors.^{12,141,175} Central to the reticular synthesis model of MOFs²⁴ is the concept that the metal clusters have an especially critical role in determining the structure, and hence the properties, of the MOF;⁵⁷ a greater understanding of the relationship between the reaction conditions and the formation of the hafnium clusters would enable improved control over and selection of cluster species and therefore over the resultant MOFs.

This thesis aims to improve the understanding of the formation of hafnium MOFs and of the role played by the synthesis conditions on the structures created in order to bring one step closer the possibility of the rational, deliberate design of MOF syntheses exploiting the wide library of possible cluster species.

This Chapter has introduced the core concepts behind defect-engineering of MOFs and summarised the current understanding of the chemistry of the reaction solutions used, particularly as applied to hafnium metal clusters. The end of this Chapter includes more

detailed descriptions and discussions of the relevant characterisation techniques used to explore the systems and materials in this work; exact experimental methods are included in the successive Chapters.

In the second Chapter the modulated synthesis conditions used to create the **hcp** UiO-67(Hf) framework are further explored, in particular the role of water in the solvent, and this understanding used in pursuit of isorecticular **hcp** analogues of other members of the UiO family.

The third Chapter investigates the mechanisms of solution formation of **hcp** frameworks and their constituent hafnium clusters and related precursors through *ex situ* and time-resolved *in situ* measurements under solvothermal conditions. This bridges the gap between *ex situ* cluster identification and *in situ* MOF crystallisation and provides insight into the relationship between the cluster formation and the MOF framework coordination.

The fourth and fifth Chapters build on this through exploration of the interactions in the reaction solvent both with and without molecular hafnium clusters, aiming to understand the intertwined roles of the different solvent components by methodically varying the solvent composition; the effects of temperature and ageing time are also explored.

Finally, the sixth Chapter summarises the findings of this thesis and the implications for the future of the field of defect-engineering applied to the synthesis of hafnium metal-organic frameworks as a route towards the deliberate and efficient design of syntheses for new and unrealised members of this important class of materials.

Chapter 2. Defect-Engineering in the Synthesis of UiO Family MOFs: New Phases and Defect Structures

While the deliberate, controlled introduction of defects—‘defect engineering’—is increasingly recognised as an important technique for tuning the properties of frameworks,^{11,167,344} the factors determining control over the degree and correlation of defects are not well understood. Defects in UiO family MOFs are often introduced through synthesis: tuning the synthesis conditions is one of the main methods of obtaining control over the number and type of defects. In particular, the synthesis temperature and the identity and concentration of modulating acid in a solvothermal synthesis not only determine the nature of the defects in the framework but also their distribution. That modulated synthesis can result in correlation of defects has led to the discovery of new defect-ordered phases of UiO family MOFs, including nano-**reO** UiO-66(Hf) and **hcp** UiO-67(Hf).

However, in contrast to the use of acids in the modulated synthesis of UiO family MOFs,^{15,127} the influence of water in the reaction mixture on the formation of defect phases of UiO family MOFs has not been as well-explored. This is despite water being essential for the formation of the metal cluster in UiO family MOFs and, in a wider chemical context, playing a critical role in zirconium and hafnium solution chemistry (the latter will be revisited in Chapters 4 and 5).^{130,132,197,212,223} Additionally, there has been little specific investigation into the potential effects on the phase of the MOF framework of using water as a solvent,¹⁶⁰ even though hydrothermal syntheses of UiO family MOFs are increasingly promoted as examples of environmentally-attractive synthesis routes since they do not use toxic organic solvents such as DMF.^{223,346}

This Chapter builds on the discovery of the role of modulating acid in the defect-engineering of UiO family MOFs to demonstrate that tailoring the synthesis conditions, among them the inclusion of water in the reaction mixture, can be used to expand the UiO family of MOFs further. This work systematically shows that the presence of water, alongside formic acid, controls the phase which forms for UiO-67(Hf) frameworks, from the original **fcu** UiO-67(Hf) through to the **hcp** phase and even to a layered-nanosheet phase. This new understanding of the importance of water is also applied to a member of the UiO-

66 family, UiO-66(Hf) (F₄BDC), again using the presence of water in the synthesis to obtain the **hcp** phase. This work further demonstrates the effectiveness of this method of defect-engineering in the rational design of MOFs, by designing a new synthetic route to the stable defect-ordered **hcp** UiO-66(Hf) phase.

In order to understand the properties of these new phases a combination of powder X-ray diffraction, thermogravimetric analysis, solution nuclear magnetic resonance spectroscopy and gas adsorption isotherm measurements are used. These characterisation techniques permit further understanding of the structural differences between the MOF phases as well as of the effect of the exact concentrations of formic acid and water on the defects introduced within the structure.

Finally, post-synthetic ligand exchange is performed on samples of both **hcp** UiO-67(Hf) and **hcp** UiO-66(Hf) in order to investigate the defect-mediated anisotropic structural properties and reactivities of these new materials.

Unless otherwise stated, the UiO family MOFs described in this Chapter are the Hf analogues.

Part of the work in this Chapter (in particular, part or all of sections 2.2.1-2.2.5) is published in the following journal article:

Firth, F. C. N.; Cliffe, M. J.; Vulpe, D.; Aragonés-Anglada, M.; Moghadam, P. Z.; Fairen-Jimenez, D.; Slater, B.; Grey, C. P. *Engineering New Defective Phases of UiO Family Metal-Organic Frameworks with Water*. *J. Mater. Chem. A* **2019**, 7 (13), 7459–7469. [Ref. 251]

MOF synthesis, postsynthetic treatment, powder X-ray diffraction and analysis, TGA analysis, SEM imaging, preparation of samples for solution NMR and adsorption isotherm measurements, and processing and interpretation of all data, were performed by Francesca Firth.

*Structural models of **hcp** UiO-66(Hf) and **hcp** UiO-66 (F₄BDC) were derived from the known **hcp** UiO-67 structure and optimised using quantum chemical calculations (density functional theory (DFT)) by Professor Ben Slater, Department of Chemistry, UCL.*

Adsorption isotherm measurements and simulated adsorption isotherms, using grand canonical Monte Carlo (GCMG) calculations, were performed by Diana Vulpe, Marta Aragonés-Anglada, Dr

Peyman Moghadam and Dr David Fairen-Jimenez, Department of Chemical Engineering and Biotechnology, University of Cambridge (at time of experiment).

Solution NMR experiments were performed by Duncan Howe and Andrew Mason, the NMR Facility in the Yusuf Hamied Department of Chemistry, University of Cambridge.

2.1 Experimental Methods

2.1.1 Synthesis

All reagents used were obtained from commercial suppliers and used without further purification. Unless otherwise stated, water was obtained from a Millipore filter unit.

Synthesis of UiO-67(Hf) defect phases.

Procedure modified from Ref. 12. HfCl_4 (Acros Organics, 99%, 0.3 mmol, 96.1 mg) and biphenyldicarboxylic acid (H_2BPDC) (Acros Organics, 98%, 0.3 mmol, 72.6 mg) were added to a 23 mL PTFE-lined steel autoclave, followed by dry *N,N*-dimethylformamide (DMF) (Sigma Aldrich, 99.85% anhydrous DMF) (for initial syntheses, non-dry DMF (Alfa Aesar, 99%) was used) (4 mL), and varying amounts of formic acid (Fisher, 98/100%) (0.25-2 mL) and water (0-0.2 mL). The autoclave was sealed and heated at 150°C for 24 hours. The resulting white microcrystalline powder (unwashed yields 149.1-234.6 mg) was filtered under vacuum, washed on the filter (DMF, Alfa Aesar, 99%, 5 mL) and the solid product dried on the filter. Phase-pure **hcp** UiO-67 formed with 1 mL formic acid and 0.05 mL water. Phase-pure **hns** UiO-67 formed with 1 mL formic acid and 0.2 mL water.

Synthesis of UiO-66(Hf) defect phases.

HfCl_4 (Acros Organics, 99%, 0.3 mmol, 96.1 mg) and terephthalic acid (H_2BDC) (Alfa Aesar, 98%, 0.3 mmol, 49.8 mg) were added to a 23 mL PTFE-lined steel autoclave, followed by dry *N,N*-dimethylformamide (Sigma Aldrich, 99.85% anhydrous DMF) (4 mL), and varying amounts of formic acid (Fisher, 98/100%) (0.5-3.0 mL) and water (0-3.5 mL). The autoclave was sealed and heated at 150°C for 24 hours. The resulting white microcrystalline powder (unwashed yields 63.1-154.3 mg) was filtered under vacuum, washed on the filter (DMF, Alfa Aesar, 99%, 5 mL) and the solid product dried on the filter. Phase-pure **hcp** UiO-66 formed with 1.5 mL formic acid and 0.4 mL water.

Hydrothermal synthesis of UiO-66(Hf) (F_4BDC) phases.

Procedure adapted from Ref. 198. HfCl_4 (Acros Organics, 99%, 0.1 mmol, 32.0 mg) and tetrafluoroterephthalic acid ($\text{H}_2\text{F}_4\text{BDC}$) (Sigma, 97%, 0.1 mmol, 23.8 mg) were added to a 23 mL PTFE-lined steel autoclave, followed by varying ratios of water and acetic acid (Sigma-Aldrich, >99.7%) (0.96 mL solvent in ratios from 0 : 100 to 100 : 0 water : acid V/V). The autoclave was sealed and heated at 120°C or 150°C for 24 hours. The resulting white

microcrystalline powder (unwashed yields 9.1-36.2 mg) was filtered under vacuum, washed on the filter (water, 5 mL) and the solid product dried on the filter. Phase-pure **hcp** UiO-66(Hf) (F₄BDC) was synthesised at 120°C with 60 : 40 water : acetic acid. This synthesis was further scaled up to HfCl₄ (0.3 mmol, 96.1 mg), H₂F₄BDC (0.3 mmol, 71.4 mg), water (1.73 mL) and acetic acid (1.15 mL). The **hcp** zirconium analogue was synthesised under the same conditions but with ZrCl₄ as the source of metal ions. The **hcp** structure was also produced when the modulating acetic acid was replaced with the same volume of formic acid.

Anhydrous synthesis of fcu UiO-66(Hf) (F₄BDC).

Procedure adapted from Ref. 54. HfCl₄ (Acros Organics, 99%, 0.1 mmol, 32.0 mg) and tetrafluoroterephthalic acid (H₂F₄BDC) (Sigma, 97%, 0.1 mmol, 23.8 mg) were added to a 23 mL PTFE-lined steel autoclave, followed by tetrahydrofuran (THF) (Fisher, analytical grade, 4 mL) and hydrochloric acid (Honeywell Fluka, fuming, 36.5-38%, 42 µL). The autoclave was sealed and heated at 80°C for 24 hours. The resulting white microcrystalline powder (unwashed yield 85.0 mg) was filtered under vacuum, washed on the filter (THF, Fisher, analytical grade, 5 mL) and the solid product dried on the filter.

2.1.2 Post-synthetic Treatment

Initial exchange experiments on hcp UiO-67(Hf)

2,5-Pyridinedicarboxylic acid (H₂PyDC) (Aldrich, 98%, 28.8 mmol, 48.1 mg) was dissolved in dry *N,N*-dimethylformamide (Sigma Aldrich, 99.85% anhydrous DMF) (10 mL) and sonicated for 10 minutes.

hcp UiO-67(Hf) synthesised according to the above protocol (75 mg) was suspended in the PyDC/DMF solution (5 mL), and the resultant mixture heated in a sealed tube at 55°C for 24 hours. Another sample of **hcp** UiO-67(Hf) (37.5 mg) was washed according to the protocol below then suspended in the PyDC/DMF solution (2.5 mL), and the resultant mixture heated in a sealed tube at 55°C for 24 hours. Both of these samples were then centrifuged at 8000 rpm for 15 minutes, and the supernatant removed. The resulting white microcrystalline sample was then washed and activated according to the protocol below.

Exchange experiments on hcp UiO-67(Hf) and hcp UiO-66(Hf)

Varying amounts of 2,5-Pyridinedicarboxylic acid (H₂PyDC) (Aldrich, 98%) were dissolved in dry *N,N*-dimethylformamide (Sigma Aldrich, 99.85% anhydrous DMF) (10 mL) and sonicated for 10 minutes.

hcp UiO-67(Hf) or **hcp** UiO-66(Hf), as-synthesised according to the above protocols (75 mg), were suspended in the PyDC/DMF solutions, and the resultant mixtures heated in a sealed tube at 55°C for 24 hours. The samples were then centrifuged at 8000 rpm for 15 minutes and the supernatant removed. The resulting white microcrystalline samples were then washed and activated according to the protocol below.

2.1.3 Characterisation

Sample washing and activation method.

Procedure adapted from Ref. 15. Unreacted ligand was removed from the sample by washing with DMF at 70°C for 24 hours, followed by two further 2-hour washing cycles. After each wash, residual DMF was removed after centrifugation of the mixture at 8000 rpm for 15 minutes. Finally, any residual DMF was removed by heating at 200°C for 24 hours.

Powder X-ray diffraction.

The crystal structure, purity and crystallinity for all samples were assessed *via* their powder X-ray diffraction (PXRD) patterns, measured using a PANalytical Empyrean diffractometer (Cu K α radiation, λ = 1.541 Å) over the 2θ range 3-40°, using a step size of 0.017° and a scan speed of 0.13°s⁻¹. Longer scans were performed with a step size of 0.017° and scan speed of 0.022°s⁻¹. Analysis of all powder diffraction data was carried out using the TOPAS Academic 4.1 structure refinement software.^{287,288,347} Simulated powder patterns of the different MOF phases were obtained using Mercury and Vesta software.^{348,349}

Solution NMR.

Solution NMR was used to probe the nature of the organic components of the samples. The samples were prepared using a method adapted from Ref. 15. NaOH (Breckland Scientific Supplies Ltd.) was dissolved in D₂O (Euro Isotop, 99%, 600 μ L) to give a 1M solution. 10 mg of sample, washed and activated as described above, was digested in 0.8 mL of the 1 M NaOH solution. ¹H NMR spectra of the resultant suspension were collected with a standard ¹H 500 MHz Bruker Avance AVIII HD Smart Probe.

Thermogravimetric Analysis.

Thermogravimetric analysis of samples was performed on a Mettler Toledo TGA/SDTA 851 thermo balance. Samples of 5-15 mg were heated to 700°C at a rate of 10°C min⁻¹.

Measurements on samples were separately performed both under a constant flow (80 mL min⁻¹) of N₂ and under a constant flow (80 mL min⁻¹) of air (19-22% O₂ in N₂), provided by Air Liquide UK Limited.

Scanning Electron Microscopy.

Samples were sputter coated with Pt to a thickness of 10 nm. Scanning electron microscopy was performed using a TESCAN MIRA3 FEG-SEM electron microscope operated at 5.0 kV, using the secondary electron detector.

Adsorption Measurements and Isotherms.

N₂ adsorption isotherms were carried out at 77 K on a Micromeritics 3Flex gas adsorption analyser. Samples were degassed in situ under vacuum at 120°C for 20 hours using the internal turbo pump. Warm and cold free-space correction measurements were performed using ultra-high purity He gas (grade 5.0, 99.999% purity). Ultra-high purity N₂ (99.9992%) was provided by Air products.

Grand canonical Monte Carlo (GCMC) simulations of N₂ adsorption were performed using the code RASPA.³⁵⁰ During each GCMC cycle, translation, rotation, insertions, deletions, and regrow moves were attempted, using 10,000 equilibration cycles and 10,000 production cycles. Van der Waals interactions were described by a 12-6 Lennard-Jones potential using a cut-off distance of 12.8 Å. The force field parameters for N₂ were taken from the TraPPE force field.³⁵¹ The Lennard-Jones parameters for the framework atoms were taken the Universal Force Field (UFF).³⁵² All MOFs were treated as rigid in the simulations. Adsorbate-adsorbate and adsorbate-adsorbent van der Waals interactions were taken into account by Lorentz-Berthelot mixing rules.^{353,354}

2.2 Results and Discussion

2.2.1 The Role of Formic Acid and Water on UiO-67(Hf) Phases.

Inspired by previous work on defects in UiO family hafnium MOFs which showed that formic acid plays a crucial role in the formation of the **hcp** UiO-67(Hf) phase¹² the effect of different concentrations of formic acid in the synthesis of UiO-67(Hf) was investigated. Powder X-ray diffraction (PXRD) was used to detect changes in the crystal structure [Figure 2.1]. This series of syntheses was performed in DMF (99% purity). The as-received DMF was not dried further so it is likely that some small amount of water was present in the reaction mixture although no water was added.

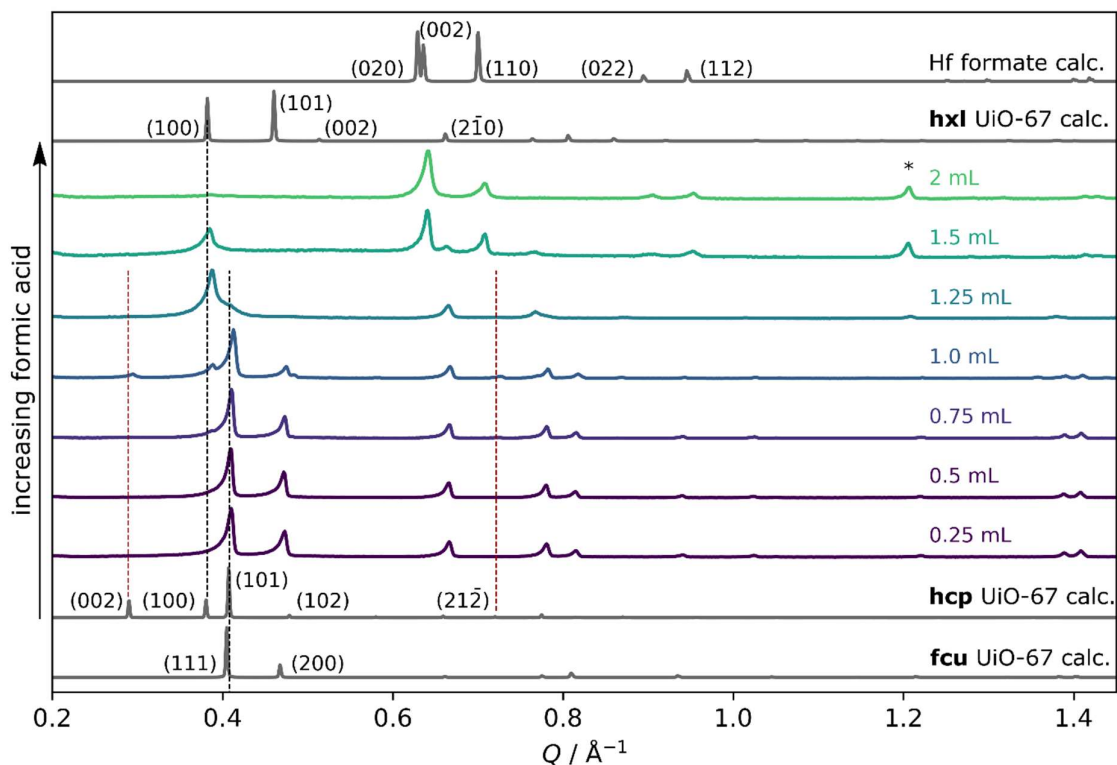


Figure 2.1. PXRD patterns of UiO-67(Hf), synthesised with different concentrations of formic acid. The calculated powder patterns of **fcu**,³⁵⁵ **hcp**¹² and **hxl** UiO-67(Hf), and the hafnium formate MOF,^{141,341} obtained from the crystal structures using the VESTA programme,³⁴⁹ are shown for comparison. Dark red dashed lines indicate the evolution of peaks specific to the **hcp** phase, and black dashed lines show peaks which are common to more than one phase. The asterisk indicates peaks due to crystallised H₂BPDC ligand.¹⁴⁰

Below 1 mL formic acid, the **fcu** phase is seen. **hcp** UiO-67(Hf) is formed when 1 mL formic acid (0.25 : 1 formic acid : DMF V/V) is used in the solvothermal synthesis. The observation of the **hcp**-characteristic reflections (002), (100) and (101) in the region 0.28-0.41 Å⁻¹ clearly indicates that the phase is different from the **fcu**, which in this region has only a (111)

reflection at the same position as the (101) reflection of **hcp**. As the volume of formic acid is increased above 1 mL a new phase forms; at 1.5 mL FcOH this phase crystallises concomitantly alongside the known hafnium formate MOF.¹⁴¹ At around 2 mL formic acid only the formate MOF forms; at high concentrations of formic acid compared to that of H₂BPDC the formate anions outcompete BPDC in binding to the clusters.^{53,341} This shows that the amount of formic acid in the synthesis changes the bulk crystal structure—the phase—of the MOF formed.

The PXRD pattern of the new material, seen most clearly in the PXRD patterns at 1.25 and 1.5 mL formic acid [Figure 2.1], strongly resembles that of the layered **hxl** UiO-67(Hf) material previously reported,¹² but with absent (*hkl*)-dependent peaks such as the **hxl** (101) reflection and with the remaining (*hk0*) reflections displaying Warren-type lineshapes, that is, an asymmetric tail-off towards high-*Q*.²⁹⁰ This lineshape results from turbostratic disorder or random-layered structures in which layers are equidistant and parallel but randomly displaced and rotated about the axis normal to the layers.²⁹⁰ As a result, the reciprocal space lattice, rather than appearing as points, is instead comprised of 'rods' (the periodicity of the crystal layers relative to the normal is effectively destroyed by the disorder, giving an infinite distance in reciprocal space). Rather than sharp Bragg reflections, this results in the absence of general reflections (*hkl*) and an asymmetric broadening of the remaining reflections towards high- 2θ (or $-Q$).

This combination of absent peaks and line broadening therefore indicates the formation of a layered phase similar to **hxl** UiO-67(Hf), but with turbostratic disorder in the *c*-direction. As the **hxl** phase is a layered-nanosheet phase, which can be delaminated into separate nanosheets (i.e., disrupted relative to the layer normal), the prefix **hns** ('hexagonal nanosheet') is proposed for this new disordered layered phase.

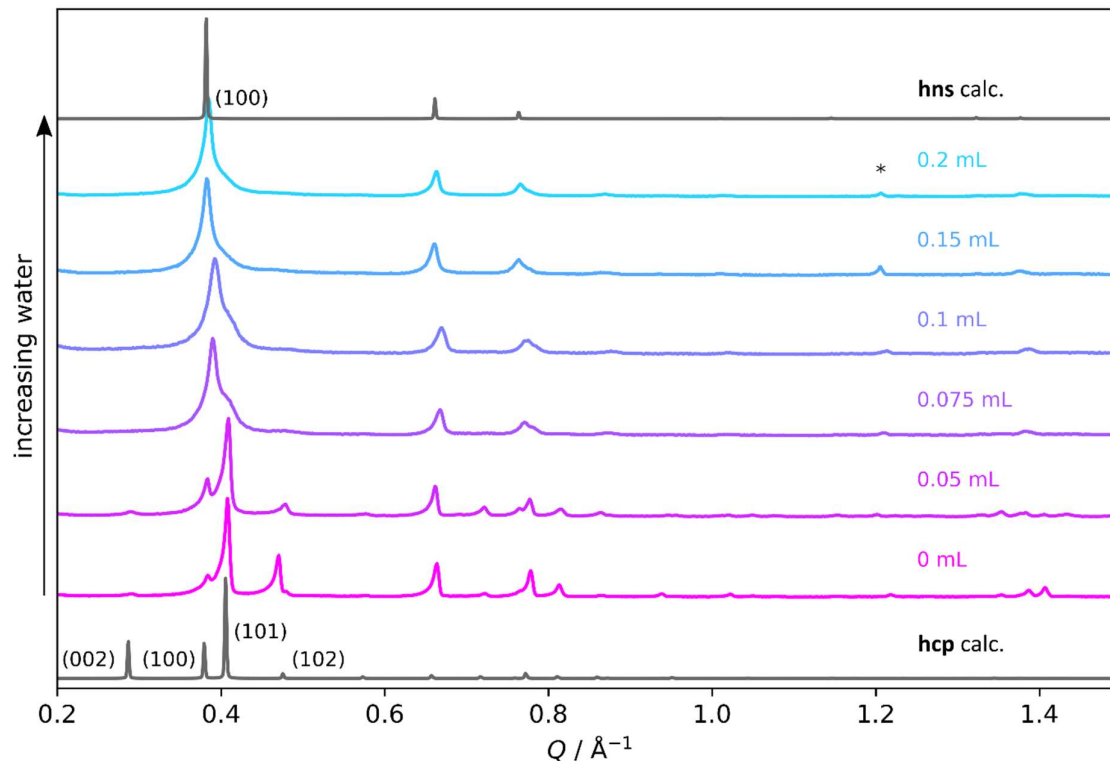


Figure 2.2. PXRD patterns of UiO-67(Hf), synthesised with 1.0 mL of formic acid and different water concentrations, showing the dependency of the phase formed on the concentration of water. Synthesis with 1.0 mL formic acid and 0.05 mL water gives phase-pure **hcp** UiO-67(Hf), and 0.2 mL water gives phase-pure **hns** UiO-67(Hf). The asterisk indicates peaks due to crystallised H₂BPDC ligand.¹⁴⁰

Noting that dissociated water can compensate for missing-linker defects in UiO-66,^{129,342,356} the effect of water in the synthesis of the **hcp** UiO-67(Hf) material was systematically investigated. In order to control the amount of water present in the synthesis, anhydrous DMF solvent was used and known volumes of water added [Figure 2.2].

At low concentrations of water (i.e., where only a small amount of ambient water was present) alongside 1.0 mL formic acid, **fcu** UiO-67 forms along with a minor phase of **hcp**. When small amounts of water are used in the synthesis, the crystallinity and phase-purity of **hcp** UiO-67(Hf) are improved as the added water appears to suppress the formation of any **fcu** impurity phase. At higher water concentrations the **hns** phase forms alongside the **hcp**, becoming phase-pure **hns** at 0.2 mL water (0.05 : 0.25 : 1 water : formic acid : anhydrous DMF V/V) as shown by the complete loss of the **hcp** (102) peak.

In order to reveal the crystal morphology of this phase-pure **hns** UiO-67(Hf) sample scanning electron microscopy (SEM) imaging was performed [Figure 2.3]. This reveals its

disordered stacking with layers stacked but randomly offset, and a hexagonal morphology, thus supporting the use of the 'hexagonal nanosheet' prefix.

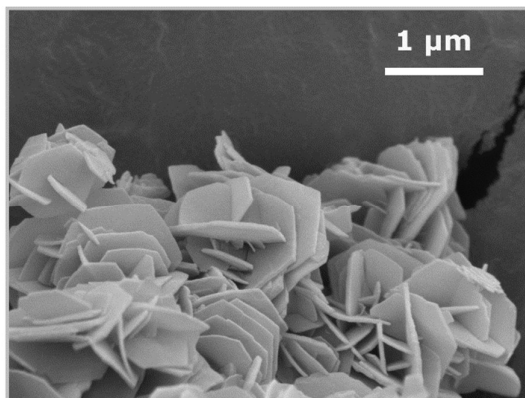


Figure 2.3. SEM image of the *hns* phase of UiO-67(Hf), illustrating the hexagonal nano-sheet morphology.

These materials, synthesised using water, are highly stable in ambient conditions; the washed **hcp** sample synthesised using this method is stable for up to 19 months (unlike the material produced by the previous synthesis by Cliffe *et al.*, which is only stable for a few days, and in contrast to the shorter stability window observed in some cases for **fcu** UiO-67(Zr³⁵⁷) [Figure 2.4 a)],¹² and the washed **hns** sample is still crystalline for up to 20 months [Figure 2.4 b)].

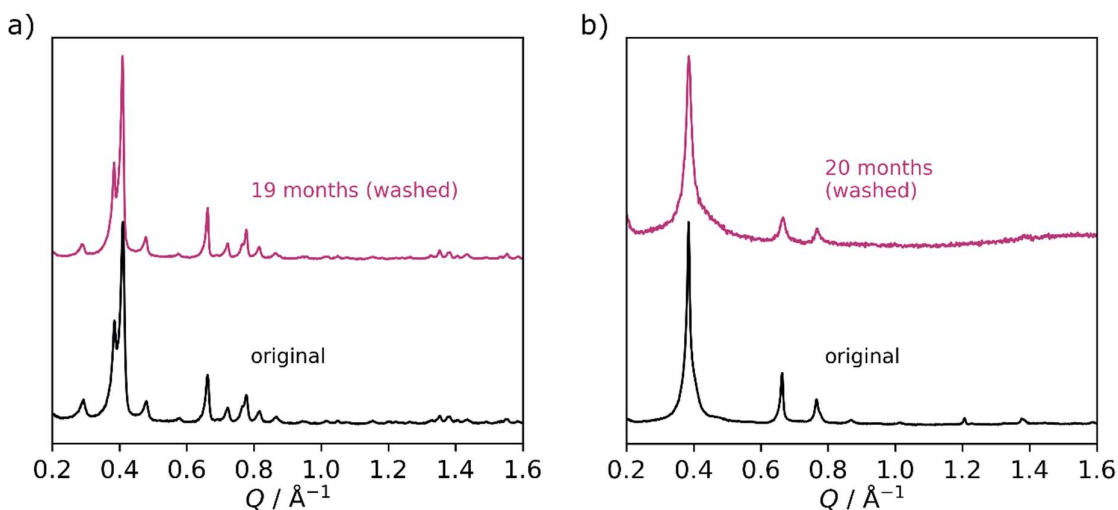


Figure 2.4. Comparison via PXRD of the degradation over time of a) *hcp* UiO-67(Hf); b) *hns* UiO-67(Hf).

The stability was found to be less good for unwashed samples, suggesting that the remaining reaction solvent may react with the MOF components. This stability, and the

insight it gives into the necessity of post-synthetic processing, is important for the prospect of these materials, particularly the nanosheets, for use in real-world applications.

2.2.2 The Effect of Water on UiO-66(Zr/Hf) (F₄BDC).

Upon observing the key role of water in the phase selection of UiO-67(Hf), other previously-reported solvothermal syntheses of UiO materials where water was used as a solvent were examined. The modulated hydrothermal methodology proposed by Ref. 198 provides a green—owing to the omission from the synthesis of toxic solvents such as DMF—and scalable approach to synthesising several MOF frameworks isorecticular to **fcu** UiO-66(Hf). However, it can be observed that the material assigned as the cubic **fcu** UiO-66(Hf or Zr) (F₄BDC) framework in that and other work by the same Authors^{198,346} displays a characteristic ‘splitting’ of the reflection indexed to the **fcu** (111) reflection into two peaks at 0.49 Å⁻¹ and 0.52 Å⁻¹, and an additional reflection is present at 0.35 Å⁻¹ [Figure 2.5]. The presence of these features strongly suggests that this is not, in fact, the **fcu** phase; moreover, these reflections are consistent with this phase being the **hcp** structure.

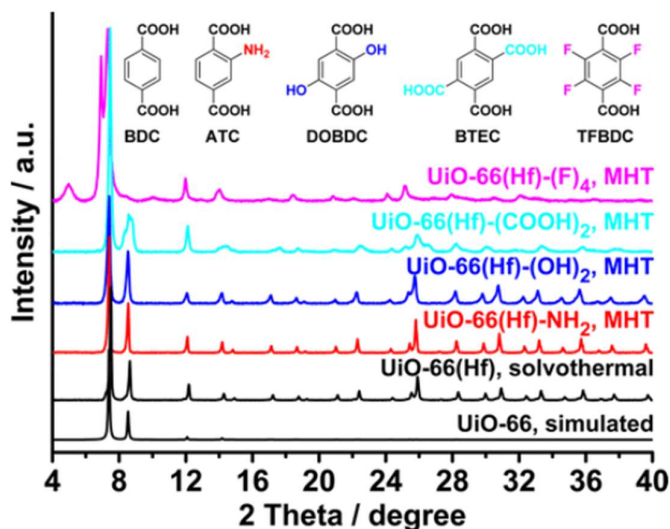


Figure 2.5. Comparison of the PXRD patterns for different UiO-66(Hf) analogues. The pattern from UiO-66 (F₄BDC), labelled as ‘UiO-66(Hf)-(F)₄’ is in pink. Reprinted with permission from Z. Hu, A. Nalaparaju, Y. Peng, J. Jiang and D. Zhao, *Inorg. Chem.*, 2016, 55, 1134–1141. Copyright 2016 American Chemical Society.

The reported synthesis was therefore repeated with both ZrCl₄ (in keeping with previous modulated hydrothermal work³⁴⁶) and HfCl₄ (in keeping with the original work and with other experiments reported in this work) as starting materials. Both of these metal analogues of UiO-66 (F₄BDC) produced experimental PXRD patterns consistent with those of Ref. 198,

including the peak splitting at $\sim 0.5 \text{ \AA}^{-1}$ mentioned above.¹⁹⁸ The PXRD pattern of the Hf analogue was indexed using a hexagonal cell and Pawley refinement²⁸⁷ was carried out to obtain accurate unit cell and instrumental parameters [Figure 2.6].

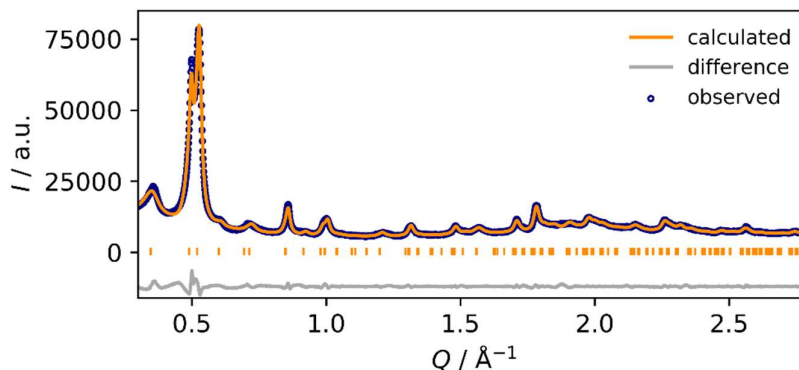


Figure 2.6. Pawley refinement of PXRD dataset of UiO-66 (F_4BDC) in space group $P6_3/mmc$ and with parameters $14.82(1) \text{ \AA}$ and $36.18(1) \text{ \AA}$ ($R_{\text{exp}} 3.086$).

Using the experimental structure as a constraint, a model structure was derived from the known **hcp** UiO-67 structure.¹² This structure was then optimised using quantum chemical calculations. Density functional theory (DFT) calculations were performed both with and without the full crystal symmetry to account for the tilting of the linkers. Optimisation with the full crystal symmetry constrains the linkers to be flat, which does not reflect the rotational disorder present in reality. Aside from the linker tilting, the model structures with and without the full symmetry are otherwise equivalent, giving no evidence of a symmetry-lowering distortion away from the hexagonal structure and suggesting that the overall symmetry of the UiO-66(Hf) (F_4BDC) structure is $P6_3/mmc$, like **hcp** UiO-67.

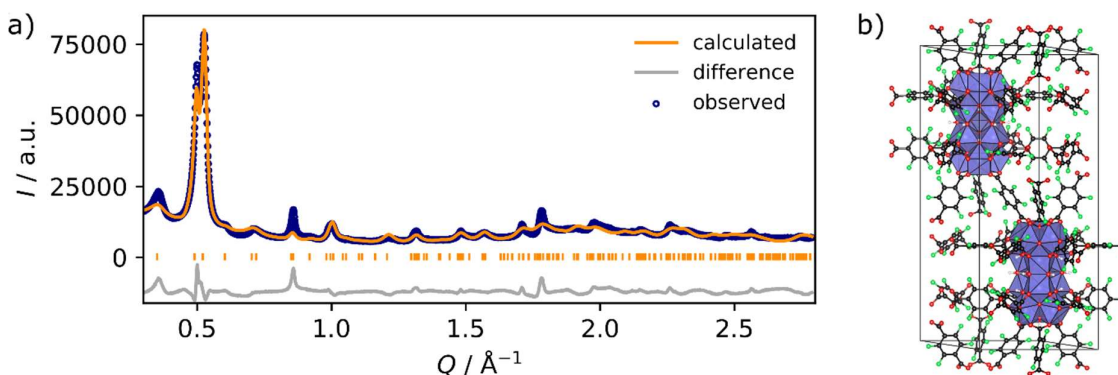


Figure 2.7. a) Refinement of the PXRD pattern of **hcp** UiO-66(Hf) (F_4BDC) against b) the optimised model structure, with linker tilting. The **hcp**-characteristic Hf_{12} double cluster in b) is shown in the polyhedral representation. Discrepancies in low- Q peak intensities are likely to be due to the presence of guests in the pores.¹² Colour scheme of structure: Hf, blue; O, red; C, black; H, white; F, green.

This triclinic optimised model, with linker tilting present, was then compared and validated against the experimental dataset using the instrumental parameters obtained from the Pawley refinement. Refinement against the optimised model of **hcp** UiO-66 (F₄BDC) structure was carried out in space group *P*6₃/*m**m**c* and gave a good fit, with cell parameters 14.793(8) Å and 35.75(5) Å (*R*_w 8.839) [Figure 2.7]. The background was modelled using a freely refining Chebyshev polynomial with seven parameters. In order to account for the (*hkl*)-dependent peak broadening an additional term was introduced using second order spherical harmonics. A Lorentzian size-broadening term and a scale factor with a *sin* (θ) dependence (to correct for the sample being thin relative to the beam penetration depth) were also applied. The discrepancies in low-*Q* peak intensities are likely to be due to the presence of guests in the pores.¹² Due to the small crystallite size and resultant peak broadening, it was not possible to carry out a full Rietveld refinement.

This water-rich synthesis of UiO-66(Zr or Hf) (F₄BDC) results in a **hcp** framework. However, it has been recently reported that a synthesis of UiO-66(Zr) (F₄BDC) with no added water produced the **fcu** phase albeit with missing-linker defects.⁵⁴ This synthesis used THF as a solvent instead and hydrochloric acid as a modulator. A repeat of this synthesis in THF was repeated and indeed found to produce the **fcu** phase [Figure 2.8]. The effect of the water content of the reaction on the phase of UiO-66 (F₄BDC), raised by the discrepancies between the materials obtained in these different syntheses, was therefore investigated. A series of syntheses of UiO-66(Hf) (F₄BDC) in DMF with varying concentrations of water was performed [Figure 2.8 a,b)]. In order to be consistent with the original reported hydrothermal synthesis acetic acid was used as the modulator.¹⁹⁸

For these samples of UiO-66(Hf) (F₄BDC) synthesised in DMF at both 120°C and 150°C the phase which crystallises depends on the ratio of water to acid in the reaction mixture. At both temperatures, with increasing concentrations of water the **hcp** material emerges, followed by a phase resembling **hns**. These materials are very sensitive to the synthetic conditions, and the sample crystallinity is poor with low concentrations of modulating acetic acid. Thus both modulating acid and the presence of water are crucial to the formation of the **hcp** phase.

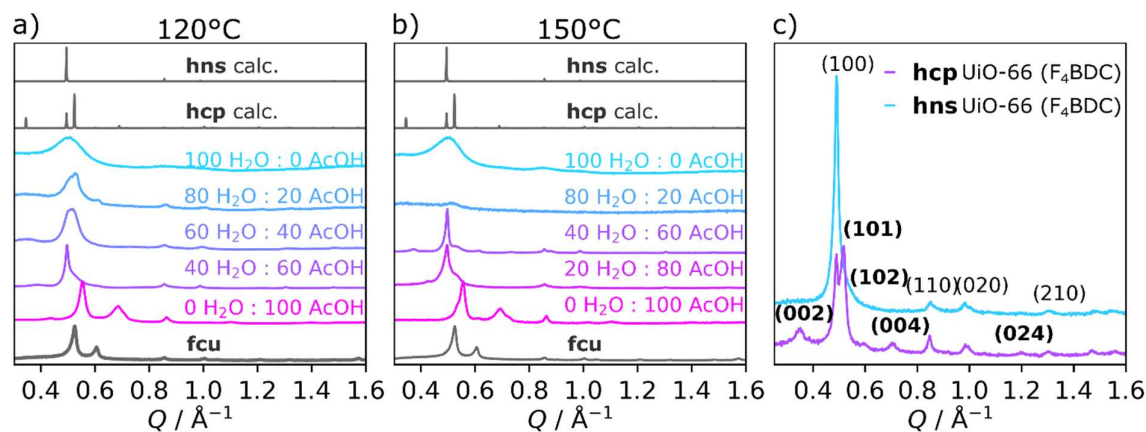


Figure 2.8. *a,b* PXRD patterns of UiO-66 (F₄BDC) synthesised with different water : acetic acid ratios at *a*) 120°C (temperature used in Ref. 198) and *b*) 150°C (the synthesis temperature for *hcp* UiO-67), compared with the predicted patterns for the *hcp* UiO-66 (F₄BDC) structure. Synthesis conditions of 20% : 80% H₂O : AcOH (120°C) and 60% : 40% H₂O : AcOH (150°C) gave no product. The *fcu* samples were synthesised in anhydrous conditions in THF; *c*) comparison of the *hcp* and *hns* phases of UiO-66 (F₄BDC), showing the absence of *l*-dependent (*hkl*) peaks (labelled in bold) in the *hns* phase as compared to the *hcp* phase.

Furthermore, upon washing with DMF or methanol and activation, the *hcp* UiO-66(Hf) (F₄BDC) sample transformed into a highly crystalline *hns* phase as did *hcp* UiO-67(Hf), shown by the loss of *l*-dependent (*hkl*) peaks in the PXRD pattern [Figure 2.8 c)]. This demonstrates that the creation of the defect-ordered *hcp* phase gives straightforward access to the layered-nanosheet material. The morphological differences between the *fcu*, *hcp* and *hns* phases were imaged using SEM [Figure 2.9]; unlike the small grain-like crystallites of the *fcu* material, the *hcp* material has a hexagonal intergrowth with a characteristic ‘desert rose’ appearance and the *hns* phase shows a delamination into sheets.

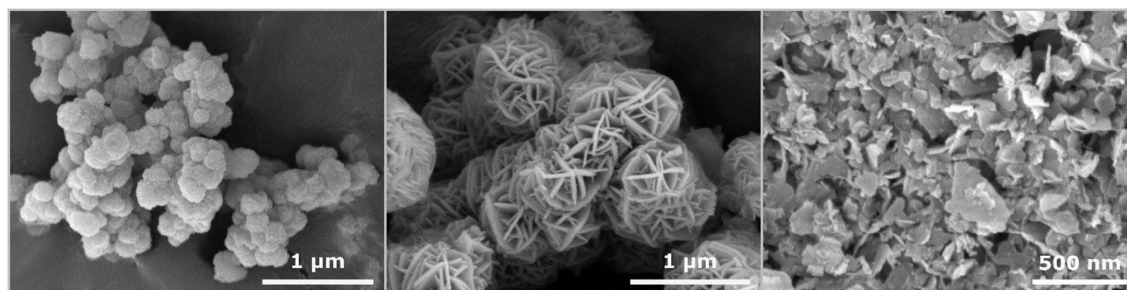


Figure 2.9. SEM images of the different phases of UiO-66(Hf) (F₄BDC): left, *fcu* sample, synthesised based on the method of Ref. 54; centre, *hcp* sample, synthesised with 60% : 40% H₂O : AcOH at 120°C; right, *hns* sample, formed by delamination of the *hcp* material.

Compared to the experiments in this and previous¹⁴¹ work on defect-mediated phases which required the presence of formic acid to form, this experiment with UiO-66(Hf) (F₄BDC) uses

acetic acid. The effect of the two modulators was compared by substituting acetic acid for formic acid in the synthesis optimised to produce **hcp** UiO-66(Hf) (F₄BDC), 60 : 40 water : acid, 120°C.

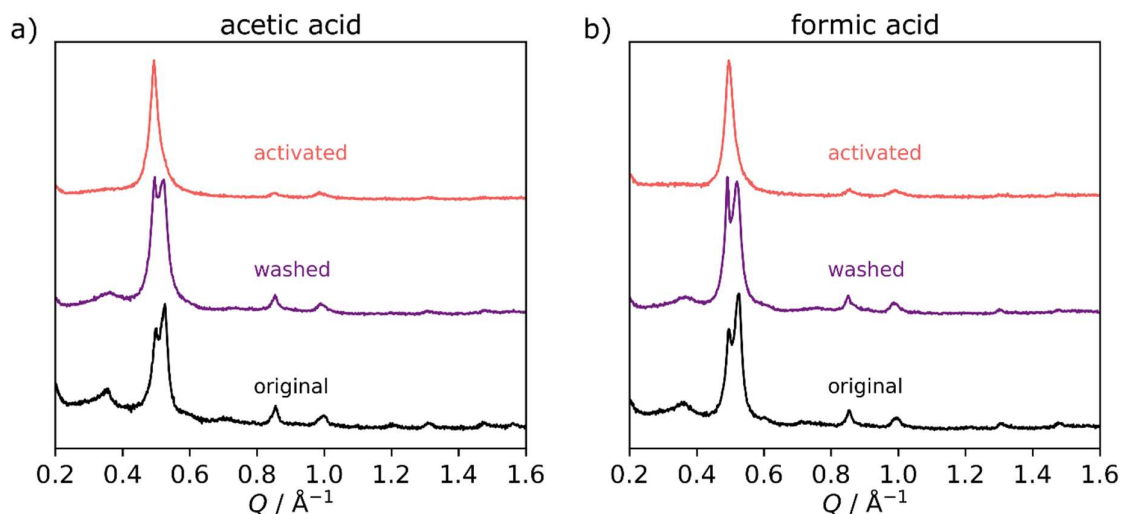


Figure 2.10. Comparison via PXRD of the outcomes of the synthesis and washing and activation processes for **hcp** UiO-66(Hf) (F₄BDC) with a) acetic acid modulator; b) formic acid modulator.

The two syntheses produced very similar materials according to PXRD [Figure 2.10], and the washing and activation processes in both cases triggered the transformation of the **hcp** material into the **hns**. Therefore, the synthesis with formic acid, as with acetic acid, permits the formation of both the **hcp** and **hns** material. This is in contrast with the synthesis of **hcp** UiO-67(Hf) where only formic acid is used; H₂F₄BDC has a greater acidity and different coordination strength compared to H₂BPDC, and acetic acid is less acidic than formic acid. This discovery suggests that the important factors for the formation of **hcp** UiO family MOFs are not only the relative coordination strengths of the linker and modulator but also the overall acidity of the solution.

2.2.3 Synthesis of **hcp** UiO-66(Hf).

The above two investigations of the BPDC and F₄BDC analogues of UiO family MOFs have established that both modulating acid and water in the synthesis in DMF of UiO family MOFs affect the phase of the material formed. Increasing the concentration in DMF of acid and water simultaneously tends to promote the formation of the **hcp** phase rather than the **fcu**, or, indeed, the nano-**reo** structure. The synthesis of the **hcp** phase of UiO-66(Hf) was

therefore pursued using this understanding of the key role of water in synthesis in combination with formic acid.

The synthesis conditions for **hcp** UiO-67(Hf) were adapted and phase-pure **hcp** UiO-66(Hf) was successfully synthesised using high concentrations of water and formic acid in DMF. At lower concentrations of either formic acid or water the **fcu** (111) peak broadens into the region where **hcp** (100) and (101) peaks would be expected but the individual **hcp** peaks are not seen. This is indicative of a low concentration of **hcp** (**fcu** remaining the major component). Phase-pure **hcp** UiO-66(Hf) only forms once volumes of at least 0.4 mL water and 1.5 mL formic acid in 4 mL DMF (0.1 : 0.375 : 1 V/V water : formic acid : DMF) are used [Figure 2.11 a-d)]. The PXRD pattern of **hcp** UiO-66(Hf) is consistent with that recently reported by Ref. 358 for the **hcp** UiO-66(Zr) material, which was published shortly after the completion of this work.

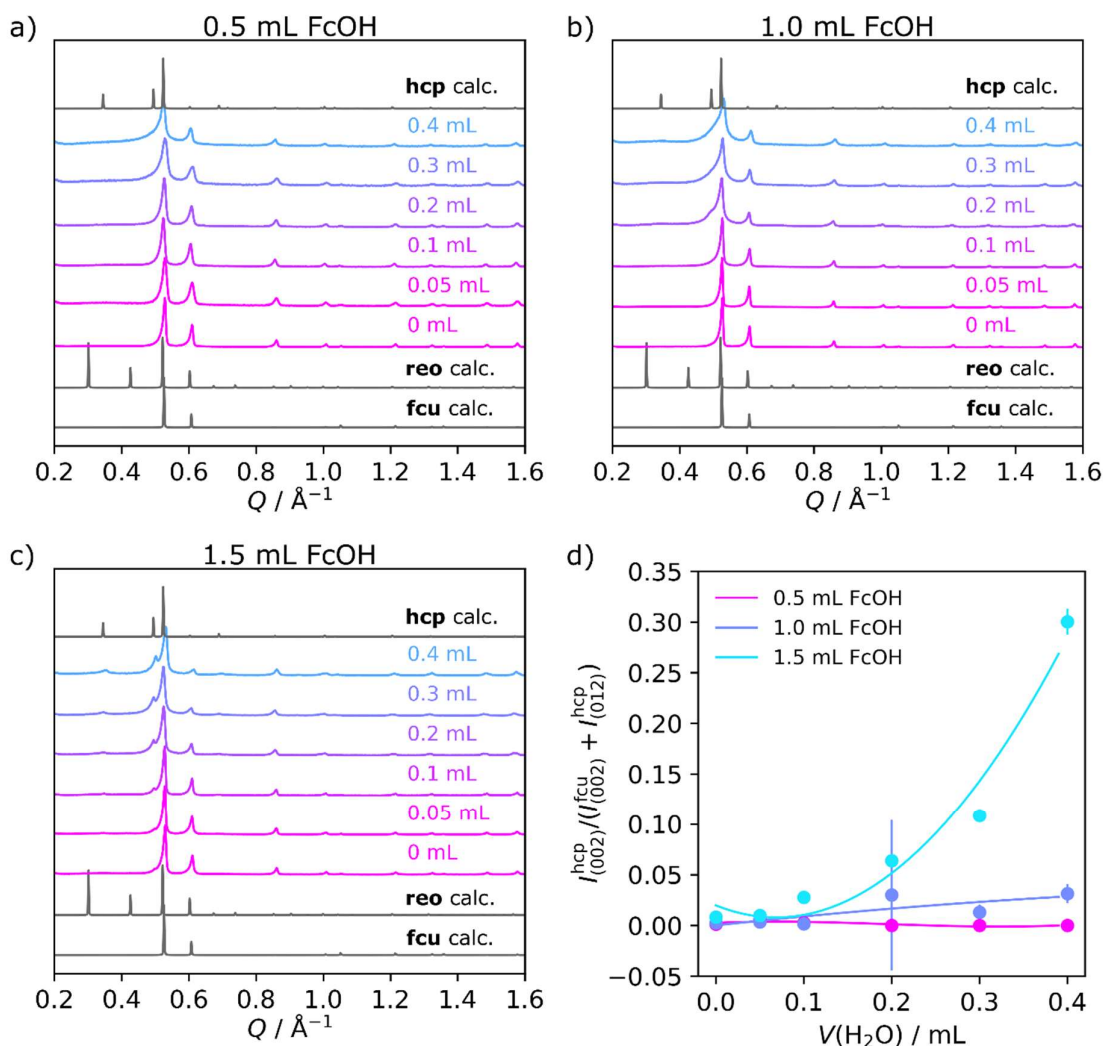


Figure 2.11. a-c) PXRD patterns of UiO-66 synthesised in 4 mL DMF with varying water concentrations and a) 0.5 mL FcOH; b) 1.0 mL FcOH; c) 1.5 mL FcOH. d) Plot of the intensity ratio of **hcp** vs **fcu** peaks, showing the emergence of the **hcp** UiO-66 phase only at higher concentrations of both formic acid and water. PXRD patterns are compared with the predicted patterns for the **fcu**,¹⁶⁵ **reo**¹⁴¹ and **hcp** UiO-66 structures.

To confirm that this phase is **hcp** UiO-66(Hf), a model structure of **hcp** UiO-66(Hf) was created based on the optimised structure for **hcp** UiO-66(Hf) (F₄BDC). Using the same approach as used to analyse the PXRD pattern of **hcp** UiO-66(Hf) (F₄BDC), the PXRD pattern of washed and activated **hcp** UiO-66(Hf) was indexed and accurate unit cell and instrumental parameters obtained from Pawley refinement [Figure 2.12].

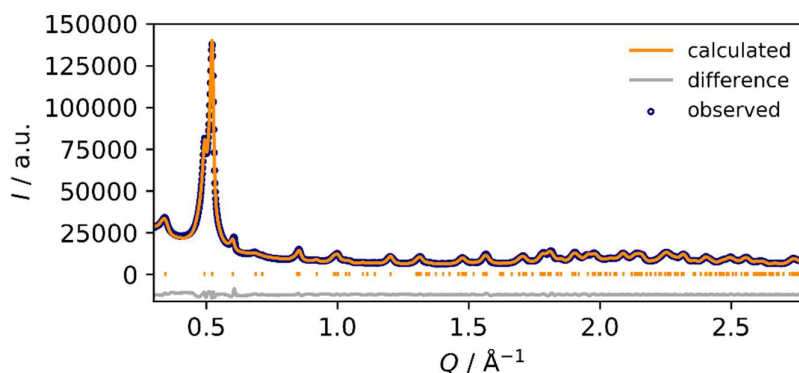


Figure 2.12. Pawley refinement of *hcp* UiO-66, synthesised in 4 mL DMF with 0.4 mL water and 1.5 mL formic acid, in space group $P6_3/mmc$ and with parameters 14.708(5) Å and 36.54(2) Å (R_{wp} 2.483).

These parameters were then used in a comparison of the experimental **hcp** dataset against the model structure, giving a good fit [Figure 2.13 a,b)]. Refinement against the **hcp** UiO-66 structure was carried out in space group $P6_3/mmc$ and gave cell parameters 14.742(3) Å and 36.50(2) Å (R_{wp} 5.259). The background was modelled using a freely refining Chebyshev polynomial with nine parameters. In order to account for the anisotropic peak broadening, an additional term was introduced using second order spherical harmonics. A Gaussian size-broadening term, a scale factor with a $\sin(\theta)$ dependence (to correct for the sample being thin relative to the beam penetration depth), and a preferred orientation term along [001] were also applied. The discrepancies in low- Q peak intensities are likely to be due to the presence of guests in the pores.¹² Again, because of the small crystallite size, it was not possible to carry out Rietveld refinement.

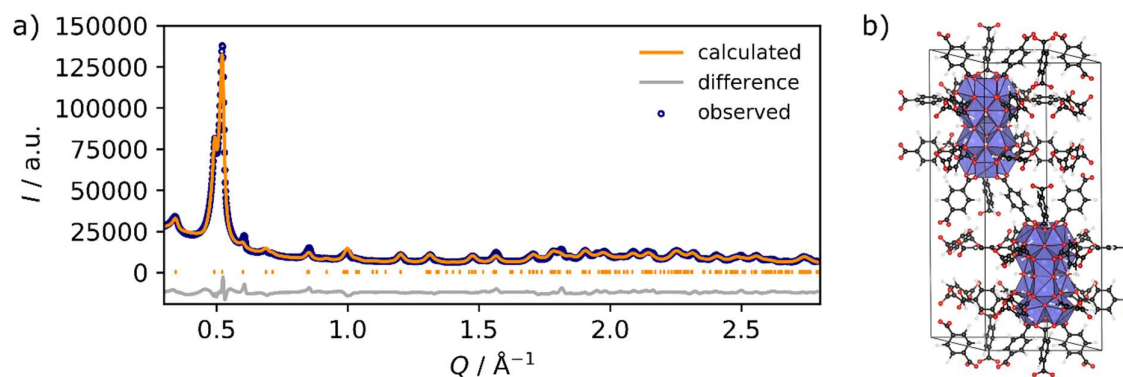


Figure 2.13. a) Refinement of the PXRD pattern of *hcp* UiO-66 against b) the proposed structure. Discrepancies in low- Q peak intensities are likely to be due to the presence of guests in the pores.¹² Colour scheme of structure: Hf, blue; O, red; C, black; H, white.

This fit of the experimental data against the model of **hcp** UiO-66(Hf) confirms that this synthesis, containing both formic acid and water, does indeed produce the **hcp** phase. Thus

again water, alongside modulating acid, is important in obtaining the **hcp** phase of UiO-66, both by promoting the formation of the **hcp** structure over the **fcu** and by suppressing the hafnium formate phase. The washed and activated **hcp** UiO-66(Hf) material synthesised in this manner is stable in ambient conditions, with little change observed in the PXRD after nine months [Figure 2.14].

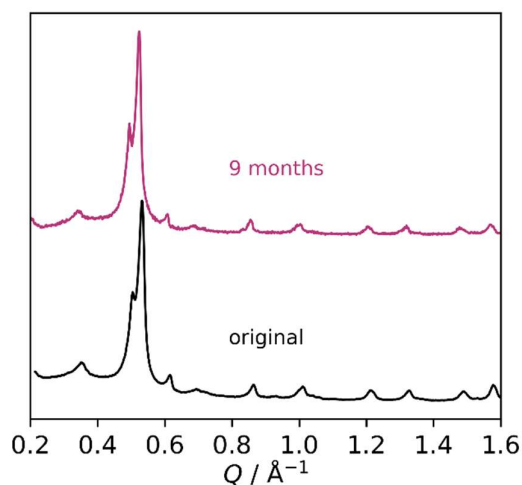


Figure 2.14. Comparison via PXRD of the degradation over time of **hcp** UiO-66(Hf).

Following the successful synthesis of **hcp** UiO-66(Hf), the effect of altering the amounts of water and formic acid in the reaction mixture was explored further. Increasing the amount of water generally decreases the crystallinity of the product [Figure 2.15 a)]; increasing the amount of formic acid improves the crystallinity [Figure 2.15 b)] such that the concentrations of water and formic acid can together be increased to high quantities without loss of crystallinity [Figure 2.15 c)]. However, neither the hafnium formate phase previously reported for both UiO-66(Hf) and UiO-67(Hf) nor the phase-pure delaminated **hns** phase seen in the investigation of **hcp** UiO-67 was produced. The effect on the **hcp** framework of increasing the concentrations of water and formic acid was therefore explored.

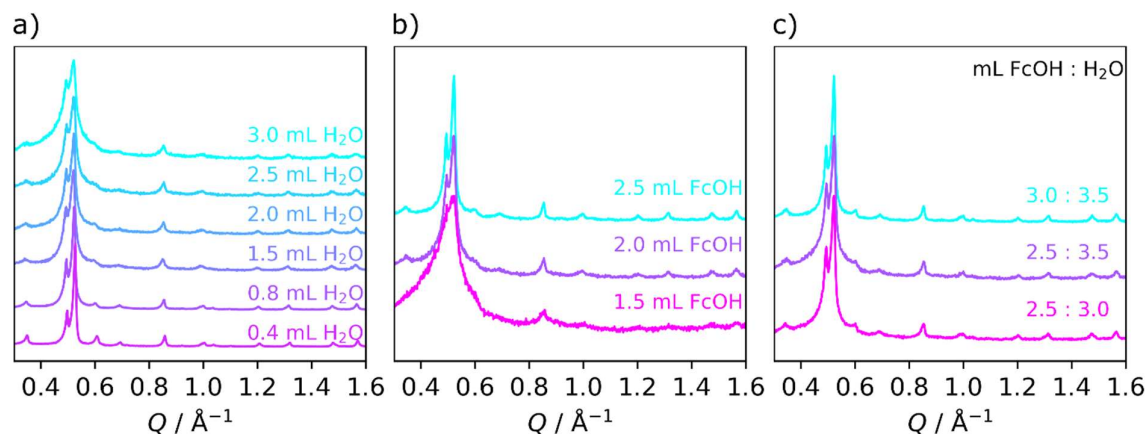


Figure 2.15. Syntheses of UiO-66(Hf) in 4 mL DMF with higher amounts of water and formic acid: a) with 2 mL formic acid and varying amounts of water; b) with 2.5 mL H₂O and increasing the amount of formic acid in the synthesis; c) synthesised with very high concentrations of water and formic acid.

2.2.4 Investigation of Defect Concentrations in hcp UiO-66(Hf) Phases via TGA and ¹H NMR Studies.

Despite adding high quantities of water and formic acid to the synthesis of UiO-66(Hf) no other phases were observed using PXRD (neither the hafnium formate MOF nor the **hns** phase). However, these reagents could still cause changes to the **hcp** phase without being apparent *via* PXRD. One possibility is that water and formic acid could be introducing missing-linker defects into the framework: it is well known that modulated synthesis of **fcu** UiO-66 often introduces missing-linker defects, whereas these are less commonly reported in **fcu** UiO-67. These missing-linker defects are compensated by modulating acid, water, or hydroxide.^{12,53,101,121–123,129} Therefore the effect of formic acid and water on the obtained **hcp** phase was investigated.

The formation of **hcp** UiO-66(Hf) occurs at higher concentrations of both formic acid and water (0.4 mL water and 1.5 mL formic acid in 4 mL anhydrous DMF) than for **hcp** UiO-67(Hf) (0.05 mL water and 1 mL formic acid in 4 mL anhydrous DMF). However, it is likely that a higher concentration of defects can be stabilised in **fcu** UiO-66(Hf) compared to **fcu** UiO-67(Hf) before the defect-ordered **hcp** phase forms.^{122,181,182}

While the recently-reported **hcp** UiO-66(Zr) was briefly noted to contain missing-linker defects,³⁵⁸ this work further investigates the presence of defect-compensating molecules in **hcp** UiO-66(Hf). This will help to establish whether water and formic acid in the synthesis not only determine the phase, as this work has demonstrated, but also control the concentration of missing-linker defects in the **hcp** phase, just as in **fcu** UiO-66.³⁵⁹

Thermogravimetric analysis (TGA) was used to measure the amount of missing-linker defects in the materials. The TGA curve of UiO-66 family frameworks shows three distinct steps, corresponding to different stages of decomposition.^{268,337,342,343} The first significant mass losses (below 150°C) are due to the loss of solvent molecules and hydrogen-bonded water.³⁴² The mass losses between 250 and 300°C correspond, in **fcu** frameworks with the Hf₆ 'single' cluster, to the dehydroxylation of the Hf₆O₄(OH)₄ cluster 'core' to Hf₆O₆,^{50,337} as well as loss of missing-linker-compensating modulator or hydroxide/water molecules (as discussed in Chapter 1).^{15,165,342} The final and largest mass loss, used to calculate the linker-cluster stoichiometry, corresponds to the decomposition of the remaining framework and the formation of HfO₂ when the TGA is performed in air or in the presence of oxygen.^{15,343}

The TGA curve of **hcp** UiO-66(Hf) samples likewise gives mass losses at similar temperatures, confirming similar structural stability [schematic shown in Figure 2.16]. In the 'dehydroxylation' step, the Hf₁₂ double cluster is assumed not to disintegrate to give separate Hf₆ clusters *via* loss of the six μ₂-OH. Instead, as with **fcu** UiO-66, it loses formate anions (FcO) and hydrogen-bonded water to give a [Hf₆O₆]₂(OH)₆ dehydroxylated 'core' of the double cluster.

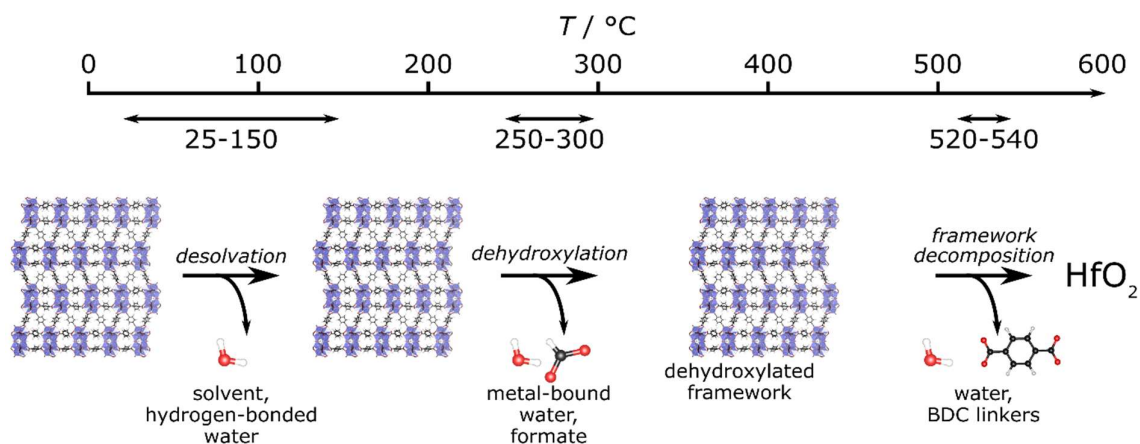


Figure 2.16. Schematic of the stages of decomposition of **hcp** UiO-66 in air, showing the molecules lost, as temperature increases.

Of the UiO-66 samples synthesised with 1.5 mL formic acid, those with >0.4 mL water are phase-pure **hcp** UiO-66 by PXRD [see Figure 2.11 c)]. However, the ratios of initial to final masses in the TGA curves for these phase-pure **hcp** samples are lower than for perfect **hcp** (with the mass ratio m/m_{final} approximately 96.3% and 90.8% of the perfect **hcp** mass ratio

for the samples synthesised with 0.4 mL water and with 1.5 mL water respectively [Figure 2.17]), indicating the presence of defects. These mass ratios also show a correlation between the framework mass and the concentration of water in the synthesis: as the concentration of water is increased, the mass ratio decreases [Figure 2.17]. Samples with 0-0.3 mL water in the reaction mixture are mixed-phase; their mass ratios relative to HfO₂ are lower than for perfect **fcu**. This is as expected for a **fcu/hcp** mixture since **hcp** UiO-66 has a lower metal : linker ratio than **fcu** (**fcu** UiO-66 has 12 linkers coordinated per Hf₆ cluster; **hcp** UiO-66 has 18 per Hf₁₂). However, without the evidence of the change in phase from PXRD data, these TGA curves could be erroneously modelled as extremely defective **fcu**. This demonstrates the need for care when using TGA data to calculate the defect concentration in UiO family MOF samples: if a sample is mixed phase, or the wrong model structure is used, there will be large systematic errors in the estimated defectivity.

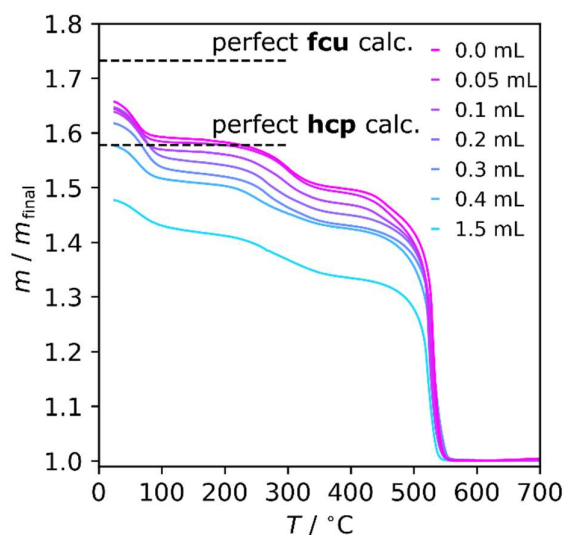


Figure 2.17. Thermogravimetric analysis performed under air of UiO-66(Hf) samples synthesised in 4 mL DMF with 1.5 mL FcOH and varying concentrations of water. The samples with 0.4 mL and 1.5 mL water were both phase-pure **hcp** by PXRD.

Solution NMR can be used to determine the organic ligand composition of a digested MOF sample. In combination with the TGA data this can be used to calculate the overall composition of the MOF samples while conserving charge balance, as described in Chapter 1 and in Table 2.I. Where the formula of defect-free **hcp** UiO-66(Hf) is $[\text{Hf}_6\text{O}_4(\text{OH})_4]_2(\text{OH})_6(\text{BDC})_9$, the general formula of defective samples containing defect-compensating formate, water and hydroxide molecules heated above 150°C is $\{[\text{Hf}_6\text{O}_4(\text{OH})_4]_2(\text{OH})_6\}(\text{BDC})_x(\text{FcO})_y(\text{OH})_z(\text{H}_2\text{O})_z$. Above this temperature solvent and water

molecules not coordinated to the metal clusters will have been lost, so the water/hydroxide cluster-capping motif at this temperature will be one hydroxide and one water (both metal-coordinated) with the number of H₂O molecules in the formula equal to the number of linker-replacing hydroxides, *z*.³⁴²

Table 2.I. Mass changes under heating of UiO-66 frameworks in air. 'BDC_{1/2}' represents the number of half-BDC ligands attached to each cluster (i.e., for perfect **fcu** UiO-66, BDC_{1/2} = 12; for perfect **hcp** UiO-66, BDC_{1/2} = 18).

<i>T</i> / °C	fcu UiO-66 (for comparison)	hcp UiO-66
25-150	Hf ₆ O ₄ (OH) ₄ (BDC _{1/2}) _{<i>x</i>} (FcO) _{<i>y</i>} (OH) _{<i>z</i>} (H ₂ O) _{<i>z</i>} · <i>z</i> H ₂ O	(Hf ₆ O ₄ (OH) ₄) ₂ (OH) ₆ (BDC _{1/2}) _{<i>x</i>} (FcO) _{<i>y</i>} (OH) _{<i>z</i>} (H ₂ O) _{<i>z</i>} · <i>z</i> H ₂ O
150-250	Hf ₆ O ₄ (OH) ₄ (BDC _{1/2}) _{<i>x</i>} (FcO) _{<i>y</i>} (OH) _{<i>z</i>} (H ₂ O) _{<i>z</i>}	(Hf ₆ O ₄ (OH) ₄) ₂ (OH) ₆ (BDC _{1/2}) _{<i>x</i>} (FcO) _{<i>y</i>} (OH) _{<i>z</i>} (H ₂ O) _{<i>z</i>}
350-500	Hf ₆ O ₆ (BDC _{1/2}) _{<i>x</i>} (OH) _{<i>z+y</i>}	(Hf ₆ O ₆) ₂ (OH) ₆ (BDC _{1/2}) _{<i>x</i>} (OH) _{<i>z+y</i>}
>550	HfO ₂	HfO ₂
Total Mass Loss		
520-540	<i>x</i> (BDC _{1/2}) + (<i>z+y</i>)(OH) - 6O	<i>x</i> (BDC _{1/2}) + (6+ <i>z+y</i>)(OH) - 12O

The presence of formate anions (FcO⁻) in the activated phase-pure **hcp** UiO-66 frameworks—that is, synthesised in DMF with 1.5 mL formic acid and 0.4 mL or 1.5 mL water—was confirmed by solution ¹H NMR on digested solutions of the MOF in 1M NaOH in D₂O [Figure 2.18, Figure 2.19]. Further deviations from the expected mass fraction in the TGA therefore indicate the presence of water or hydroxide as additional capping molecules.

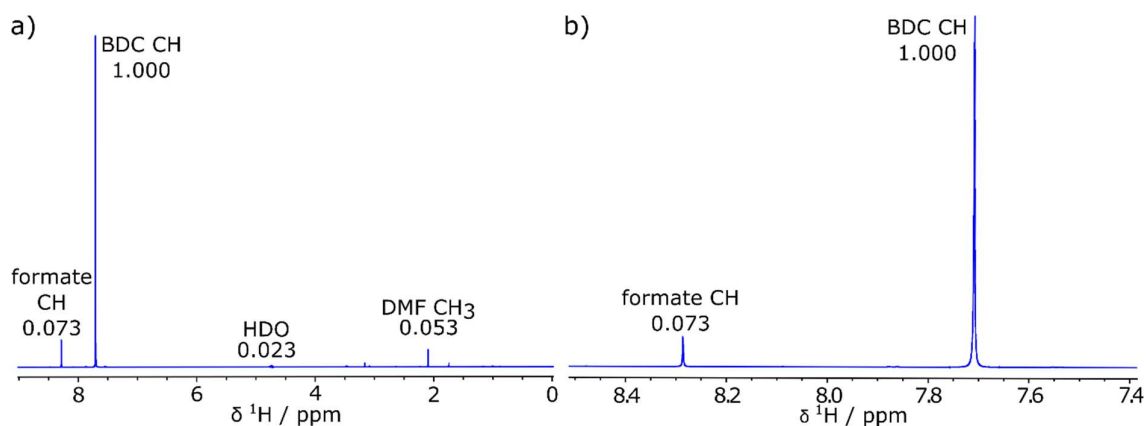


Figure 2.18. ¹H NMR spectra (background-suppressed) of **hcp** UiO-66 synthesised in 4 mL DMF with 0.4 mL H₂O and 1.5 mL FcOH, washed and activated, and digested in 1M NaOH/D₂O: a) full spectrum; b) expanded spectrum. Integrals are normalised to BDC CH.

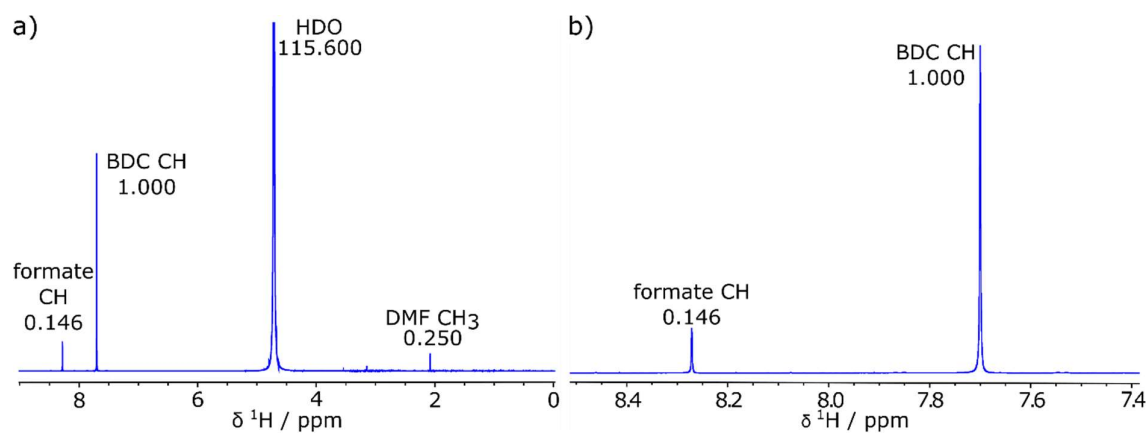


Figure 2.19. ¹H NMR spectra of **hcp** UiO-66 synthesised in 4 mL DMF with 1.5 mL H₂O and 1.5 mL FcOH, washed and activated, and digested in 1M NaOH/D₂O: a) full spectrum; b) expanded spectrum. Integrals are normalised to BDC CH.

Calculations based on the mass losses in the TGA performed in air indeed confirm that the sample contains water/hydroxide capping ligands as well as BDC and formate [Figure 2.20] (details of the calculation can be found in the Appendix). Where x = BDC ions, y = formate ions, and z = hydroxide/water [see Table 2.I], the **hcp** UiO-66 sample synthesised with 0.4 mL water and 1.5 mL formic acid is found to have $x = 6.63(11)$, $y = 1.93(4)$, $z = 2.81(22)$, i.e., 26(1)% of terephthalate (BDC) linkers replaced. For the sample synthesised with 1.5 mL water and 1.5 mL formic acid, the calculation gives $x = 4.81(11)$, $y = 2.80(7)$, $z = 5.58(22)$, i.e., 47(1)% of BDC linkers replaced. Therefore, the **hcp** material can incorporate missing-linker defects to a high level, compensated by both formate and water/hydroxide as in **fcu** UiO-66.

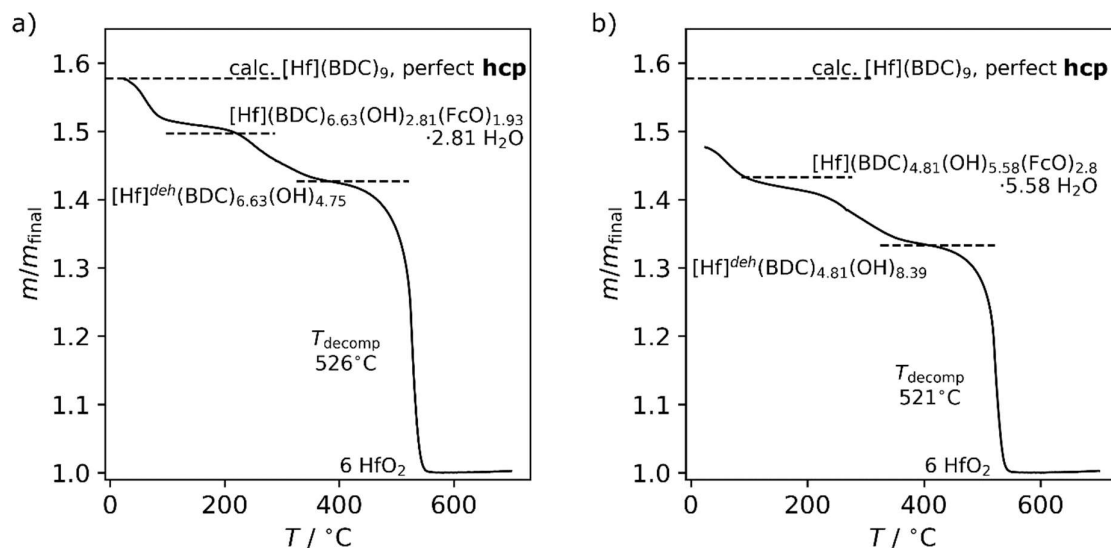


Figure 2.20. TGA curves for **hcp** UiO-66 synthesised in 4 mL DMF with a) 1.5 mL formic acid and 0.4 mL water; b) 1.5 mL formic acid and 1.5 mL water. $[\text{Hf}]$ represents the $[\text{Hf}_6\text{O}_4(\text{OH})_4]_2(\text{OH})_6$ cluster, and $[\text{Hf}]^{\text{deh}}$ represents the dehydroxylated $[\text{Hf}_6\text{O}_6]_2(\text{OH})_6$ cluster; the calculated mass fraction for a perfect, non-defective **hcp** sample is shown for comparison. T_{decomp} is calculated as the temperature at which the rate of mass loss (dm/dT) is greatest.

Water in the synthesis also allows control over the phase purity of the sample, as established earlier. Hence not only the phase but also the defectivity of the sample can be tuned by adjusting the water concentration in the synthesis.

2.2.5 Adsorption Isotherm Measurements of **hcp** UiO-66(Hf).

As expected, the change in the MOF structure from **fcu** to **hcp**, with the accompanying change in the cluster, affects the surface area and size of the pores in the sample. This is demonstrated by its sorption behaviour [Figure 2.21]. The new phase **hcp** UiO-66 (Hf) has a Brunauer-Emmett-Teller (BET) area (N_2) of $422 \text{ m}^2\text{g}^{-1}$ (when synthesised with 0.4 mL water), which is lower than the $655\text{--}940 \text{ m}^2\text{g}^{-1}$ reported for the **fcu** UiO-66 (Hf) phase.^{139,164,360} This sample is a phase-pure **hcp** sample with the lowest level of defects obtained in this work, so the measured BET area will be closest to that of a perfect **hcp** sample. A decrease in the BET surface area is expected, due to the greater density of the double-cluster material as opposed to the single cluster phase. This decrease is also displayed in the literature BET areas of **hcp** compared to **fcu** UiO-67(Hf) and is generally observed as a result of cluster condensation in other materials, such as oxides.^{12,361}

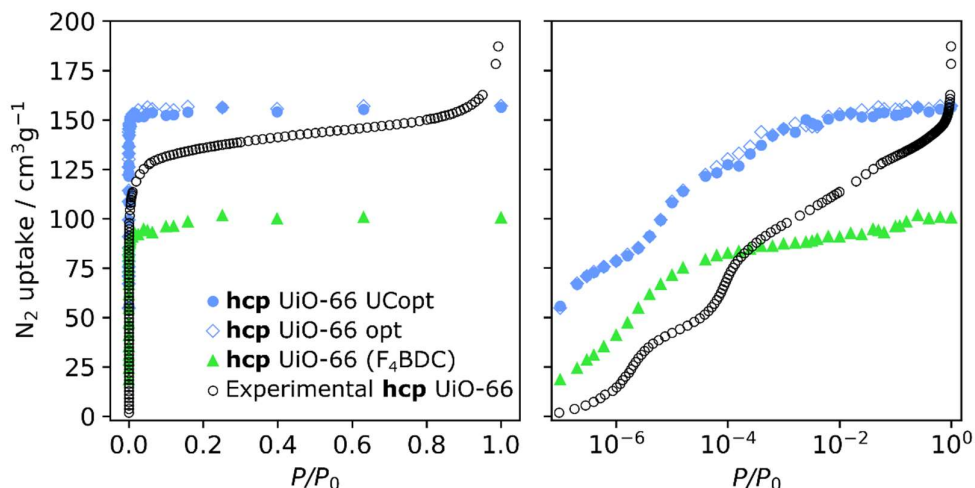


Figure 2.21. Simulated and experimental N_2 isotherms for **hcp** UiO-66 (right: semi-logarithmic scale). The simulated N_2 adsorption isotherm for UiO-66 (F_4BDC) is plotted for comparison.

The simulated N_2 adsorption isotherms [Figure 2.21], using grand canonical Monte Carlo (GCMC) calculations based on the model **hcp** UiO-66 crystal structure, agree well with the experimentally-observed isotherms at saturation pressures.^{350,360} At lower pressure, they show a typical overprediction of the host-guest interaction.³⁶² The simulations were performed using two **hcp** UiO-66 structures generated from the model **hcp** structure of UiO-66 (F_4BDC). The first structure (**hcp** UiO-66 opt) corresponds to the geometrically optimized material after exchanging all F atoms to H while keeping the unit cell parameters fixed. The second structure (**hcp** UiO-66 UCopt) was generated by optimizing the geometry while relaxing the unit cell parameters. The simulations for both of these structures, carried out at 77 K, almost overlap, suggesting that the proposed **hcp** UiO-66 structure is very close to the known **hcp** UiO-66 (F_4BDC) structure and does not show any flexibility. For comparison, the BET area of $370\text{--}380\text{ m}^2\text{g}^{-1}$ calculated for **hcp** UiO-66 (F_4BDC) from these simulations is consistent with the published BET value of $328\text{ m}^2\text{g}^{-1}$.¹⁹⁸

Usually for microporous powder samples a Type I isotherm is seen, corresponding to the filling of the narrow pores which have high affinity with the guest (N_2) molecules; this is seen in the simulated isotherm, performed on a perfect model crystal without any defects.³⁶³ In the case of the experimental sample, however, the isotherm of **hcp** UiO-66(Hf) is of Type II, displaying a small positive slope in the range $0.0001\text{--}0.9 P/P_0$ followed by a suddenly increased uptake at high P/P_0 ,^{98,363,364} and therefore indicating the presence in the sample of mesoporosity.^{129,167,169,344} Missing-linker defects in **fcu** UiO-66 are known to create

mesopores;⁹⁸ in UiO-66 samples with missing-linker defects and known mesoporosity, pore volumes of up to 1.0 cm³g⁻¹ corresponding to pore apertures of 11.5 Å, and diameters even of 1-5.5 nm, have been observed.^{98,141,142,365} This is in comparison to purely microporous UiO-66, which yields pore volumes of 0.426 cm³g⁻¹, with 6 Å apertures and 30 Å diameter.^{50,166,366} Here, calculations from the isotherms of **hcp** UiO-66 give a Horvath-Kawazoe pore width of 7.13 Å and average pore diameter of 68.7 Å, which support the existence of mesopores in the **hcp** sample.³⁶⁷⁻³⁷¹

2.2.6 Post-synthetic Treatment

Unlike the **fcu** phase, the **hcp** structure is not isotropic; the formation of the hafnium 'double' cluster results in a higher intercluster connectivity in the *ab* plane, which leads to the anisotropic chemical stability of **hcp** UiO-67(Hf) demonstrated in the ease of forming the **hxl** layered-nanosheet phase.¹² While **hcp** UiO-66(Hf) has the same Hf₁₂ clusters, and hence the same differences in connectivity between the *ab* plane and the *c* direction, the **hxl** and **hns** analogues of UiO-66(Hf) have proved elusive. **hcp** UiO-66(Hf) can withstand high amounts of missing-linker defects, introduced through the use of formic acid and water in the synthesis, whereas **hcp** UiO-67(Hf) is only formed with a narrow range of concentrations of these missing-linker-inducing species.

In order to better understand the anisotropic stability of these two isoreticular frameworks, their responses to post-synthetic modification were explored. The linker 2,5-pyridinedicarboxylate (PyDC) was used as it has precedent in use as a linker in UiO family MOFs,³⁴⁰ in mixed-linker defective frameworks,¹⁰⁷ and in postsynthetic exchange reactions on UiO-66.¹¹¹ The difference of linker length between BPDC in **hcp** UiO-67 and PyDC should make any bulk structural changes in this framework more evident.

Postsynthetic ligand exchange in defective **fcu** and nano-**reo** UiO family MOFs is known to preferentially occur at missing-linker defect sites.¹¹¹ Thus different modes of exchange are possible: substitution of one defect-compensating ligand (such as formate or water/hydroxide) for another; substitution of a two defect-compensating ligands or one framework linker by a different linker species with complete coordination by both carboxylate groups ('defect healing');¹²⁹ or replacement of one framework linker by two ligands (creating a new missing-linker defect). In the case of PyDC, incomplete coordination

can occur, where only one carboxylate group of a PyDC ligand coordinates to a metal cluster, leaving one uncoordinated carboxylate/carboxylic acid group; this could also result in steric clash between ligands. While the PYDC ligand does have the potential to coordinate *via* the pyridyl nitrogen, this has not been observed in UiO family MOFs; additionally, electron-withdrawing groups such as pyridyl have been found to produce high levels of substitution.⁷¹

Upon post-synthetic soaking of an **hcp** UiO-67(Hf) sample in a DMF solution of H₂PyDC at 55°C the resultant material was then washed and activated in preparation for ¹H NMR analysis. However, the samples showed clear differences by PXRD, depending on whether the **hcp** MOF had been washed prior to analysis. A sample from which the original reaction solvent containing water and formic acid was largely removed *via* washing displayed a slight reduction of crystallinity after soaking, whereas an unwashed sample showed clear structural changes [Figure 2.22 a,b)]. Both postsynthetically-treated cases, however, have a slight shift of peaks to low-*Q*, indicating an expansion of the cell.

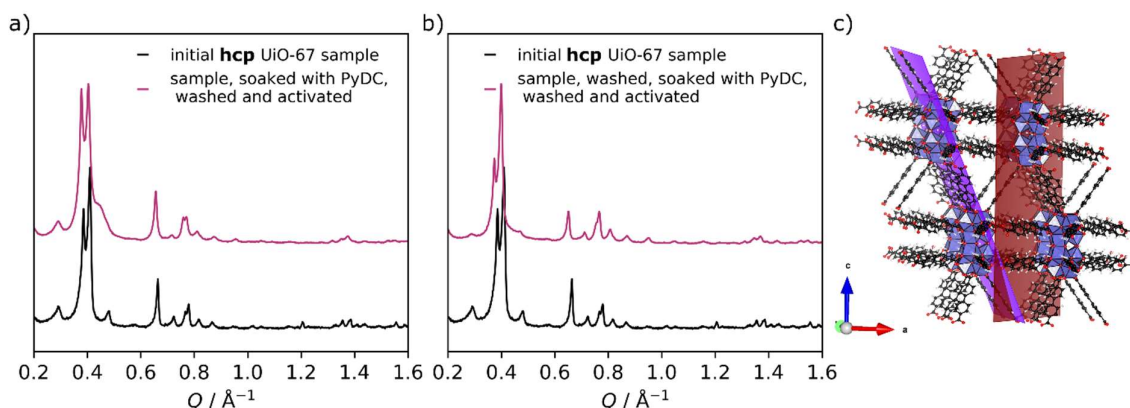


Figure 2.22. Comparison by PXRD of different samples of **hcp** UiO-67(Hf) postsynthetically treated with H₂PyDC: a) the original sample was treated as-is, b) the original sample was washed prior to treatment, c) crystal structure of **hcp** UiO-67(Hf) showing the (101) and (2 $\bar{1}$ 0) planes in purple and maroon respectively.

For the unwashed-soaked sample, the (100) reflection greatly increases in relative intensity to the (101), as might be seen in a sample partially delaminated to form the **hxl** layered-nanosheet phase, and the **hcp** (101) reflection displays an unusual asymmetric lineshape or shoulder, with extra intensity to high-*Q*. This lineshape is not the characteristic Warren broadening seen for the turbostratically-disordered **hns** nanosheet phase but implies that there is some disruption of the regular stacking separation in the *c*-direction. There is also a smaller shoulder for the washed-soaked sample.

Pawley refinement of the samples indicates changes to the cell parameters for both postsynthetically-treated samples; an additional peak was included to account for the ‘shoulder’ [Table 2.II]. Both samples show a decrease in the *c*-parameter relative to a pristine washed and activated **hcp** UiO-67(Hf): the unwashed-soaked sample, which has the greatest change by PXRD, has an 0.81% smaller *c*-parameter. The washed-soaked sample, for which less change is observed by PXRD, has a larger *c*-parameter than the unwashed-soaked sample, but still 0.40% smaller than the pristine sample.

Both samples also show a change in the *a* and *b* parameters, with increases of around 0.59% for the unwashed-soaked sample and 0.52% for the washed-soaked sample. However, for both samples, the (2 $\bar{1}$ 0) reflection at 0.66 Å⁻¹ is still present, intense and without a shoulder, which suggests that there is no significant disruption of long-range ordering in the *ab*-plane [Figure 2.22 c)].

Table 2.II. Change in cell parameters from Pawley refinement of the samples of **hcp** UiO-67(Hf) in the initial PyDC exchange reactions.

Sample	<i>a, b</i> parameters / Å	<i>c</i> parameter / Å	Extra peak: <i>Q</i> / Å ⁻¹ ; intensity	<i>R</i> _{wp}
Initial hcp UiO-67(Hf), washed and activated	19.020(4)	43.714(23)	-	6.79
Sample, soaked with H ₂ PyDC, washed and activated	19.132(8)	43.36(5)	0.4403(7) ; 9.5(4)	4.38
Sample, washed, soaked with H ₂ PyDC, washed and activated	19.119(4)	43.54(3)	0.427(5) ; 2.5(3)	3.57

As expected from the PXRD, the unwashed-soaked sample has greater changes in structure than the washed-soaked sample. For both samples it appears that some linker exchange has occurred in all directions. Exchange in the *c*-direction appears to decrease the *ab*-plane separation as well as causing disruption to the stacking sequence. These two observed effects suggest a significant loss of connectivity and a lack of steric clash between the exchanged ligands, potentially resulting from replacement by some formate or

water/hydroxide groups rather than PyDC alone. Swelling in the *ab*-plane occurs, implying that substitution also takes place in this plane but to a lesser extent. The swelling is potentially due to steric clash of imperfectly-exchanged ligands, but without sufficient loss of connectivity to cause the structure to break.

This behaviour is in keeping with that previously seen in the delamination of **hcp** UiO-67(Hf), as well as previous quantum-chemical calculations indicating that (although loss of *ab*-plane linkers is still possible) the loss/replacement of *c*-direction linkers is more favourable than that in the *ab*-plane.¹² This linker loss is also increasingly favourable as more *c*-direction linkers are lost per unit cell¹² so that, rather than random *c*-direction linkers being lost, there is a cooperative effect; this is likely to lead to partial delamination or change in stacking, as is evidenced by the changes in the *c*-direction in these exchanged samples.

The difference between the samples is striking as it gives evidence that the remaining traces of formic acid and water in the unwashed sample are key to this structural change occurring. In order to investigate the exchange effects occurring and to understand the similarities and differences between different members of the UiO family, post-synthetic treatment with varying amounts of H₂PyDC was therefore repeated on unwashed samples of both **hcp** UiO-67 and **hcp** UiO-66.

As the concentration of PyDC relative to **hcp** UiO-67 increases [Figure 2.23 a)], the original (101) reflection is gradually lost and replaced by a broad 'shoulder' peak, which becomes more intense and shifts to higher-*Q*. The **hcp** (002) reflection also disappears and the original (100) reflection appears to gain more of a Warren-type lineshape, both indicative of a disruption of stacking in the *c*-direction.

The position of the broad peak does not approach that of the **hcp** UiO-66 (101) reflection, which might be expected if all of the *c*-direction BPDC linkers in **hcp** UiO-67 are replaced by the shorter PyDC linkers fully connecting in their place; this implies that the linker substitution is not complete. The position of this broad peak does, however, vary, generally increasing (suggesting a decrease of the stacking separation due to *c*-direction linker loss) until high concentrations of PyDC are used, when the position moves sharply to lower-*Q* [Figure 2.23 c)]. Earlier in this section, a decrease in stacking separation was proposed to be due to substitution including formate and water/hydroxide due to the reduced likelihood of

steric clash. While the *c*-parameters could not be determined accurately from Pawley refinement, the observed decrease in the position of the broad peak at high concentrations of PyDC suggests that further ligand exchange by PyDC (without coordination of both carboxylate groups) produces steric clash and forces the *ab*-planes further apart.

The Pawley refinements also showed a similar trend in the *a*- (and *b*-) parameters; decreasing at low concentrations of PyDC and then increasing at high concentrations. These changes are less pronounced than those due to substitution in the *c*-direction, confirming the anisotropic behaviour of the **hcp** material.

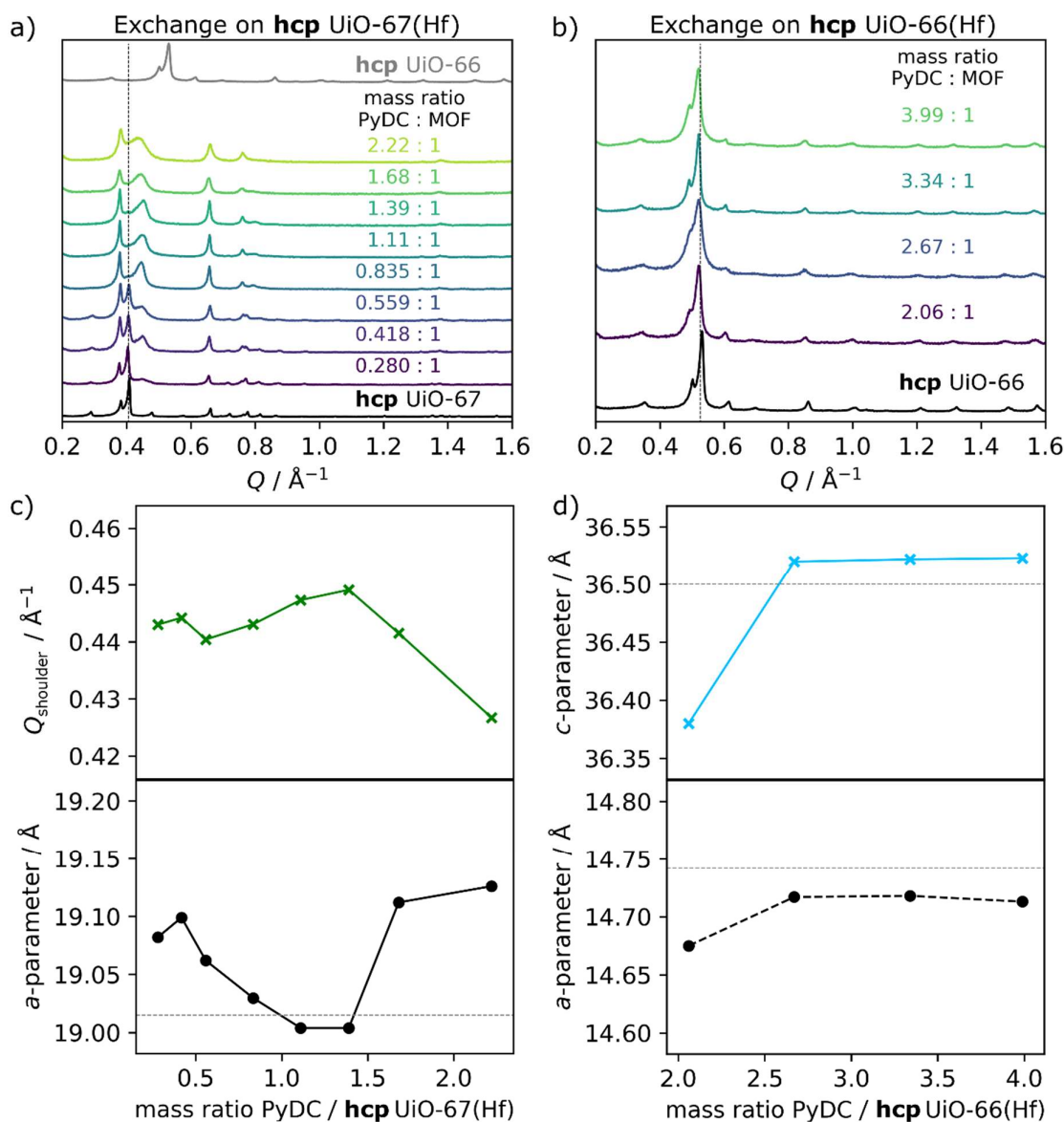


Figure 2.23. PXRD patterns of a) *hcp* UiO-67(Hf); b) *hcp* UiO-66(Hf), both treated post-synthetically with varying concentrations of PyDC (given as the mass ratio relative to the mass of the original MOF sample). In both plots the original position of the (101) reflection is indicated with a grey dashed line; c) change in the *a*-parameter and the location of the broad ‘shoulder’ peak for the *hcp* UiO-67(Hf) samples; d) change in the cell parameters for the *hcp* UiO-66(Hf) sample. The expected cell parameters for pristine samples are indicated with grey dashed lines.

In the postsynthetic treatment of *hcp* UiO-66 no ‘shoulder’ indicating *c*-direction disorder is observed even to high relative concentrations of PyDC, and the (002) reflection remains visible [Figure 2.23 b)]. Pawley refinement, however, indicates that at lower concentrations of PyDC the *c*-stacking decreases significantly relative to the pristine sample, potentially due to linker replacement by formate and water/hydroxide, before increasing to just larger than in the pristine sample as the amount of PyDC increases, suggesting again that PyDC

substitutes into the framework at higher concentrations [Figure 2.23 d)]. While the replacement of BDC by PyDC would not be expected to produce a large change in the *c*-stacking (since they have similar lengths), an increase in the stacking separation and no obvious turbostratic disorder might be expected if the substitution occurs randomly between different planes and not in sufficient quantity to cause significant loss of connectivity.

The *a*- and *b*-parameters are also lower than for the pristine sample, again increasing as the concentration of PyDC increases, further supporting the idea that formate and water/hydroxide substitute originally, followed by replacement by PyDC.

Overall, the reflections become broader, perhaps due to an overall loss of crystallinity, but there is no evidence of asymmetric or Warren-type broadening, suggesting that if linker substitution does occur it is not to the same degree or the same location-selectivity as seen in **hcp** UiO-67.

To obtain further understanding of these two systems, in particular to determine whether—and to what extent—PyDC is present in the samples, TGA and ¹H NMR were performed.

The TGA data shows that during post-synthetic treatment the mass of ligand in the material increases as the concentration of PyDC used increases for samples of both **hcp** UiO-67 and **hcp** UiO-66 [Figure 2.24]. Perfect replacement of linkers by PyDC ('healing' the defects^{113,129}) would not result in a significant mass increase, so this observation supports the non-perfectly-coordinated incorporation of PyDC into the frameworks, such as the replacement of one linker coordinated at both ends by two PyDC ligands, each coordinated at one end and with one end uncoordinated and 'free' within the pore. For both frameworks the treatment appears to weaken the MOF structurally; T_{decomp} for **hcp** UiO-67 drops from 534 to 518°C across the sample range, and for **hcp** UiO-66 it drops to 494°C, which again suggests that not all of the exchanged ligands fully coordinate—i.e., that the connectivity of the framework decreases. Additionally, the final decomposition is less well-defined, supporting the hypothesis that the MOF is structurally weakened by incomplete coordination. This may in part cause the reduction in crystallinity as seen above for **hcp** UiO-66.

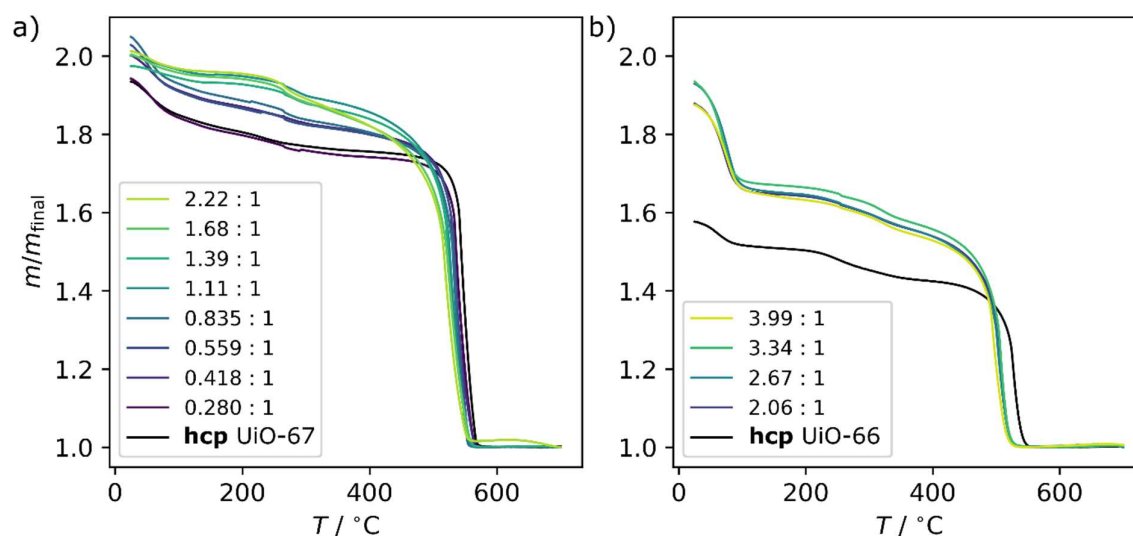


Figure 2.24. TGA comparison of samples after post-synthetic treatment with varying concentrations of PyDC (relative to the mass of the original MOF sample): a) **hcp** UiO-67(Hf); b) **hcp** UiO-66(Hf).

The plateaux usually seen in the pristine MOF samples, corresponding to the framework post-desolvation and post-dehydroxylation, are not clear in the PyDC-treated samples, further suggesting that the PyDC ligands are not all identically coordinated (resulting in their loss at different temperatures).

Furthermore, for **hcp** UiO-66(Hf) samples the first mass loss, which corresponds to ‘desolvation’ or loss of guests in the pores, is much greater in the PyDC-treated samples, suggesting that not all of the PyDC used has coordinated even partially to the clusters but remains in the sample despite the washing and activation; some of the BDC lost in exchange might also remain in the pores. This effect is not however seen for the **hcp** UiO-67 samples. This could be due to the smaller pore size of **hcp** UiO-66 compared to **hcp** UiO-67, making it difficult for the ligand exchange to occur in **hcp** UiO-66.

Owing to the lack of clear ‘plateau’ in the TGA data from which to calculate the mass of framework-coordinated ligand it was not possible to determine the composition of the MOF samples, especially the amount of capping water/hydroxide. However, ^1H NMR allows the calculation of the ratio of PyDC and formate to BDC/BPDC ions in each framework [Figure 2.25].

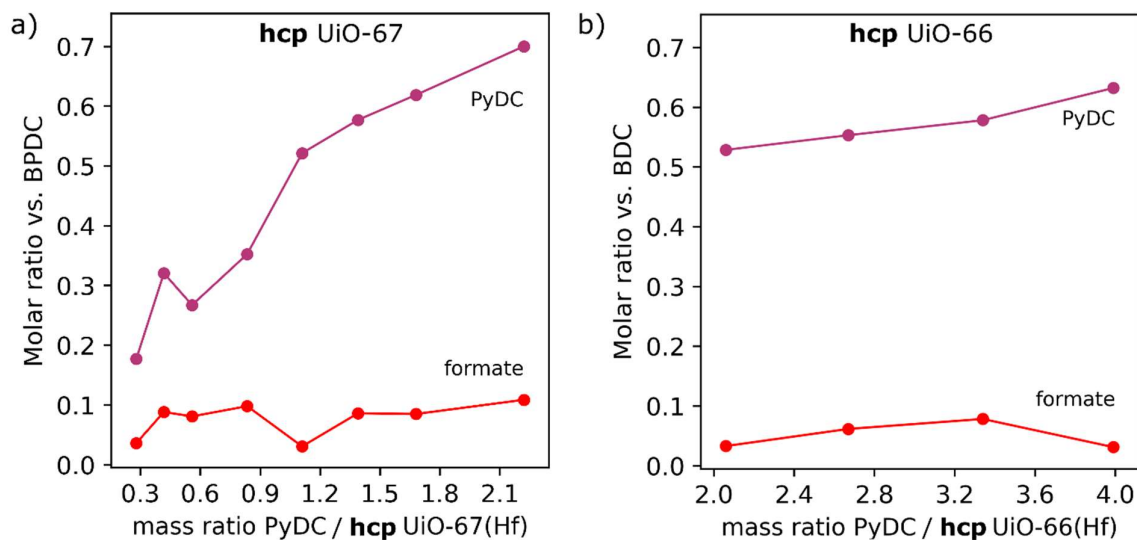


Figure 2.25. Molar ratio of ligand species to a) BPDC in **hcp** UiO-67(Hf); b) BDC in **hcp** UiO-66(Hf) samples, after post-synthetic treatment with varying concentrations of PyDC.

As the concentration of PyDC in the exchange solutions increases in both cases, the amount of PyDC in the digested framework also increases. As mentioned above, some of the PyDC in the framework, particularly in **hcp** UiO-66, could remain in the pores rather than coordinating to the framework, so it is not possible to determine whether the increase in PyDC in the treated samples is entirely due to coordination to the metal clusters. The **hcp** UiO-66 samples appear less responsive to increased concentrations of PyDC than the **hcp** UiO-67 samples, requiring higher concentrations of PyDC to observe significant changes to the ligand incorporation *via* ^1H NMR or TGA; that the PyDC has to enter the sample pores prior to exchange could cause this effect.

The amount of formate, however, stays relatively constant. Since the only source of formate was either initial defects or residual reaction solvent in the pores, and therefore roughly the same in samples of the same MOF, the proportion of initial substitution by formate would not be expected to differ between samples. That formate is at all present after postsynthetic treatment contrasts with observations in **fcu** UiO-66(Zr) that formate is preferentially, and completely, exchanged.¹¹¹ The amount of formate present relative to linker after postsynthetic treatment is similar across all samples—for both **hcp** UiO-66 and **hcp** UiO-67 [Figure 2.25]. Preferential exchange of PyDC with formate would result in an increase in PyDC and decrease in formate, relative to linker. Preferential exchange of PyDC with linker would result in an increase in both PyDC and formate, relative to linker. The observed

trends therefore suggest that the PyDC preferentially replaces any water/hydroxide present and then exchanges with the BDC/BPDC linkers and formate ligands at a similar rate.

This does not conflict with the mechanism proposed above, in which framework linkers first exchange with formate and/or water/hydroxide, then with PyDC. In fact, this mechanism could be the reason why relatively high amounts of PyDC are able to substitute into the MOF samples at all.

This analysis of the responses of **hcp** UiO-67(Hf) and **hcp** UiO-66(Hf) to postsynthetic treatment with PyDC reveals marked differences between the frameworks. While both undergo linker exchange with PyDC, **hcp** UiO-67 is more responsive than **hcp** UiO-66, showing greater changes by PXRD, TGA and ¹H NMR with the addition of lower amounts of PyDC than in the case of **hcp** UiO-66, potentially due to the greater ability of PyDC to easily access cluster sites *via* the pores in the framework with the longer linker. **hcp** UiO-67 shows a clear loss of connectivity and resultant stacking disorder in the *c*-direction, although substitution also occurs in the *ab*-plane. For **hcp** UiO-66 a less anisotropic response, and no significant stacking disorder, is observed. That the response is increased by the presence of residual formate and water/hydroxide allows the following mechanism to be proposed. Linkers first exchange with formate and water/hydroxide already present in the pores of the material, then exchange with PyDC occurs—preferentially with water/hydroxide, but also with formate and remaining linkers. Exchange of linkers with the less bulky ligands helps to explain observed decreases in cell parameters, while incomplete substitution of PyDC can cause steric clash and hence swelling.

2.3 Conclusions

This Chapter demonstrates that water plays a key role in the synthesis of defect phases of UiO family MOFs. Alongside formic acid, water is instrumental in allowing control over the phase formed, causing the condensation of the metal clusters into the Hf_{12} double clusters characteristic of the **hcp** phase [Figure 2.26]. Beginning with the first known example of the **hcp** phase, **hcp** UiO-67, the discovery of the critical role of water in phase-selection was applied to other members of the UiO family and this understanding used to synthesise the **hcp** phase of the canonical UiO-66.

This demonstration that other **hcp** analogues of UiO family MOFs, including **hcp** UiO-66(F_4BDC), can be made with water and acid as solvents shows that these defect-engineering processes can be applied to multiple members of this important MOF family. That both formic acid and acetic acid, along with the presence of water, can be used as modulators in this synthesis, whereas only formic acid was successful with **hcp** UiO-66 and **hcp** UiO-67, suggests that the Hf_{12} double clusters can form in the presence of different modulating acids. For the full framework to form, the relative coordination strengths of the linker and modulator are important. The discovery that a **hcp** framework forms with BDC linker and formic acid modulator, or with F_4BDC linker and formic or acetic acid modulator, suggests that the overall acidity of the solution is also crucial in determining the type and nuclearity of metal cluster. Inspired by this, the effect of solution acidity and relative concentrations of acid and water on the growth of both the metal clusters and the full framework will be explored in later Chapters.

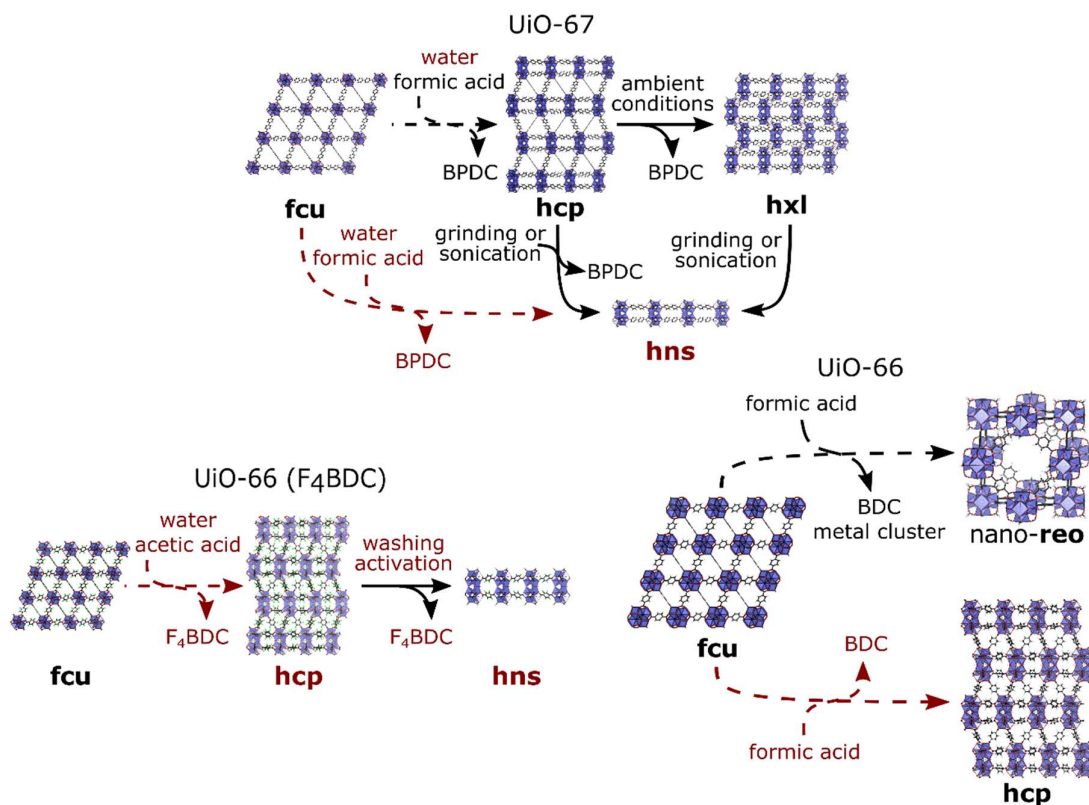


Figure 2.26. Summary of the reported and new phases of UiO-67 (top), UiO-66 (lower right) and UiO-66 (F₄BDC) (lower left). Dashed arrows show the differences in the synthesis conditions used to prepare different phases; solid arrows show post-synthetic treatments. Text in black indicates phases or syntheses already known prior to this report; text in red indicates phases or syntheses discovered or assigned in this report. Crystal files of previously-reported phases from Refs. 12,141,165.

For both UiO-67(Hf) and UiO-66(Hf), water and formic acid together enable a degree of control over both the phase and the crystallinity of the MOF formed. The **hcp** phase of UiO-66, and the **hcp** and **hns** phases of UiO-67 and UiO-66(F₄BDC) can be obtained through careful control of the amounts of water and formic acid present. Water also improves the crystallinity and phase-purity of **hcp** and **hns** UiO-67. Although the **hns** phase of UiO-66 was not obtained even with high concentrations of water and formic acid in the synthesis, the crystallinity of the **hcp** phase obtained is affected. Water and formic acid are observed to have opposite effects on the crystallinity of the framework; increasing the amount of water reduces the crystallinity of the material.

This Chapter establishes that water can introduce missing-linker defects into the **hcp** UiO-66 framework, similarly to formic acid and other acid modulators. It establishes that, by controlling the concentration of water, as well as acid, in the synthesis the number of such

defects in the sample can be tuned. The characterisation of the **hcp** UiO-66(Hf) material shows that it can sustain missing-linker defects to high concentrations (in this work, concentrations of up to 47% missing-linker defects were measured) compensated by the introduction of formate, water and hydroxide groups, creating mesopores as shown by pore size measurements. Thus the role of water and of formic acid concerns not just the metal clusters—and hence the framework growth—but also the defectivity of the material, acting in competition with the ligands.

For **hcp** UiO-67 and **hcp** UiO-66(F₄BDC), however, increasing the amounts of water and modulating acid leads instead to the formation of two-dimensional UiO MOF nanosheets with hexagonal topology, **hns** UiO-66 (F₄BDC) and **hns** UiO-67 [Figure 2.26]. The **hns** material results from the introduction of directionally-correlated missing-linker defects. The creation of stable Zr/Hf MOF-based nanosheets in this way represents a potential strategy for synthesising MOF membranes and other nanomaterials with a high degree of control and crystallinity, which has exciting potential for many real-world applications such as battery separators.⁴¹

The formation of the **hns** nanosheet phases appears to be possible due to the directionality of the **hcp** framework caused by the anisotropic linker coordination to the Hf₁₂ double cluster, which creates weakness in-between the *ab*-planes; linker defects are known to occur preferentially in the *c*-direction.¹² Investigation of the changes in **hcp** UiO-67 following post-synthetic ligand exchange reactions reveals that the *c*-direction linkers are also favoured for substitution, resulting in a loss of connectivity in this direction and hence increasing disorder in the stacking sequence. In **hcp** UiO-66 anisotropic substitution is less evident, although exchange does affect the *c*-direction spacing, likely due to the difficulty of PyDC penetrating into the pores. Imperfect substitution of PyDC is likely to cause swelling of the framework. These exchange reactions affecting the framework structure also reduce the thermal stability of the materials. Post-synthetic ligand substitution is also enhanced by the presence of water and formic acid; these are not only incorporated as defect-compensating ligands on the clusters in the initial synthesis, but can also substitute for linkers themselves during postsynthetic exchange. The resulting water and hydroxide ligands in particular seem to be favoured for substitution by PyDC. That water and formic acid also affect the

reactivity and stability of the framework once it has formed, due to reactions on the cluster surface, encourages further investigation into the behaviour of the metal clusters in the presence of water and formic acid over time.

Chapter 3. Formation Routes of UiO Family Hafnium Metal-Organic Frameworks and Clusters in Solution using *in situ* X-ray Pair Distribution Function Analysis

The structures of hafnium metal-organic frameworks (MOFs) are very sensitive to small changes in synthetic conditions, as discussed in Chapter 1. By adjusting the synthesis conditions of UiO family MOFs, distinct and different framework topologies can be created: increasing the temperature,¹² concentration of water and concentration of acid modulator allows selectivity between the different phases, such as the **fcu** and **hcp** phases of UiO-66(Hf) [Figure 3.1]. However, to exploit this capability, and work towards the synthesis of other new UiO family MOF related materials, the formation mechanism of the new phases must first be understood.

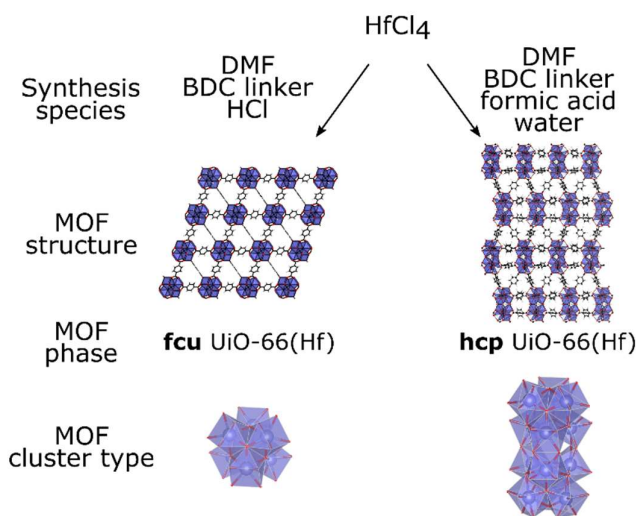


Figure 3.1. Differences in synthesis conditions of UiO family MOFs lead to the formation of different MOF phases.²⁵¹ A synthesis performed with HCl leads to the **fcu** MOF structure with Hf₆(μ₃-O)₄(μ₃-OH)₄ ‘single’ clusters, while a synthesis performed with formic acid and water leads to the **hcp** MOF structure with [Hf₆(μ₃-O)₄(μ₃-OH)₄]₂(μ₂-OH)₆ ‘double’ clusters: the type and nuclearity of the metal cluster affects the topology via the change in linker coordination site number and geometry. The metal-oxide coordination polyhedra are also shown. Colour scheme: Hf or Zr, blue; O, red; C, black; H, white.

Despite advances in understanding,^{175,252,294} including studies on the structure of Hf and Zr metal clusters and on the effects of different variables (including acid modulator and water) on the crystallisation of UiO-66,^{74,275} a full picture of the formation routes of UiO family

MOFs is still far off. In particular, it is unknown when the crucial structural differences between the UiO family MOF phases emerge (i.e., selectivity of the **hcp** phase over the **fcu**). One of the key differences between these frameworks is the shape and nuclearity of the hafnium metal clusters acting as framework nodes: these metal clusters are often modelled as ‘secondary building units’ which direct the framework topology.⁵⁷ However, the evolution of these Hf clusters during MOF synthesis is not fully understood; it is unclear whether the different clusters form *via* different routes, or if they pass through common intermediates, and the timing of the cluster interlinking relative to the timing of the formation of the different clusters is also unknown [Figure 3.2]. While previous *in situ* measurements to probe crystallisation of the **hcp** phase of UiO-67(Hf) suggested that inorganic (i.e., largely free from organic ligands) pre-crystalline species formed at early stages in the synthesis,¹² the identity of this material was not determined, despite being likely to be a key intermediate in the formation and crystallisation of UiO family MOFs.

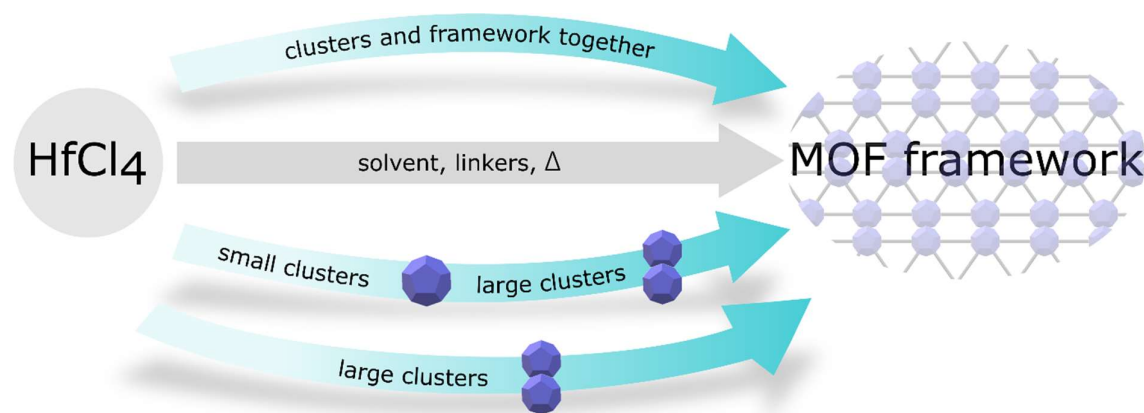


Figure 3.2. Schematic showing potential formation routes of the **hcp** UiO-66(Hf) framework, in particular the evolution of the metal clusters.

This Chapter bridges the gap between *ex situ* cluster identification and *in situ* MOF crystallite growth. Using X-ray pair distribution function (XPDF) analysis, it explores the nature of the Hf metal clusters which form in different reaction solutions, including in a mixture of DMF, formic acid and water, conditions related to those used to synthesise UiO family frameworks in the previous Chapter. This work also compares the solution formation of the **hcp** MOF to that of its constituent Hf₁₂ double clusters.

In order to study the *in situ* formation of UiO family MOFs, a series of experiments (summarised in Table 3.I) was designed based on the conditions used in the laboratory

syntheses of these materials as described in the previous Chapter. While UiO family MOFs are typically synthesised from zirconium salts, in this work the hafnium analogues are used, due to the chemical similarity of Hf compared to Zr but—particularly importantly for this Chapter—greater X-ray scattering power.

An initial measurement of the behaviour of the HfCl_4 metal salt in water alone is used as a test experiment, since the behaviour of ZrCl_4 in water is well-established. The focus then turns to a 65:25:10 (by volume) DMF : formic acid : water mixture (referred to below as ‘DFW 65:25:10’) as a solvent, setting out to elucidate the behaviour of the UiO-related system throughout the reaction at different temperatures. An investigation is also performed into whether the stages and rate of cluster formation are affected by the presence of additional coordinating linkers, and the timing of the framework growth and crystallinity relative to the cluster formation is explored, by performing reactions at the two different temperatures both with and without terephthalic acid (H_2BDC) linker, i.e., reactions with the potential to form UiO-66-type structures (containing H_2BDC , at 150 and 120°C), and molecular-cluster-only reactions (no H_2BDC , at 150 and 120°C) [Table 3.I].

Table 3.I. Summary of experimental conditions used in the XPDF studies, listing the solvent, nature of linkers (if any) and temperatures used.

Experiment	Solvent	Linker	Temperature
1	Water	No	R.T.
2	DFW 65:25:10*	No	R.T.
3	DFW 65:25:10*	No	150°C
4	DFW 65:25:10*	BDC	150°C
5	DFW 65:25:10*	No	120°C
6	DFW 65:25:10*	BDC	120°C

*The notation ‘DFW 65:25:10’ gives the ratio of DMF : formic acid : water

Alongside a careful structure search for plausible cluster models, this Chapter therefore demonstrates that *in situ* X-ray pair distribution function measurements can be used to identify and track the evolution of different Hf cluster species during UiO family MOF synthesis, from solution stages to the full crystalline framework. The effect of changing the reaction temperature is also explored. This understanding is used to propose a formation mechanism for the **hcp** UiO-66(Hf) MOF: first the metal clusters aggregate from the Hf₆ cluster (as in **fcu** UiO-66) to the **hcp**-characteristic Hf₁₂ double cluster, and following this, the crystalline **hcp** framework forms.

The entirety of the work in this Chapter is published in the following article:

Firth, F.C.N.; Gaultois, M.J.; Wu, Y.; Stratford, J.; Keeble, D.S.; Grey, C.P.; Cliffe, M.J. Exploring the Role of Cluster Formation of UiO Family Metal-Organic Framework with In Situ X-Ray Pair Distribution Function Analysis. *J. Am. Chem. Soc.* **2021**, 143 (47), 19668-19683. [Ref. 255]

The in situ experiments were performed at Beamline I15-1, Diamond Light Source, beamline staff Dr Dean S. Keeble, proposal number EE18630-1. The experiments were performed by Francesca Firth, Dr Michael Gaultois, Dr Yue Wu and Dr Matthew Cliffe, with technical assistance and setup from Dr Dean S. Keeble.

The code for Diffpy-CMI was initially adapted by Dr Joshua Stratford, Yusuf Hamied Department of Chemistry, University of Cambridge (at time of experiment). Dr Erlendur Jónsson, Yusuf Hamied Department of Chemistry, University of Cambridge assisted in setting up and modifying scripts for DiffPy-CMI.

The powder X-ray diffraction measurements were performed by Dr Chris Truscott, part of the Chemical Crystallography Facility in the Yusuf Hamied Department of Chemistry, University of Cambridge.

Analysis of the XPDF datasets, including optimisation of the Diffpy-CMI code, was performed by Francesca Firth.

3.1 Experimental Methods

3.1.1 Synthesis

All reagents used were obtained from commercial suppliers and used without further purification. Unless otherwise stated, water was obtained from a Millipore filter unit.

In situ reaction mixtures were prepared in a 2.5 mm fused-quartz capillary, sealed with a Teflon cap before being loaded into the *in situ* cell.

An aqueous solution of HfCl₄ (30 wt%) was prepared through dissolution of HfCl₄ (Acros Organics, 99%) in deionised water and sonication for 10 minutes.

The conditions for the synthesis of the **hcp** UiO-66(Hf) MOF were adapted from Chapter 2 (Ref. 251), with quantities reduced to account for the smaller *in situ* reaction volume. The concentrations of HfCl₄ and, where relevant, organic linker, were increased to improve signal to noise. The compositions of the reaction mixtures are described below.

HfCl₄ (4.8 mg, 0.015 mmol) and terephthalic acid (H₂BDC) (Alfa Aesar, 98%, 2.5 mg, 0.015 mmol) were added to a capillary, followed by dry *N,N*-dimethylformamide (Sigma Aldrich, 99.85 % anhydrous DMF) (65 µL), formic acid (Fisher, 98/100%) (25 µL) and water (10 µL), then sonicated for 10 minutes. Reactions were also performed without the terephthalic acid ligand, to assess its importance in cluster formation. HfCl₄ (116 mg, 0.362 mmol) was sonicated for 10 minutes with dry DMF (6.5 mL), formic acid (2.5 mL) and water (1.0 mL). 0.1 mL of the resulting solution was measured into the capillary.

A sample of **hcp** UiO-66(Hf) was prepared for *ex situ* measurement according to the method described in Chapter 2, with a dry DMF : formic acid : water ratio of 4 : 1.5 : 0.4.

3.1.2 X-ray Pair Distribution Function Measurements

Total scattering X-ray diffraction patterns were collected at beamline I15-1 at the Diamond Light Source using an X-ray energy of 76.7 keV ($\lambda = 0.161669 \text{ \AA}$). Initial calibration measurements were performed on a NIST 640c silicon standard.

Ex situ measurements were performed at room temperature on samples packed in 1.5 mm borosilicate capillaries sealed with wax.

In situ measurements were carried out using a heated steel sample holder with openings for the X-ray beam to pass through the sample. Inside the steel sample holder, the 2.5 mm fused-quartz capillary was positioned so that the beam passed through it close to the base, so that any solid formed during the reaction would not precipitate out of the path of the beam. Once the capillary was loaded, heating was started with a fast ramp, then scattering detection and temperature measurements proceeded at a rate of one scan per minute. Two separate thermocouples measured the temperature of the capillary and of the sample holder. The experimental setup of the hydrothermal cell is shown in the Appendix. Diffraction measurements of capillaries containing pure water and the 65:25:10 DMF : formic acid : water solvent were taken at room temperature and at 150°C for use as backgrounds. *In situ* experiments were performed at room temperature, 120°C and 150°C.

3.1.3 Powder X-ray Diffraction

The crystal structure, purity and crystallinity for all samples were assessed *via* their powder X-ray diffraction (PXRD) patterns, measured using a Empyrean X'Pert Pro diffractometer (Cu K α radiation, $\lambda = 1.541 \text{ \AA}$) over the 2θ range 3-40°, using a step size of 0.017° and a scan speed of 0.13°s⁻¹.

3.1.4 Analysis

The detector geometry was refined using DAWN³⁷² using the scattering from NIST 640c silicon powder, and the resulting sample to detector distance was 234.5 mm. The sample diffraction data were integrated using DAWN³⁷² and processed, with solvent background subtraction, and corrections applied for meaningful instrument intensity cutoff and polynomial smoothing, using the PDFgetX3 software package³⁰⁵ using the following parameters: $q_{\text{max,inst}} = 30.2 \text{ \AA}^{-1}$, $q_{\text{min}} = 1 \text{ \AA}^{-1}$, $q_{\text{max}} = 22.5 \text{ \AA}^{-1}$, $r_{\text{poly}} = 1.24 \text{ \AA}$.

Structural models were quantitatively refined against XPDF data using the DiffPy-CMI software package³⁰⁹. The resolution peak dampening term Q_{damp} was constrained to $Q_{\text{damp}} = 0.035 \text{ \AA}^{-1}$, this value derived from refinement against a NIST 640c Si standard. The delta1 parameter accounts for correlated-atomic-motion-derived peak broadening in the 'high temperature limit' (with a $1/r$ dependence) was set to 2 \AA following an initial refinement. The isotropic displacement parameters (U_{iso}) were derived from the reported values for Hf clusters determined from single-crystal data (owing to the potential for poor signal-to-noise

ratios in the *in situ* datasets due to fast reaction rates and low cluster concentrations in the path of the X-ray beam), and set to 0.18 \AA^2 for H, 0.075 \AA^2 for C and 0.06 \AA^2 for O. U_{iso} for Hf was obtained from refinement against an *ex situ* dataset of **hcp** UiO-66(Hf) and subsequently fixed at 0.0069 \AA^2 . Refinement of isolated cluster models and the optimised full structure model of **hcp** UiO-66(Hf) was carried out with refinement parameters set to $q_{\text{min}} = 1 \text{ \AA}^{-1}$, $q_{\text{max}} = 22.5 \text{ \AA}^{-1}$, $r_{\text{poly}} = 1.24 \text{ \AA}$ and $r_{\text{min}} = 1.5 \text{ \AA}$. XPDF patterns of the cluster models were simulated using the DiffPy-CMI software package,³⁰⁹ with the optimised parameters as detailed above. Peak tracking and analysis of processed XPDF and powder X-ray diffraction (PXRD) data were performed using the NumPy and SciPy packages.^{373,374}

3.2 Results

3.2.1 Cluster Models

Since there are many possible cluster structures adopted by Zr and Hf in solution, it is first important to identify all the relevant clusters which could be present in the systems used in this work, in order to build a model to refine against the experimental datasets. A systematic search of the Cambridge Structural Database (CSD) was therefore performed. Species with 3-21 Zr or Hf atoms per structural unit (as defined by the database entries, including both clusters in molecules and those in extended frameworks) were considered. The majority of $n < 3$ search results contained higher-nuclearity clusters, but with the molecular formula reduced to an empirical formula; very few clusters with $n > 21$ are observed. This search yielded over 1300 structures, including molecular clusters and 'infinite' structures with clearly defined repeating subunits. All structures containing heterometallic clusters (other than mixed hafnium and zirconium clusters) were then discarded. In order to compare the different cluster substructures, the metal (hydr)oxo 'core' clusters were extracted from the remaining species by stripping out the peripheral ligands. This reduced the number to 170 unique results; some of these results, showcasing the beautiful diversity of these cluster species, are presented in Figure 3.3.

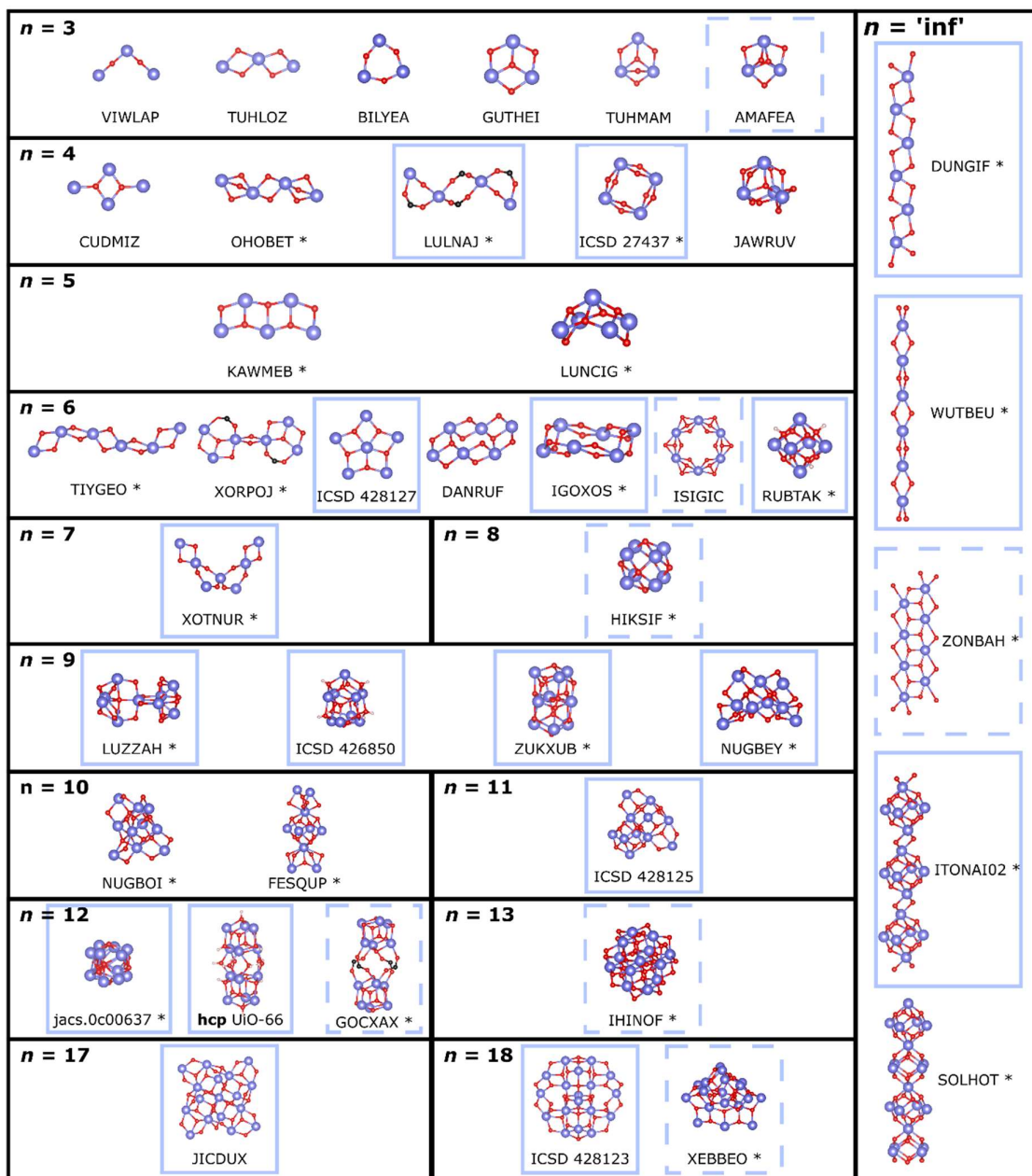


Figure 3.3. Hafnium and zirconium 'core' clusters extracted from entries in the CSD. Where possible, the CSD or ICSD identifier is given. Asterisks demarcate zirconium analogues. Species inside a solid blue box are known to contain water in the synthesis. Species inside a dashed blue box may have had residual water in the synthesis. Cluster structure colour scheme: Hf, blue; O, red; C, black; H, white. It is noted that, since the database search, the HIKSIF Zr_8 cluster has been subsequently shown to be instead a Zr_6 cluster similar to those in the RUBTAK structure.¹⁰⁶

The 'core' cluster candidates were then reduced to 25 species by considering only those feasible in typical MOF reaction conditions and within the constraints of the experimental conditions used in this work [Figure 3.4 a)]. Those species discarded included core clusters appearing only once, those with syntheses reported to be irreproducible, those from

syntheses requiring more than a few days (i.e., with reaction times more than two orders of magnitude longer than used in the experiments in this work), those synthesised at temperatures below 0°C, and those only reported to form in anhydrous conditions.

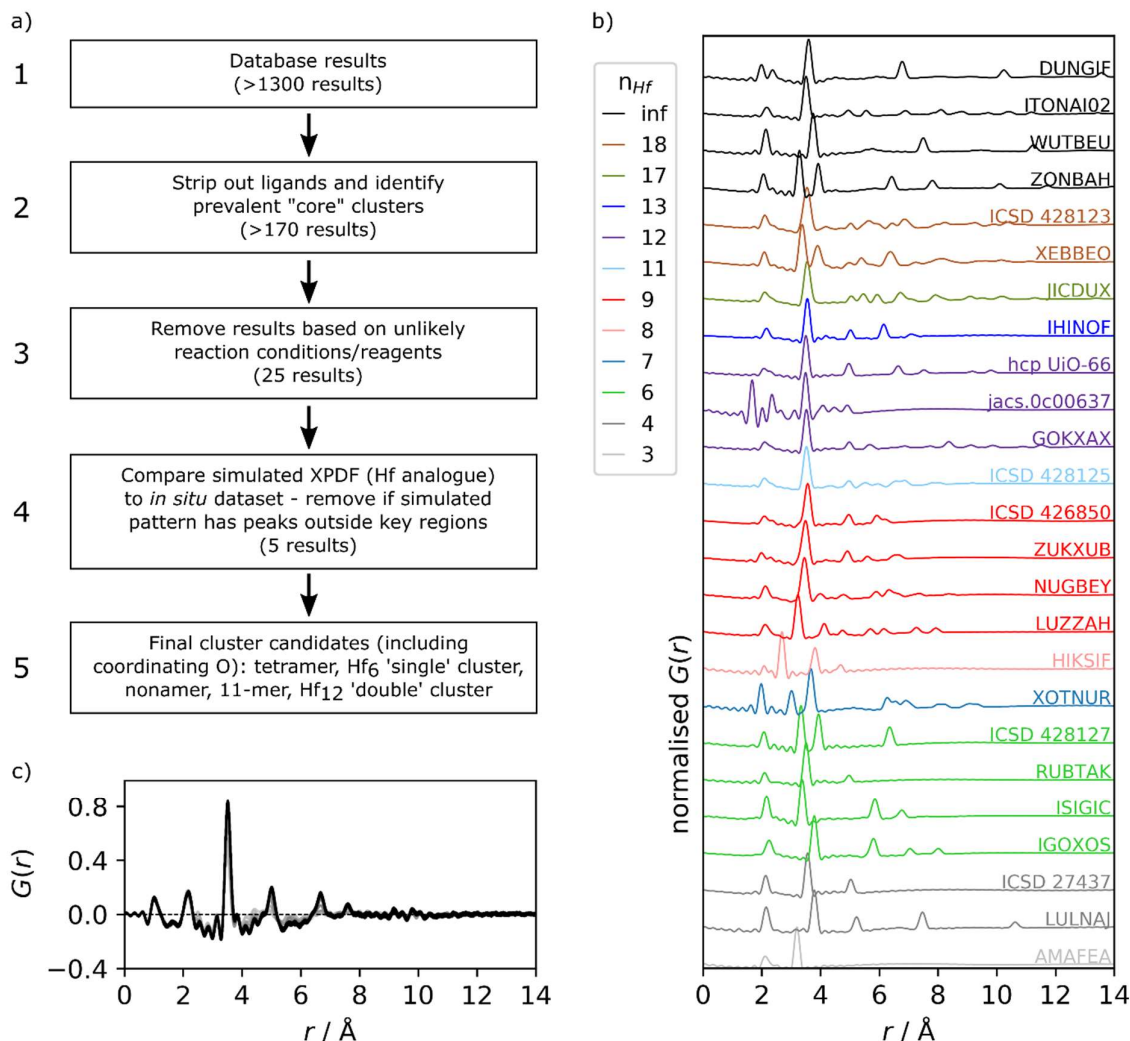


Figure 3.4. a) Route used to find an appropriate set of cluster candidates; b) Simulated XPDF patterns of remaining clusters at step 3 (annotated with their CCDC/ICSD codes), with each dataset normalised to its most intense peak; cluster datasets have been colour-coded according to the number of Hf atoms in the cluster (n_{Hf} in the legend). c) *in situ* dataset of a linker-free reaction in DFW 65:25:10 solvent at 150°C, showing regions of characteristic peaks used as boundaries for step 4. Cluster structure models were obtained from crystal structure files and edited using the VESTA programme.³⁴⁹ References: $n=3$;²⁰⁶ $n=4$;^{200,375} $n=6$;^{50,67,208,376} $n=7$;³²⁸ $n=8$;¹⁸⁷ $n=9$;^{190,194,377,378} $n=11$;⁶⁷ $n=12$;^{12,194,215} $n=13$;³⁷⁹ $n=17$;²²⁰ $n=18$;^{67,380} 'infinite' structures^{151,153,154,252}

The remaining 25 clusters (all of which can be seen inside blue or blue-dashed boxes in Figure 3.3) included the classic (**fcu**) UiO M₆ single cluster and **hcp** UiO M₁₂ double cluster [see Figure 3.1]. (Of note, one of these original 25 clusters, the HIKSIF Zr₈ cluster, has

subsequently been shown to be instead a Zr₆ cluster,¹⁰⁶ consistent with the stability of this particular cluster type.)

Once the potential clusters were identified, the set was narrowed further by considering whether the clusters could give rise to X-ray pair distribution function (XPDF) patterns like those seen in the *in situ* experimental data. Initial examination of an *in situ* XPDF dataset of a linker-free reaction in DFW 65:25:10 solvent [Figure 3.4 c)] revealed that low-*r* peaks were only experimentally observed in six regions (as illustrated in Figure 3.5). For this linker-free reaction, no peaks above $r = 11 \text{ \AA}$ were observed. While intercluster interactions in UiO-66(Hf) MOFs are expected to occur at distances greater than 11 \AA , these reactions in solution are likely to be highly dynamic and so non-covalent or -ionic interactions between molecular clusters in solution are unlikely to be long-lived enough to result in discrete peaks due to motional averaging, in contrast with interactions between interlinked clusters in a framework. Applying the constraint that the simulated XPDF of the 'core clusters' should not have peaks outside the regions seen in the *in situ* dataset narrowed down the 25 chemically feasible core clusters to five.

All species in this 'five cluster model' were edited to obtain the Hf (rather than Zr) analogues, in keeping with the composition of the reaction mixtures featured in this work.

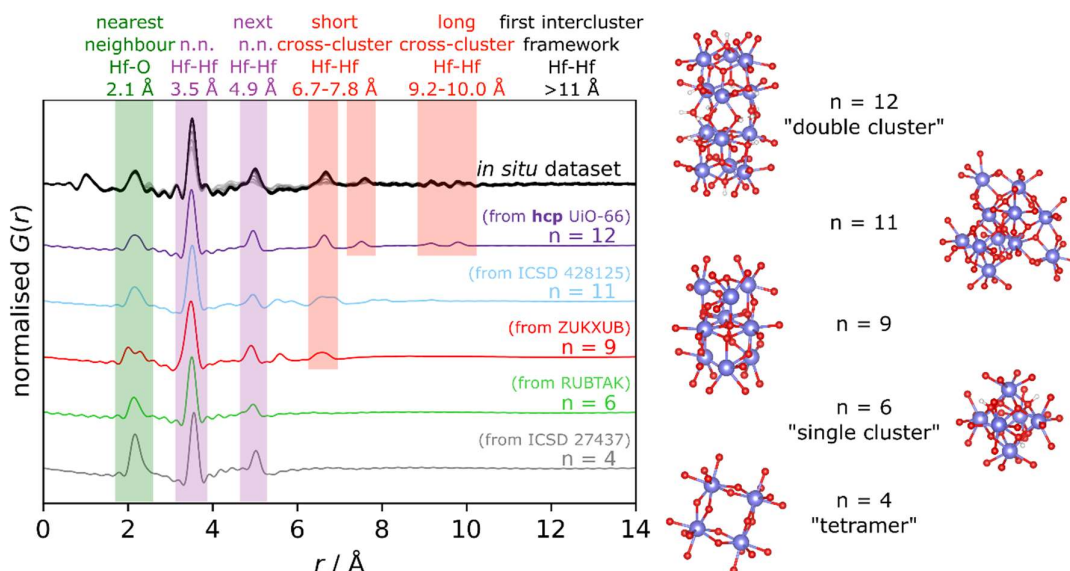


Figure 3.5. Final cluster options and their simulated XPDF patterns, with key peak areas highlighted, and an *in situ* dataset of a linker-free reaction at 150°C for comparison. Cluster structure colour scheme: Hf, blue; O, red; H, white. Cluster structure models were obtained from crystal structure files^{50,67,194,196,251} and edited using the VESTA programme to give the Hf analogues and remove peripheral ligands.³⁴⁹

In order to obtain a consistent set of cluster models, peripheral ligands were removed from the original structures. However, in the reactions in this work, it is likely that the clusters are coordinated by a combination of carboxylate groups²⁰¹ (formate and/or BDC, where present in the synthesis), and water/hydroxide²⁵¹ (the tetramer is predominantly coordinated by water only).^{196,201} Coordinating oxygen atoms were therefore added to the five core cluster models, to allow for the presence of non-specific peripheral ligands while avoiding chemically-unrealistic undercoordinated metal centres.

3.2.2 Refinement against hcp UiO-66(Hf)

Due to the similarity between the calculated XPDF patterns of the five core clusters, and the possibility of more than one cluster type existing in some reaction solutions, simple visual comparison of experimental datasets with the simulated patterns was not used. Instead, quantitative least-squares refinement of the structures against the experimental data using Diffpy-CMI was used to determine the composition of the reaction mixtures.³⁰⁹

This method of refinement was first tested on an *ex situ* dataset of **hcp** UiO-66(Hf) [Figure 3.6], refining a structural model calculated from the crystal structure obtained in Chapter 2/Ref. 251 against the experimental dataset. A good fit was achieved to high interatomic distances r , allowing the value of U_{iso} for Hf to refine (this value was used for all subsequent *in situ* refinements).

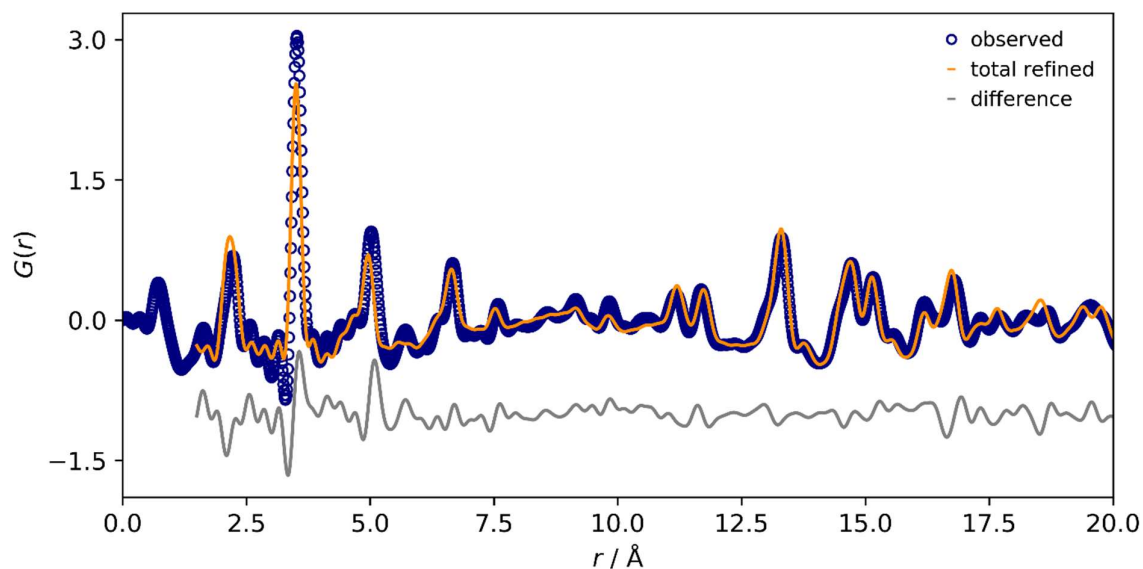


Figure 3.6. Refinement of the crystal structure of *hcp* UiO-66(Hf) against the dataset of crystalline *hcp* UiO-66(Hf) suspended in dry DMF (R_w 0.348). Structural parameters were taken from the crystal structure of *hcp* UiO-66(Hf) as defined in Chapter 2/Ref. 251, and the nanoparticle size used for refinement was set to 10,000 Å.

3.2.3 Behaviour of HfCl₄ in Water

The cluster species in solution are, in contrast with the sample of *hcp* UiO-66(Hf), not crystalline, and so refinement against their datasets was performed using non-periodic models derived from the cluster models described above. To validate that the refinement approach also works for noncrystalline, solvated species, a refinement was carried out against XPDF data from a sample with known composition, aqueous HfCl₄. In the absence of any additional acidic, basic or stabilising ligand species, this is known to form the [M₄(OH)₈(H₂O)₁₆]⁸⁺ cluster.²⁰⁴

A refinement was performed of the ‘five-cluster model’ including all five core clusters as described above [Figure 3.5] against an XPDF measurement of this solution of aqueous HfCl₄ (30 wt%, room temperature), allowing the relative concentrations of the clusters to vary. The refinement converged to give a contribution from the tetramer only [Figure 3.7 a)], as expected,^{196,200,203} confirming the viability of this refinement approach even for non-periodic, structurally closely-related clusters.

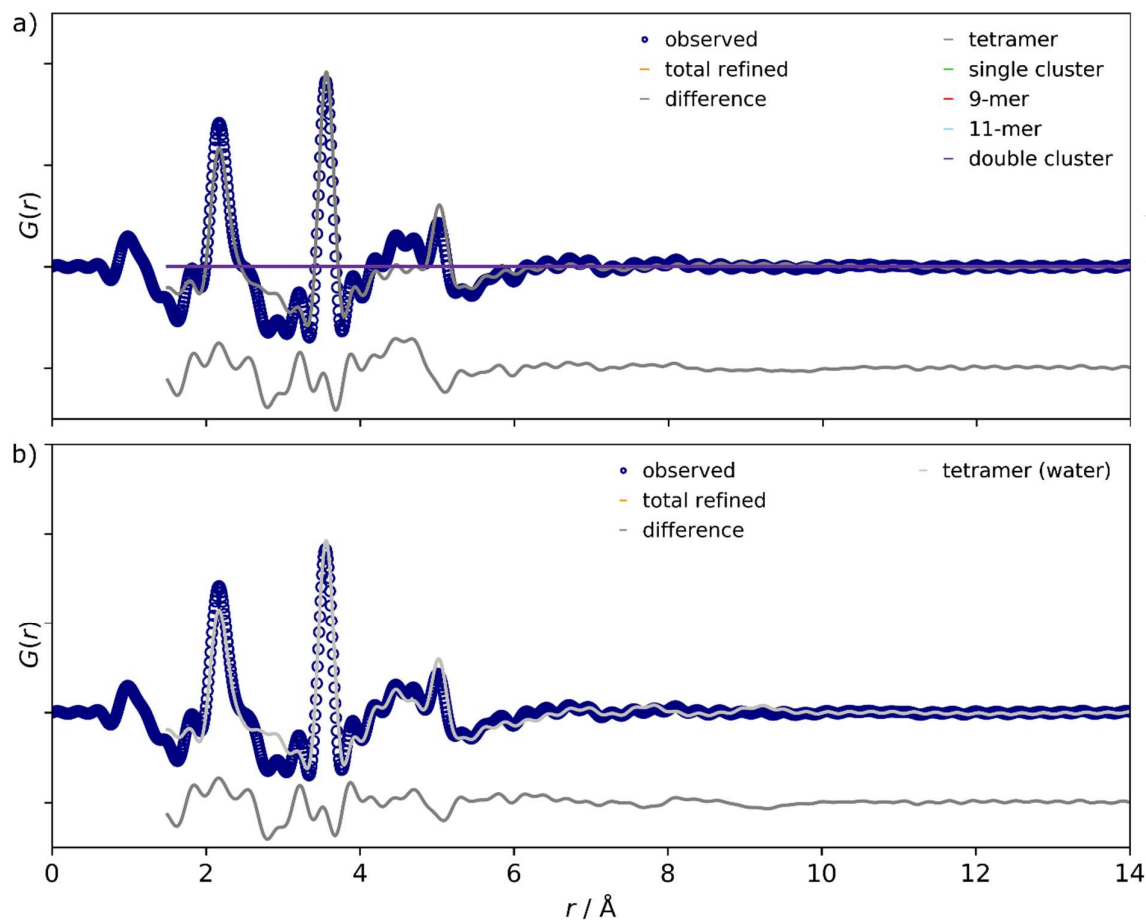


Figure 3.7. HfCl_4 in water. Refinement of a) the 5-cluster model against the XPDF dataset of HfCl_4 in water at room temperature ($R_w = 0.346$) (Scale factors of all species except the tetramer are less than 0.05% of the scale value of the tetramer); b) the tetramer- H_2O model¹⁹⁶ against the XPDF dataset of HfCl_4 in water at room temperature ($R_w = 0.319$).

A significant misfit in the region around 4.5 Å was found in this initial refinement [Figure 3.7 a)]. This initial model did not take account of any potential structuring of water as a coordination sphere around the cluster.^{130,204} The tetramer model was therefore augmented with an additional coordination shell of 24 water molecules. In this augmented tetramer model, 'tetramer- H_2O ', the oxygens of the water molecules were placed in the locations of the water of crystallisation and chloride counterions in the crystal structure of zirconyl chloride octahydrate [Figure 3.8].^{196,202} Hydrogen atoms were omitted due to their low scattering contrast in X-ray experiments. The simulated XPDF of this augmented tetramer model, 'tetramer- H_2O ', shows both significant intensity at about 4.5 Å, and broader, weaker contributions at 7–9 Å, both due to non-nearest-neighbour $\text{Hf}_{\text{cluster}} - \text{O}_{\text{solvent}}$ distances [Figure 3.8]. Refining this tetramer- H_2O model against the experimental XPDF data [Figure 3.7 b)] improved the quality of fit, $R_w[\text{tetramer}] = 0.345$ vs $R_w[\text{tetramer}\cdot\text{H}_2\text{O}] = 0.319$. The fit was

particularly improved in the aforementioned region around 4.5 Å suggesting that in aqueous solution there is a highly structured coordination sphere of water around the $[\text{Hf}_4(\text{OH})_8(\text{H}_2\text{O})_{16}]^{8+}$ cluster.

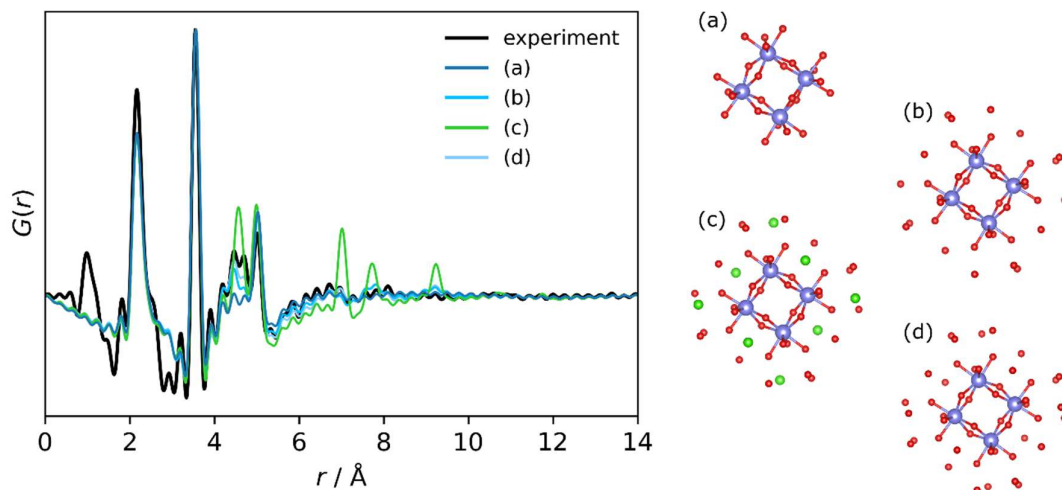


Figure 3.8. Simulated XPDF patterns of the Hf tetramer with different coordination shells of water and Cl, normalised to the most intense peak. The experimental dataset of HfCl_4 in water is included for comparison. Models were obtained from the crystal structure of HfCl_4 in water¹⁹⁶ using VESTA.³⁴⁹ a) the original tetramer, with no water coordination shell; b) the tetramer with the first water coordination shell; c) the tetramer with the first coordination shell and chloride; d) 'tetramer· H_2O ', the tetramer with the first water coordination shell and additional water in the same location as the chloride in (c). H atoms are omitted from the models, since H has a very low X-ray scattering power and so makes little difference to the XPDF pattern. Cluster structure colour scheme: Hf, blue; O, red; Cl, green.

3.2.4 Behaviour of HfCl_4 in DMF : Formic Acid : Water Solvent

Having confirmed the viability of this method in identifying Hf clusters in solution, the focus now returns to the behaviour of the clusters in conditions related to UiO family MOF syntheses. Of particular relevance are reactions in DMF : formic acid : water solvents, both with and without terephthalate (BDC) linker, and at different temperatures. By examining the conditions which trigger the difference in cluster nuclearity previously shown to result in different UiO-66(Hf) MOF structures (Chapter 2, Refs. 12,251), this work aims to try and identify at what stage of the reaction these differences occur.

Initially, a comparison was made of the species formed at room temperature, in a solution comprising HfCl_4 in DMF, formic acid and water, versus HfCl_4 in water only.

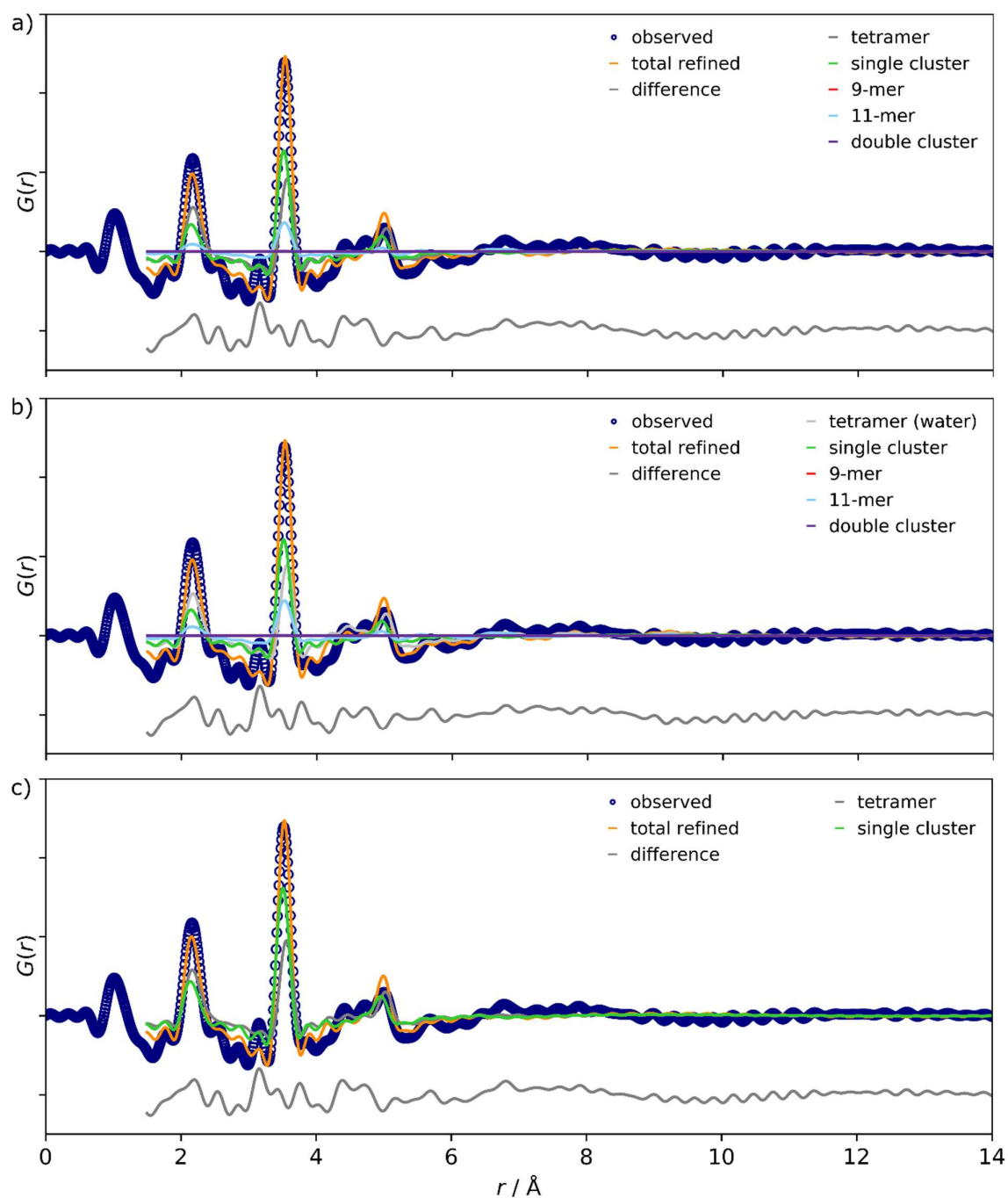


Figure 3.9. HfCl_4 in DFW solvent. Refinements against the dataset of HfCl_4 in DFW 65:25:10 solvent, R.T., against a) the 5-cluster model ($R_w = 0.265$); b) the 5-cluster model, but replacing the tetramer with the tetramer· H_2O ($R_w = 0.256$); c) a mixture of the tetramer (no water) and the single cluster ($R_w = 0.267$).

Refinement of the five-cluster model against the room-temperature dataset from HfCl_4 in DFW 65:25:10 solvent (65:25:10 V/V dimethylformamide (DMF) : formic acid (FcOH) : water)

[Figure 3.9 a)] gave the best fit, where all clusters had non-negligible values^{††}, with a mixture of only the tetramer and the **fcu** UiO-66 type⁵⁰ hexanuclear single cluster [see Figure 3.5], with no significant contribution from any higher-nuclearity species. A high degree of correlation was however observed between the refined proportions of the 11-mer and the single cluster owing to similarities between the XPDF patterns of the species. However, the correlations were reduced, and the fit improved, when the tetramer·H₂O was used instead of the tetramer in the five-cluster model [Figure 3.9 b)]. This suggests that the refinement model was using contributions from the 11-mer to fit the weak signals arising from the solvent restructuring at 7-9 Å [Figure 3.9 b)].

The refinement was then repeated with the tetramer·H₂O and the single cluster only [Figure 3.10 b)], showing a good fit with a 58:42 ratio of scale factors (albeit correlated), which was an improvement on that obtained from refinement of a mixture of the tetramer (without water) and the single cluster [Figure 3.9 c)], again suggesting some solvent structuring remains.

Compared to the XPDF of HfCl₄ in water, which contains only the tetramer cluster, the XPDF of room-temperature HfCl₄ in DFW 65:25:10 solvent has lower intensity at 2.1 Å [Figure 3.10 a)], implying a lower number of Hf-O nearest neighbours relative to Hf-Hf nearest neighbours: the tetramer has a ratio of 4 : 1 Hf-O : Hf-Hf nearest neighbours, whereas for the single cluster this ratio is 2 : 1. There is also less intensity at 4.5 Å, suggesting a reduced water coordination shell.

^{††} A better fit based on R_w values alone can be obtained by adding e.g. less than 0.5% of another cluster species. This can be assumed to be effectively zero—given the level of noise in the dataset, the ‘addition’ of the cluster to the model does not provide a meaningful improvement to the fit.

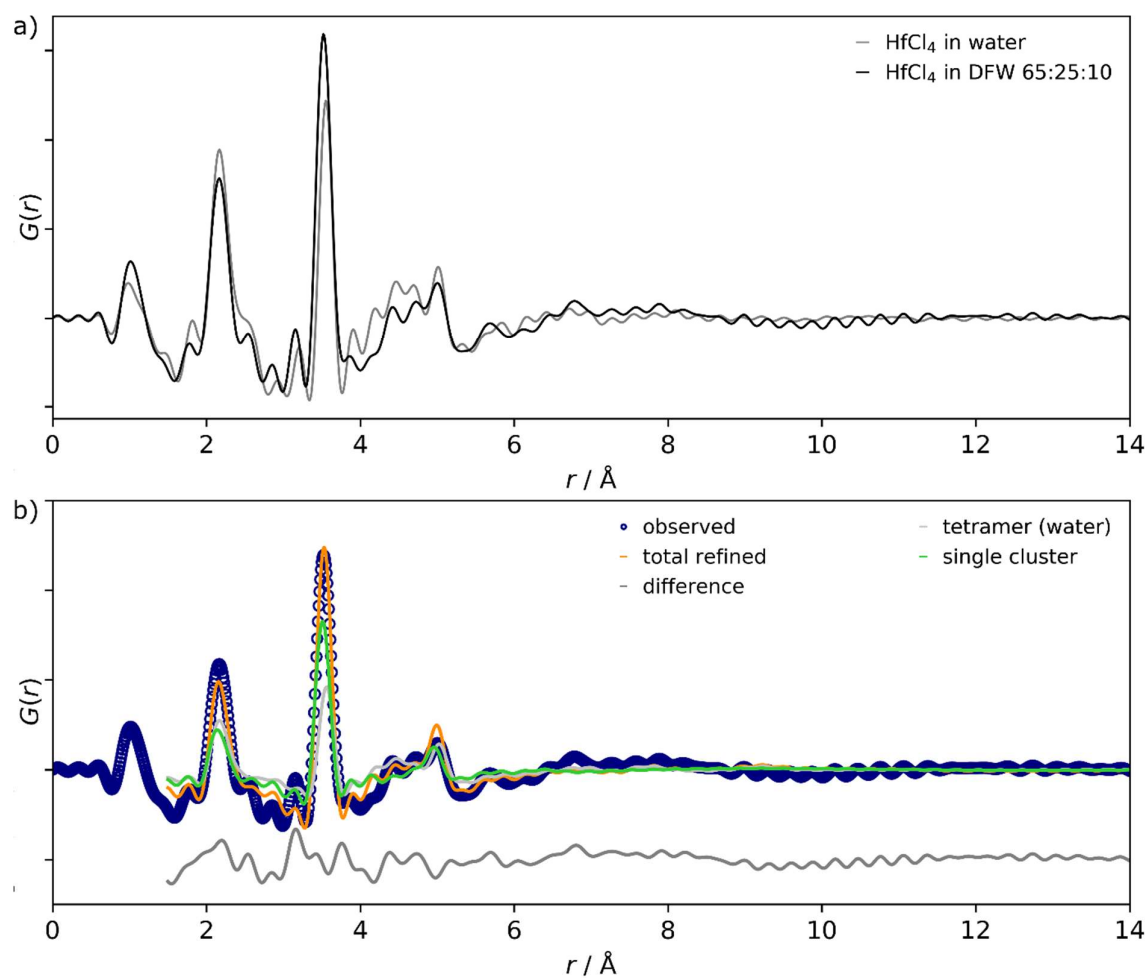


Figure 3.10. a) comparison of normalised datasets of HfCl_4 in water and HfCl_4 in DFW 65:25:10 solvent; b) HfCl_4 in DMF : formic acid : water solvent. Refinement of both the tetramer $\cdot\text{H}_2\text{O}$ and single cluster models, against the XPDF dataset of HfCl_4 in DFW 65:25:10 solvent at room temperature ($R_w = 0.259$).

Additional refinements were performed to explore the contributions by the tetramer and single cluster separately, and the extent of solvent reorganisation [Figure 3.11 a,b)].

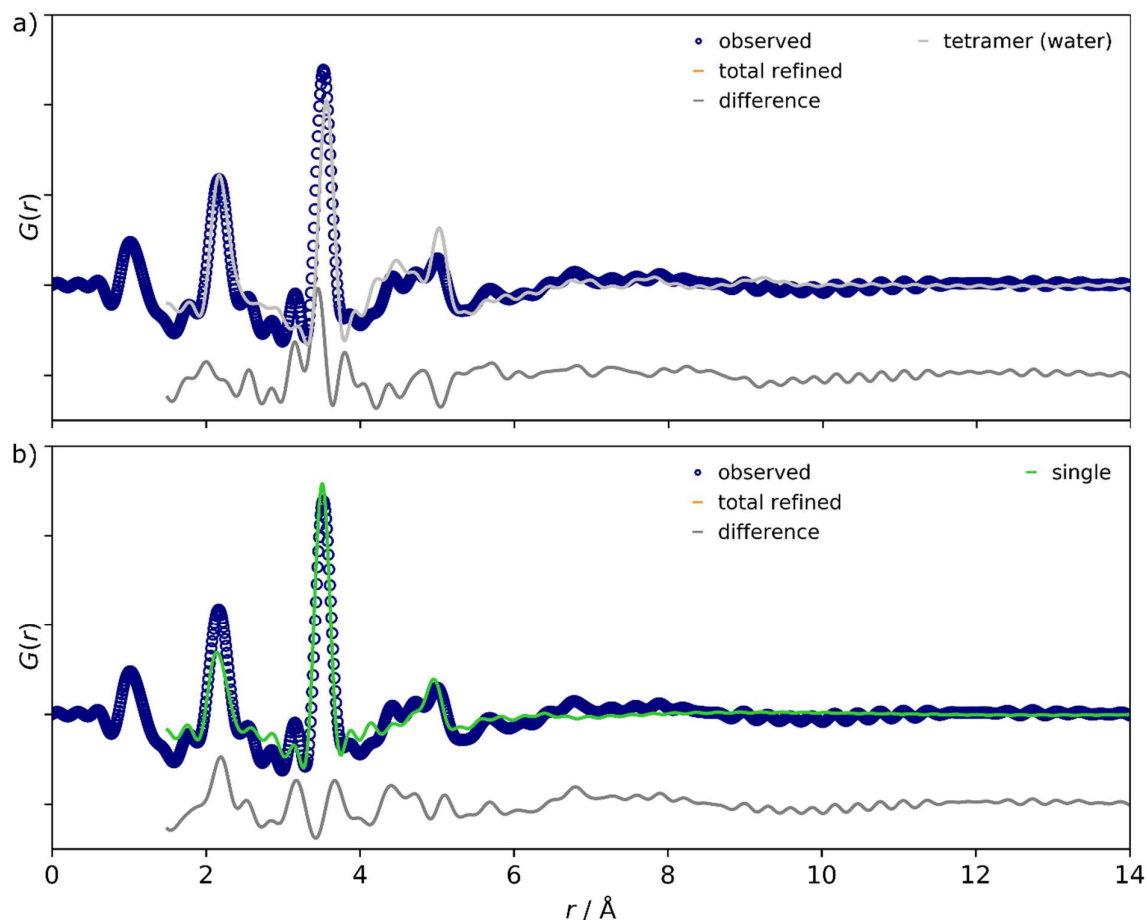


Figure 3.11. HfCl_4 in DMF : formic acid : water solvent. Refinement of a) the tetramer· H_2O model only (R_w 0.424); b) the single cluster model only (R_w 0.345), against the XPDF dataset of HfCl_4 in DFW 65:25:10 solvent at room temperature.

These results overall indicate that the solvent structuring in this sample due to water is lower than that would be present in a sample of only the tetramer· H_2O , even though water is in large excess compared to Hf in the sample of HfCl_4 in DFW 65:25:10 solvent (1 : 232 : 183 : 153 molar ratio Hf : DMF : formic acid : water). Longer-range solvent interactions, however, are still in evidence as shown by the intensity modulation 6-8 Å and the small peak at 6.8 Å, which are both much better fit by the tetramer· H_2O model (which, unlike the single cluster model, addresses solvent structuring; similar intensity modulations have been observed elsewhere in the XPDF of solvated species²⁷³).

The XPDF analysis of this dataset of HfCl_4 in DFW 65:25:10 solvent corroborates that a change of solvent system, without any change in temperature, is already sufficient to cause some degree of cluster aggregation, from the tetramer to the UiO-type single cluster. Some tetramer still remains, potentially due to the solution not reaching complete equilibrium. In

other studies, where a large excess of acid relative to metal ions produced predominantly the single cluster, the solutions were allowed to age for several weeks prior to measurement, whereas the times between synthesis and measurement in this study were under 6 hours.²⁰¹ Neither the Hf₁₂ double cluster, however, nor any other cluster of nuclearity $n > 6$, was observed in this study of HfCl₄ in DFW 65:25:10. The single cluster species is known to be particularly stable,^{50,81} as well as being found in a wide range of syntheses and conditions,^{151,159} which suggests that changing the type and concentration of modulating acid, or the reaction time, is not sufficient alone for further cluster aggregation;^{50,81,151,159,199,201} higher temperatures may also be required to encourage the formation of higher-nuclearity clusters.^{12,251,291}

3.2.5 Behaviour of HfCl₄ in DMF : Formic Acid : Water Solvent at Raised Temperatures

Previous work has shown that **hcp** UiO-66(Hf), containing dodecanuclear 'double clusters', requires higher synthesis temperatures compared to **fcu** UiO-66(Hf), which contains the hexanuclear single cluster.^{12,251} Therefore, the effect of raised temperature on a solution of HfCl₄ in DFW 65:25:10 solvent was investigated *in situ*, so as to observe any potential cluster intermediates. These experiments are performed at two temperatures: 150°C, the temperature used for the lab syntheses of **hcp** UiO-66(Hf) and **hcp** UiO-67(Hf), and 120°C, at which temperature **hcp** UiO-67(Hf) did not form.¹² In order to compare the behaviour of the molecular cluster solution with a MOF reaction mixture, and to explore the effect of the presence of additional coordinating linkers, reactions were performed at these two different temperatures both with and without terephthalate (BDC) linker.

Peak Area Tracking

Alongside the refinement method used in this Chapter so far, for these four *in situ* datasets a complementary analysis method was used to detect changes in the reaction mixture composition. The area under a peak corresponding to a distance between atoms A and B in an XPDF dataset is a function of the atomic numbers of atoms A and B, the number of said atoms, and, in the $G(r)$ normalisation, $1/r_{AB}$; for different cluster species with similar interatomic distances, the number of atoms with these separation distances is likely to be different for each species, and thus the area of the peak will vary. By tracking the change in

area under the peak over time, the emergence of different cluster species can therefore be detected. While this analysis, focussing on changes in individual peaks, does not produce a quantitative cluster composition as refinement against the entire dataset does, it also avoids the potential of refinement to overlook the emergence of weak peaks or to give an erroneous output based on a local rather than global minimum; therefore, if in agreement, both methods of analysis together provide a higher measure of confidence in the output.

Larger clusters can often be distinguished from smaller clusters by the presence of XPDF peaks at higher r values. Clusters with very similar peak positions, such as the tetramer and single cluster, can potentially be distinguished due to their different peak areas. Based on the identification of key peaks in the XPDF of the five-cluster model [see Figure 3.5], and on comparison of the room-temperature datasets [Figure 3.10], the area under the peak at 3.5 Å (the nearest neighbour Hf-Hf) is larger for the single cluster than for the tetramer (in the single cluster each Hf has four nearest neighbours, while in the tetramer each Hf has only two nearest neighbours). In all of the *in situ* reactions the area under this peak initially increases, corresponding to a reduction in the proportion of tetramer. This is further corroborated by the increase in the area under the peak at 4.9 Å at the start of the reaction, corresponding to an increase in the amount of next-nearest neighbour Hf-Hf interactions, which also indicates the formation of clusters other than the tetramer. The growth of the peaks at 3.5 and 4.9 Å indicates species of higher nuclearity than the tetramer are forming, but this analysis alone cannot distinguish between the growth of single cluster and the Hf₁₂ double cluster.

However, these peak changes generally precede the growth of the peak at 9.2 Å, which is only seen in the Hf₁₂ double cluster [see Figure 3.5], allowing the appearance of the double cluster to be distinguished separately from the single cluster. While in the room temperature experiments the tetramer is found alongside the single cluster, the elevated-temperature data suggest that once the temperature is raised, higher nuclearity clusters are favoured (as expected¹³⁰) over the tetramer.

Figure 3.12 shows the change in $G(r)$ over time for the reactions both with and without linker, and at the two different elevated temperatures.

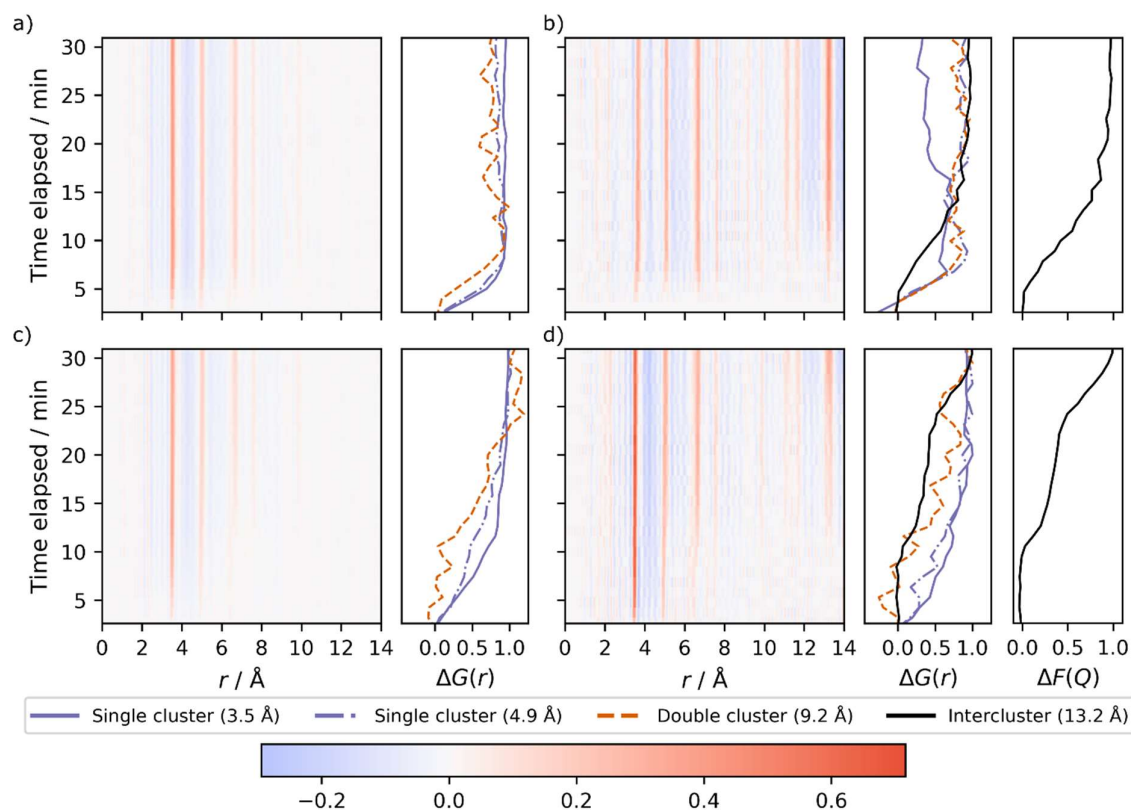


Figure 3.12. Colour plots showing the change in the $G(r)$ s over time at 150 and 120 °C: a) 150°C, no BDC linker; b) 150°C, with BDC linker; c) 120°C, no BDC linker; d) 120°C, with BDC linker. $\Delta G(r)$ is shown to the right of each plot, calculated as $[G(r)_t - G(r)_{t_{\text{initial}}}] / [G(r)_t - G(r)_{t_{\text{initial}}}]_{\text{max}}$ (experimental data may continue slightly beyond the bounds of the plots shown). The crystalline component is analysed via $F(Q)$ peak tracking, where the change in the intensity of the reflection at 3.01 \AA^{-1} is plotted as $\Delta F(Q)$. $G(r)$ intercluster and $F(Q)$ peak tracking are only shown for reactions containing BDC (that is, reactions which form a framework). (Experimental data may continue slightly beyond the bounds of the plots shown).

The change in area $\Delta G(r)$ of the key peaks is also shown and labelled as follows. The peaks at 3.5 and 4.9 Å are labelled ‘single cluster’, as they are more intense in the single cluster than in the tetramer and so their growth indicates a move away from the tetramer; the peak at 9.2 Å is only present in, and therefore labelled as, the ‘double cluster’; and, in linker-containing reactions, the peak at 13.2 Å corresponds to an interlinked-cluster separation distance, labelled as ‘intercluster’. These areas are normalised by the maximum change in $G(r)$ over the course of the reaction with the calculation $\Delta G(r) = \frac{G(r)_t - G(r)_{t_{\text{initial}}}}{[G(r)_t - G(r)_{t_{\text{initial}}}]_{\text{max}}}$ to better display the changes over the observed course of the reaction.

Least-Squares Refinement

As a complementary analysis, least-squares refinements were also performed in the same manner as for the room temperature reactions, using the five-cluster model for refinements of each time step in the datasets. These initial refinements [Figure 3.13] included no significant contribution from the nonamer and 11-mer throughout any of the reactions, meaning that only the tetramer, single cluster and double cluster are present in measurable concentrations. A second analysis was then performed with only these three clusters (i.e., omitting the nonamer and 11-mer) [Figure 3.14]. In these refinements of the heated *in situ* reactions, the single cluster is always observed first, with the double cluster emerging at later stages; this agrees with the analysis from the peak-tracking data.

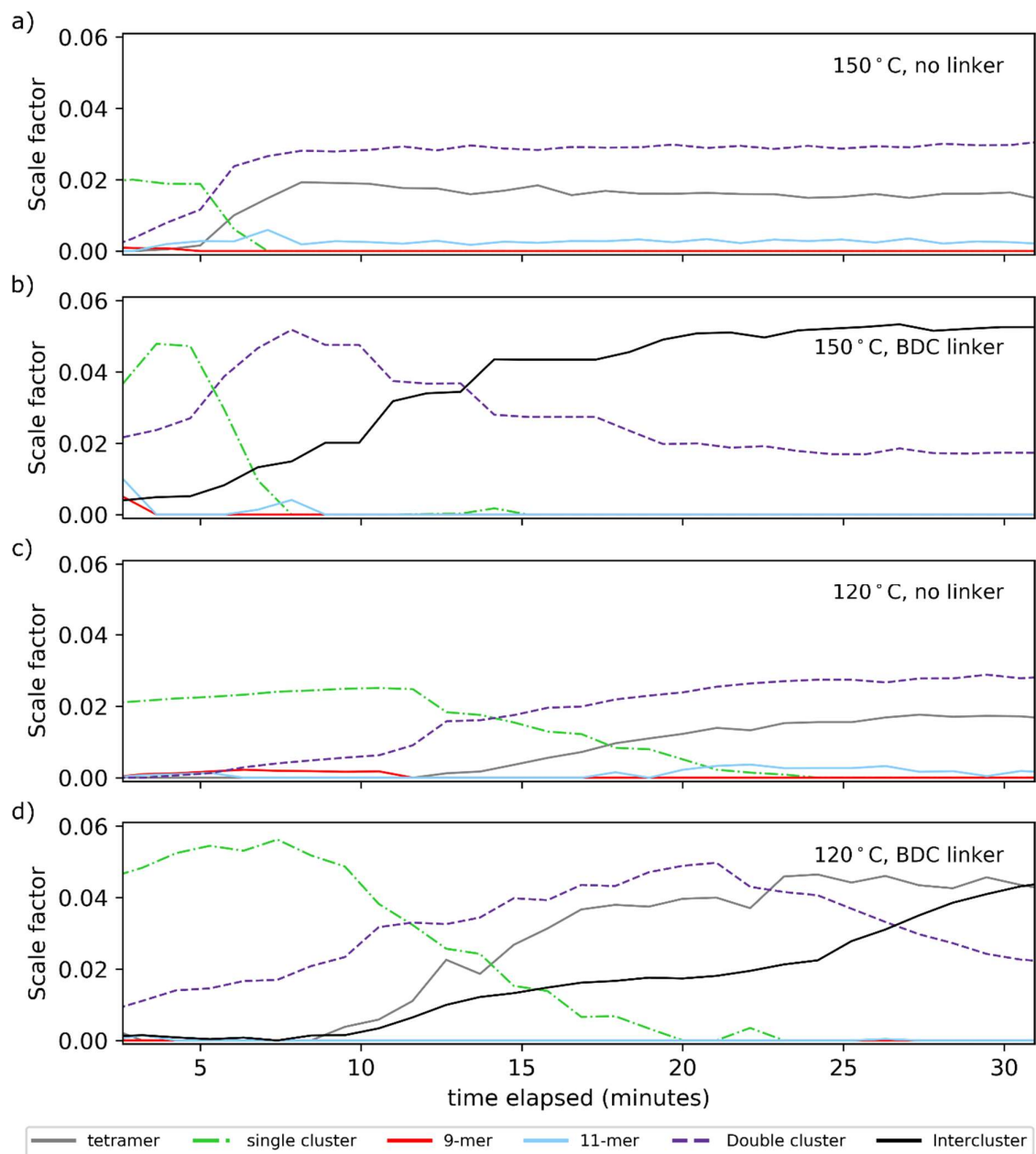


Figure 3.13. Tracking refined proportions of cluster species (including nonamer and 11-mer) over time for the four in situ reactions: a) 150°C, no BDC linker; b) 150°C, with BDC linker; c) 120°C, no BDC linker; d) 120°C, with BDC linker. Uncertainty margin for each species is omitted due to correlation.

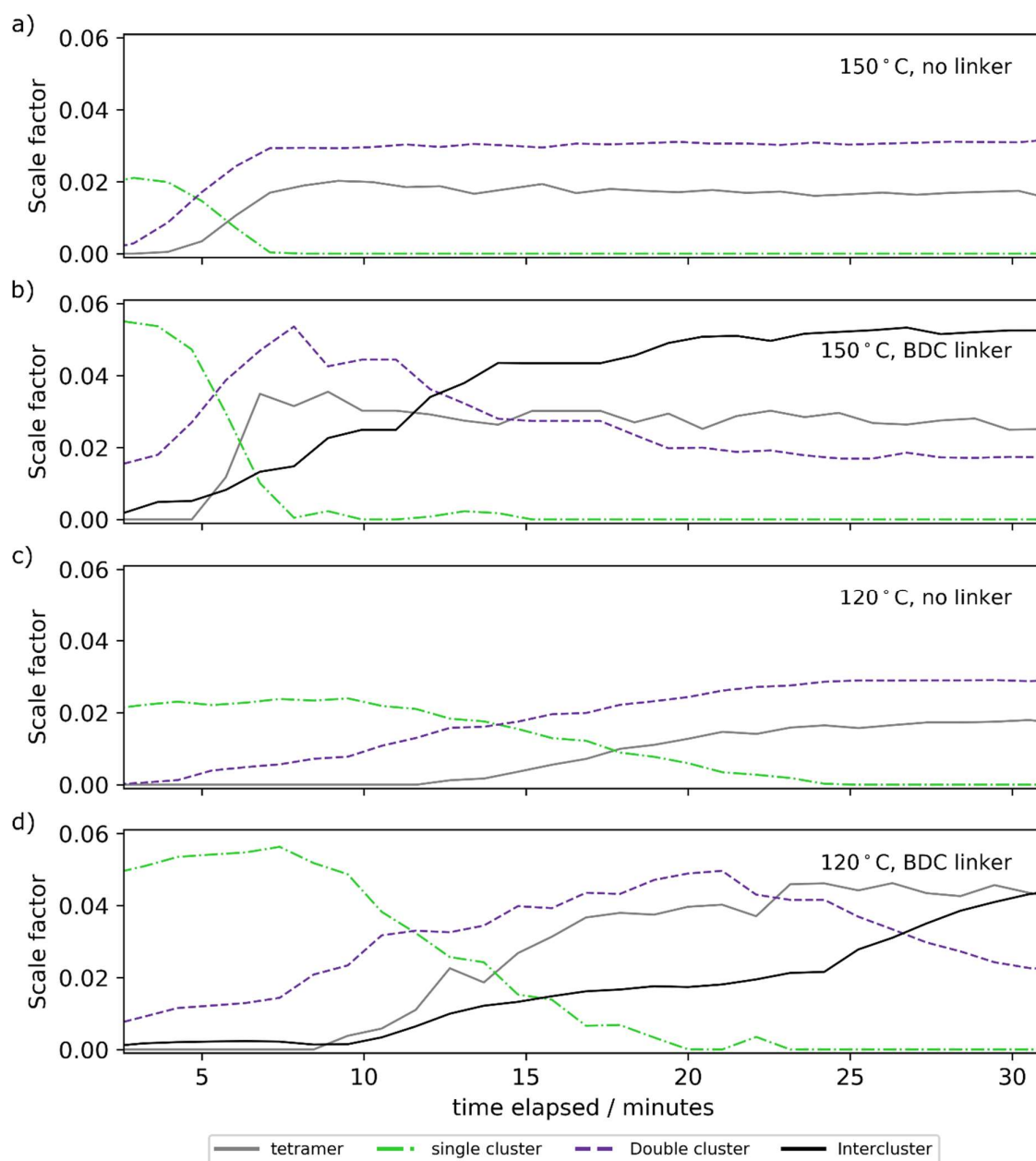


Figure 3.14. Tracking refined proportions of cluster species (omitting 9-mer and 11-mer) over time for the four *in situ* reactions: a) 150°C, no BDC linker; b) 150°C, with BDC linker; c) 120°C, no BDC linker; d) 120°C, with BDC linker. Uncertainty margin for each species is omitted due to correlation.

Due to the high correlation between the proportions of these remaining cluster species, the exact ratios of these species as the reactions progressed could not be confidently determined using this method. However, from the cluster proportions obtained from this refinement [Figure 3.14], in all of the *in situ* reactions the growth in the concentration of the double cluster occurs alongside a reduction in the amount of single cluster, and there is no delay between the loss of single cluster and the formation of the double cluster. This suggests that the double cluster forms by the direct combination of single clusters, rather than forming

directly from the tetramer (a pathway not involving the single cluster) or requiring the breakdown of single clusters into lower nuclearity clusters prior to the formation of the double cluster.

In these refinements, the amount of tetramer appears to increase over time, which is unexpected as lower-nuclearity species are disfavoured at higher temperatures. That the composition change from single to double clusters could result in the increase in proportion of low-nuclearity species is unlikely. However, the amount of tetramer is highly correlated to the amount of double cluster or framework present [Figure 3.14] and increases at similar times. Furthermore, if the tetramer were indeed present, the increase in peak area at 3.5 Å seen in Figure 3.12 would not be so significant (as the tetramer has a lower area under this peak than the higher-nuclearity species). This suggests that, rather than the tetramer being in fact present, the least-squares refinement is using the tetramer to compensate for some change in peak shape or broadness, which cannot be obtained from the existing double cluster/framework models. Changes in peak shape and broadness can indicate thermal motion or cluster distortions, as have been observed in other work for heated Zr and Hf clusters.^{268,381} While it is possible to permit structural distortions in the cluster models, or to allow the correlated atomic motion and thermal displacement parameters to refine, the increased noise in the data due to the fast reactions, and the high degree of correlation between parameters in the refinements, mean any calculated changes in these parameters are unreliable. The tracked peak areas, however, do not have this issue, as, for a given peak, the broadness of the peak due to thermal displacement or distortion will not affect the number of hafnium atoms, which determines the overall peak area. Thus both methods of analysis complement each other in enabling understanding of the cluster behaviour and composition.

Intercluster Coordination and Crystallisation in Linker-Containing Systems

The linker-containing systems display intercluster coordination, following the formation of clusters. When considered against the five-cluster model, which consists of molecular clusters with most XPDF peaks occurring between 2 and 11 Å [see Figure 3.5], peaks in these systems beyond 11 Å only arise from intercluster distances in an interlinked framework. In these systems of HfCl₄ in DFW 65:25:10 solvent, these peaks, such as that at 13.2 Å,

correspond to distances between clusters joined by BDC linkers. In BDC-free reactions, these inter-cluster peaks are entirely absent, as no framework forms. In the BDC-containing reactions at both temperatures, the growth of these inter-cluster peaks occurs both following, and at a slower rate than, the intra-cluster peaks. This shows that intercluster coordination occurs following, rather than simultaneously with, the cluster formation, in keeping with previous work which suggested that the non-crystalline precursor of the framework (i.e., the cluster material) is in large excess prior to the framework coordination and growth.¹²

While long-range correlations in XPDF data may indicate the likelihood that a material is crystalline, or at least containing sizeable domains of ordered structure, reciprocal space data, including Bragg diffraction, are more sensitive to crystal formation and so can be used to distinguish between different crystalline structures and those with more disordered or glassy structures.^{21–23,80,141} Alongside the XPDF analysis therefore, in order to further understand the behaviour of the linker-containing systems—i.e., their potential to form a crystalline MOF framework—the reciprocal-space structure factor, $F(Q)$ was examined [Figure 3.15]. In particular, since these systems—containing BDC linkers, and Hf_{12} double clusters—have the potential to form **hcp** UiO-66(Hf), the changes at 3.01 \AA^{-1} (shown in Figure 3.12 for the BDC-containing reactions as $\Delta F(Q)$, defined as the change in $F(Q)$ between times t_{initial} and $t = t$, divided by the maximum change in $F(Q)$ over the course of the reaction) were tracked as an indication of the formation of **hcp** UiO-66(Hf), this reflection at 3.01 \AA^{-1} being indexed to the intense and characteristic $\{063\}$ Bragg reflection of the crystalline **hcp** framework. This Bragg peak is indeed seen in the BDC-containing reactions, meaning that the systems which are capable both of forming Hf_{12} double clusters and of interlinking using BDC do in fact form the crystalline **hcp** MOF. As expected, the BDC-free materials do not form any crystalline species. While these datasets do not allow determination of the amount of material which is crystalline, or whether there is also some noncrystalline MOF or molecular cluster species remaining, comparing the Bragg scattering to the total scattering allows the crystallisation of the MOF to be observed in connection with the precrystalline stages of growth of the clusters.

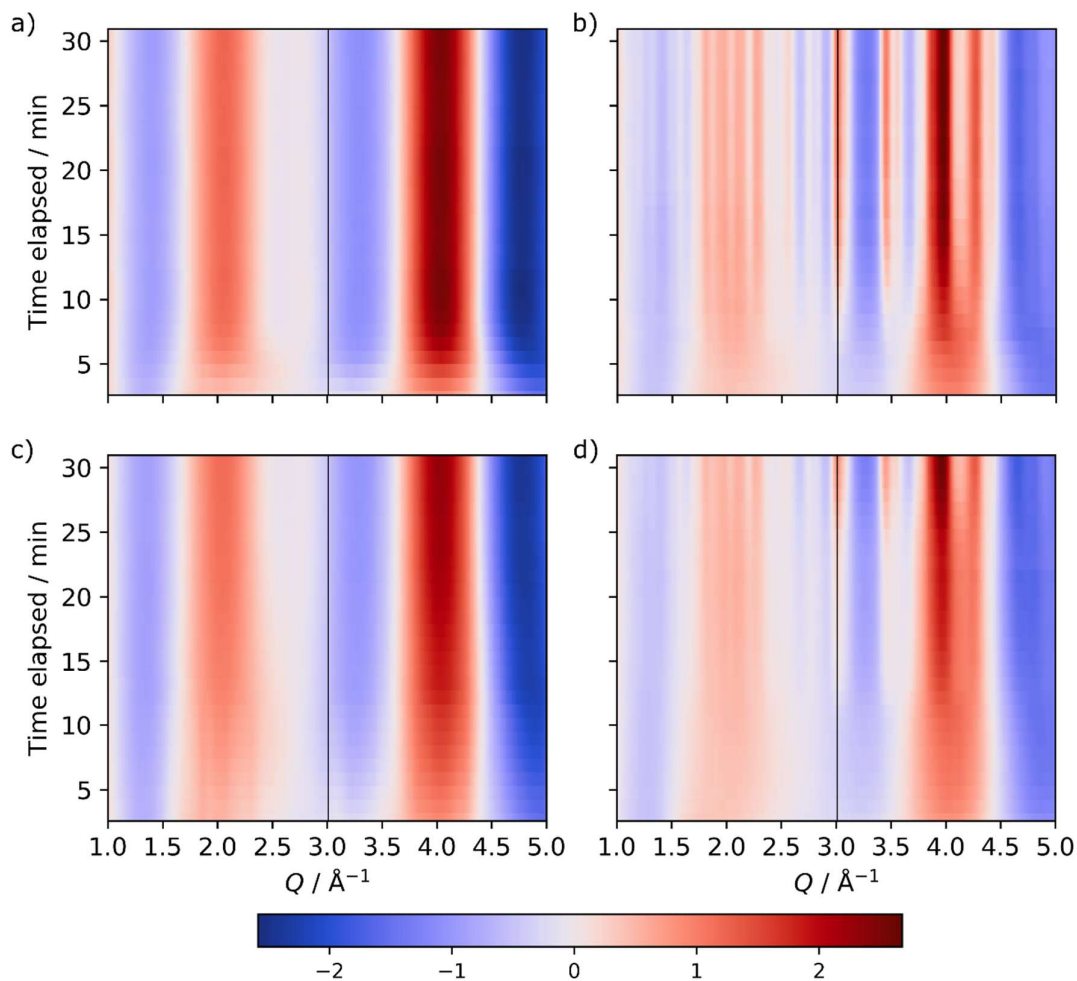


Figure 3.15. 2D datasets of $F(Q)$ for the in situ datasets over time, at a) 150°C, no BDC linker; b) 150°C, with BDC linker; c) 120°C, no BDC linker; d) 120°C, with BDC linker. 3.01 \AA^{-1} , the location of the Bragg peak tracked in Figure 3.12 for those datasets containing the BDC linker, is shown on the plots with a thin black line.

The growth of the Bragg peak at 3.01 \AA^{-1} coincides with the growth of the framework inter-cluster peaks, including that at 13.2 \AA , in the XPDF [Figure 3.12], suggesting that the connection of the clusters into a framework occurs simultaneously with the crystal formation, rather than first forming as an amorphous linked-cluster polymeric phase with subsequent rearrangement to become crystalline.

The changes in the $F(Q)$ data indicate that the **hcp** UiO-66(Hf) material is formed in both the BDC-150 and the BDC-120 reactions [Figure 3.12 b,d), Figure 3.15 b,d)]. However, there appear to be two stages to the growth in the framework at 120°C, shown both by the tracked intercluster peak in $G(r)$ at 13.2 \AA [Figure 3.12 d)], and by the changes in the 3.01 \AA^{-1} reflection in $\Delta F(Q)$ [Figure 3.15 d)]. The timing of stages of growth of the reactions—including plateaux and times of fastest growth—are shown in Table 3.II.

Table 3.II. Key times (peak maximum, and fastest growth) in the evolution of peaks during the in situ reactions, obtained from processed data with peak-tracking code as seen in Fig. 5. Smoothing to reduce contribution from noise was applied in Python with a Savitzky-Golay filter, polynomial order 2. Data shaded in purple represent peaks found in the single cluster $G(r)$; data shaded in orange represent peaks found in the double cluster $G(r)$; data shaded in grey represent peaks indicating intercluster or framework growth in both $F(Q)$ and $G(r)$. Times are rounded to 1 decimal place to give meaningful values. Times of fastest growth were determined by finding the maximum of the rate of change $dG(r)/dT$; plateau values were calculated as the midpoint of the plateau.

	150°C no BDC	150°C BDC	120°C no BDC	120°C BDC
Change in peak being tracked	Time / min			
$G(r)$ 3.5 Å fastest growth	3.9	2.6	6.4	*
$G(r)$ 3.5 Å maximum	10.1	8.5	22.4	20.4
$G(r)$ 4.9 Å fastest growth	3.9	5.7	5.3	*
$G(r)$ 4.9 Å maximum	9.3	9.0	29.5	26.9
$G(r)$ 9.2 Å fastest growth	6.0	4.7	11.6	12.6
$G(r)$ 9.2 Å maximum	11.3	9.3	26.3	25.1
$G(r)$ intercluster fastest growth	-	9.9	-	11.6, 26.6
$G(r)$ intercluster maximum	-	29.9	-	Not reached in time range; mid-plateau at 18.9
$F(Q)$ 3.01 Å ⁻¹ fastest growth	-	9.9	-	11.5, 26.1
$F(Q)$ 3.01 Å ⁻¹ maximum	-	25.6	-	Not reached in time range; mid-plateau at 18.9

*noise too great relative to change in gradient

The first stage of crystalline framework growth in the BDC-containing reaction at 120°C occurs once some double cluster has formed, with a sudden increase in the intensity of the reflection at 3.01 Å⁻¹ at c. 11.5 minutes [Table 3.II] indicating rapid framework growth. But, after an initial increase in intercluster (13.2 Å) peak area, the rate of framework formation slows and plateaus around 18.9 minutes (likely limited by the amount of available double cluster, which does not reach a maximum until around 25.1 minutes, according to the $G(r)$ tracking). The second stage of crystalline framework growth, with fastest growth at c. 26.1 minutes, occurs once the double cluster peaks in the $G(r)$ have reached their maximum (i.e., once there is significant excess of the 'free' double cluster), with a higher rate, as the amount of double cluster is no longer limiting.

These reactions were performed with different concentrations and a different solvent ratio to the lab syntheses, in order to work in the *in situ* capillary. In order to determine whether the results produced *in situ* could be representative of reactions occurring in a standard lab synthesis, the reactions were repeated in a laboratory vessel with the same concentrations and solvent ratio as used *in situ*.

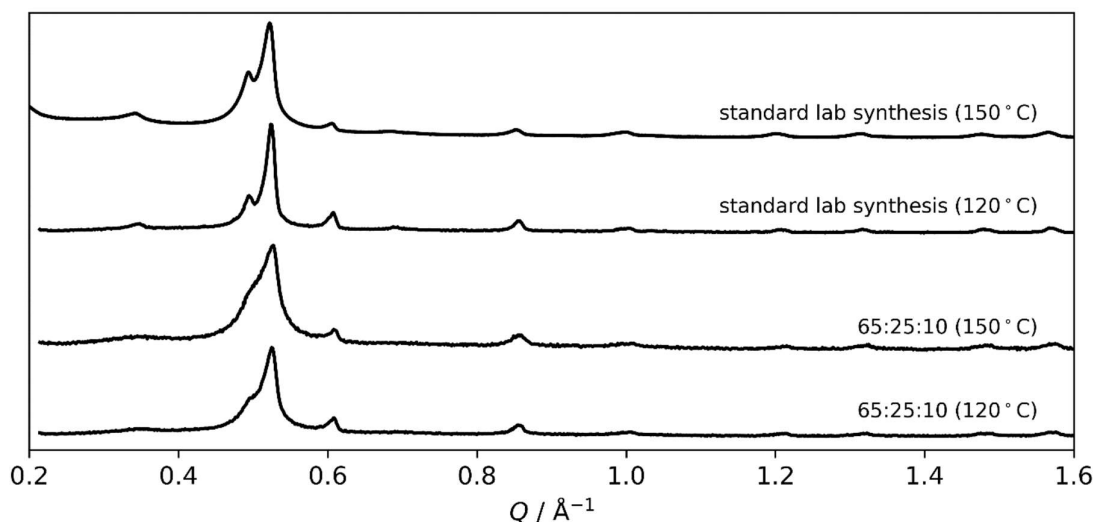


Figure 3.16. PXRD patterns of *hcp* UiO-66(Hf), produced both with the concentrations used *in situ* in 65:25:10 solvent, and in standard laboratory reactions as in Chapter 2/Ref. 251, at 120°C and 150°C.

Both reactions in the laboratory vessel, both at 150°C and 120°C, produced **hcp** UiO-66(Hf), showing that the *in situ* experiments have the same outcome as a laboratory synthesis [Figure 3.16]. Although it was previously assumed that a laboratory synthesis at 120°C

would not produce the **hcp** material, in keeping with the results for **hcp** UiO-67(Hf),¹² the success of the 120°C laboratory synthesis based on the *in situ* conditions inspired further investigation. A synthesis was therefore attempted at 120°C, based on the *ex situ* conditions used in Chapter 2 to synthesize **hcp** UiO-66(Hf).²⁵¹ This synthesis also produced the **hcp** phase [Figure 3.16].

This result shows that the insights obtained by the *in situ* study in this Chapter can be used to inspire new and successful laboratory-based syntheses.

3.3 Discussion

This investigation using X-ray pair distribution function analysis provides previously unknown insights into the formation of Hf metal clusters in solution, both as molecular clusters and in the synthesis of **hcp** UiO-66(Hf) MOFs. XPDF has been previously used *in situ* to show the formation of MOF crystallites and to examine the behaviour of clusters within an existing MOF framework;^{268,294} this Chapter takes this powerful technique one step further to show the cluster aggregation in solution prior to and during MOF crystallisation. The results obtained here are not directly comparable to a standard lab-based synthesis, due to the difference in conditions required to increase the signal-to-noise when performing the experiment in a capillary rather than a standard lab reaction vessel; to account for the smaller reactor volume, higher concentrations are used. This investigation has nevertheless shown that the materials produced *in situ* in this work are consistent with those produced *ex situ* in a standard lab reaction and can therefore be used to help in understanding the processes that occur in solution in a laboratory synthesis of **hcp** UiO-66(Hf). While Chapter 2 showed that the synthesis conditions, including temperature and amounts of water and formic acid, are crucial in determining the phase of UiO-66(Hf) MOF which forms, the results in this Chapter reveal details of the formation mechanisms of the **hcp** UiO-66(Hf) framework and its constituent metal clusters, which can provide clues as to the role of the different synthesis conditions.

3.3.1 The Role of Acid

This Chapter shows that in water, HfCl_4 forms the tetramer cluster $[\text{Hf}_4(\text{OH})_8 \cdot 16\text{H}_2\text{O}]^{8+}$, surrounded by a structured coordination shell of water, as expected at room temperature. With a change of solvent system to DMF : formic acid : water, a mixture of the tetramer and the single cluster (with a core of $[\text{Hf}_6(\mu_3\text{-O})_4(\mu_3\text{-OH})_4]$) is obtained, with less short-range structured solvent surrounding the clusters (although some solvent structuring is still evident). This suggests that the acid is a critical species in causing the formation of the single cluster; acid is thought to be implicated in the decomposition of the tetramer species.²¹² However, in this room-temperature experiment, both the tetramer·H₂O and the single cluster coexist in solution, even though both water and formic acid are in large excess (modulator : metal molar ratio of 183 : 1). This contrasts with the analysis in a previous XPDF investigation (of Zr species rather than Hf), which suggested that solutions of ZrCl_4 in

either DMF/HCl (37 wt% in water) solvent (1 : 10.3 : 41.5 molar ratio metal : acid : water) or in DMF/H₂O solvent without added acid (1 : 28.8 molar ratio metal : water) produced predominantly the single cluster.²⁹⁴ Although the hydrolysis reactions necessary for cluster interconversion are known to be kinetically hindered,²⁰⁹ that study employed neither heating nor ageing to overcome these kinetic limitations, so it is surprising that a mixture of single cluster and tetramer was not observed, especially given the lower concentrations of acid and water relative to metal in that study.²⁹⁴

The observation in this work of the importance of acid to the formation of the single cluster is corroborated by an EXAFS study,²⁰¹ which revealed that the addition of acetic acid to the tetramer in aqueous solution triggers a rearrangement *via* a (too short-lived to be identifiable) intermediate to form the single cluster. In the EXAFS study, a mixture of the two clusters (as observed here) was only seen with modulator : metal ratios below 10 : 1, which is a far smaller ratio than in this work, despite acetic acid being less reactive than the formic acid modulator used here.²⁰⁹ This difference is likely because the reaction solutions in the EXAFS study were aged for weeks prior to measurement in order to obtain equilibrium, which will greatly affect the degree of cluster hydrolysis and conversion.

3.3.2 The Role of Water

This work shows for the first time the formation of the Hf₁₂ double cluster from the Hf₆ single cluster. This conversion could be achieved *via* the hydrolysis reactions common to these Hf and Zr species, through terminal hydroxide groups on the single clusters²⁵¹ joining clusters together to give the 12-mer, with its characteristic 'belt' of six μ_2 -OH groups.

These clusters have four coordination sites per metal not taken up by cluster-core bridging μ_3 -O or μ_3 -OH groups; thus the single cluster has 24 available sites, and the double cluster has 36 (due to the bridging μ_2 -OH groups). The single cluster therefore has the formula [Hf₆O₄(OH)₄]_{L24} and the double cluster [Hf₁₂O₈(OH)₈(OH)₆]_{L36} (or the equivalent [Hf₆O₄(OH)₄]₂(OH)₆L₃₆), where, in the BDC-free solutions used in this work, each terminating singly-coordinating L group could either be half of one bidentate formate anion (as formate takes up two coordination sites), or the combination of: one metal-bound OH and one metal-bound H₂O.²⁵¹

The cluster-joining reaction could therefore, for example, take the form of $2([\text{Hf}_6\text{O}_4(\text{OH})_4]\text{L}_{18}(\text{OH})_3(\text{H}_2\text{O})_3) \rightarrow [\text{Hf}_{12}\text{O}_8(\text{OH})_8(\text{OH})_6]\text{L}_{36} + 797.6\text{H}_2\text{O}$, i.e., three metal-coordinated terminating OH groups on each single cluster could form the 'belt' of six μ_2 -OH, releasing six metal-coordinated water molecules. The joining of clusters alone would give an entropy penalty when considering ΔG for the reaction—this release of water molecules could alleviate the entropy penalty or even make the cluster-joining entropically favourable. While this release of water may seem counterintuitive to the previous observation that water in the synthesis is required for the formation of **hcp** UiO frameworks,^{12,251} this cluster joining reaction requires at least 3 L = (OH) and 3 L = (H₂O) groups on each single cluster (that is, a maximum of 18/24 L sites being coordinated by carboxylate groups); potentially, with less water in the synthesis, insufficient water is present, either in solution or as terminating groups on the clusters, to permit this cluster-joining.

These two observations in this work, of the formation conditions of the single cluster and of the double cluster, therefore help to explain why both water and formic acid are necessary in forming **hcp** UiO frameworks: formic acid is crucial for the formation of the single clusters, while water is also necessary in order for these single clusters to join to form the double clusters of the **hcp** framework.

3.3.3 The Role of Temperature

This work also shows that the double cluster requires elevated temperatures to form. Compared with studies which did not demonstrate any interconversion between pre-synthesised single and double molecular clusters at room temperature,²⁹¹ the observation in this work demonstrates that double clusters can form from single clusters, but that elevated temperatures are necessary. This is in keeping with earlier work showing that the **hcp** UiO-67(Hf) framework, containing the double cluster, requires a higher temperature to form compared to the **fcu** framework.¹²

In this work, the behaviour of the reaction mixtures was examined at two elevated temperatures: 150°C and 120°C. By carrying out the reactions at a lower temperature, any kinetically limited processes—such as hydrolysis reactions²⁰⁹—should be slowed down. In both reactions carried out at 120°C, growth of all peaks, especially the intra-cluster peaks, was significantly slower than at 150°C (the 3.5, 4.9 and 9.2 Å peaks reached their maximum

at 22.4, 29.5 and 26.3 minutes respectively for the no-BDC reaction at 120°C, compared to 10.1, 9.3 and 11.3 minutes for the no-BDC reaction at 150°C [Table 3.II]), suggesting that these cluster reactions (including the formation of the double cluster from single clusters) are indeed kinetically limited. Despite the slower transformation at lower temperatures, no additional cluster species were observed. The formation of the nonamer or 11-mer would require additional μ_3 -bridging O and OH, which are disfavoured at lower temperatures¹³⁰ particularly once a cluster is saturated with terminating coordinating groups,⁶⁷ whereas the μ_2 -OH bridging in the Hf₁₂ cluster could occur *via* a much more straightforward nucleophilic attack of OH²⁰⁷ from one cluster to another. Thus at both 150°C and 120°C, the double cluster is obtained preferentially to other high-nuclearity clusters.

Elevated temperatures also thermodynamically favour processes which result in an increase in entropy. From the above discussion of the role of water, the formation of the double cluster is one such process, due to the increase in entropy from the release of structured water upon cluster joining. As well as the metal-coordinated water released as single clusters join to form double clusters, there is also strong evidence for coordination shells of water—including hydrogen-bonded water—around clusters,^{251,342} some which would also be released upon cluster joining. This indicates that higher temperatures favour the formation of the double cluster for thermodynamic, as well as kinetic, reasons.

3.3.4 Framework Growth and Temperature

Perhaps surprisingly, the reactions in this work at both 120 and 150°C produced the **hcp** UiO-66(Hf) framework. This contrasts with previous work, in which **hcp** UiO-67(Hf) required a temperature of 150°C to form (and not 120°C),¹² and also with literature, in which **fcu** UiO-67(Hf) is usually synthesised at lower temperatures including 120°C.^{14,138,140} As this work has shown that, at both temperatures, the double cluster forms, the clue to this behaviour could lie in the framework formation. At both of these temperatures, the growth rates of the intra-cluster peaks do not appear to change with the presence of BDC linker in the reaction. While there is a different concentration of Hf in the linker-containing reaction mixtures, *vs* the molecular-cluster-only reactions, meaning they cannot be directly compared, this nevertheless suggests that the linkers do not play a critical part in initial

cluster formation and become involved later in the reaction through post-cluster-formation ligand exchange (in agreement with previous research on ligand exchange^{129,291,382}).

As a result of the different binding strengths of different carboxylic acids,^{130,135} the low solubility of H₂BDC in DMF/formic acid solutions,¹² and the ratio of formic acid to BDC in these reactions being in excess of 40 : 1, it is not surprising that the BDC linkers may be outcompeted initially by formate (or water/hydroxide), and so coordinate to clusters later in the reaction. As hydroxide groups are more strongly coordinated than carboxylate groups,^{6,37} the joining of the single clusters to form the double cluster could therefore occur before the terminating ligands can exchange (in the linker-containing reactions) for dicarboxylate linkers (which would either 'trap' the single cluster species or slow down the cluster conversion). Alongside the discovery in this work that the growth of the crystalline framework occurs simultaneously with, rather than after, the linking of clusters together, this further suggests that once the clusters link up into a framework, the dicarboxylate linkers are less labile, and that dissociation (required for rearrangement) is kinetically and entropically less favourable. This would therefore mean that, despite the lower temperature used here, the successful formation and linking-up of the double cluster determines the formation of the **hcp** framework over the **fcu**.

The framework topology is determined by the double clusters, which form at both 150°C and 120°C. That **hcp** UiO-66(Hf) forms at 120°C even in the less concentrated, laboratory syntheses, whereas **hcp** UiO-67(Hf) does not, suggests that, the nature of the linker—terephthalate for UiO-66 and biphenyldicarboxylate for UiO-67 frameworks—is key to the formation of the MOF in terms of its ability to coordinate competitively to the clusters. The two-stage framework growth of **hcp** UiO-66 at 120°C described in this work may shed light on the previous discovery that an *ex situ* reaction with a UiO-67(Hf) reaction mixture at 120°C resulted in a poorly crystalline material,¹² rather than either the **fcu** or the **hcp** framework. If that previous *ex situ* UiO-67(Hf) reaction mixture follows a similar framework growth pattern to the two-stage pattern shown in this work, then the first stage of framework growth could occur before the cluster aggregation from single to double clusters is complete. This could involve the cluster coordination sites being 'blocked' towards further attack by exchange of dicarboxylic acid linkers with the cluster-terminating ligands,²¹⁷

resulting in a mixture of coordinated single and double clusters, with different and less compatible coordination geometries.

This further suggests that, by adjusting the temperature of the reaction to take advantage of the different rates of cluster condensation and of framework growth, it may be possible to allow more time for the clusters to join together prior to coordination by inter-cluster linkers, and so obtain 'multi-cluster' species intermediate between the double cluster and previously-observed infinite 1-D chains, all based on the Hf_6 single cluster unit.¹⁵²

3.3.5 Summary

Building on the previous studies, this work corroborates that cluster formation in these UiO systems is determined by a complex interplay of temperature, ageing, concentration of metal salt and the type, concentration and pK_a of acid (which can act as a modulator and as directing groups^{48,67,378}). The complex processes discussed in this work motivate further exploration to enable understanding in greater detail, and hence improved exploitation of these materials. With careful control over the timing of linker addition, and consideration of the coordination-site-preferential exchange between linkers and terminating ligands known to occur with molecular double clusters²⁹¹ (particularly involving the ligands at the 'narrow' ends of the cluster),¹² this enhanced understanding of cluster formation in UiO systems could lead to intentional control of the framework growth, potentially providing routes to ordered mixed-linker frameworks, double-cluster-containing nanosheets such as those reported in Chapter 2,^{12,251} or as-yet-unknown 'multi-cluster' MOFs.

3.4 Conclusions

This work has demonstrated that XPDF data can successfully capture the pre-crystalline stages of Hf MOF formation during *in situ* solvothermal reactions, including distinguishing between different metal clusters in solution. This technique is used to explore the response of HfCl₄ to different reaction temperatures and solvents, in particular those conditions used to synthesise the **hcp** UiO-66(Hf) MOF, using a combination of refinement and peak area calculations to track subtle changes in the XPDF between different systems and over the course of *in situ* reactions. In water the dominant cluster form is the tetramer, but in a mixture of DMF, formic acid and water, it quickly begins to convert to the hexanuclear single cluster form even at room temperature; the formic acid is likely to act as a directing group, but it was not possible to identify any intermediates in the transition from tetramer to single cluster. Heating this reaction mixture results in an initial decrease in the proportion of tetramer, followed by the growth of the double cluster alongside a reduction in the amount of single clusters. This provides strong support for a mechanism for double cluster formation directly from pairs of single clusters with μ_2 -OH bridges created between them, rather than forming directly from the tetramer or requiring the single clusters to break down and reform larger clusters. No double clusters were observed at room temperature, suggesting that aggregation to form higher-nuclearity clusters is favoured by higher temperatures and the rate of double cluster formation increases with temperature. Once the double clusters form, they then undergo ligand exchange to link together in a framework, with BDC in place of terminating ligands; this framework appears to form directly as a crystalline MOF, with no evidence of a transformation from amorphous to crystalline. *Via* this analysis a mechanism is proposed for the formation of **hcp** UiO-66 [outlined in Figure 3.17]. The formation of the metal clusters prior to the framework coordination and growth is a confirmation that, for these UiO family MOFs, the clusters are indeed the 'building units'^{55,57} which direct the framework topology, rather than the resultant MOF structure being determined by the clusters and linkers concomitantly.

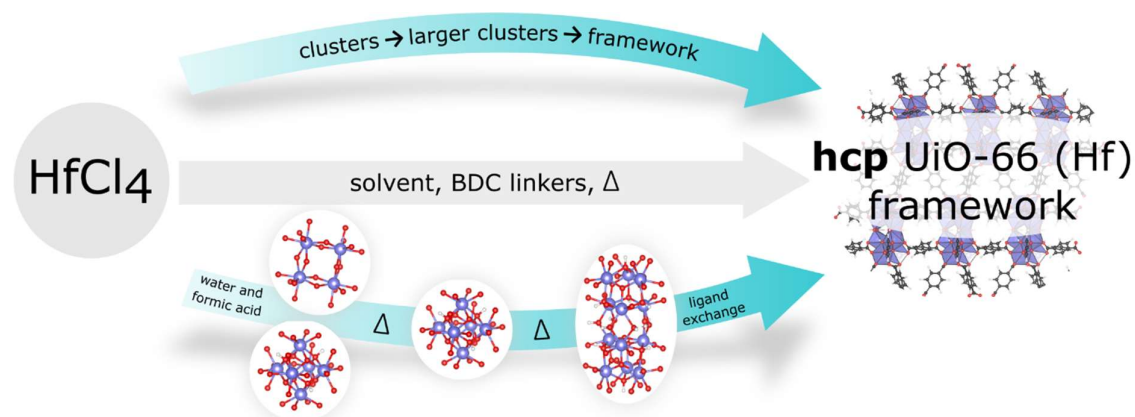


Figure 3.17. Summary of stages in the formation of hcp UiO-66(Hf) in solvothermal conditions

While the insights into the behaviour of Hf (and Zr) MOFs during their synthesis presented in this work are key to understanding the formation of these important materials, further questions are raised. In particular, it is clear from this and previous work that water and formic acid are key to the formation of the different clusters, as well as the frameworks of which they are a part, but this study does not provide answers regarding the exact role of each of the components of the solvent in the formation of both the clusters and the full **hcp** framework, or the reason why specific concentrations of these components are required for the MOFs to form. This work therefore motivates further investigation into the interactions both within the solvent, and between the solvent and the clusters, including exploring the effect of changing the solvent composition. Studying the behaviour of systems produced in standard lab syntheses is also crucial, in order to determine whether the understanding obtained from this work, using synchrotron *in situ* conditions, can be generalised to typical MOF syntheses.

Chapter 4. Studying Solution Interactions in Reaction Mixtures of Hafnium Clusters

Throughout the work presented in this thesis it is evident that the composition of the solvent, and the subsequent interactions between the solvent and the metal ions and clusters, play a significant role in determining the nature of the metal clusters and resultant MOF structures that form.^{15,175} Chapter 3 provided insights into the formation mechanism of the **hcp** UiO-66(Hf) MOF and its constituent Hf₁₂ ‘double clusters’ in a solvent comprising dry *N,N*-dimethylformaldehyde (DMF), formic acid (FcOH) and water (DFW 65:25:10). The exploration of the formation of hafnium clusters in this solvent using *in situ* XPDF analysis further showed that the cluster is sensitive to the reaction conditions including the composition of the solvent, forming variously the tetramer, ‘single’, and ‘double’ clusters with metal-oxo-hydroxo cores of Hf₄(OH)₈, Hf₆O₄(OH)₄, and {Hf₆O₄(OH)₄}₂(OH)₆ respectively [Figure 4.1].

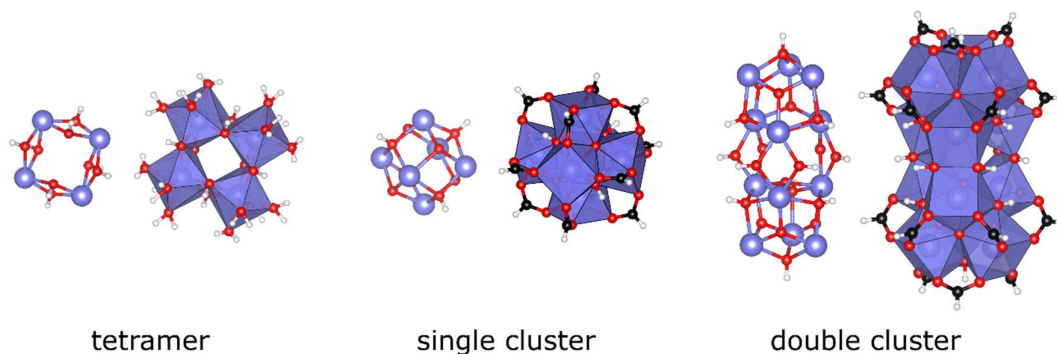


Figure 4.1. Schematic showing the different hafnium clusters discussed in this Chapter: the [Hf₄(OH)₈(H₂O)₁₆]⁸⁺ tetramer, found in aqueous solutions, the [Hf₆O₄(OH)₄]¹²⁺ single cluster, and the [Hf₁₂O₈(OH)₈(OH)₆]¹⁸⁺ double cluster. Clusters are shown in two representations: left, the metal-oxo-hydroxo core; right, polyhedral representation with example ligands (water for the tetramer, formate for the single and double clusters). Cluster structure colour scheme: Hf, blue; O, red; H, white; C, black. Cluster structure models were obtained from crystal structure files^{50,67,194,196,251} and edited using the VESTA programme.³⁴⁹

The formation of zirconium molecular clusters is well-studied, primarily in the solid state. Clusters with the M₆O₄(OH)₄ core are frequently synthesised with an excess of monocarboxylic acid and in the absence of water, and hence are surface-terminated by carboxylate groups, sometimes with a range of bonding modes.^{215,216,291,331,383} The double cluster with core {M₆O₄(OH)₄}₂(OH)₆ is also known,³⁸⁴ although rarer than the ‘double cluster’ formed by bridging carboxylates or alkoxides rather than μ₂-OH groups.^{191,291} Similar

to the single clusters, these are usually reported with carboxylate terminating groups; in many of these species, the coordinating groups are involved in dynamic exchange in solution. The tetramer species, meanwhile, is predominantly reported with water terminating ligands especially in aqueous solution;^{204,292} in the presence of carboxylate groups, some have been suggested to coordinate to the tetramer as an intermediate²⁰⁹ in the rearrangement to form the single cluster.²⁰¹

The cluster-terminating ligands shown on the clusters in polyhedral representation in Figure 4.1 are suggestions based on this: the tetramer is shown coordinated by water, and the single and double cluster by formate. However, for solutions of hafnium chloride in the DMF : formic acid : water solutions used in this work, single and double clusters are likely to be terminated with a mixture of formate, hydroxide and water ligands (in keeping with these ligands being observed as defect-compensating species in the MOF frameworks).²⁵¹ Owing to the potential for different ratios of cluster-surface ligand species, and the potential for a variety of coordination geometries, a range of ligand environments are possible. Including the cluster-structure bridging μ_2 - and μ_3 -OH groups, therefore, there are a range of different cluster surface species likely to be present in these solutions, summarised in Table 4.I.

Table 4.I. Summary of types of proton environment on the clusters discussed in this work.

	$[\text{Hf}_4(\text{OH})_8(\text{H}_2\text{O})_{16}]^{8+}$ tetramer	$[\text{Hf}_6\text{O}_4(\text{OH})_4]^{12+}$ single cluster	$[\text{Hf}_{12}\text{O}_8(\text{OH})_8(\text{OH})_6]^{18+}$ double cluster
μ_2 -OH per cluster	8	0	6
μ_3 -OH per cluster	0	4	8
Surface-terminating ligands?	Predominantly water 32 H per cluster	Formate (HCOO^-) and/or water/hydroxide 12-36 H per cluster and multiple environments, depending on ligand ratio	Formate (HCOO^-) and/or water/hydroxide 18-54 H per cluster and multiple environments depending on ligand ratio

Chapter 3 did not, however, investigate these differences in coordinating ligands, owing to the insensitivity of XPDF to lighter elements such as ^1H . It is also important to explore and understand the interactions in the solvent, including the identity and behaviour of the metal clusters themselves within these systems.²⁹⁵ In order to investigate the solvent and cluster ligands, however, a technique sensitive to these components must be used. Contrasting with the sensitivity of XPDF towards metal species, nuclear magnetic resonance spectroscopy (NMR) can be used to understand the chemical environments and behaviour of lighter elements, such as ^1H and ^{13}C , which are predominant in the solvents used in this work.

Solution ^1H NMR is already established as a technique for determining the ligands on metal clusters, including zirconium analogues of the single cluster observed in this work.^{72,291,312,328} Strong ^1H peaks arising from ligand environments can be obtained in solutions prepared by dissolving high concentrations of a pre-prepared, dried cluster sample in a standard solvent such as C_6D_6 .^{72,291,312} This technique has been used to differentiate between different ligands on the single cluster and an M_{12} cluster (although not the double cluster investigated in this

work).²⁹¹ However, most solution NMR experiments have focussed on the ligands and have not reported the ¹H NMR signals from the μ_2 - or μ_3 -OH groups integral to the cluster.³²⁸ One exception is the detection of signals arising from μ_2 -OH groups at ~1.5 ppm in a trinuclear zirconium complex.³¹² In a solution NMR study of the zirconium tetramer $[\text{Zr}_4(\text{OH})_8(\text{H}_2\text{O})_{16}]^{8+}$ in aqueous solution by Åberg and Glaser,²⁹² no μ_2 -OH signals were reported through either ¹H or ¹⁷O NMR, although some terminal water environments could be detected. The few reports of μ_3 -OH environments have been *via* solid-state ¹H NMR of UiO-67 MOFs, in which resonances at shifts of 0-3 ppm were assigned to these μ_3 -OH cluster-structure environments on the single cluster in the MOF.^{357,385}

Solution NMR is also a valuable tool used to explore the interactions inside the solvents used in MOF synthesis. Performed *in situ* during MOF synthesis, it can track the incorporation of linkers into the growing MOF.²⁷⁸ It can also be used to understand the intermolecular interactions in the solvent such as hydrogen-bonding (either as a donor or acceptor), due to the changes in electron density:³⁸⁶ several parameters, including chemical shift, are affected by the presence and strength of hydrogen-bonds.³⁸⁷⁻³⁸⁹ However, using solution NMR to investigate both the metal clusters and the solvent is rare.

Hence, in the investigation on which this Chapter is based, solution NMR is used alongside complementary *ex situ* XPDF analysis to investigate more fully the hafnium clusters found in this work, as well as to improve understanding of the solution processes which underpin the behaviour of the clusters and hence the synthesis of the MOFs which are the focus of this thesis. In order to understand the effect of the reaction conditions on the metal clusters, both the cluster identity and the solvent and ligand interactions must be determined. To distinguish between the effects arising from the presence of the metal, and those from inter-solvent-molecule interactions, the behaviour of the reaction solvent must be explored with and without metal clusters present. This Chapter therefore explores the solutions of molecular clusters investigated with *in situ* XPDF analysis in Chapter 3, using solution NMR and XPDF techniques on samples both with and without metal salt and with and without heating. This information is then used, alongside that from previous Chapters, to bring together an improved picture of the way in which the synthesis conditions determine the structure of the hafnium clusters that are crucial to the formation of different MOF phases.

The initial solution NMR experiments were performed by Didi Rinkel, Department of Chemistry, University of Cambridge. All other solution NMR experiments were performed by Francesca Firth.

Assistance in setting up NMR experiments was given by Duncan Howe, part of the NMR Facility in the Department of Chemistry, University of Cambridge, and NMR tubes were provided by James Ellison, Department of Chemistry, University of Cambridge.

Samples for ex situ XPDF experiments were synthesised and prepared by Francesca Firth. The ex situ XPDF experiments were performed at Beamline I15-1, Diamond Light Source, beamline staff Dr Maria Diaz-Lopez and Dr Phil Chater. Dr Harold Geddes and Professor Andrew Goodwin, Inorganic Chemistry Laboratory, University of Oxford are thanked for coordinating the Oxford Warwick Midlands Solid State Chemistry consortium XPDF time via BAG CY26330-2.

All data analysis was performed by Francesca Firth.

4.1 Experimental Methods

4.1.1 Synthesis

An aqueous solution of HfCl₄ (30 wt%) was prepared through dissolution of HfCl₄ (Acros Organics, 99%) in water (Fisher, HPLC grade) and sonication for 10 minutes.

The conditions for the synthesis of the hafnium clusters were adapted from Chapters 2 and 3. The concentrations of HfCl₄ were increased from those used in Chapter 3 to improve the signal-to-noise ratio in the NMR spectra. The compositions of the reaction mixtures are described below.

HfCl₄ (varying mol/V) was added to a vial, followed by dry *N,N*-dimethylformamide (Sigma Aldrich, 99.85% anhydrous DMF) (different V/V quantities), formic acid (Fisher, 98/100%) (different V/V quantities) and water (Fisher, HPLC grade) (different V/V quantities), then sonicated for 10 minutes. NMR and XPDF experiments were then performed on the samples not undergoing heat treatment at varying times after synthesis. Those samples undergoing heat treatment were transferred to a 23 mL PTFE-lined steel autoclave, which was sealed and heated at 150°C for 24 hours. The reaction mixture was allowed to cool to room temperature. Metal-free solutions were prepared according to the same protocol but omitting the metal salt.

NMR and XPDF experiments were then performed on these samples at varying times after synthesis.

4.1.2 Solution NMR

One-dimensional ¹H, one-dimensional ¹H-¹H selective gradient nuclear Overhauser effect spectroscopy (NOESY), one-dimensional ¹H-¹H selective gradient rotating frame Overhauser effect spectroscopy (ROESY), and two-dimensional ¹H-¹H nuclear Overhauser effect spectroscopy (NOESY) spectra were recorded on a Bruker AVIII HD Smart Probe ($\omega_{1H} = 500$ MHz) spectrometer fitted with a BCU chiller unit to allow for variable-temperature experiments. Due to the high concentrations of chloride, formate and hydronium ions in the samples, solutions were loaded into medium-wall (0.77 mm wall thickness, 3.43 mm internal diameter) Wilmad NMR tubes to improve the ease of shimming.

Spectra were referenced to C₆D₆ at 7.16 ppm (δ ¹H), loaded inside a sealed capillary in the NMR tube in order to reduce unwanted additional solvent interactions in the samples.

¹H NMR spectra were recorded using a zg30 pulse sequence with a 30° pulse length of 12.50 μ s, a recycle delay of 1 s and 128 scans. 1D selective NOESY spectra were recorded using a pulse sequence with a 90° pulse length of 12.50 μ s, a mixing time of 0.8 s, a recycle delay of 2 s and 32 scans. 1D selective ROESY spectra were recorded using a pulse sequence with a 90° pulse length of 12.50 μ s, a mixing time of 0.3 s, a recycle delay of 2 s and 32 scans.

¹H-¹H two-dimensional NOESY spectra were measured with 4 scans per increment and a mixing time of 0.8 s.

¹³C NMR spectra and experimental details can be found in the Appendix.

4.1.3 X-ray Pair Distribution Function Measurements

Samples were made according to the protocol above before being loaded into 1.56*2.00*40 mm fused-quartz capillaries.

Total scattering X-ray diffraction patterns were collected at beamline i15-1 at the Diamond Light Source using an X-ray energy of 76.7 keV ($\lambda = 0.161669$ Å). Initial calibration measurements were performed on a NIST silicon standard. Diffraction measurements of capillaries containing the 65:25:10 DMF : formic acid : water solvent, both as-mixed, and after heating at 150°C for 24 h, were taken at room temperature for use as backgrounds.

4.1.4 X-ray Pair Distribution Function Analysis

The diffraction data were processed and analysed as described in Chapter 3. For *ex situ* samples the resolution peak dampening term Q_{damp} was constrained to $Q_{\text{damp}} = 0.0371$ Å⁻¹, this value derived from refinement against the NIST Si standard. For low-water samples, the parameter q_{max} was set to 20.0 Å⁻¹ due to noise in the data.

4.2 Results

4.2.1 Initial Hafnium-free Solutions

Chapter 1 discussed the hydrogen-bonding interactions between the different components of the DMF : formic acid : water reaction solvent. However, as outlined in Chapter 1, previous studies have focussed on pairs of these components, rather than all three.^{230,234,239,240} Solution ¹H NMR experiments were therefore performed on a range of different solutions in this space in order to determine and understand the interactions between these three components.

Formic acid and water each have the potential for stronger hydrogen-bonding compared to DMF;^{230,240} in order to identify the effect of adding DMF, the behaviour of solutions containing different ratios of water and formic acid only was first explored [Figure 4.2 a)].

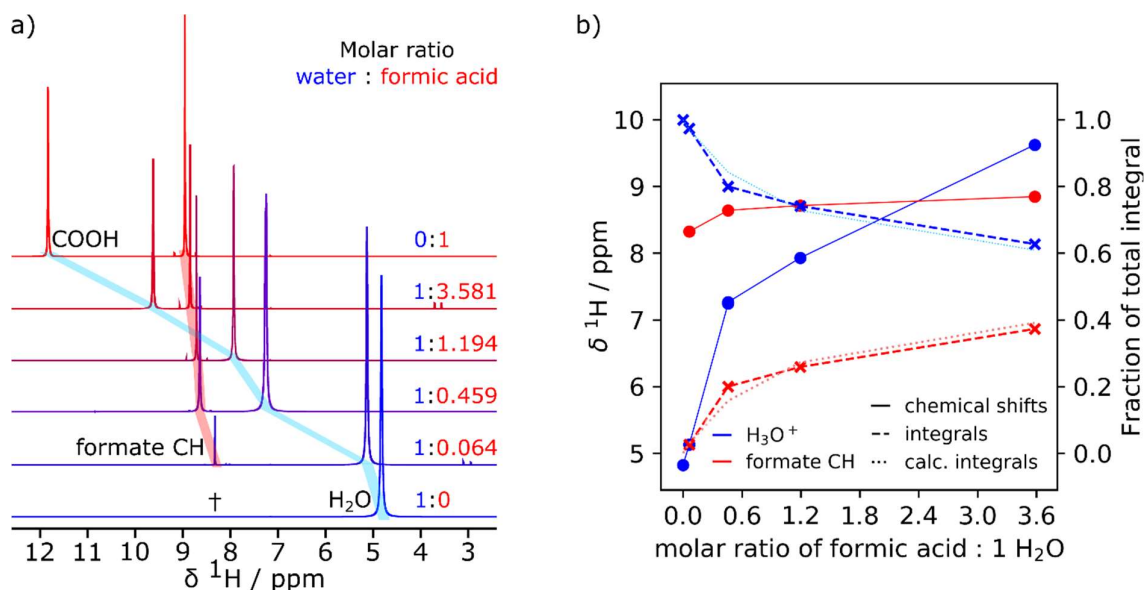


Figure 4.2. a) ¹H NMR on solutions containing different ratios of formic acid and water, referenced to C₆D₆ at 7.16 ppm indicated by † on the spectrum (in a capillary, in order to reduce unwanted solvent interactions). A single peak resulting from exchange between water, H₃O⁺ and formic acid COOH is seen, as indicated by the blue shading. The change in shift of the formate CH proton is tracked in red shading. The impurity in some spectra at 3-4 ppm is residual DMF contaminant in the NMR tube³⁹⁰; b) Plot showing the change in chemical shift and integral area of the ¹H environments. The integral fraction is defined as follows: $I_{\text{formic acid CH}} = \frac{n_{\text{formic acid}}}{2n_{\text{formic acid}} + 2n_{\text{water}}}$ and $I_{\text{H}_3\text{O}^+} = \frac{n_{\text{formic acid}} + 2n_{\text{water}}}{2n_{\text{formic acid}} + 2n_{\text{water}}}$, as there are two (different) protons per formic acid molecule and two (equivalent) protons per water molecule.

Two resonances are seen in the ¹H NMR spectra of these solutions. The formic acid/formate CH protons are readily assigned on the basis of their ¹³C satellite peaks and thus the second peak must originate from water/H₃O⁺ and COOH protons. No peak is observed for the

formic acid COOH proton, likely due to fast exchange with the water; in pure formic acid, this peak is observed at 11.8 ppm [Figure 4.2 a)].

In order to confirm the assignments the expected integrals were then calculated.

The water/H₃O⁺ peak calculated fraction ($I_{\text{H}_3\text{O}^+} = \frac{n_{\text{formic acid}} + 2n_{\text{water}}}{2n_{\text{formic acid}} + 2n_{\text{water}}}$) is calculated based on the total amount of water and formic acid COOH protons, rather than just the water protons—i.e., assuming fast exchange and therefore an averaging of their environments. The measured integrals over the range of samples (given as a fraction of total integral) are very close to the calculated expected values [Figure 4.2 b)].

Changes in shift are observed for both the formate CH and the 'H₃O⁺' ¹H environments, with the H₃O⁺ environment changing most dramatically. The measured chemical shifts of both environments increase as the concentration of acid increases, with a particularly large increase until the amount of acid reaches roughly 50% that of the water. This suggests that, as expected, the formate CH is likely to be involved in hydrogen-bonding alongside the water,²³⁹ with the degree of hydrogen-bonding of the formate CH increasing as the amount of acid increases. Increases in ¹H chemical shifts in samples with the potential for hydrogen-bonding indicate a decrease in hydrogen-bond length,³⁸⁸ with the shift changing as much as 20.49 ppm Å⁻¹ for OH---O interactions.³⁸⁶ Additionally, in fast-exchanging systems the observed chemical shift is in fact a time-averaged shift weighted by the relative concentrations of the two environments in exchange: thus, as expected, as the concentration of acid increases the H₃O⁺ peak moves away from the shift of 'pure' water at 4.82 ppm and towards the shift of the 'pure' formic acid COOH peak at 11.8 ppm. This therefore results in the largest change occurring between pure water and 0.5 : 1 formic acid : water molar ratio.

The interactions in the solvent containing DMF alongside water and formic acid [Figure 4.3] were then considered. DMF : formic acid : water solvent mixtures show broadly similar ¹H chemical shift trends to mixtures of only formic acid and water as the concentration of formic acid increases [Figure 4.3 a)]. The H₃O⁺ environment again shows a dramatic increase in shift from 4.82 ppm in the solution with no formic acid through to 9.50 ppm in a DFW 65:50:10 solution (65 : 50 : 10 DMF : formic acid : water volume ratio; 1 : 1.58 : 0.66 molar ratio), with the shift of the DMF and formate environments increasing more subtly.

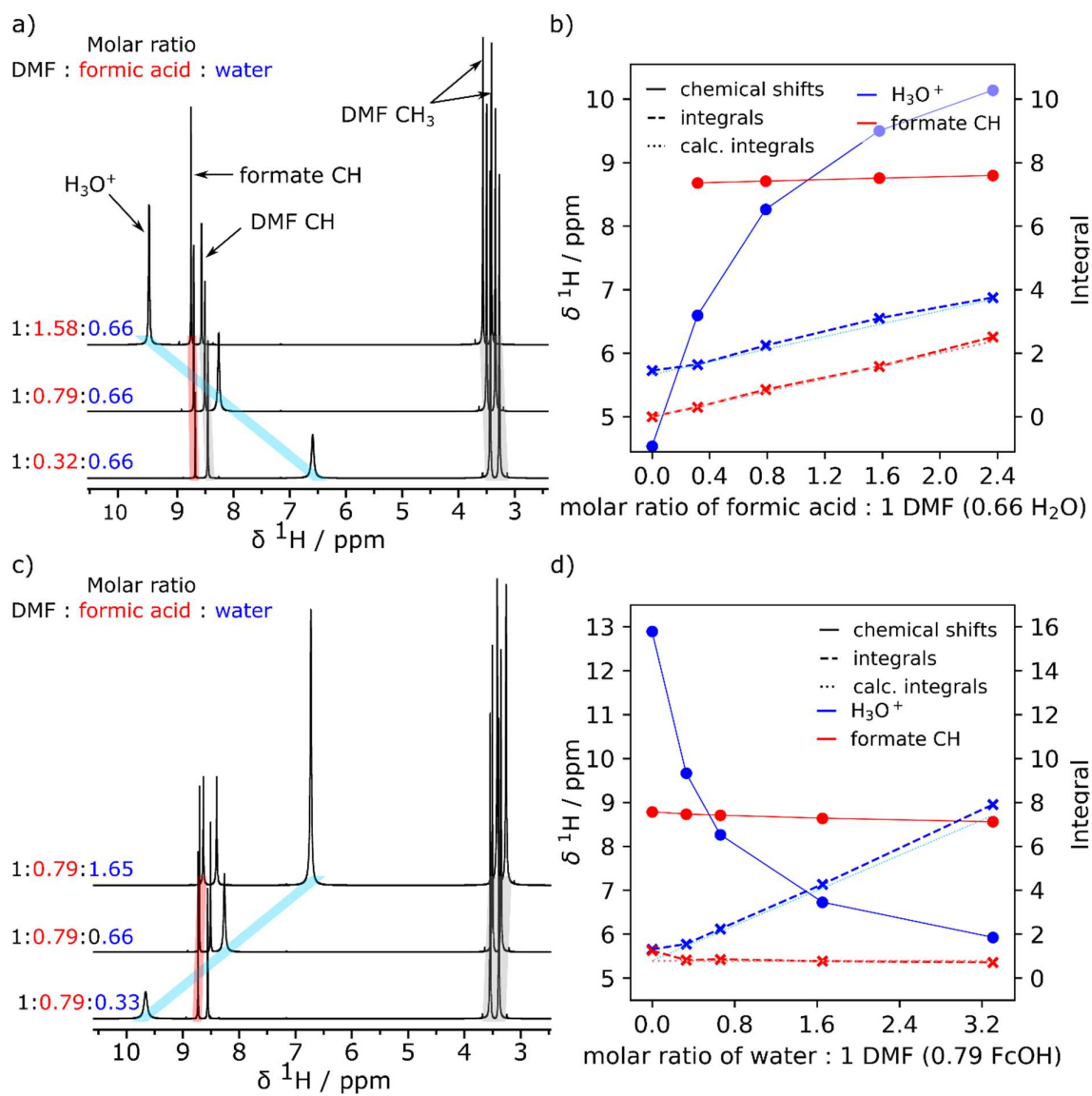


Figure 4.3. ¹H NMR, and corresponding plot of chemical shift and integral change of solutions of DMF : formic acid : water, with a,b) varying formic acid and c,d) varying water. The peaks are tracked using colour: DMF CH₃ and CH peaks are shaded in grey, the formate CH peak is in red, and the water/H₃O⁺ peak is in blue.

The chemical shift of all the DMF proton environments increases roughly uniformly with the concentration of acid [Figure 4.3 a)] suggesting that there are more hydrogen-bonds present in the system, potentially provided by interactions with the formic acid. The formate CH chemical shift also increases slightly, with a very similar trend to that seen for the system without DMF. The shift of the H₃O⁺ peak also increases but does not quite display the same trend as for the DMF-free system. For the formic-acid-free datasets the chemical shift of the water/H₃O⁺ protons is higher in pure water [see Figure 4.2] than for DMF-water [see Figure 4.3 b)], confirming that as expected the presence of DMF at non-low concentrations disrupts the water hydrogen-bonding.^{230,234} However, at the highest formic acid concentrations the

solvent containing DMF has a higher H_3O^+ ^1H shift than the DMF-free water/formic acid mixture does [Figure 4.2 b), Figure 4.3 b)]. For these datasets with and without DMF, the water : formic acid ratio is the same in each case; moreover, no side reactions have occurred to alter these ratios. Therefore the change in chemical shift of the H_3O^+ environment with the presence of DMF cannot be explained by a change in concentration weighting due to a different water : formic acid ratio. This suggests that the presence of DMF contributes to hydrogen-bonding with the acidic formic acid COOH protons, increasing their shift and resulting in a higher time-averaged $\text{H}_3\text{O}^+/\text{H}_2\text{O}$ ^1H chemical shift value.

As the concentration of water in DMF : formic acid : water solvent increases [Figure 4.3 c)], the opposite trends are observed to those when the concentration of formic acid increases [Figure 4.3 a)] as is expected since the overall concentration of formic acid decreases. As the concentration of water increases, the decrease in ^1H chemical shift of formate CH appears almost linear [Figure 4.3 d)], suggesting a steady disruption in the hydrogen-bonding around formic acid. The chemical shift of the H_3O^+ peak also decreases, but non-linearly, suggesting a compound effect of a decrease in shift resulting from the concentration-weighted average and an increase in shift due to increased hydrogen-bonding as the concentration of water increases.

An additional factor contributing to the change in chemical shift of the DMF and water environments could be the acidity of the solution affecting the shielding and hydrogen-bonding strength rather than the molecules themselves creating more or fewer hydrogen-bonds; the chemical shift of the formate CH peak is already known to be sensitive to pH.³⁹¹ The effect of changing the acidity of a DMF/water solution was therefore explored using dilutions of hydrochloric acid as the chloride ions do not interact via hydrogen-bonding. The ^1H chemical shifts of the DMF and H_3O^+ environments in DMF : HCl(aq) solution (varying the concentration of HCl) were then compared to their shifts in the DMF : formic acid : water solution (varying the amount of formic acid) [Figure 4.4]. Although pH is difficult to standardise in non-aqueous solutions,³⁹² in this work a simple calculation of pH is used as a guide to compare the acidity of the different solutions.

Across the examined acidity range, the DMF : HCl(aq) solutions show minimal changes in the ^1H shift of all environments. This contrasts strongly with the effect seen in the DMF :

formic acid : water solutions in which a reduction in the amount of formic acid increases the calculated pH but strongly decreases the chemical shift of all environments. This indicates that the chemical shift of these solutions is affected by the concentration of acid capable of forming hydrogen-bonding interactions, rather than the acidity alone *per se*.

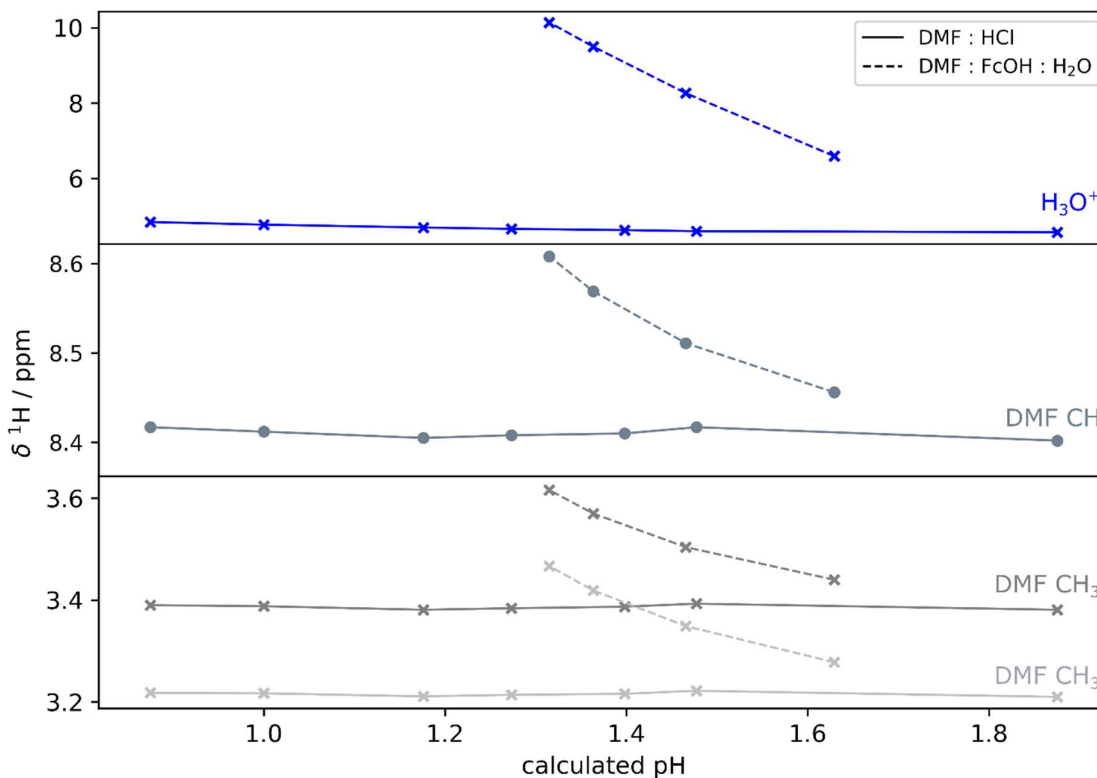


Figure 4.4. Plot of the change in ¹H chemical shift of proton environments as the pH of the solution changes. Environments in DMF : HCl(aq) solution are shown with a solid line; environments in DMF : formic acid : water solution are shown with a dashed line. The pH was calculated based on the overall concentration of protons due to the presence of acid; HCl was assumed to dissociate completely, while the dissociation of formic acid was calculated using the constant $K_a = 1.77 \times 10^{-4}$. Reaction with DMF was not included in the model. The volumes of added water were kept constant between experiments to reduce the number of variables.

These observed trends due to variation in hydrogen-bonding are congruent with the different strengths of hydrogen-bonds between different solvent molecules. This further supports the hypothesis that these systems contain significant microheterogeneity, with structuring of water within the bulk solvent due to a preference for strong hydrogen-bonds between water molecules.²³⁰

4.2.2 Unheated Hafnium-containing Solutions

HfCl₄ in water

The effect of adding the metal salt HfCl₄ was then considered. Aqueous solutions of HfCl₄ contain the [Hf₄(OH)₈(H₂O)₁₆]⁸⁺ tetrameric species surrounded by a further coordination shell of water,^{196,200,255} as confirmed by XPDF analysis results presented in Chapter 3. These solutions were examined first.

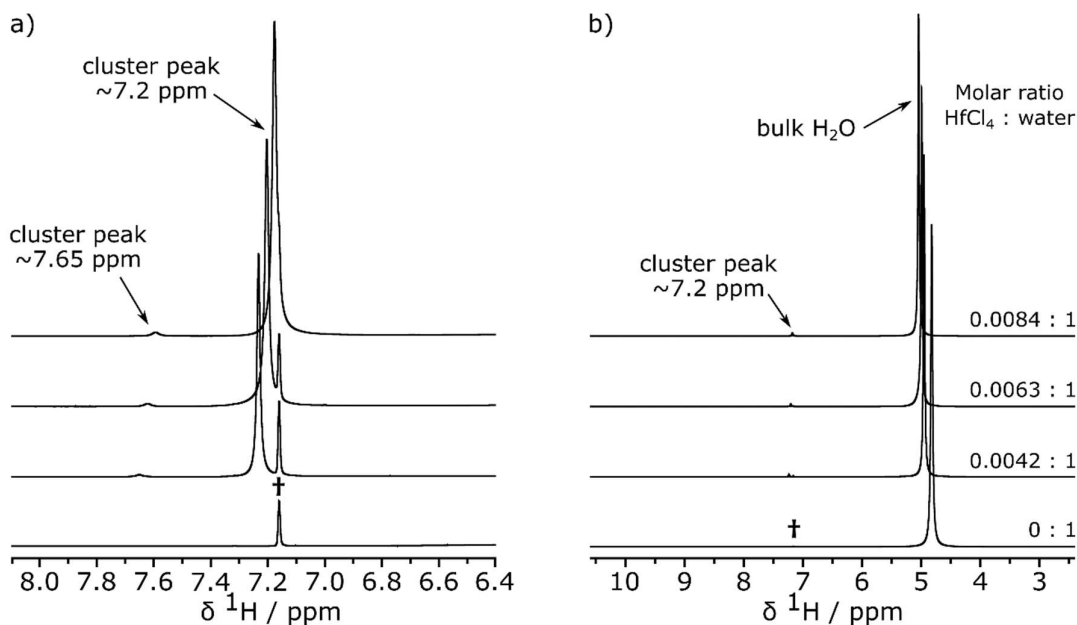


Figure 4.5. Solution ¹H NMR of HfCl₄ in water: a) full spectrum, b) expanded view. The reference solvent is C₆D₆ with a singlet signal at 7.16 ppm, marked by the dagger sign †.

As the concentration of HfCl₄ increases, the ¹H shift of the 'bulk' water increases [Figure 4.5 b)]. On the formation of the tetramer, H⁺ ions are released into the water, increasing the acidity of the solution. Additionally, the tetramer is known to be very acidic,²⁹² which could lead to the chemical shift of its surrounding additional coordination shell of water^{130,204} being higher as 'bound' water is known to have higher chemical shifts as well as potentially stronger hydrogen-bonding.³⁹³ Overall, these two effects could lead to the chemical shift of the weighted-average H₂O/H₃O⁺ environment increasing. The observed chemical shift increases with the concentration of the metal salt due to the increased amount of tetramer present in solution.

Additional peaks are also observed in the spectrum with lower intensity compared to the 'bulk' water peak [Figure 4.5 a)]. These peaks, at ~7.2 and ~7.65 ppm, only appear in the Hf-containing solutions and increase in intensity as the concentration of Hf increases, and

therefore can be related to the presence of hafnium cluster species. For both environments, their ^1H chemical shift decreases as the concentration of tetramer increases, in contrast to the shift of the 'bulk' water. The spin-lattice relaxation time T_1 at room temperature for the bulk water was measured as 1.64 s, whereas T_1 for the ~ 7.2 ppm cluster peak was 246 ms, suggesting that overall this cluster environment exchanges very rapidly with the water; the ~ 7.65 ppm environment exchanges more slowly, with a T_1 of 1.24 s.

To investigate these peaks further, a variable-temperature experiment was performed on a solution of 0.0042 : 1 molar ratio HfCl_4 : water [Figure 4.6]. At 278 K the most intense cluster peak has an integral ratio of 0.0044 : 1 relative to the bulk water peak (i.e., approximately 1 proton per Hf) [Figure 4.6 a)]. The smaller cluster peak has an integral of $\sim 9\%$ that of the larger peak. At higher temperatures, both peaks become less intense and broader, the more intense peak having an integral ratio of 0.0009 : 1 relative to the bulk water (0.21 protons per Hf) and the less intense peak having an integral $\sim 7\%$ of this, at 328 K. These decreases in intensity are likely due to the increased ligand exchange in solution at higher temperatures. That the ratio of the two small cluster-related peaks remains similar over the temperature range again suggests that they are both related to a hafnium cluster species. As the temperature increases, the ^1H shifts of the cluster environments decrease, similar to the bulk water resonance [Figure 4.6 b)]: the most intense peak shifts from ~ 7.37 ppm at 278 K to ~ 7.07 ppm at 328 K, and the smaller peak shifts from ~ 7.78 ppm to ~ 7.42 ppm. The decrease in shift of the 'bulk' water peak is likely due in part to the reduction in strength of hydrogen-bonds as the temperature increases. With increased exchange, it might be expected that the two peaks would become closer together in chemical shift; however, in this case, that the amount of 'bulk' water is far greater than the amount of cluster would mean that, due to concentration weighting, any effect on the chemical shift would be much more pronounced for the cluster peaks.

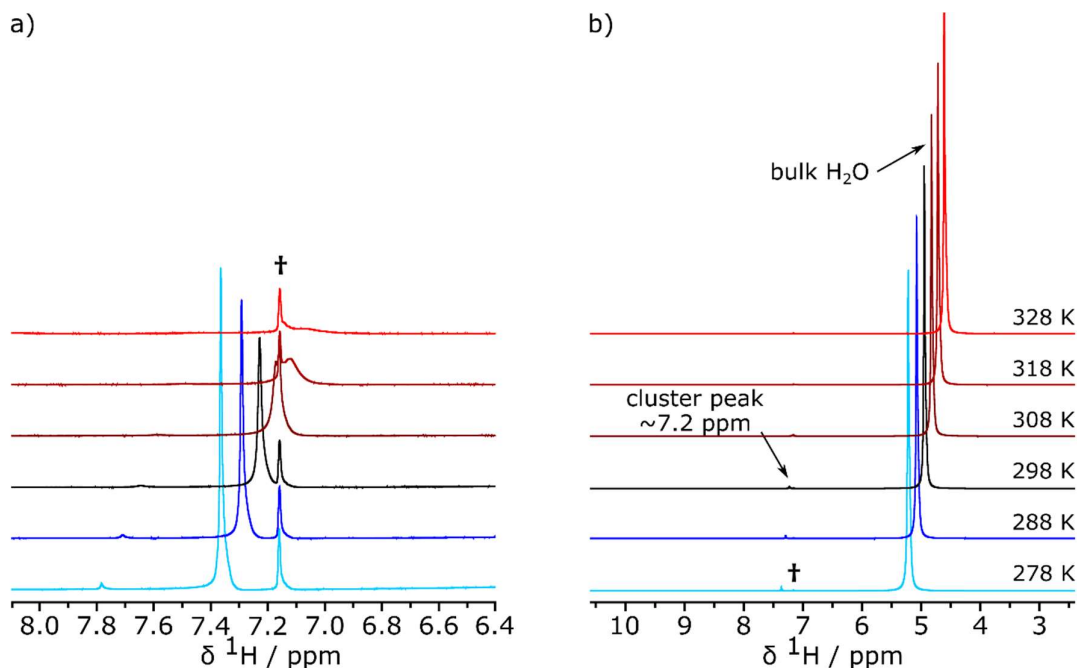


Figure 4.6. ^1H NMR spectra acquired at different temperatures of a solution of HfCl_4 in water, containing the tetramer. The dagger sign indicates the C_6D_6 reference signal at 7.16 ppm.

Åberg and Glaser²⁹² previously reported that the ^1H NMR spectrum at 270 K of the zirconium tetramer in water had a peak at ~ 7.9 ppm, which they assigned to the ‘inert’ terminal water molecules coordinated to the tetramer, accounting for two protons per metal centre. The integral and chemical shift of this peak were found to vary with both temperature and concentration of metal salt. The most intense of the two peaks seen in this work, recorded at 298 K, is at ~ 7.2 ppm referenced to C_6D_6 at 7.16 ppm [Figure 4.5 a)] but this ^1H environment is nevertheless likely to be the same as that observed by Åberg and Glaser, at ~ 7.9 ppm referenced to acetone at 2.04 ppm.²⁹² In this work, the experiment was performed at a temperature 8 K higher than in the literature example, and with a concentration 9.4 times lower, both of which help to explain the lower shift of the peak in this work as compared to the literature. Even at low temperatures, neither this work nor the literature report any signal from the $\mu_2\text{-OH}$ groups. Åberg and Glaser ascribe this to fast exchange in the system;²⁹² the measured lifetime of the large cluster-related peak in this work is indeed short. Unlike in this work, the literature report²⁹² did not observe a second cluster-related environment; although from XPDF analysis the solution contains only the tetramer, the low intensity of the second resonance seen in the ^1H NMR spectra suggests that the species responsible is of very low concentration (particularly if the resonance is due to a cluster environment with multiple equivalent protons, hence with a cluster species

concentration of $1/n_{\text{protons in environment}}$) and so is unlikely to cause significant changes to the XPDF pattern. This resonance is tentatively assigned to a small amount of monomeric solvated Hf(IV) species.²¹²

HfCl₄ in DFW 65:25:10 solvent, unheated

Having characterised the tetramer in aqueous solution, the room-temperature solution of HfCl₄ in DMF : formic acid : water ('DFW') solvent was then examined. In Chapter 3, a solution of HfCl₄ in DFW 65:25:10 (65 : 25 : 10 V/V) was found to contain a mixture of the tetramer and the Hf₆ single cluster. Since for the NMR studies in this Chapter a higher concentration of HfCl₄ in the same DFW 65:25:10 solution was used, predominantly in order to obtain good signal-to-noise ratios for the small cluster-related peaks, an *ex situ* XPDF experiment was performed in order to identify the clusters present.

In the previous Chapter a cluster model of a 52 : 48 mixture of the Hf₄ tetramer with water coordination shell ('tetramer·H₂O') and the Hf₆ single cluster gave a good fit when refined against an XPDF dataset of a lower concentration of HfCl₄ in the same DFW 65:25:10 solvent (molar ratio of 1 : 0.0043 DMF : HfCl₄). Using this cluster model in a refinement against the more concentrated solution in this experiment (molar ratio of 1 : 0.028 DMF : HfCl₄), a good fit was obtained with a ratio of 51 :49 tetramer·H₂O : single cluster [Figure 4.7], with a similar cluster ratio and R_w value to the fit obtained to in the previous, less concentrated sample.

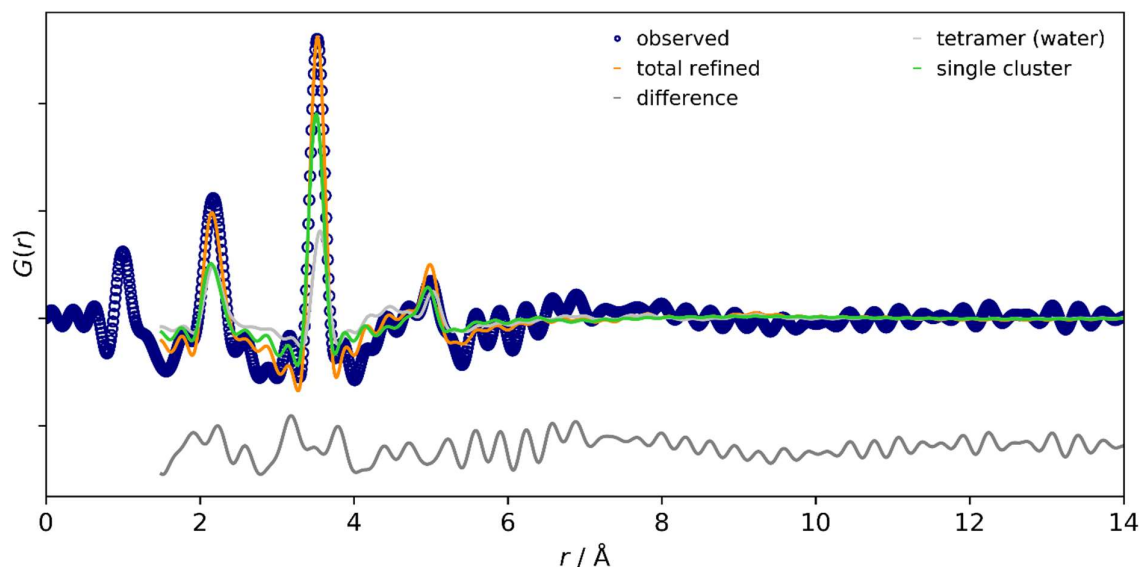


Figure 4.7. Refinement of a mixture of the tetramer·H₂O and the single cluster against an XPDF dataset of HfCl₄ in DFW 65:25:10 solvent ($R_w = 0.282$).

With the understanding that this solution contains a mixture of the single and double cluster, the ^1H NMR of the solution was then examined. In order to determine whether changing the concentration of hafnium has an effect, the ^1H NMR spectra were acquired as a function of concentration (noting that large changes in Hf concentration had little effect on the cluster ratio, as determined in the XPDF experiments).

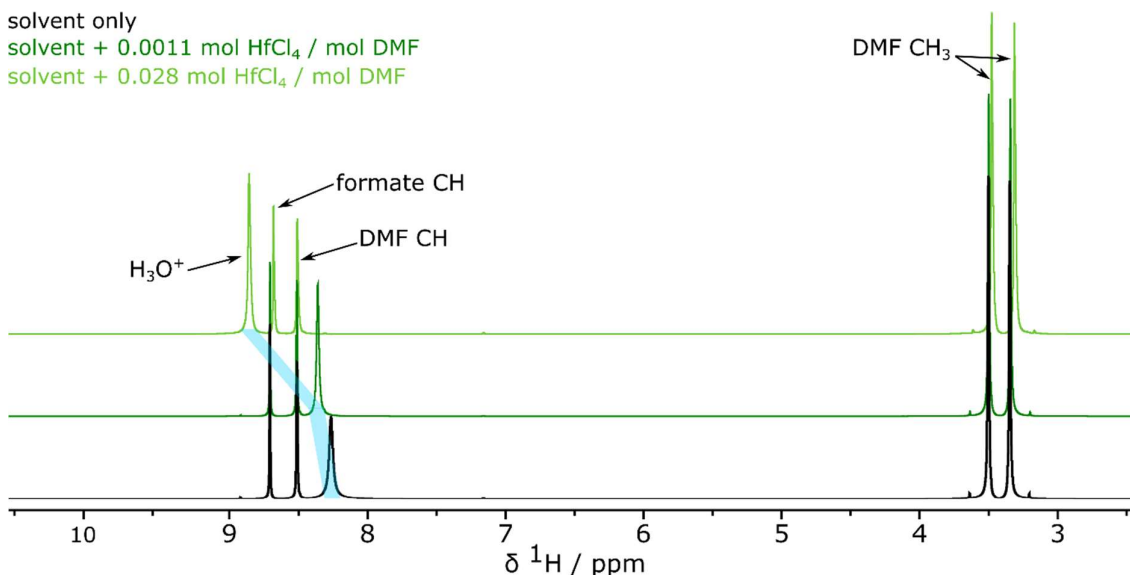


Figure 4.8. ^1H NMR of solutions of HfCl_4 in DFW 65:25:10 solvent. The change in the shift of the H_3O^+ peak is tracked by blue shading.

The ^1H NMR peaks from the bulk solvent are affected upon changing the concentration of HfCl_4 [Figure 4.8]. The DMF signals, as well as the formate CH signal, decrease shift to lower frequencies. The H_3O^+ signal becomes more intense as the amount of HfCl_4 increases as well as increasing substantially in shift even more than was observed in the aqueous HfCl_4 solution. This is likely due to the release of protons (and hence an increase in acidity) upon the formation of metal-oxo and metal-hydroxo groups in the clusters. Some water may also coordinate to the clusters or form a solvation shell around them,^{204,254,255} further increasing the weighted-average chemical shift. This structuring of water around the clusters could reduce the amount of water able to form hydrogen-bonds in the ‘bulk’ solvent, lowering the shifts of the other solvent molecules.²³⁰ The formate CH signal at ~ 8.7 ppm decreases in intensity as the concentration of Hf increases, suggesting a decrease in the amount of formic acid in solution—potentially due to the coordination of formate groups to cluster species [see Figure 4.1, Table 4.I]. Any binding of formate groups to clusters would also cause the release of protons and make the solution more acidic. A reduction of the amount of free

formic acid in solution would also reduce the amount of hydrogen-bonding possible with other solvent molecules and slightly reduce the chemical shifts.

Based on the concentration of HfCl_4 any cluster-related peaks are likely to be of low intensity relative to the solvent peaks. Several small peaks are indeed observed in the spectra of the HfCl_4 solutions at 6.6-6.7 ppm and ~ 7.6 ppm (which are not present in the Hf-free spectrum) [Figure 4.9]. These signals were present, albeit with subtly different chemical shift, with both concentrations of HfCl_4 . Henceforth the highest concentration of Hf (0.0279 : 1 molar ratio HfCl_4 : DMF) was used in all subsequent experiments in order to obtain the most signal from cluster-related environments.

The number of protons represented by the ~ 6.6 ppm peak in the solution with the highest concentration of Hf (35.9 : 1 molar ratio DMF : Hf, or 0.0279 : 1 molar ratio Hf : DMF) was determined by adding a known quantity of the NMR standard DSS (sodium trimethylsilylpropanesulfonate) to the solution. The ratio of the number of protons in this cluster environment to the total expected moles of Hf in the solution is 0.35 : 1, which is of the order of magnitude expected for cluster-related peaks but lower than the number of protons in these clusters.

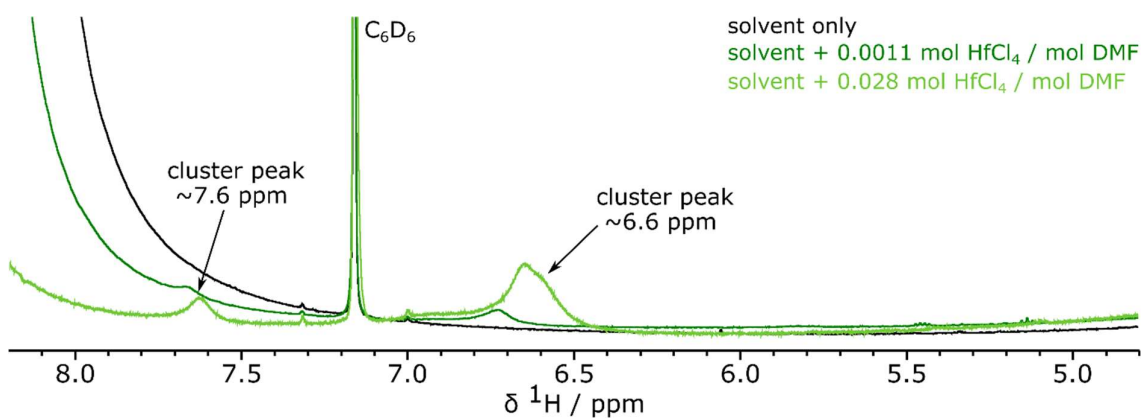


Figure 4.9. ^1H NMR of solutions of HfCl_4 in DFW 65:25:10 solvent, expanded view. The reference solvent is C_6D_6 with a singlet signal at 7.16 ppm.

In the ^1H NMR spectra of HfCl_4 in DFW 65:25:10 no peak is seen resembling the most intense peak observed in the spectrum of the tetramer in aqueous solution at ~ 7.2 ppm. This is in contrast with the refinement of the XPDF data where the tetramer was one of the species

present in the DFW 65:25:10 solvent; however, as the clusters are now in a different solvent, they are not guaranteed to have the same shift as in water.

Furthermore, unlike previous solid state NMR reports in which signals in the 0-3 ppm range were assigned to the μ_3 -OH environments of the single cluster in MOF frameworks,^{357,385} no cluster-type peaks were observed in the 0-3 ppm region. This could potentially be due to overlap with the more intense DMF CH₃ peaks but also to the chemical environment of the cluster protons being different in MOFs compared to the isolated clusters in the solvent system used in this work. Shifts observed in solid state NMR may also not be directly comparable to those in solution NMR due to differences in chemical shift referencing and the potential for interaction with the solvent, including hydrogen-bonding between water in the solvent and the μ_3 -OH;³⁴² these sites are also likely to be undergoing rapid exchange with the bulk water and so not detected.

While relaxation times are caused by multiple phenomena, short T_1 relaxation times are often an indication of motion,³³³ and here are a measure of the lifetimes of the different environments and of the exchange processes. The T_1 values of the DMF environments are all 1.7-2.2 s, and the formate CH has a T_1 of 2.73 s, whereas the H₃O⁺ environment and ~6.6 ppm cluster environments have shorter lifetimes at 860 ms and 1.10 s respectively. While further work is required to analyse the relaxation times as a function of temperature, this suggests that the cluster environments are undergoing dynamic exchange, which could help explain why the cluster-related peaks are less intense than expected.

In order to further understand the cluster environments present in this unheated mixed-cluster sample, two-dimensional nuclear Overhauser effect³⁹⁴ spectroscopy, or NOESY, experiments were performed. In this type of experiment any cross-peaks in the resulting two-dimensional spectrum indicate a correlation between the two environments involved:³⁹⁵⁻³⁹⁷ positive peaks indicate either chemical exchange between the environments or negative NOEs (in the case of large molecules which tumble slowly), while negative peaks are due to positive NOEs (the case for small molecules which tumble rapidly).^{395,398} Thus different environments engaging in chemical exchange, or which are in close proximity, can be identified through this experiment.

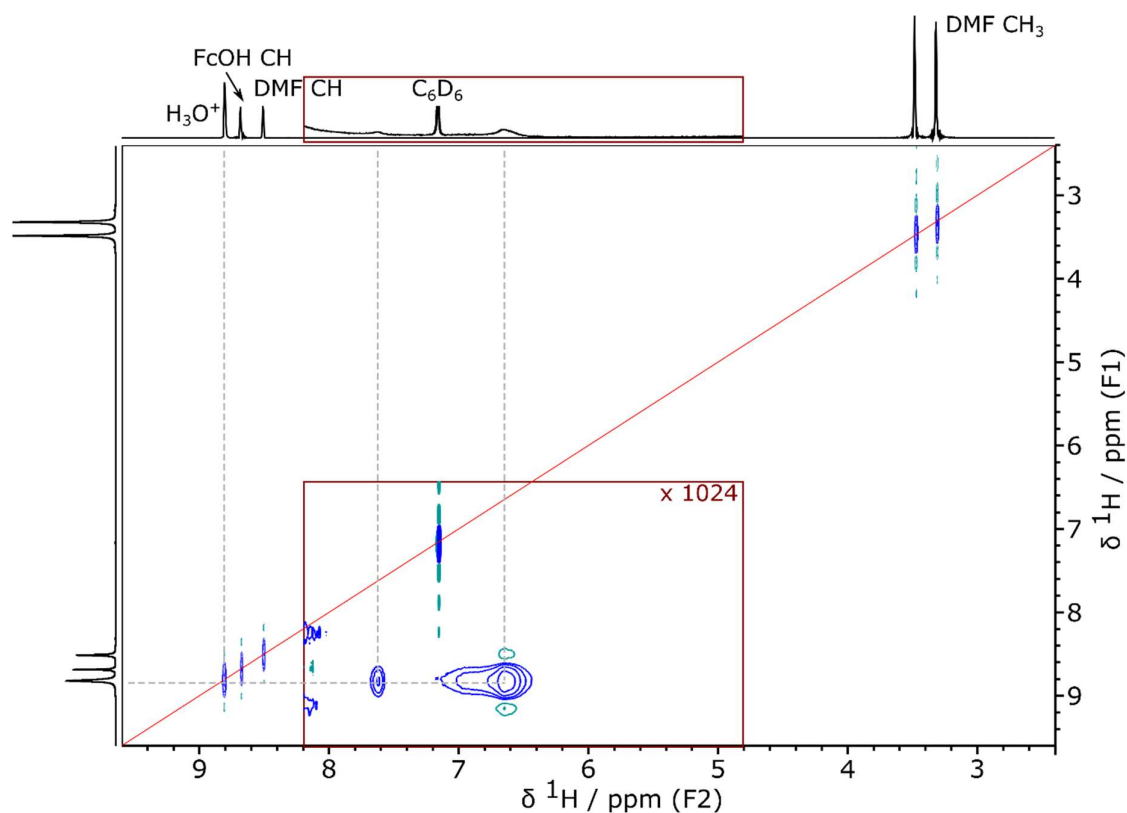


Figure 4.10. Two-dimensional ^1H - ^1H NOESY spectrum of HfCl_4 in DFW 65:25:10 solvent at room temperature, at time $t=0$ after synthesis. The indirect dimension spectrum is given as an external projection from a one-pulse ^1H experiment. The sections in the dark red boxes are scaled up to show the small cross peaks due to cluster-related environments. The diagonal is indicated with a bright red line. Positive contours are shown in blue, negative in green. Guide lines are given, dashed and in grey.

A ^1H - ^1H NOESY spectrum of the solution of HfCl_4 in DFW 65:25:10 [Figure 4.10] does not show any clear cross-peaks between the solvent environments; these could potentially be hidden by t_1 noise (this t_1 noise is caused by T_1 relaxation during the mixing time, so that coherence is lost between the direct and indirect dimensions—the species that relaxes quickly relative to the NMR mixing time is essentially connected with all frequencies in the indirect dimension when it is re-excited after the mixing time has elapsed). For the environments related to the clusters the NOESY spectrum has cross-peaks only between the H_3O^+ environment at 8.82 ppm and the cluster-related peaks. Cluster peaks are not seen on the diagonal, again consistent with fast relaxation; cross-peaks are not visible in the indirect dimension, potentially either being obscured due to t_1 noise or due to the low concentration of the cluster environments relative to H_3O^+ . The cross-peaks between the cluster and H_3O^+ peaks in the direct dimension cross-peaks are positive, likely indicating chemical exchange (the single cluster and tetramer are not large so negative NOE as an explanation for the

positive phase is less likely) and suggesting that the cluster surfaces are terminated by some water/hydroxide ligands; the tetramer is very likely to have water as ligands.

A 1-dimensional selective NOESY experiment, irradiating on the H_3O^+ peak at 8.82 ppm to investigate correlation to this environment and inverting this peak, gives negative peaks for the cluster (i.e., the same phase as the H_3O^+ peak) [Figure 4.11]. In comparison, a 1-dimensional selective rotating frame Overhauser effect spectroscopy (ROESY) experiment, again irradiating on the H_3O^+ peak, gave extremely weak negative peaks for the cluster [Figure 4.11]. ROESY produces correlations in a similar way to NOESY except only chemical exchange peaks have the same phase as the irradiated peak; thus, the combination of these selective 1D experiments allows confirmation that these cross-peaks are due to chemical exchange, rather than from an NOE and thus through-space proximity. This suggests that water/hydroxide groups on the clusters may be exchanging with other waters on the cluster and a surrounding coordination shell of water (rather than a first coordination shell comprising formic acid).²⁵⁴

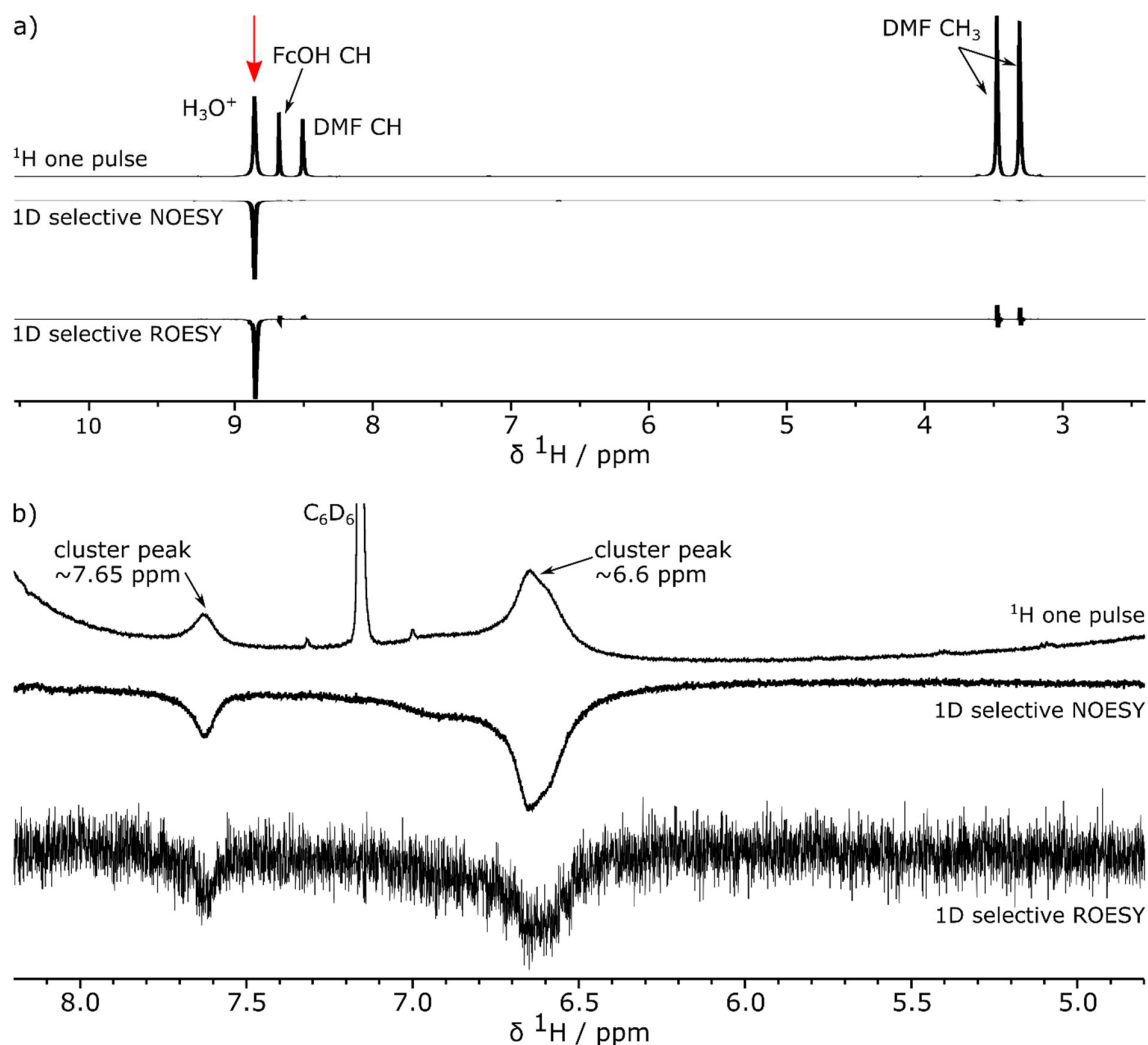


Figure 4.11. ^1H NMR, 1-dimensional selective NOESY and 1-dimensional selective ROESY: a) expanded view of the cluster environments; b) full spectra. For the selective NOESY and ROESY, the sample was irradiated on the H_3O^+ peak at 8.85 ppm (indicated by a red arrow), and the irradiated peak inverted (i.e., phased to be negative).

The cluster peak at ~ 6.6 ppm is broad and asymmetric. In ^1H NMR spectra acquired at lower temperatures [Figure 4.12 b)], three separate environments were observed in the region of this peak, at 6.59, 6.71 and 6.93 ppm, likely owing to slower exchange on the NMR timescale. The peak at 7.65 ppm broadened but did not split further on lowering the temperature. While the ‘cluster’ peaks are relatively unchanged in shift, the peaks due to the ‘bulk’ solvent increase in shift—in particular, the H_3O^+ peak shifts significantly to higher frequency—as the temperature decreases, likely due to increased hydrogen-bonding as a result of less thermal motion [Figure 4.12 a)].

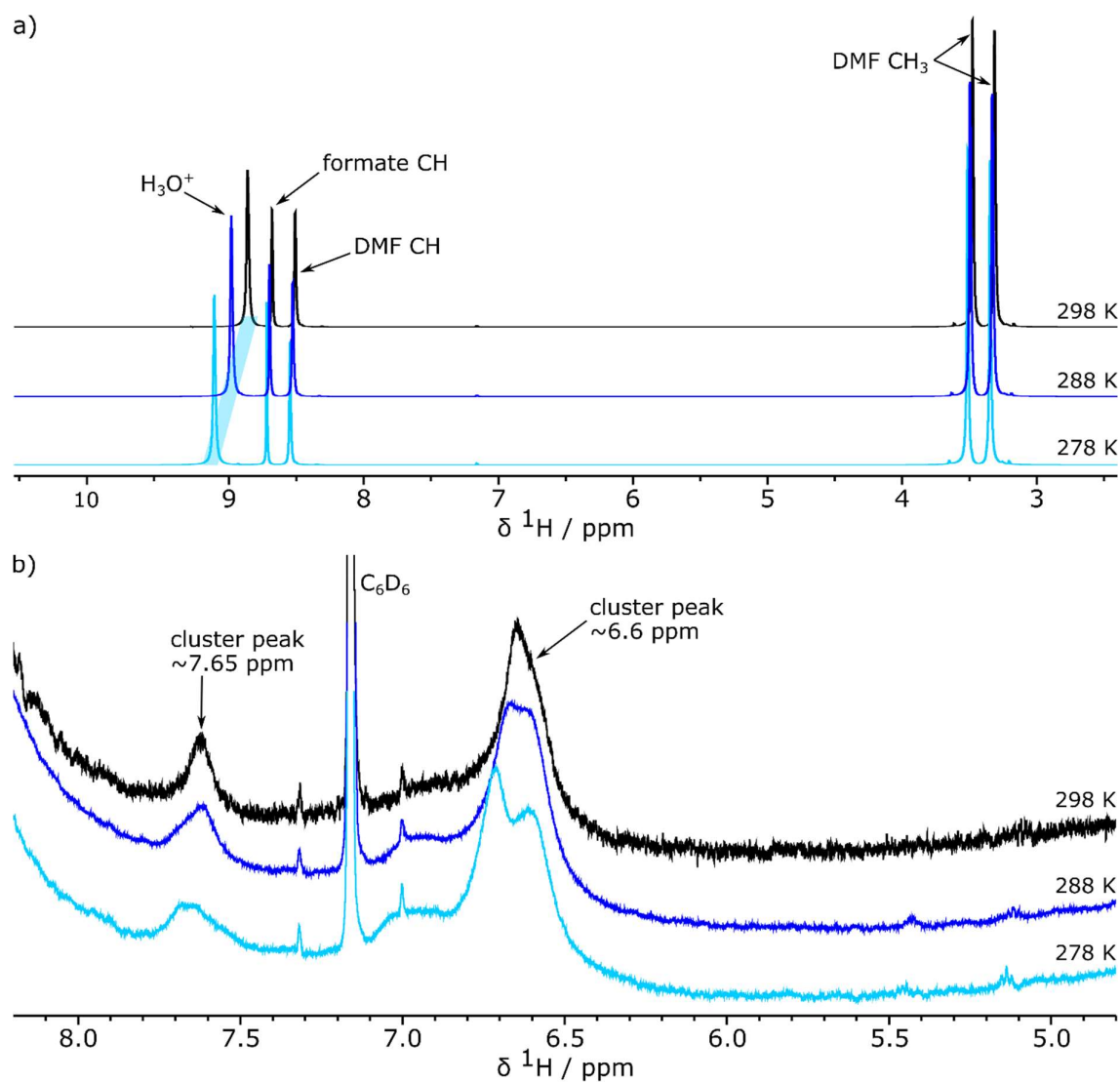


Figure 4.12. Variable-temperature ^1H NMR of HfCl_4 in DFW 65:25:10 solution, a) full spectrum, b) expanded view to show the cluster peaks. The change in shift of the H_3O^+ peaks is tracked with blue shading.

A two-dimensional ^1H - ^1H NOESY experiment was then acquired at 278 K to explore the correlations between the different environments distinguishable at this temperature. [Figure 4.13]. Positive cross-peaks are visible at 6-8 ppm between the H_3O^+ environment and all four of the separate cluster environments identified in the one-dimensional spectra. # At this low temperature some positive cross-peaks were also observed between the formate CH

The four cluster peaks are also visible *via* selective one-dimensional NOESY experiments irradiating on the H_3O^+ . The two peaks with correlation to the formate CH on the two-dimensional NOESY are also just visible in a selective one-dimensional NOESY experiment irradiating on the formate peak. The signal-to-noise is too high to permit observation of weaker peaks. See the Appendix for spectra.

environment and the two most intense cluster peaks (at 6.59 and 6.71 ppm). This suggests that, as well as water/hydroxide, some formate groups are likely to be ligands on the clusters present, although overall perhaps fewer, or less strongly bound, than hydroxide/water.

The tetramer is usually modelled with water/hydroxide coordinating groups only, while the single cluster may have a combination of formate and water/hydroxide. Depending on symmetry and combination of ligands, the single cluster could have many different ligand proton environments; fast exchange between coordinated groups and with the solvent would reduce the observed number. The number and correlation of cross-peaks observed in these spectra are therefore plausible for a mixture of tetramer and single cluster species with dynamic exchange occurring between ligand species on the cluster surface and the solvent, moreso at higher temperatures.

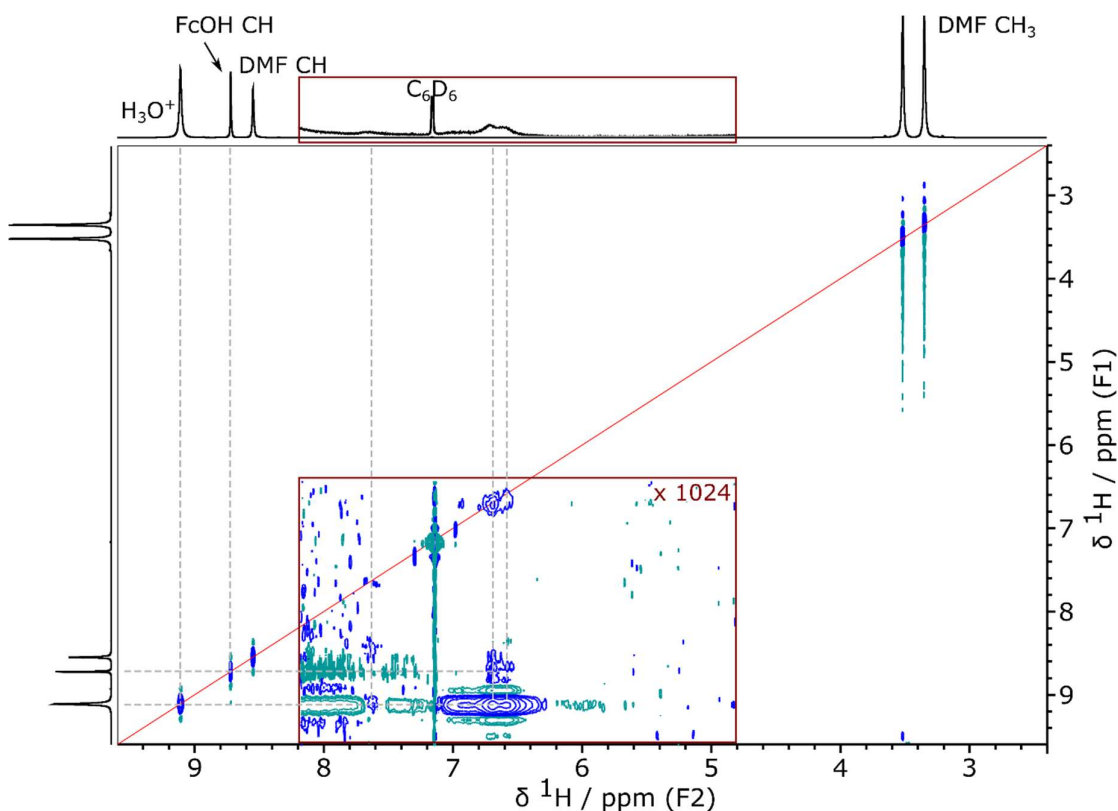
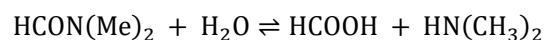


Figure 4.13. Two-dimensional ^1H - ^1H NOESY spectrum of HfCl_4 in DFW 65:25:10 solvent cooled to 278K. The indirect dimension spectrum is given as an external projection from a one-pulse ^1H experiment. The sections in the dark red boxes are scaled up to show the small cross peaks due to cluster-related environments. The diagonal is indicated with a bright red line. Positive contours are shown in blue, negative in green. Guide lines are given, dashed and in grey.

The appearance of multiple cluster-related ^1H peaks in these spectra of HfCl_4 in DFW 65:25:10, particularly visible in the spectra recorded at 278 K, supports the evidence of the

XPDF refinement that there is more than one cluster species present. However, these could not be assigned separately to the single cluster or tetramer. From the XPDF analysis in Chapter 3, upon heating a sample of HfCl₄ in DFW 65:25:10 any tetramer present disappears prior to the formation of the double cluster. An *in situ* experiment was therefore performed in order to investigate the effects of heating this solution, although not to temperatures expected to produce the double cluster. In this experiment a solution of HfCl₄ in DFW 65:25:10 was heated in stages in the spectrometer, acquiring a ¹H NMR spectrum every 10 K up to 358 K followed by an additional spectrum once returned to room temperature [Figure 4.14] (heating was not attempted above 358 K due to the risk of pressure buildup in the NMR tube).

The changes in shift of the DMF peaks and formate CH peak as the temperature increases are in keeping with those observed in the low-temperature spectra [see Figure 4.12]. As the temperature increases, especially above 338 K, new peaks are also visible at ~8.9 ppm (broad) and 3.1-3.2 ppm. These are indicative of dimethylammonium (DMAH), H₂N(CH₃)₂⁺, which is produced upon the hydrolysis of DMF:



The peak at 3.1-3.2 ppm is assigned to the CH₃ groups and that at ~8.9 ppm is assigned to the NH protons.²⁴⁵ Comparing the integrals suggests that by 358 K, the highest temperature, around 10% of the DMF has been hydrolysed. This is despite the presence of formic acid already in the solution, which opposes the hydrolysis reaction. The intensity of the formic acid peak increases slightly over the course of the reaction since it is produced in the DMF hydrolysis. Formic acid can also decompose at higher temperatures (see Chapter 1);²⁴⁶ however, that the peak increases suggests that over this temperature range any loss of formic acid due to decomposition is low.

The H₃O⁺ peak decreases shift the most during heating, especially after 338 K. Its relative integral also decreases throughout the heating, reaching around 87% of the pre-heating integral, suggesting that the decrease in shift is not due to a change in the weighted-average of water and formic acid COOH, (or else the shift of the H₃O⁺ peak would increase with the decrease in water concentration). This suggests that the decrease in shift is instead due to a reduction in hydrogen-bonding.

Upon returning to room temperature the chemical shifts of the DMF and formic acid protons return to approximately their original values, suggesting that the hydrogen-bonding in the system is restored to its original strength. Between the 358 K and cooled solutions, the integral of the formic acid peak increases from 110% of the original to 160%.

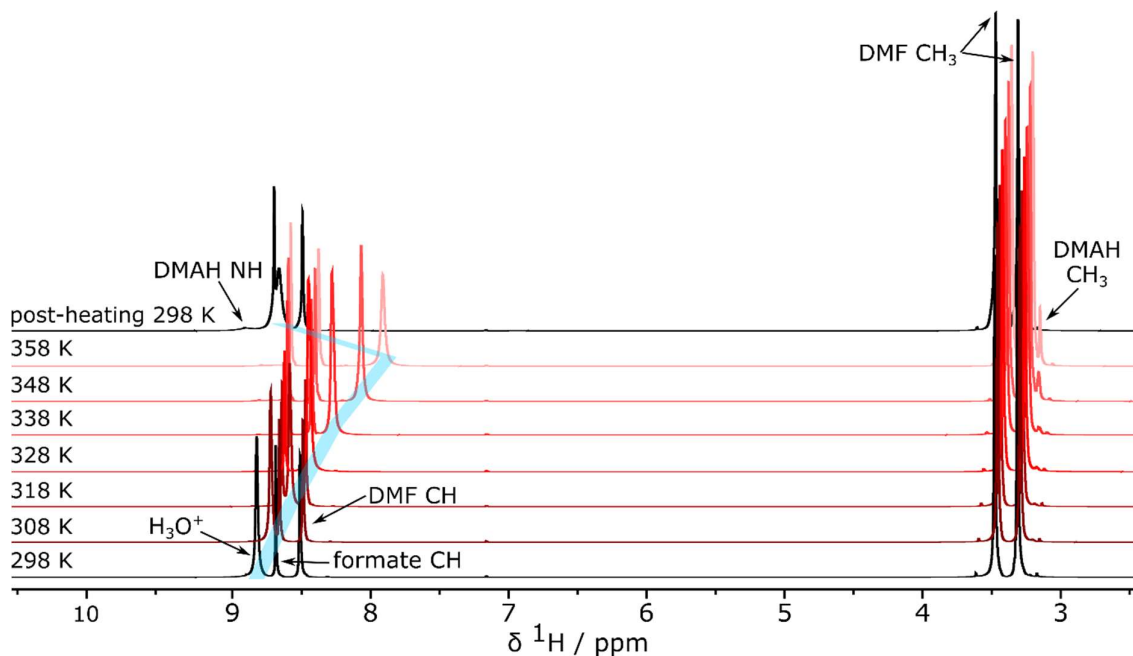


Figure 4.14. ^1H NMR spectra of HfCl_4 in DFW 65:25:10, taken as the temperature is increased in steps of 10 K. The change in shift of the H_3O^+ peaks is tracked with blue shading.

Unlike with the other environments the H_3O^+ peak does not return fully to its original shift after cooling and its relative integral is only about 60% that of the original (although the peak is almost twice as broad as the original room temperature peak). No further hydrolysis appears to occur on cooling which strongly suggests that during the cooling process water is lost from the 'bulk' solvent and formic acid is released—potentially from coordination around metal clusters. Dimethylammonium remains in the solution after cooling.

Similar to the bulk solvent environments, the cluster-related peaks also initially decrease in shift as the temperature increases; they also broaden, suggesting faster exchange is occurring [Figure 4.15]. However, after 338 K, the peak at 7.65 ppm disappears entirely, suggesting a chemical change has occurred; furthermore, the broad multi-peak signal originally at 6.6 ppm broadens substantially before seeming to disappear, and a new peak at 6.8-6.9 ppm appears. These changes are retained even after cooling; the new peak, found at 6.93 ppm after cooling, is not asymmetric (unlike the peak at 6.6 ppm before heating). This suggests

that whatever chemical change has occurred is retained after cooling, and that some cluster environments are lost during heating.

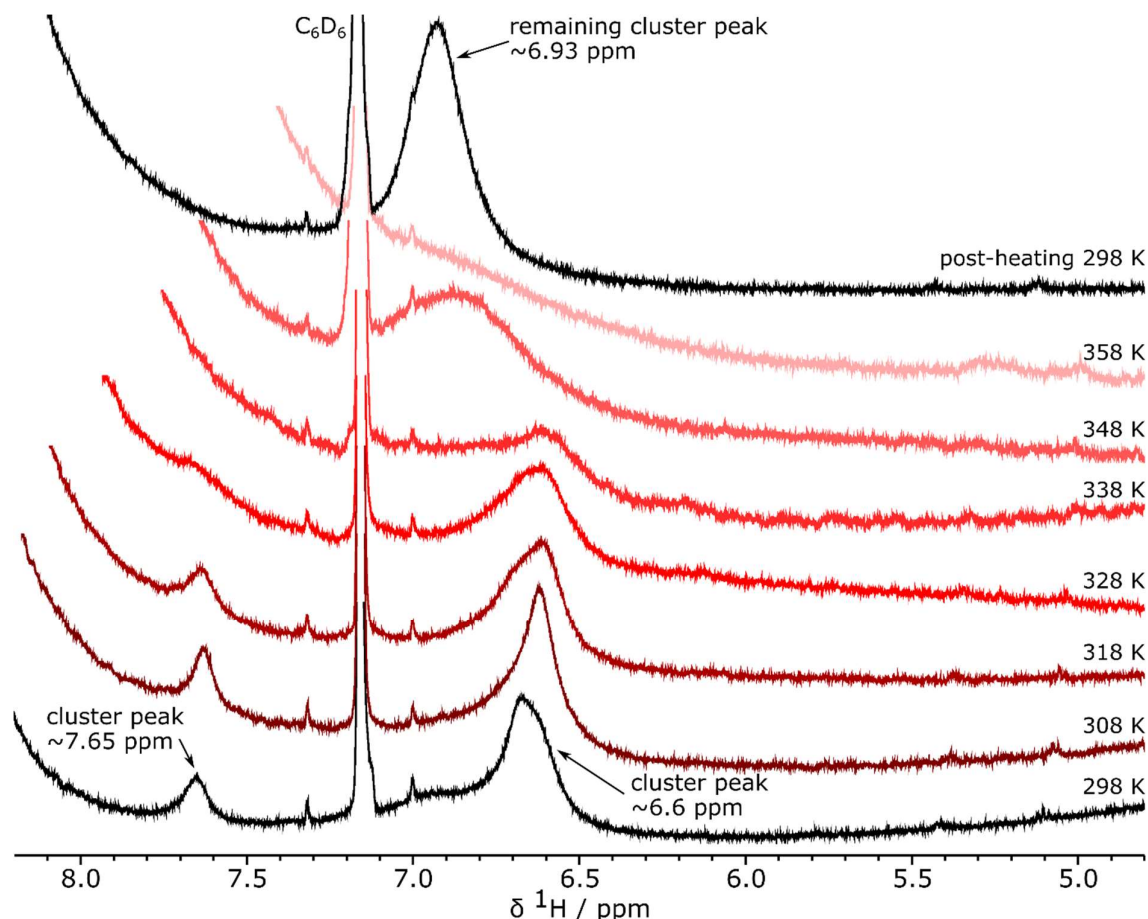


Figure 4.15. ^1H NMR spectra of HfCl_4 in DFW 65:25:10, taken as the temperature is increased in steps of 10 K, expanded to show the region where cluster-related peaks are found.

At room temperature the DFW 65:25:10 solution contains both the tetramer and the single cluster (by XPDF refinement). However, the *in situ* XPDF work in Chapter 3 indicated that the tetramer is disfavoured by higher temperatures whereas the single cluster remains present. Combined with this knowledge, therefore, the *in situ* heating experiment suggests that the environment which remains after heating, at 6.93 ppm, is related to the single cluster. This further suggests that some part of the environments within the ~ 6.7 ppm peak is related to the tetramer species. The nature of the peak at 7.65 ppm, which did not have any correlation to formate in the low-temperature two-dimensional NOESY experiment [Figure 4.13], is more difficult to understand.

Repeating the heating experiment, but remaining at 358 K for a shorter time, upon cooling to room temperature the cluster environment at ~ 6.93 ppm is clearly visible but the peaks at

~6.6 ppm and ~7.65 ppm are also still present in the ^1H NMR spectrum [Figure 4.16]. This agrees with the assessment that the changes observed upon heating are caused by changes in intensity of the different cluster environments, rather than just a movement of the existing cluster environments to higher chemical shift. This again implies that during heating the amount of single cluster increases and the amount of tetramer decreases.

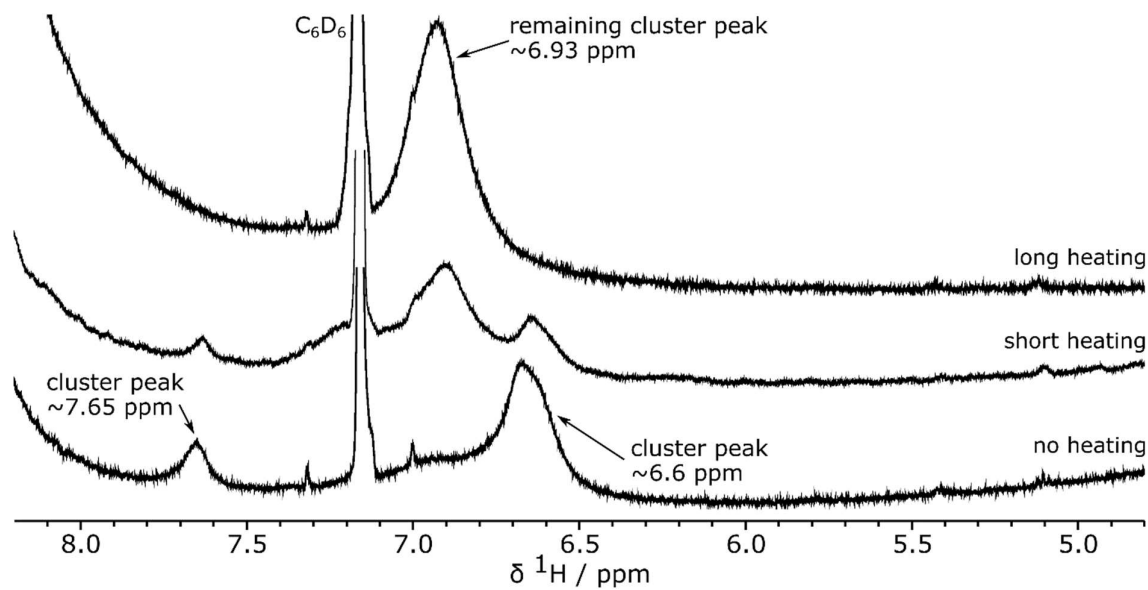


Figure 4.16. ^1H NMR spectra of HfCl_4 in DFW 65:25:10 after different heating periods, expanded to show the region where cluster-related peaks are found.

No changes which might be expected upon the formation of the double cluster are observed in either heating experiment. More, and different shift, peaks could result from the double cluster due to its different symmetry compared to the other clusters [Table 4.I]. This is not surprising as the double cluster requires temperatures higher than 358 K/85°C to form;^{251,255} MOF reactions at temperatures below 120°C still retain the single cluster.¹⁴

Two-dimensional NOESY NMR of the cluster environment region at selected temperatures during the heating process [Figure 4.17] indicates that, as the temperature increases, the correlation between the H_3O^+ peak and the cluster peak originally at ~6.6 ppm remains. The change in the shape of this environment, suggesting the growth of the peak at ~6.93 ppm assigned to the single cluster, is clearly visible in the contours at 338 K. At low temperature, some of the peaks at ~6.6-6.7 ppm showed a correlation to the formate CH peak [see Figure 4.13]. However, in these higher-temperature spectra there is no sign of correlation to the formate CH peak. The initial presence of these correlations suggests that some of the

environments ~6.6-6.7 ppm were related to the single cluster species; however, that these environments are no longer present after heating suggests that the nature of coordination to the single cluster species changes at higher temperatures.

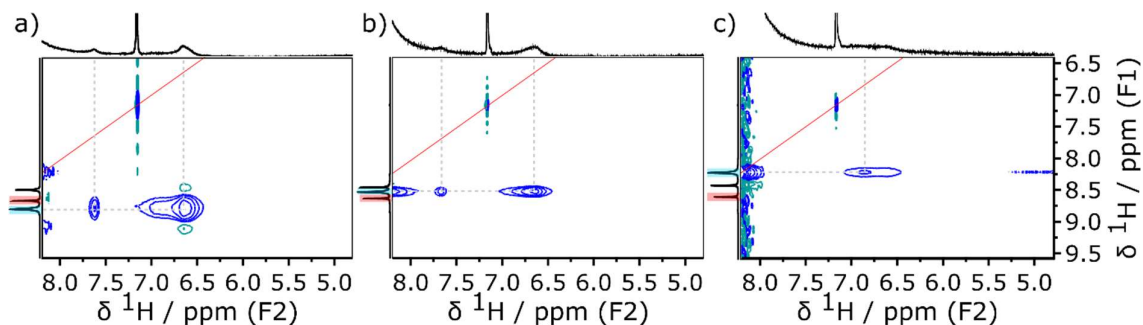


Figure 4.17. ^1H - ^1H NOESY spectra of HfCl_4 in DFW 65:25:10, cropped and expanded to show the cluster peaks, at a) 298 K, b) 318 K, c) 338 K. The H_3O^+ environment and the formate CH environment in the indirect projections (external projections from one-pulse ^1H experiments) are shaded in blue and red respectively. Positive contours are shown in blue, negative in green. The indirect dimension spectrum is given as an external projection from a one-pulse ^1H experiment. The sections in the dark red boxes are scaled up to show the small cross peaks due to cluster-related environments. The diagonal is indicated with a bright red line. Positive contours are shown in blue, negative in green. Guide lines are given, dashed and in grey.

This investigation, together with the XPDF refinement of the sample of HfCl_4 in DFW 65:25:10, suggests that at room temperature both the single cluster and the tetramer are present. On heating for some time above 338 K, while the double cluster does not form, the tetramer is lost and the amount of single cluster increases. This change does not revert upon cooling and therefore allows the cluster environments observed in the ^1H spectrum to be attributed separately to the tetramer and the single cluster.

4.2.3 Reactions at 150°C

Having investigated the solution in DFW 65:35:10 at room temperature, conditions known to create a mixture of the tetramer and single cluster, the logical next step was to examine solutions based on the reaction conditions in which the $\{[\text{Hf}_6\text{O}_4(\text{OH})_4]_2(\text{OH})_6\}^{18+}$ 'double' cluster forms. The *in situ* XPDF work in Chapter 3 indicated that a solution of HfCl_4 in DFW 65:25:10 heated to 150°C for 24h would in all likelihood contain this double cluster.²⁵⁵ As above, before analysing the cluster-containing solution, the metal-free solvent was first investigated to determine any changes in the solvent alone due to this heating process.

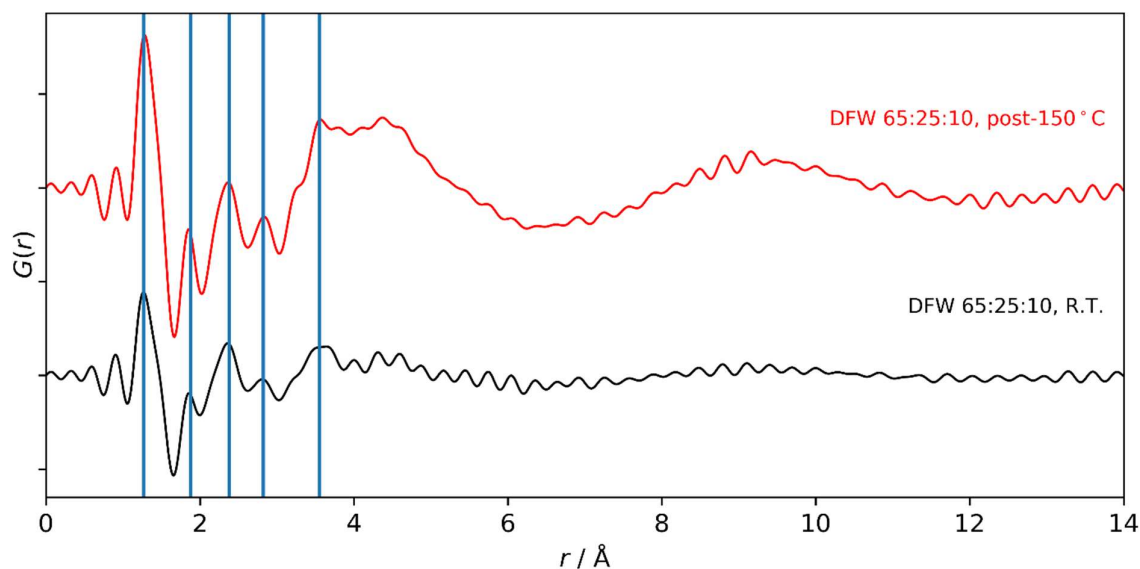


Figure 4.18. Plot of the X-ray pair distribution functions of HfCl_4 -free DFW 65:25:10 solvent at room temperature, both without heating and post-heating at 150°C . Vertical lines show the position of peaks at 1.26, 1.88, 2.38, 2.82 and 3.55 Å.

The XPDF patterns of the solvent both pre- and post- heating display some similarities, especially at low r values [Figure 4.18. Both samples show peaks at 1.26 Å (albeit with subtly different peak shapes) likely due to the C=O, carboxylate C-O, and amide C-N bonds from DMF and formic acid. Peaks at 1.88 and 2.82 Å are potentially from intramolecular hydrogen-bonding; in DMF solutions, including with water, hydrogen-bonding often results in H---Y (where Y is the hydrogen-bond acceptor atom) distances of around 1.9 Å and X-H---Y distances of around 2.9 and 3.6 Å,^{227,230} with further weak intermolecular interactions giving rise to peaks at ~5.5 Å.²²⁸ While there are no clear peaks in the XPDF towards higher r values there are still differences between the samples: the post-heated sample shows a significant baseline modulation particularly around 4.5 and 9 Å, suggesting significant intermolecular structuring of the solvent.²⁷³

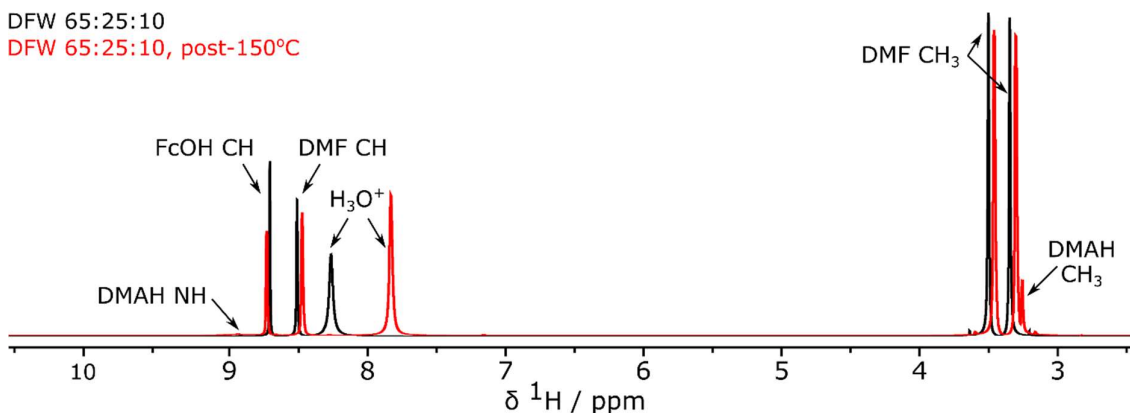


Figure 4.19. ^1H NMR of DFW 65:25:10 solvent at room temperature, both as-mixed, and after being heated at 150°C for 24 hours.

The ^1H NMR spectrum also shows clear changes between the heated and unheated solvents [Figure 4.19]. Upon heating hydrolysis has occurred, as evidenced by the presence of extra peaks from dimethylammonium; from the integral ratios it appears that around 5% of the DMF has been hydrolysed. Although an increase in the amount of formic acid would be expected as a result of this hydrolysis, the formate CH peak has decreased by about 25% suggesting that formic acid decomposition has also occurred.^{246,248} The DMF peaks in the spectrum have a lower shift suggesting weaker hydrogen-bonding, potentially due to the loss of water in the hydrolysis, and the H_3O^+ peak has the greatest decrease in shift as would be expected in a system where there is less hydrogen-bonding.

HfCl₄ in DFW 65:25:10 solvent, reacted at 150°C

The result of heating the Hf-containing DFW 65:25:10 solvent was then investigated. The previous investigation of heating a solution of HfCl_4 in DFW 65:25:10 to 358 K (85°C) suggested that this temperature causes the cluster composition to change from a mixture of the tetramer and single cluster to predominantly the single cluster [Figure 4.15], but not the $\{[\text{Hf}_6\text{O}_4(\text{OH})_4]_2(\text{OH})_6\}^{18+}$ double cluster; the double cluster was however observed in the *in situ* XPDF experiments in Chapter 3 upon heating to 150°C. A sample of HfCl_4 in DFW 65:25:10 solvent was therefore heated at 150°C for 24 hours in order to encourage the formation of the double cluster. A room-temperature XPDF dataset of this sample gave a good fit with the Hf_{12} double cluster model [Figure 4.20] in keeping with the similar results from the previous *in situ* work described in Chapter 3.²⁵⁵

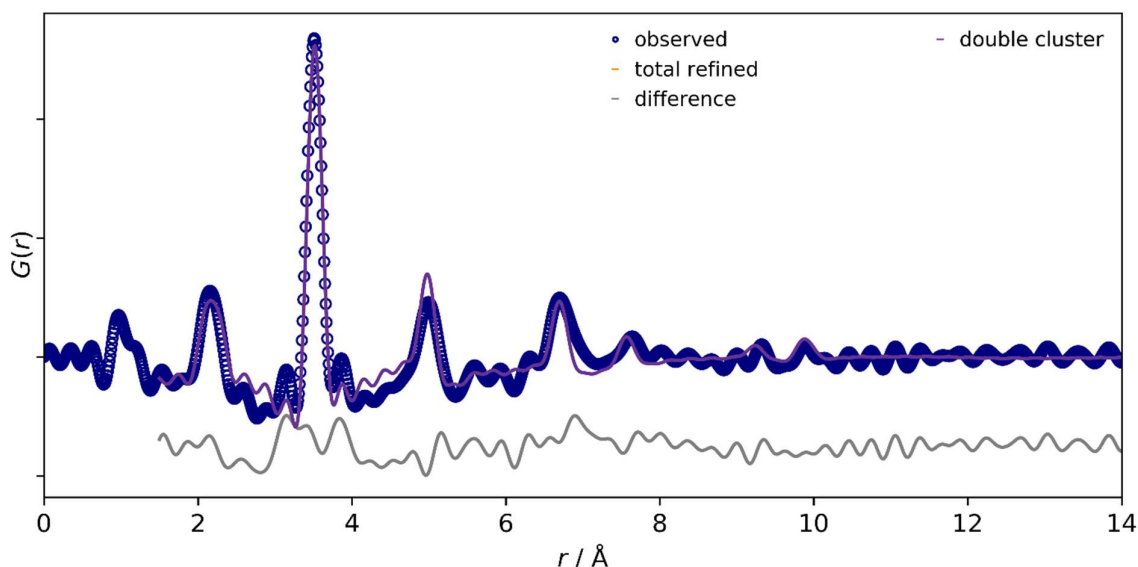


Figure 4.20. Refinement of the double cluster model against an XPDF dataset of HfCl_4 in DFW 65:25:10 solvent, following heating at 150°C for 24 hours ($R_w = 0.268$).

The ^1H NMR spectrum of this solution containing the double cluster shows evidence of DMF hydrolysis with the appearance of the dimethylammonium signals [Figure 4.21]; the relative integrals suggest that around 14% of the DMF was hydrolysed, approximately three times more than in the Hf-free solvent [Figure 4.19]. Zirconium (IV) has previously been implicated in accelerating the decomposition of DMF,³⁹⁹ and it is not unrealistic that the hafnium (IV) complexes in these solutions might have a similar effect. Again, the formate CH peak is decreased by about 25% compared to the solvent-only case, although in the Hf-containing solution this could potentially be explained both by the aforementioned formic acid decomposition reaction and by coordination of formate to the Hf_{12} double cluster, both processes removing formate from the ‘bulk’ solvent.

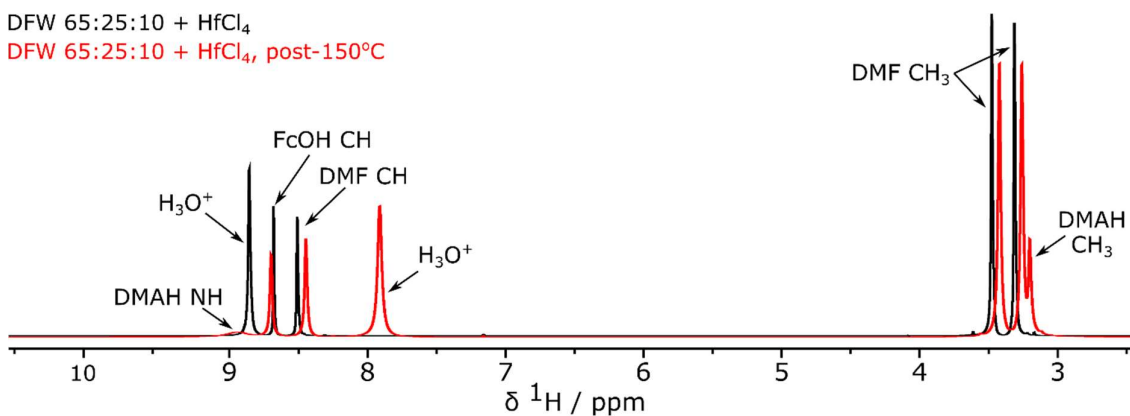


Figure 4.21. ^1H NMR comparison of HfCl_4 in DFW 65:25:10 solvent, after heating to 150°C , with the unheated sample.

The shifts of the DMF peaks in the Hf-containing solution are decreased more after heating than are the shifts of the DMF peaks in the Hf-free heated solution [Figure 4.21], suggesting that—just as in the unheated Hf-containing solution—the hydrogen-bonding in the solvent has decreased upon addition of the metal salt and cluster formation. The relative integral of the H_3O^+ peak is similar to that found in the unheated solution of HfCl_4 in DFW 65:25:10, and is midway between that found in the unheated Hf-free solvent and that in the heated Hf-free solvent, suggesting that less water was lost from solution than expected given the consumption of water in DMF hydrolysis. This H_3O^+ peak also has a lower shift than for the Hf-free heated solvent and significantly lower than for the unheated Hf-containing solution, suggesting that the extra intensity of this peak is not due to the release of additional protons into solution (which would increase the shift due to acidity).

Clues to the extra water apparently present after the reaction can be found in the formation route of the double cluster suggested in Chapter 3 based on the *in situ* XPDF data.²⁵⁵ Water is likely to be released upon loss of the tetramer in the early stages of heating. The single cluster is likely to have predominantly water and hydroxide groups as surface-terminating coordinating groups; in order to form the ‘belt’ of six μ_2 -OH groups which joins the two single clusters into a double cluster, six water molecules must be released. Some of the potential coordination shell of water around the clusters would be released upon the condensation of the double cluster from two single clusters. This could partially counteract the loss of water via DMF hydrolysis and result in the observed decreased H_3O^+ chemical shift relative to the Hf-free solvent.

With the knowledge that the sample heated to 150°C contains the double cluster, the region of the ^1H spectrum known to contain cluster-related peaks was explored. There is a distinct difference in this region of the spectrum compared to the cluster peaks seen in the unheated sample previously, as well as to the cluster peak observed after heating to 85°C [Figure 4.22]: this solution in which the double cluster is found displays many new distinct peaks in the region 5-7.5 Å. The presence of additional peaks is as expected given that, based on its size and symmetry, the double cluster has more possible ligand/cluster-structure environments than either the tetramer or the single cluster [Table 4.I].

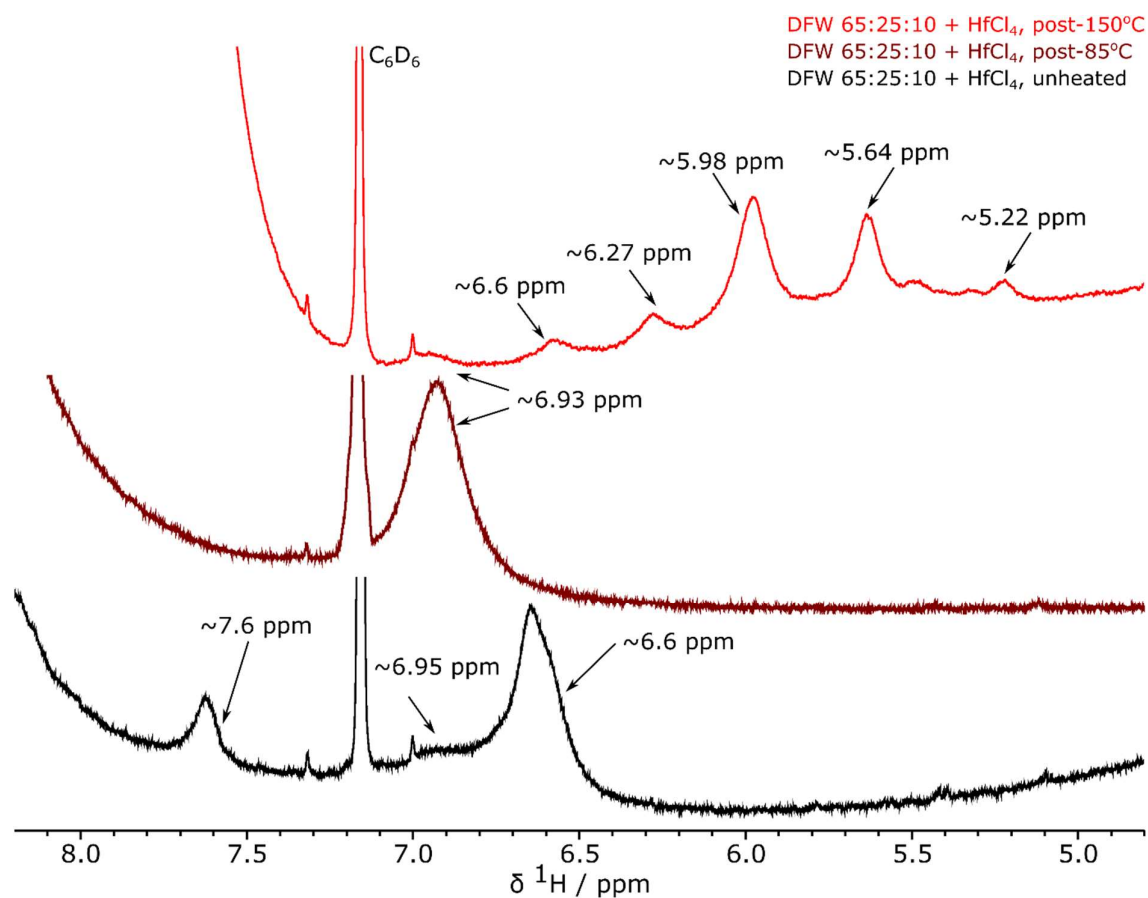


Figure 4.22. ^1H NMR comparison of HfCl_4 in DFW 65:25:10 solvent, after heating to 150°C , with the unheated sample. The spectrum is expanded, focussing on the region containing cluster-related peaks. The peak at 7.16 ppm is the C_6D_6 reference.

Some of the peaks in the spectrum of the double cluster solution, however, are similar to those observed in the spectra of the smaller clusters. There is a peak at ~ 6.93 ppm, the same shift as that assigned to the single cluster, which might be expected given that the double cluster comprises two single clusters joined together. There is also a peak at ~ 6.6 ppm, which is seen in the spectrum of the unheated sample containing the single cluster and the tetramer but not in the post-heating single cluster spectrum. Since upon heating the tetramer is expected to be lost, and that some of the environments in the region at ~ 6.6 ppm are assigned to environments on the unheated single clusters, the presence of this peak in the spectrum of the double cluster does not necessarily indicate that the tetramer is present. Instead, this could suggest that the ligands on the double cluster are arranged more similarly to those on the unheated single cluster than those on the single cluster after

heating. In these dynamic systems (especially at elevated temperatures) ligand rearrangement occurring is not surprising.

NOE experiments were used to understand these proton environments further. For the bulk solution, correlations are seen between the solvent molecules, including likely exchange between the H_3O^+ and the dimethylammonium NH environments, as well as interactions between H_3O^+ and the DMF CH_3 groups potentially indicating proximity due to hydrogen-bonding (this may have been obscured in the unheated solution by t_1 noise).

Multiple positive cross peaks are visible in the two-dimensional ^1H - ^1H NOESY spectrum [Figure 4.22] in the cluster-related region, both between the cluster peaks and H_3O^+ and between some cluster peaks and the formate CH peak. Cluster-related cross-peaks are not visible in the indirect dimension, potentially due to being obscured by t_1 noise. However, there are cluster peaks visible on the diagonal. Compared with the unheated sample of HfCl_4 in DFW 65:25:10, where a spectrum had to be acquired at 278 K to observe cluster peaks on the diagonal and cross-peaks between the cluster peaks and the formate CH, this suggests that the lifetimes, and therefore the exchange rates, for the double-cluster-related environments are longer than for either the tetramer or the single cluster. It also suggests that, in comparison to the single cluster, the double cluster has an increased preference for coordination to formate groups.

While it appears that negative cluster cross-peaks are present at 6.41-7.60 ppm, this phenomenon is in fact due to the combination of baseline distortion and scaling of the spectrum to make the cluster peaks visible. The regions between the distortions are situated in the locations of the smallest, least distinct cluster peaks (at 6.53 and 6.89 ppm), suggesting that the distortions are preventing positive cross-peaks between these cluster environments and H_3O^+ from being visible.

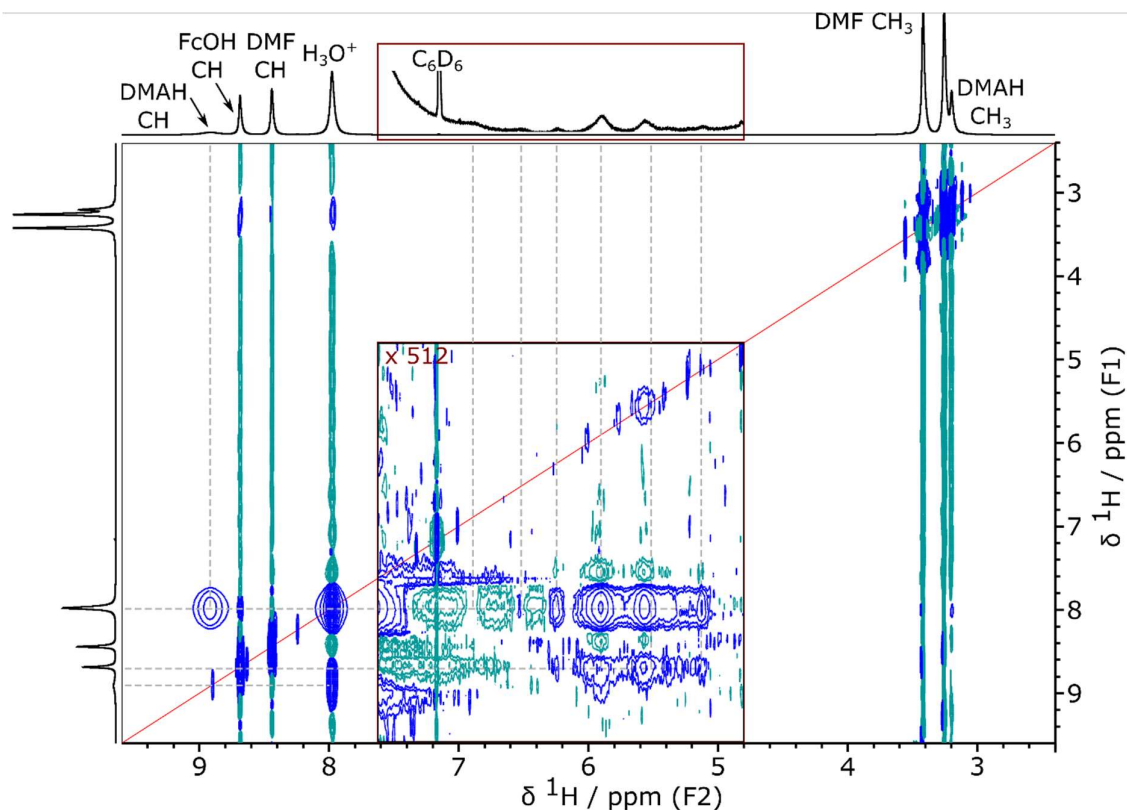


Figure 4.23. Two-dimensional ^1H - ^1H NOESY spectrum taken at room temperature of HfCl_4 in DFW 65:25:10 solvent, after heating to 150°C . The indirect dimension spectrum is given as an external projection from a one-pulse ^1H experiment. The sections in the dark red boxes are scaled up to show the small cross peaks due to cluster-related environments. The diagonal is shown with a bright red line. Positive contours are shown in blue, negative in green. Guide lines are given, dashed and in grey.

A 1-dimensional selective ^1H NOESY experiment, irradiating on the H_3O^+ peak to investigate correlation to this environment, gave strong correlations to the dimethylammonium NH environment; the negative peak for the DMF CH is possibly due to this environment also being saturated, being close in shift to the irradiated signal [Figure 4.24 a)]. This 1D experiment also gave negative peaks for all of the cluster environments [Figure 4.24 b)], showing at least eight different distinguishable environments. A 1-dimensional selective ROESY experiment did not show any correlations between H_3O^+ and the cluster peaks, neither from exchange nor from NOE [Figure 4.24 b)], which is unexpected as peaks from correlations are visible in the 2D and 1D NOESY experiments; this further corroborates that the cluster species in this post- 150°C sample are not the same as the tetramer or single cluster, as the sample containing the tetramer and single cluster in unheated DFW 65:25:10 did show correlation between the cluster environments and the H_3O^+ peak in the 1-dimensional ROESY as well as in the NOESY. In keeping with the observed asymmetry of

the 2D NOESY in which correlations from H_3O^+ and formate CH to the cluster peaks are seen, but not vice versa, selective 1D NOESY experiments irradiating the cluster peaks did not produce any visible correlation (see Appendix); this is potentially because the concentration of cluster relative to solvent is very low.

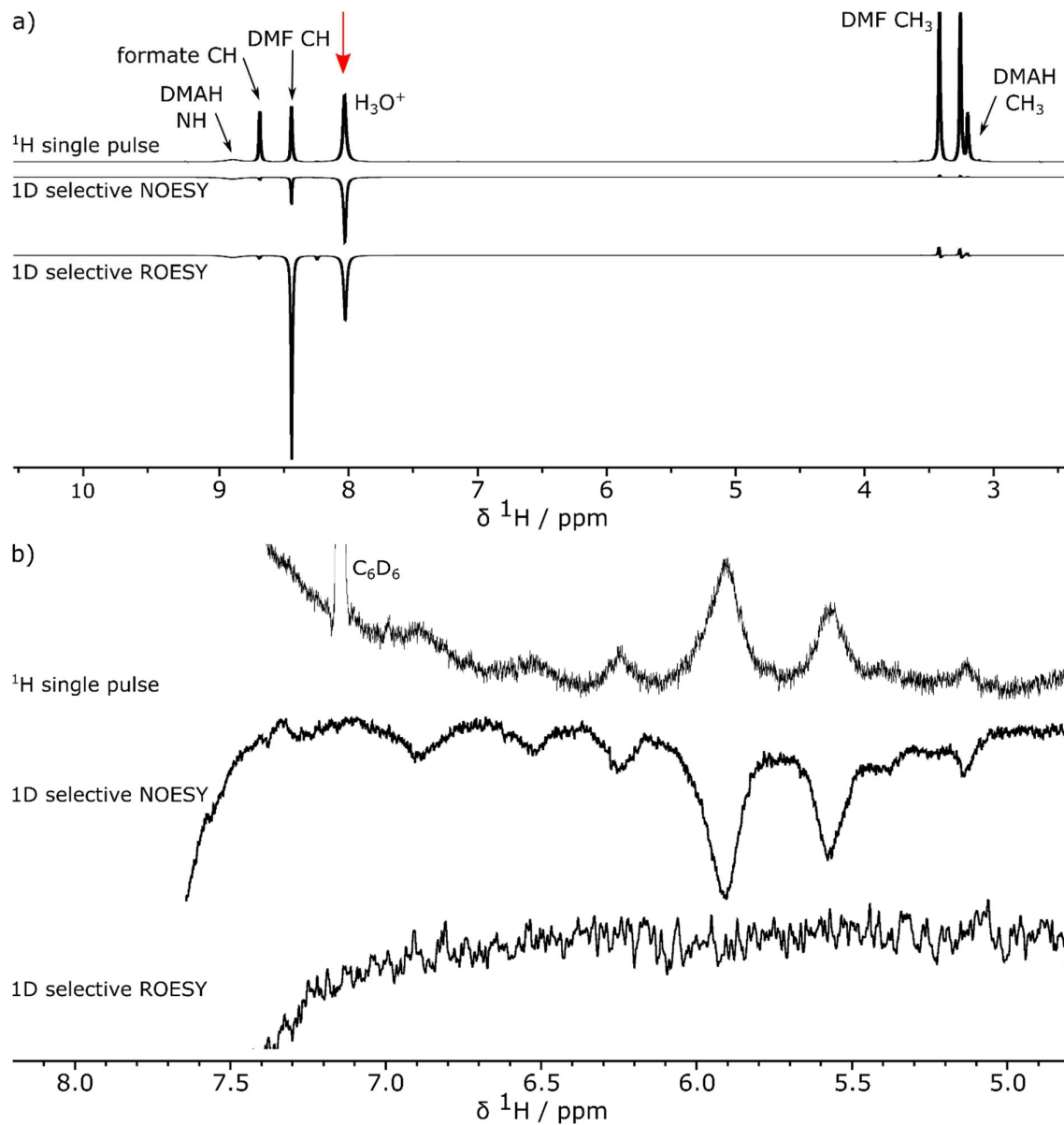


Figure 4.24. ^1H NMR, 1-dimensional selective NOESY and 1-dimensional selective ROESY: a) expanded view of the cluster environments; b) full spectrum. For the selective NOESY and ROESY, the sample was irradiated on the H_3O^+ peak at 8.016 ppm (indicated by a red arrow), and the irradiated peak inverted (i.e., phased to be negative).

4.3 Discussion

From the above study of the changes in the solvent upon heating, as well as the previous work in this thesis, it is possible to start to build a picture of these systems of Hf clusters in solution.

In water, it is well-established that the tetramer, $[\text{Hf}_4(\text{OH})_8(\text{OH}_2)_{16}]^{8+}$, is the dominant cluster species, and that water structures around it in coordination shells.^{204,212,255} The presence of the hafnium ions and the release of protons upon the formation of metal-oxo and metal-hydroxo bonds make the solution very acidic. Previous studies indicate that the metal-coordinated water, as well as the 'bulk' water, generally have short lifetimes due to fast exchange, although exchange can be slowed down if there is a high enough concentration of counterions which can surround the clusters.²⁹² In this Chapter a sharp peak in the ^1H NMR spectrum is assigned to the protons from some 'slowly'-exchanging water molecules coordinated to the metal atoms of the tetramer, similar to that observed in the literature.²⁹² Even though this environment is observed in the spectra, the integral is smaller than would be expected, suggesting that, while some water molecules exchange slowly enough for the cluster environment to be observed separately from the 'bulk' water peak, there is still some fast exchange occurring; indeed, this peak has a comparatively short relaxation time, as might be expected from a species in such a dynamic environment. Exchange could occur not just between environments on the cluster, but also with the water coordination shell around the tetramer identified in the XPDF analysis in Chapter 3.²⁵⁵ At low temperatures, the peak increases in intensity, again in keeping with an environment in dynamic exchange, but does not separate into separate environments; the structure of the tetramer appears relatively unchanged over a range of temperatures.

A second, weaker peak is also observed at ~ 7.65 ppm, which was not previously observed in the literature, and which has a longer T_1 than the other environment. Since the bridging μ_2 -OH groups on the tetramer (if observed) would be expected at a lower shift, being less acidic, this weak peak has been assigned to a minor hafnium species, potentially a hydrated or hydroxo monomer.²¹²

The single cluster, $[\text{Hf}_6\text{O}_4(\text{OH})_4]^{12+}$, is known to be particularly common, both in solution and in MOF structures, and can be found with a range of coordinating/terminating cluster

surface ligands.^{215,216,291,331,383} This cluster can form from the tetramer species upon the addition of acid,²⁰¹ hence the existence of the single cluster alongside the tetramer in the DMF : formic acid : water solutions is not surprising. However, the exact mechanism for the conversion of tetramer to single cluster is still unknown, although likely to involve carboxylate ligands in these solutions.^{201,209} The solution ¹H NMR experiments performed in this Chapter show that the ligands coordinated to the single cluster in these solutions are a mixture of water/hydroxide and formate, potentially with water/hydroxide dominant, and that these ligands undergo exchange with the 'bulk' solvent. From the exchange behaviour of the cluster ligands, clusters are also likely to have coordination shells of water, although they may also have secondary shells of predominantly formic acid.²⁵⁴ Together with the acidity caused by the dissolution of the hafnium salt, the coordination of formate and hydroxide groups to the clusters and the subsequent release of protons into the solvent are likely to increase the acidity of the solutions further. Furthermore, the uptake of water and formate in coordination to the clusters will reduce the hydrogen-bonding in the 'bulk' solvent.

Chapter 3 determined that upon heating solutions of hafnium in DMF : formic acid : water, the metal clusters—a mixture of single cluster and tetramer at room temperature—form first as the single cluster throughout, and then aggregate into $\{[\text{Hf}_6\text{O}_4(\text{OH})_4]_2(\text{OH})_6\}^{18+}$ double clusters.²⁵⁵ This Chapter builds on this understanding. As the temperature is increased, but is not yet sufficiently high to cause the formation of the double cluster, the amount of single cluster increases and the amount of tetramer decreases, and the cluster species continue to exchange terminating ligands with water. No correlation to formic acid is seen in the one- and two-dimensional exchange experiments at higher temperatures, suggesting that water/hydroxide coordinating groups are more prevalent than formate. Changes in the ¹H NMR spectrum after heating also suggest that the coordinating groups rearrange during the heating process, again as expected in these dynamic solutions.

Upon heating the hydrogen-bonding in the solvent is disrupted, in particular the DMF-DMF and DMF-water interactions (i.e., the water-water interactions are least weakened).²⁴³ Concurrently, as the temperature rises until close to 150°C (near the boiling point of DMF) the DMF is increasingly hydrolysed, producing formic acid and dimethylammonium ions,

which overall increases the pH of the solution.²⁴⁵ Even in metal-free solutions, the heated solvent has a different composition and subtly different structure, with ¹H peaks in the NMR spectrum changing shift and width. As the temperature rises the amount of water in the solvent decreases while the amount of formic acid increases slightly, likely due to hydrolysis. The presence of formic acid already in the solution, beyond that required to trigger the formation of or coordination to the single cluster, is (by changing the hydrolysis equilibrium position) likely to prevent as large an increase in pH as might otherwise be caused by the hydrolysis. However, the presence of the additional dimethylammonium ions and the removal of water molecules in the hydrolysis process are also likely to change the solvent interactions—including reducing hydrogen-bonding—further. Inside this complex system, when metal clusters are present the metal ions in the clusters themselves appear to increase the DMF hydrolysis reaction.

Clusters are known to aggregate at higher temperatures. Heating beyond 358 K (85°C) is required for double clusters to form (without ageing), and the formation of double clusters is indeed seen to occur at temperatures of 150°C both in this and in previous Chapters. The proposed formation route for the double cluster, involving the condensation of two single clusters *via* the formation of six μ_2 -OH bridges, relies on there being at least three water/hydroxide groups per single cluster; thus, the potential increase in water/hydroxide coordinating groups on the single cluster as the temperature rises would favour the formation of the double clusters. That the cluster-surface ligands are more dynamic at higher temperatures will favour the breaking and formation of Hf-O bonds required in the formation of the double cluster. An increase in temperature is also usually accompanied by an increase in diffusion coefficients. As well as water-water interactions being more favourable than water-DMF interactions, it is plausible that the single clusters, surrounded by their coordination shells of water, might come into increasingly frequent proximity, helping to make the double cluster formation more likely.

4.4 Conclusions

The last Chapter demonstrated that, in the formation of hafnium MOFs, the metal clusters are crucial in determining the structures which form. While the intercluster linkers must coordinate with the correct geometry for the framework to form, the clusters form prior to coordination by the linkers and therefore are 'building units' directing the resulting framework topology. Understanding the solution environment and interactions of these clusters is therefore key to controlling both their synthesis and their coordination behaviour.

This Chapter explored the interactions of these clusters with the reaction solvent. All three types of clusters, the $[\text{Hf}_4(\text{OH})_8]^{8+}$ tetramer, the $[\text{Hf}_6\text{O}_4(\text{OH})_4]^{12+}$ single cluster, and the $[\{\text{Hf}_6\text{O}_4(\text{OH})_4\}_2(\text{OH})_6]^{18+}$ double cluster, have surface ligands (or terminating groups) derived from solution species. ^1H solution NMR revealed that these cluster-surface ligands are in a dynamic exchange with the solvent, making the cluster-related peaks in the NMR spectrum less intense than might be expected for the concentration of the species. Measurement of the relaxation times of the cluster-related peaks also reveals short lifetimes, supporting the model that the ligands are involved in a complicated series of dynamics, involving exchange and hydrogen-bonding interactions with the surroundings; varied-temperature NMR experiments show that the exchange increases at higher temperatures.

Two-dimensional NMR was used to observe the correlations between the different environments as a result of these exchange processes. This enabled some identification of the cluster-surface species. While the tetramer is coordinated predominantly by water, the single and double clusters have a combination of water/hydroxide and formate, with the double cluster showing more affinity for formate groups than does the single cluster. However, as a result of the fast exchange, short lifetimes, and low concentration of the cluster environments relative to the 'bulk' solvent, the exact relationships—in particular, any exchange between cluster environments, and the mechanisms of exchange—remain undetermined. This motivates further work, such as performing simulations with different cluster ligand compositions and different solvent coordination shells, to fully understand these processes.

The cluster species also contain bridging μ_2 and μ_3 -OH groups, but the techniques used in this Chapter were not able to detect these species. This might again be a result of fast

exchange and hydrogen-bonding in the systems;³⁴² however, the observation of these species as a 'fingerprint' to the identity of the cluster would be extremely valuable. Infrared spectroscopy could therefore be used alongside ¹H NMR in future studies of these cluster systems in reaction solutions.³⁸³

This Chapter explored the interactions in this limited set of solutions where the cluster composition was already known. However, Chapter 2 demonstrated that the composition of the solvent—in particular, the amounts (both absolute and relative) of formic acid and water—were key to the formation of MOFs with different cluster species. Furthermore, the effect of ageing these solutions is of particular relevance in understanding the postsynthetic behaviours of these MOFs. The next Chapter therefore builds on the work explored thus far, using a combination of XPDF and ¹H solution NMR to investigate the clusters and their reaction solutions under different conditions.

Chapter 5. Varied Reaction Conditions of UiO Family Cluster Precursor Solutions

The last Chapter explored the interactions in solutions of hafnium metal clusters related to those found in UiO family MOFs. Building on the discovery in Chapter 3 of the formation of the tetramer, single cluster and double cluster in DMF : formic acid : water solvent, this investigation of the cluster coordination environments provided insights into their exchange behaviour and hence into the importance of the solvent in directing and determining the cluster species which form. The last Chapter successfully showed that one solvent composition could be used to vary the resultant cluster formation, depending on heating. However, in the defect-engineering of UiO family MOFs in Chapter 2, it is evident that the solvent *composition* is crucial in determining the MOF structure which forms, as well as the constituent cluster species; it was not possible for a single solvent composition to be successfully used in the synthesis of **fcu** UiO-67(Hf), comprising single clusters, **hcp** UiO-67(Hf), and **hns** UiO-67(Hf), both of the latter comprising double clusters with different ratios of coordinating linkers. Although Chapter 2 showed that different ratios of DMF, formic acid and water in the solvent affect the MOF structure that forms, with different nuclearities of metal cluster, the effect of changing the concentration of different solvent components specifically on the metal clusters and their terminating ligands is unknown. Likewise, the *in situ* studies in Chapter 3 only explored clusters in two solvents, water and DFW 65:25:10, again making the role played by the different solvent components difficult to determine.

Using the knowledge of the tetramer, single cluster and double cluster environments obtained in Chapter 4, this Chapter seeks to explore the effect of varying the solvent components known to affect the formation of UiO family MOFs on the metal clusters: the amounts of formic acid and water in solutions of HfCl₄ are varied, both with and without heating, so that the effects of each variable can be explored independently. Additionally, ageing of metal cluster species in solution has been found to affect the nuclearity and coordinating ligands of metal clusters,^{130,190,201,218} including those used to synthesise MOFs;²⁵²

ageing in reaction solvent has also been found to cause hafnium MOF structures to degrade faster.¹² Therefore ageing these solutions of different composition is also investigated.

The in situ XPDF experiments were performed at Beamline I15-1, Diamond Light Source, beamline staff Dr Dean S. Keeble, proposal number EE18630-1. The experiments were performed by Francesca Firth, Dr Michael Gaultois, Dr Yue Wu and Dr Matthew Cliffe, with technical assistance and setup from Dr Dean S. Keeble.

Samples for ex situ XPDF experiments were synthesised and prepared by Francesca Firth. The ex situ XPDF experiments were performed at Beamline I15-1, Diamond Light Source, beamline staff Dr Maria Diaz-Lopez and Dr Phil Chater. Dr Harold Geddes and Professor Andrew Goodwin, Inorganic Chemistry Laboratory, University of Oxford are thanked for coordinating the Oxford Warwick Midlands Solid State Chemistry consortium XPDF time via BAG CY26330-2.

All solution NMR experiments and analysis of all data, including optimisation of the Diffpy-CMI code for XPDF data analysis, were performed by Francesca Firth.

5.1 Experimental Methods

Samples for solution NMR and *ex situ* XPDF were prepared as described in Chapter 4.

Samples for *in situ* XPDF were prepared as described in Chapter 3.

Solution NMR measurements and *ex situ* XPDF measurements and analysis were performed as described in Chapter 4.

In situ XPDF measurements and analysis were performed as described in Chapter 3.

5.2 Results

5.2.1 Reactions with Different Solvent Compositions

Room Temperature Solutions

This thesis has shown thus far that the presence of both water and formic acid is greatly influential on the interactions in the system and therefore on the synthesis of the metal clusters (and any resultant MOF). To examine further the effect of each of these components on the solvent and on the metal clusters which form, the amounts of formic acid and water in the solvent were varied (as was done in Chapter 4 for Hf-free solutions [Figure 4.3]) for Hf-containing reactions.

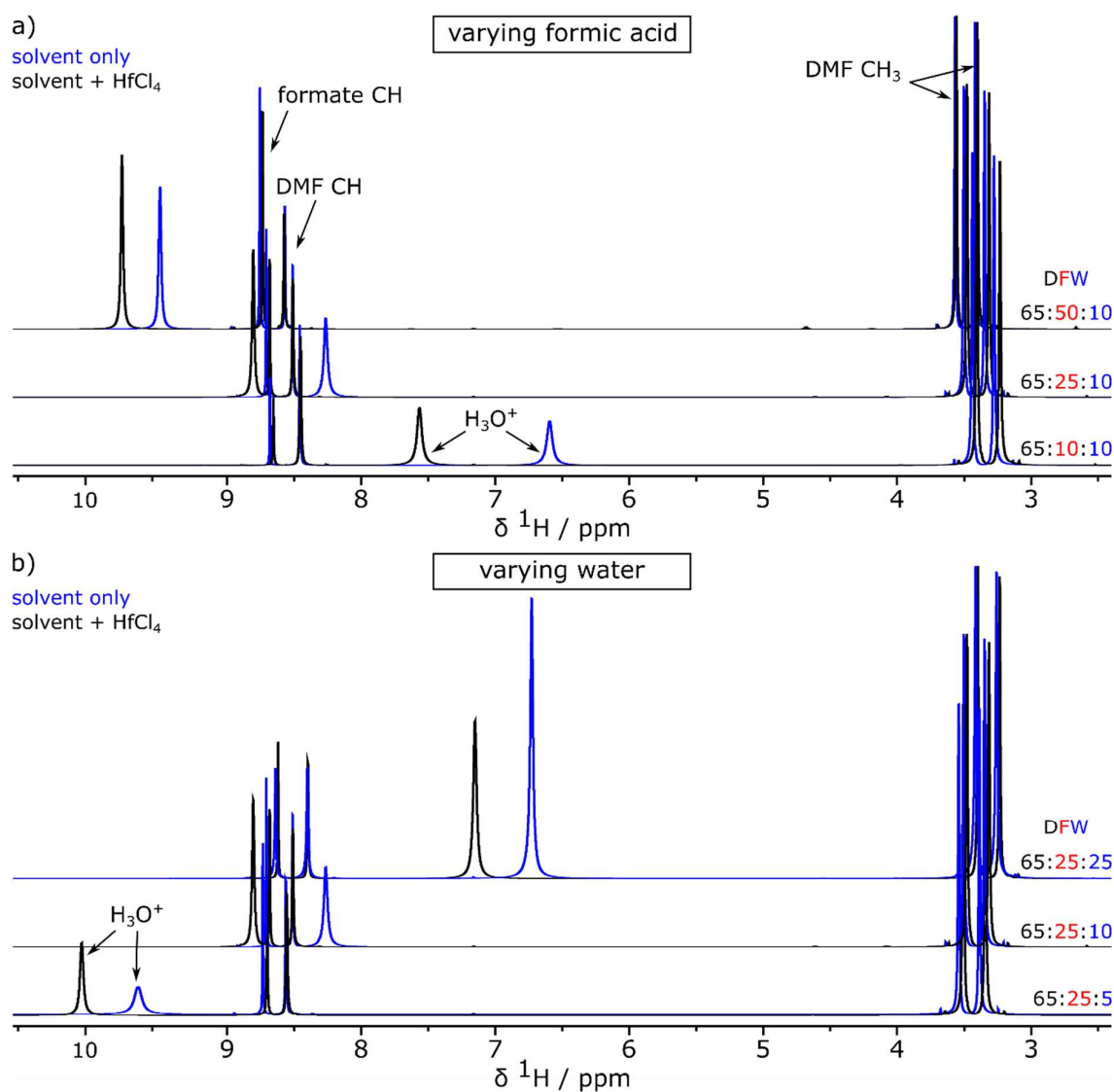


Figure 5.1. ¹H NMR of solutions with different compositions, all at room temperature: a) varying formic acid content; b) varying water content.

While the trends for the 'bulk' solvent peaks in these room-temperature Hf-containing solutions [Figure 5.1] resemble those seen in Chapter 4 in the cluster-free solutions [Figure 4.3], including the dramatic changes in shift of the H_3O^+ environment upon changing the amount of either formic acid or water, in the cluster region the peaks do not display similar clear patterns of chemical shift upon changing the amount of acid or of water [Figure 5.2].

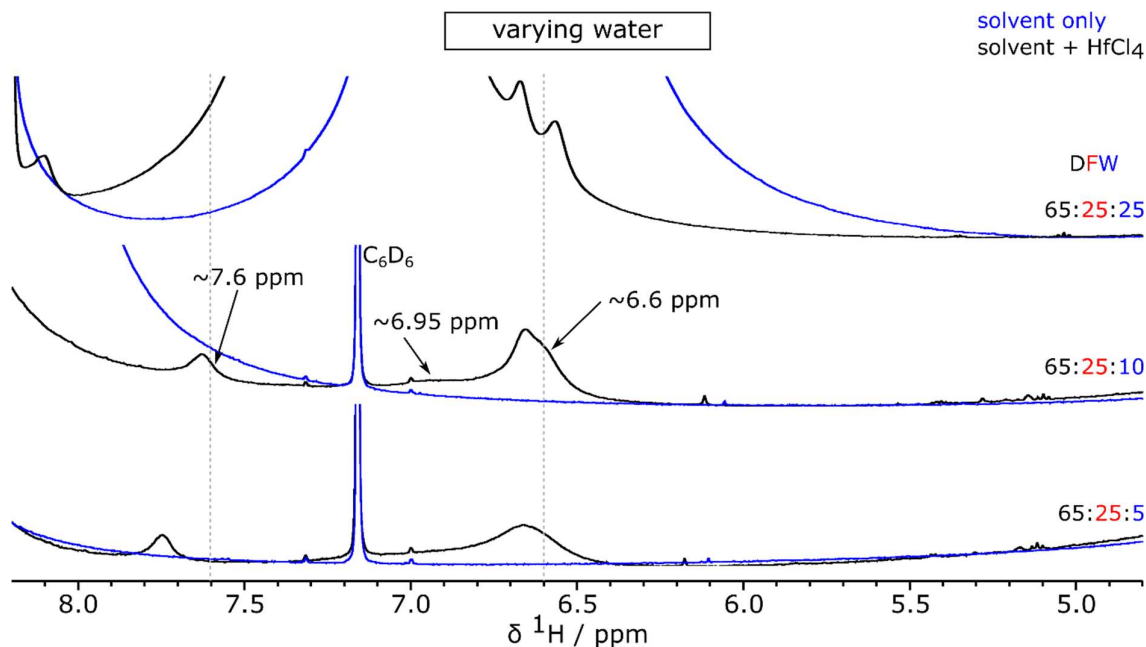


Figure 5.2. ^1H NMR of solutions with different water content, all at room temperature, expanded to show the cluster peak region. Guide lines (grey, dashed) are given at 6.6 and 7.6 ppm.

The peaks characteristic of the tetramer and single cluster in solution are predominant, but there are some key changes. The effects of changing the amount of water are considered first [Figure 5.2]. With low amounts of water the cluster peaks, in particular the multi-environment peak at ~ 6.6 ppm, are much weaker than seen previously. This peak is much less asymmetric than in the DFW 65:25:10 case, suggesting fewer environments are present. In Chapter 4 these cluster environments were found to be largely correlated with water/hydroxide, especially at room temperature, which explains why the NMR peaks have low intensity at low quantities of water. This suggests that these peaks either represent environments which prefer to coordinate with water, or which belong to clusters which do not form well with insufficient water.

Inspecting the NMR spectrum of the solution with high amounts of water (1 : 0.79 : 1.65 DMF : formic acid : water molar ratio, or DFW 65:25:25), the peak at ~ 6.6 ppm is split into

two separate peaks, suggesting that at high water concentrations these environments (in particular that at ~6.6 ppm) are far more distinct. This spectrum is similar to the low-temperature spectrum of the solution of Hf in DFW 65:25:10 [Figure 4.12] in which reduced exchange allowed different environments to be observed. It also resembles to the spectrum after short heating [Figure 4.16] in which the amount of single cluster is likely to be higher than the amount of tetramer. The peak observed at ~8.1 ppm in this DFW 65:25:25 solvent has a much higher shift than is seen in DFW 65:25:10 (~7.6 ppm, ascribed to the tetramer in Chapter 4). More water present in DFW 65:25:25 might lead to a greater water coordination shell around the clusters and hence a higher ^1H shift due to greater hydrogen-bonding/exchange.

A comparison of the XPDF patterns of the solutions with DFW 65:25:10 and DFW 65:25:25 solvents reveals similarity in the location and intensity of peaks [Figure 5.3 a)], indicating that overall the clusters present are likely to be the same in both samples. In particular, no peaks corresponding to the double cluster are seen. However, the height of the peak at 2.1 Å (Hf-O nearest neighbours) relative to that at 3.5 Å (Hf-Hf nearest neighbours) is lower for the high-water dataset, indicative of a decrease of the amount of tetramer in the sample (as discussed in Chapter 3). On refinement, this solution of Hf in DFW 65:25:25 gives a good fit to the model of the tetramer·H₂O and single cluster, just as is observed for the solution of Hf in DFW 65:25:10 [Figure 5.3 b)]. In the DFW 65:25:25 sample (1 : 35.8 : 28.3 : 59.1 molar ratio Hf : DMF : formic acid : water) the tetramer : single cluster ratio is 1 : 1.21 whereas in DFW 65:25:10 (1 : 35.8 : 28.3 : 23.7 molar ratio Hf : DMF : formic acid : water) the tetramer : single cluster ratio is 1 : 0.95, i.e., at higher water, the amount of single cluster increases.

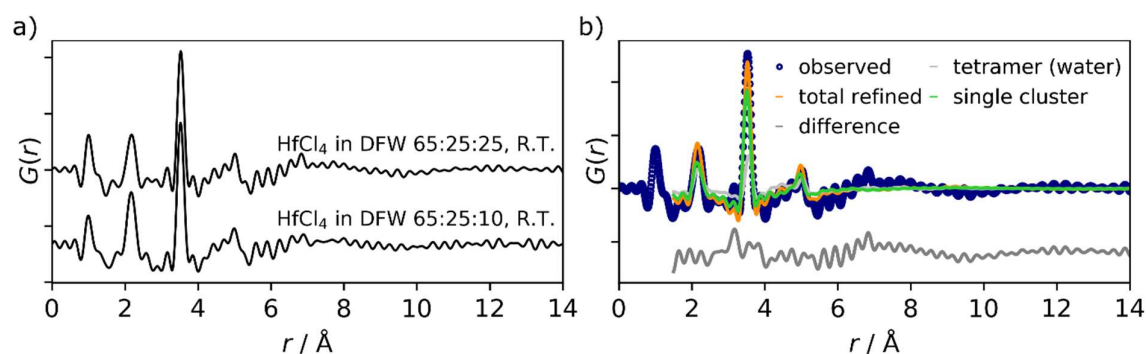


Figure 5.3. a) Comparison of datasets of HfCl_4 in different solvents at room temperature; b) refinement of a mixture of the tetramer·H₂O and the single cluster against an XPDF dataset of HfCl_4 in DFW 65:25:25 solvent ($R_w = 0.356$).

This change in cluster composition indicated by both the XPDF and the ^1H NMR data seems counterintuitive, as the tetramer is the dominant species in aqueous solution; however, the presence of DMF and especially formic acid is enough to change the system away from one where the tetramer is dominant. As noted in Chapter 4, none of the DFW solutions show the characteristic peaks from the ^1H NMR of the tetramer in aqueous solution.

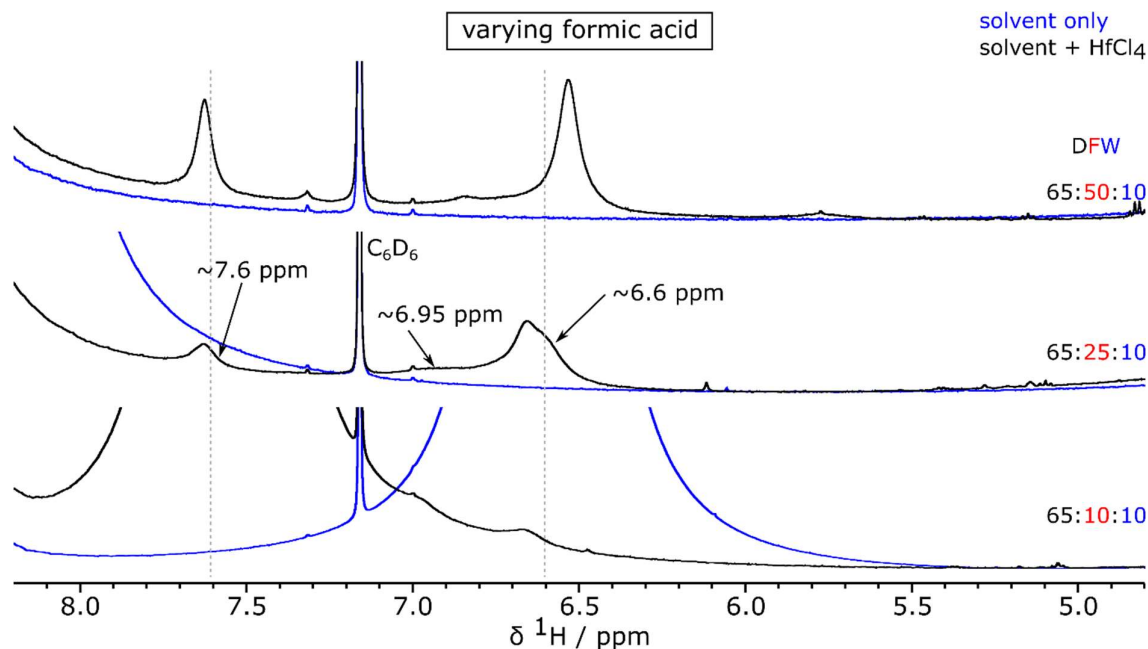


Figure 5.4. ^1H NMR of solutions with different compositions, all at room temperature, expanded to show the cluster peak region. Guide lines (grey, dashed) are given at 6.6 and 7.6 ppm.

Investigating the effect of changing the amount of formic acid in the solvent, again changes in the shift and intensity of the cluster peaks are seen [Figure 5.4]. At low formic acid concentrations some cluster peaks can be identified but they are weak (and obscured by the ‘bulk’ solvent peak) suggesting that cluster formation is disfavoured with insufficient formic acid. As the amount of formic acid is increased, the cluster peaks are more pronounced, becoming sharper and with increased separation in chemical shift. The increase in intensity of the cluster-related peaks as the amount of formic acid increases could be due to the formation of more clusters. In the spectrum of Hf in DFW 65:50:10 there is no asymmetry like that observed for the peak at ~ 6.6 ppm in DFW 65:25:10, meaning that fewer environments are present. With low water and high formic acid, the tetramer would be expected to be disfavoured,^{201,209} which suggests that the remaining sharp peaks are resulting from predominantly the single cluster—potentially even the peak at ~ 7.6 ppm previously ascribed to the tetramer. Although neither of the sharp peaks in DFW 65:50:10 has the same

shift as the peak assigned to the single cluster (~6.93 ppm) after heating the sample in DFW 65:25:10 to 85°C [Figure 4.22], this can be explained by the different solvent composition and lack of heating of this sample. A lack of heating may also permit more configurations of cluster-surface ligands, resulting in more than one peak.

Heated Solutions

Solutions of HfCl₄ heated to 150°C were then considered and compared to their heated Hf-free equivalents [Figure 5.5].

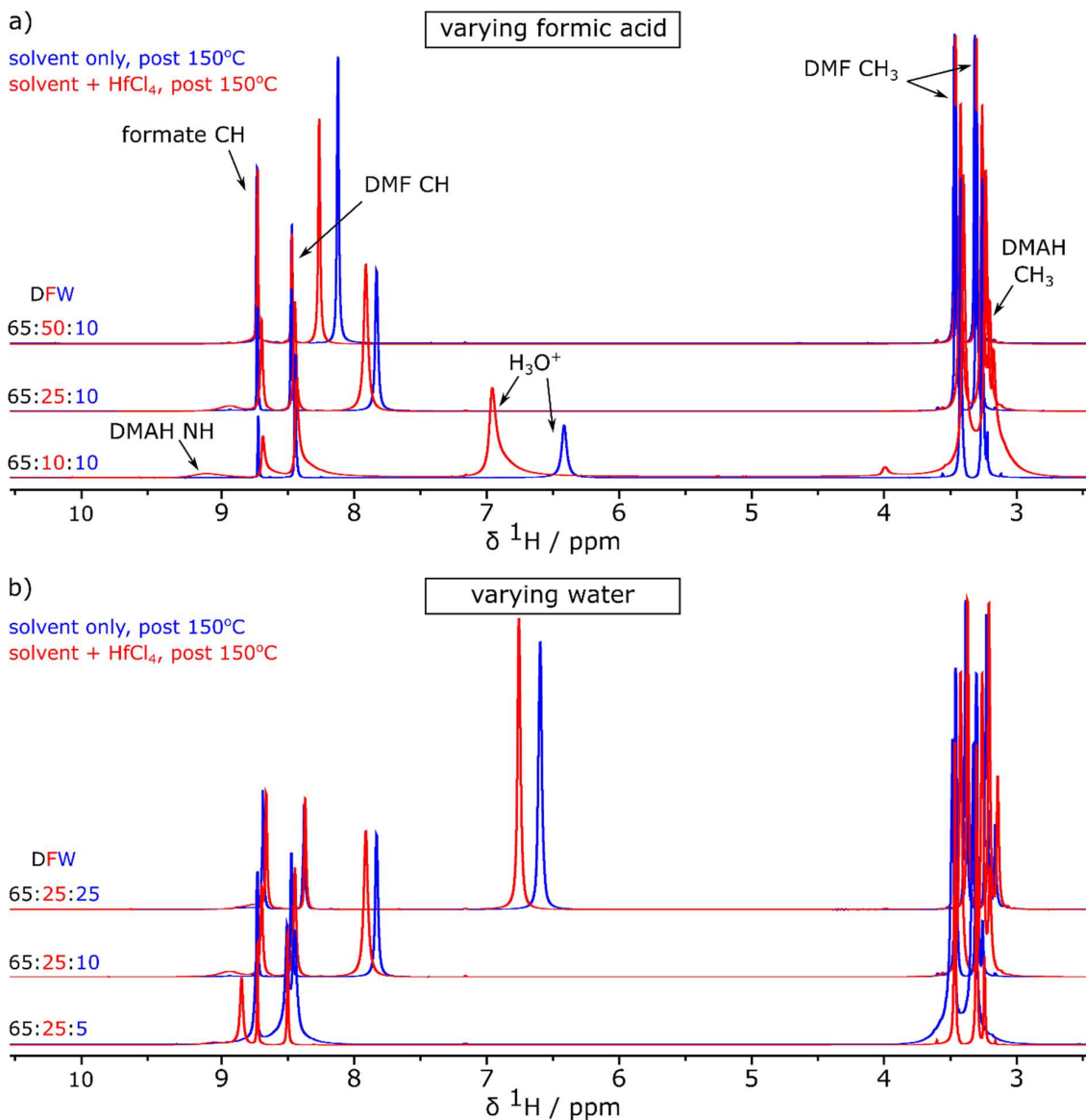


Figure 5.5. ¹H NMR of solutions with different compositions, all after heating at 150°C for 24h: a) varying formic acid; b) varying water concentrations.

Hydrolysis clearly occurs both in Hf-free and Hf-containing solutions, from the appearance of the DMAH environments. As before, the Hf-containing solutions have a greater degree of hydrolysis, as do solutions with higher amounts of water relative to formic acid, as expected from consideration of the hydrolysis equilibrium. The 'bulk' solvent peaks again display the trends seen previously. Compared to the heated Hf-free solvent the solutions with Hf display a slightly lower shift for all 'bulk' solvent peaks except H_3O^+ , indicating a reduction in hydrogen-bonding. The H_3O^+ peak again exhibits dramatic changes of shift. The H_3O^+ peak has a higher shift for the Hf-containing solutions, again as expected for solutions with more hydrolysis resulting in more formic acid present and therefore a higher weighted-average $\text{H}_2\text{O}/\text{H}_3\text{O}^+/\text{COOH}$ shift.

The cluster-characteristic regions of the spectra again provide valuable insight into the changes occurring following changes to the solvent composition [Figure 5.6]. The solvent compositions in these heated samples in which cluster peaks are observed are far more limited than for the unheated samples, suggesting that the double cluster may require more specific conditions to form than the single cluster/tetramer. Cluster-related peaks are most clear in the spectrum of the solution in DFW 65:25:10 already known to contain the double cluster. In both the low-water and high-formic-acid cases peaks are present but with very low intensity.

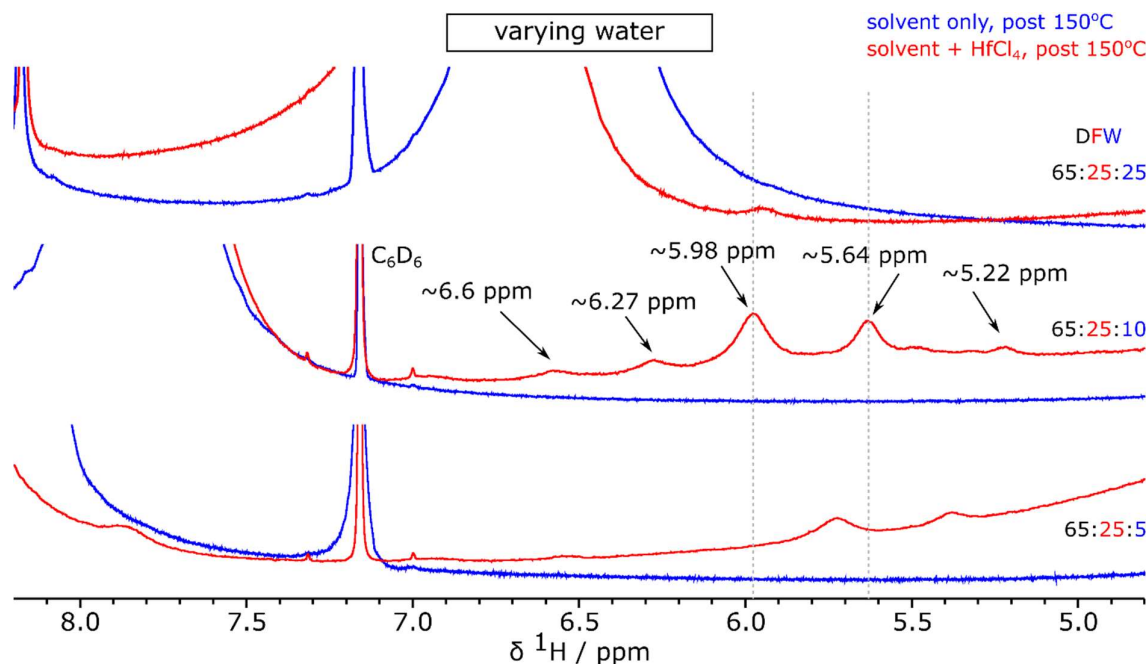


Figure 5.6. ^1H NMR of solutions with varying amounts of water, all after heating at 150°C for 24h, expanded to show the region with cluster-related peaks. Guide lines (grey, dashed) are given at 5.64 and 5.98 ppm.

The sample of Hf with low amounts of water has small cluster-related peaks at ~ 5.4 ppm, 5.7 ppm and ~ 7.8 ppm [Figure 5.6]. Using XPDF to elucidate the cluster composition, an *in situ* XPDF dataset in the low-water DFW 65:25:5 solvent (molar ratio 1 : 0.32 : 0.33 DMF : formic acid : water) showed that over the heating process the relative amounts of the single and double cluster change little and that the tetramer is no longer present [Figure 5.7].

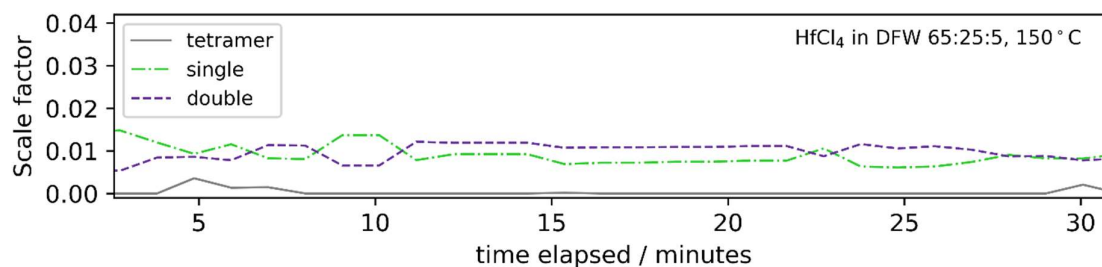


Figure 5.7. Scale factors over time of the clusters in DFW 65:25:5 solvent, obtained from refinement of *in situ* XPDF data. The proportion of tetramer was close to 0 throughout the reaction.

Since the relative amounts of single and double cluster changed little over the heating reaction, a refinement was performed against an averaged dataset, giving the best fit to a 45.2 : 54.8 ratio of double cluster : single cluster [Figure 5.8].

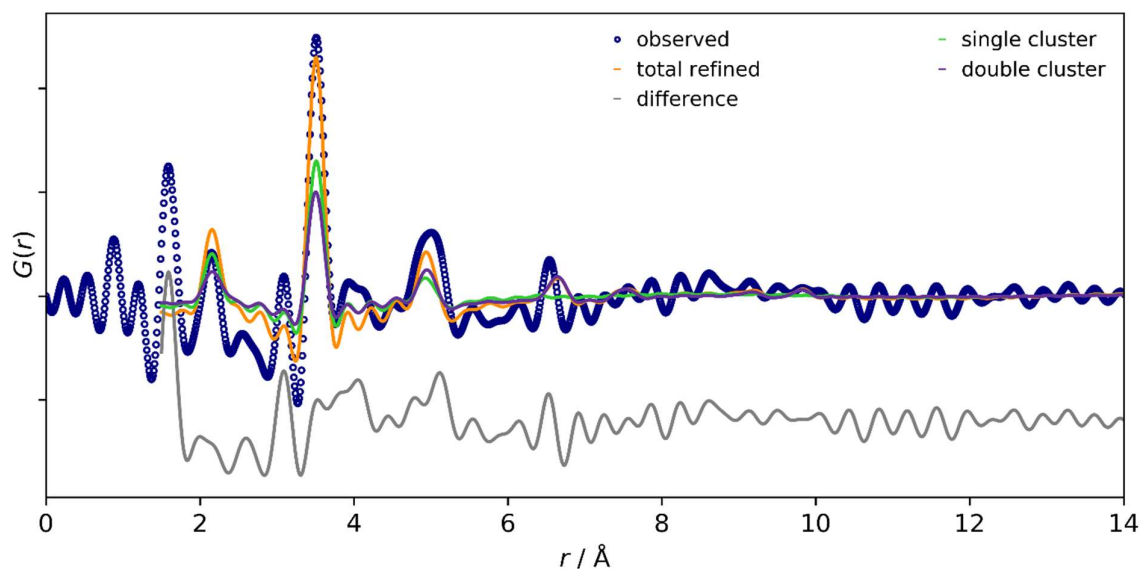


Figure 5.8. Refinement of the *in situ* XPDF dataset of HfCl_4 in DFW 65:25:5 solvent ($R_w = 0.607$) against a model of the double cluster and single cluster.

That this low-water sample does *not* contain a majority of the double cluster reinforces the understanding that water is crucial for the formation of the double cluster from the single cluster. This also provides insight into the assignment of the peak seen at ~ 7.8 ppm in the spectrum of HfCl_4 in the low-water solvent, which resembles peaks observed at a similar shift in unheated samples [Figure 5.2, Figure 5.4]. That it is observed in this spectrum of the heated sample, which contains no tetramer, suggests that this peak can be ascribed to environments on the single cluster.

A further heated *in situ* XPDF was performed on a solution of HfCl_4 with an even lower concentration of water (DFW 65:25:1 solvent, molar ratio 1 : 0.32 : 0.07 DMF : formic acid : water). Throughout the reaction, the cluster composition was essentially unchanged and so the XPDF data were again averaged. A refinement against this dataset resulted in the best fit to the single cluster, although upon inspection of the XPDF pattern the material appears to be of poor quality [Figure 5.9].

This suggests that not only is the double cluster inaccessible without sufficient water present, but that the single cluster also does not form well with very low compositions of water. The *in situ* XPDF experiment may not be directly comparable to the ^1H NMR data, as it contained a lower concentration of Hf; however, at higher concentrations of Hf, as used in the ^1H NMR experiments, the double cluster is potentially even less likely to form due to a lower Hf : water ratio.

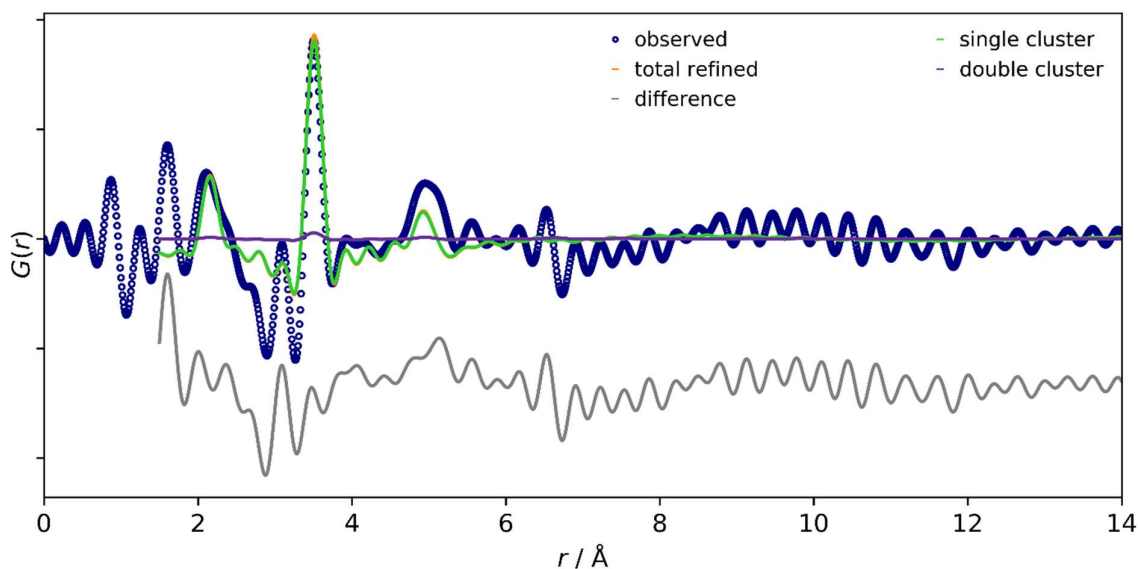


Figure 5.9. Refinement of the single and double cluster models against an in situ XPDF dataset of HfCl_4 in DFW 65:25:1 solvent ($R_w = 0.659$)

Turning to samples with varying amounts of formic acid, the solution with low formic acid (DFW 65:10:10, molar ratio 1 : 0.32 : 0.66 DMF : formic acid : water) appears to have no cluster peaks at all in the ^1H NMR spectrum [Figure 5.10].

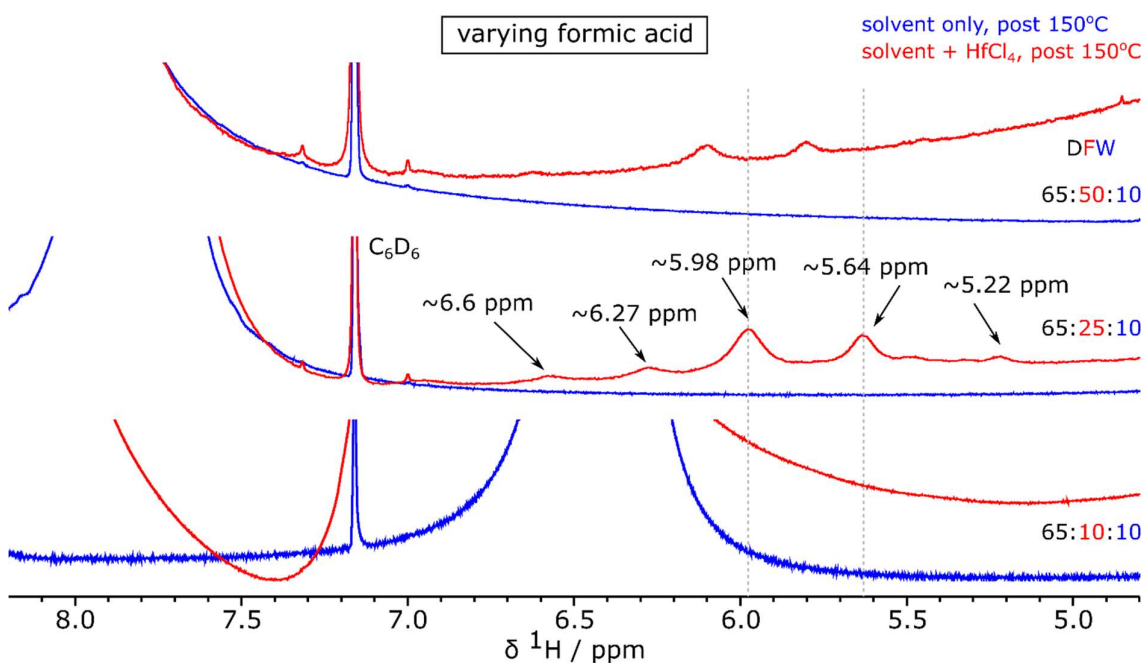


Figure 5.10. ^1H NMR of solutions with varying amounts of formic acid, all after heating at 150°C for 24h, expanded to show the region with cluster-related peaks. Guide lines (grey, dashed) are given at 5.64 and 5.98 ppm.

Due to the 'bulk' solvent peak overlap in the same region, XPDF analysis was performed on this solution to determine if any clusters form. This dataset also reveals no discernible

cluster structure except for a peak at 3.5 Å (the nearest-neighbour Hf-Hf distance) [Figure 5.11]. While this indicates that some manner of Hf complex is present, it is of too low quality to be determined from this data. When compared with the unheated solution [Figure 5.4] in which weak cluster-related peaks are observed, this shows that in these heated conditions the presence of sufficient acid is evidently crucial to the formation of any clusters.

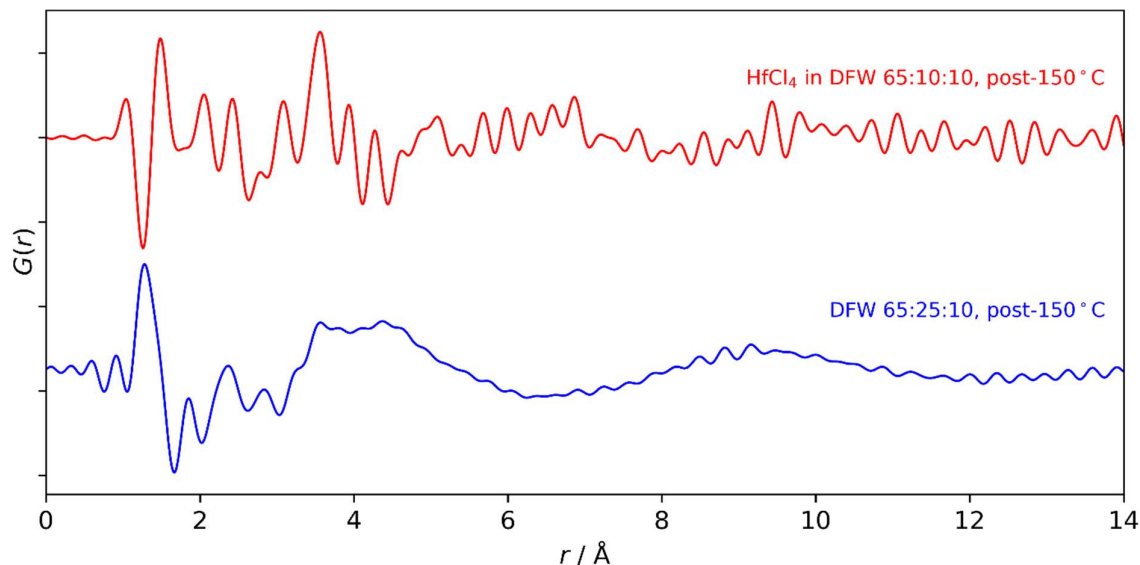


Figure 5.11. Plot of the normalised X-ray pair distribution functions of DFW 65:25:10 solvent and HfCl_4 in DFW 65:10:10 solvent at room temperature, both post-heating at 150°C.

5.2.2 Aged Solutions

It is well known that zirconium and hafnium complexes change structurally over time and that this can have an effect on synthesis as well as the identity of the product.^{74,133,252,400} In earlier work, hafnium MOF structures are observed to degrade faster over time¹² and have increased response to postsynthetic treatments (see Chapter 2) when not washed after synthesis: that is, with some of the reaction solvent likely to remain in the MOF.²⁵¹ With this understanding, the effect of ageing the molecular clusters in their reaction solutions was explored.

Room Temperature Solutions

In all of the solvent ratios tested the chemical shift of all peaks in the ^1H NMR spectrum decreases over time [Figure 5.12]. While DMF and formic acid peaks decrease in shift only slightly, the H_3O^+ environment decreases the most, although never reaching the shift of the peak in the Hf-free solutions. At the longest timescales, the solutions display peaks from dimethylammonium, indicating that DMF hydrolysis occurs even without heating. The

amount of hydrolysis is greater in solutions with less formic acid, which opposes the hydrolysis reaction. Additionally, the H_3O^+ peak also becomes broader and less intense over time as the amount of water in the solution decreases due to the hydrolysis; the integral of the formate CH peak increases as formic acid is produced during DMF hydrolysis.

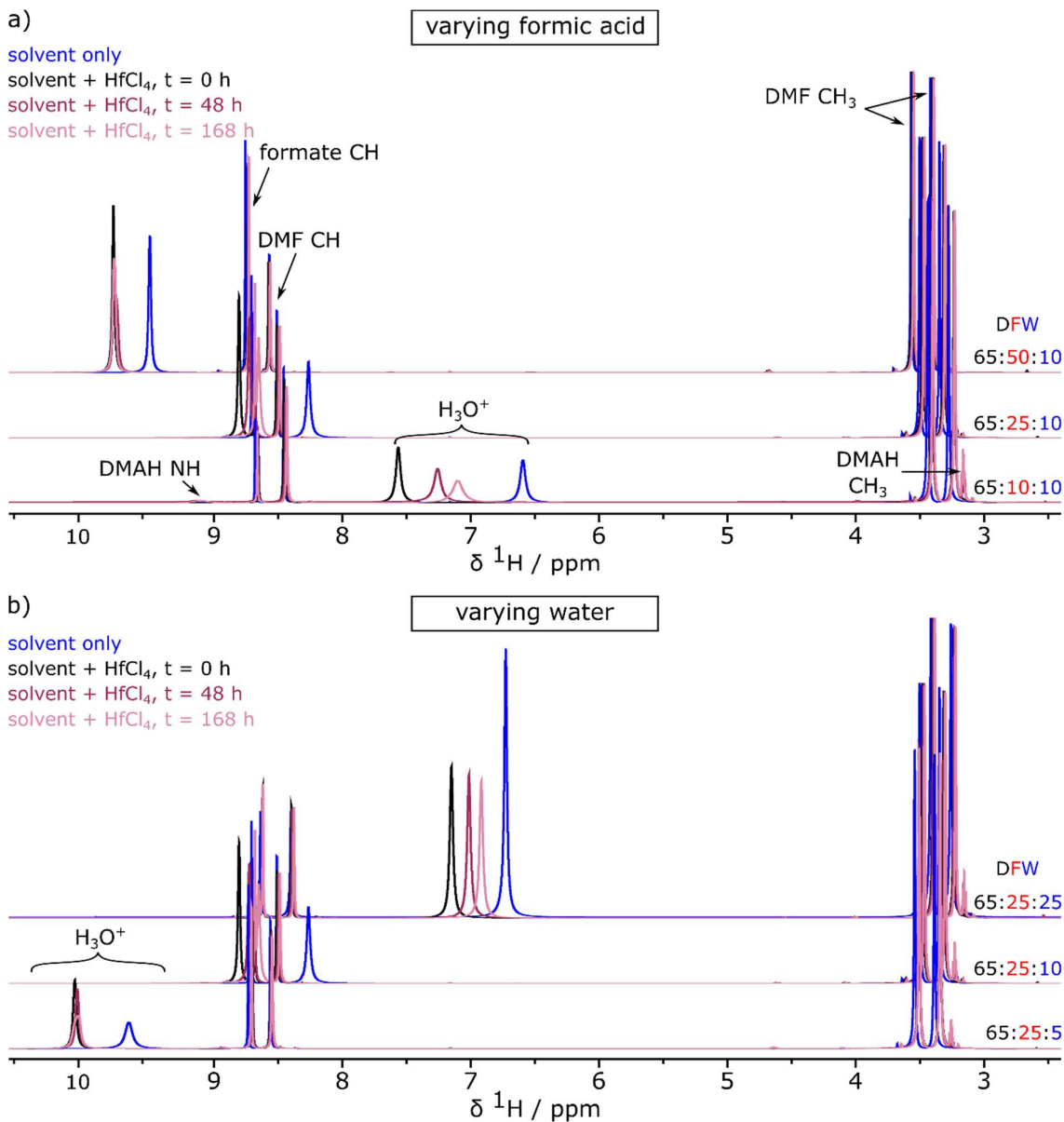


Figure 5.12. ^1H NMR of HfCl_4 in different solvents, room temperature, measured at different time intervals after synthesis: a) varying formic acid; b) varying water.

Changes in the solvent composition occur upon ageing, not least due to the hydrolysis of DMF. Some of these changes to the solvent can also be seen in the XPDF patterns of DFW 65:25:10 solvent only [Figure 5.13] as well as of the solutions of HfCl_4 in DFW 65:25:10 [Figure 5.14].

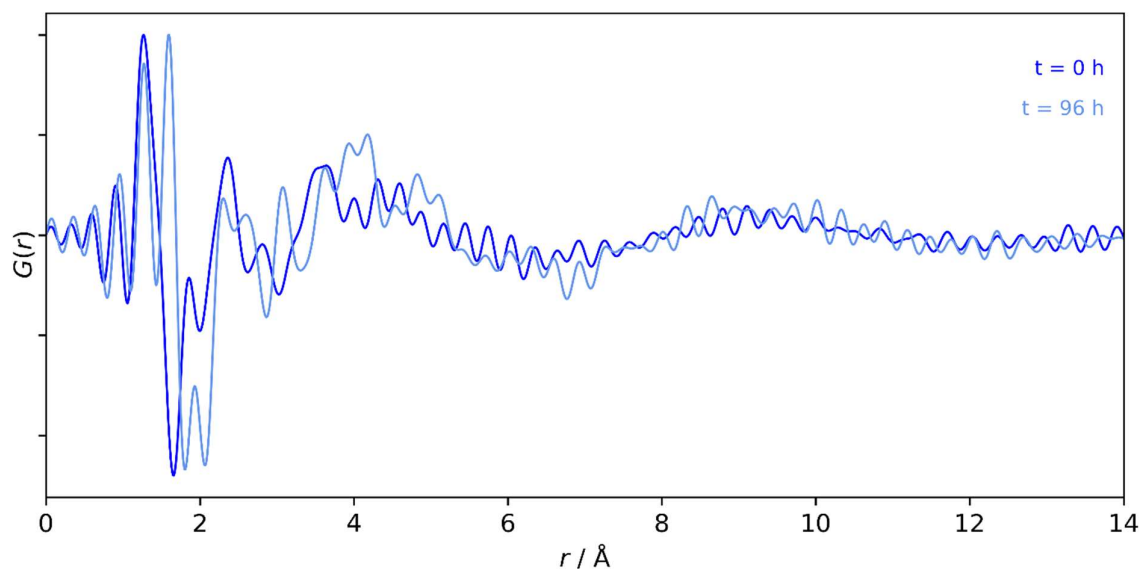


Figure 5.13. Comparison of normalised XPDF datasets for Hf-free DFW 65:25:10 (room temperature) at different times after synthesis.

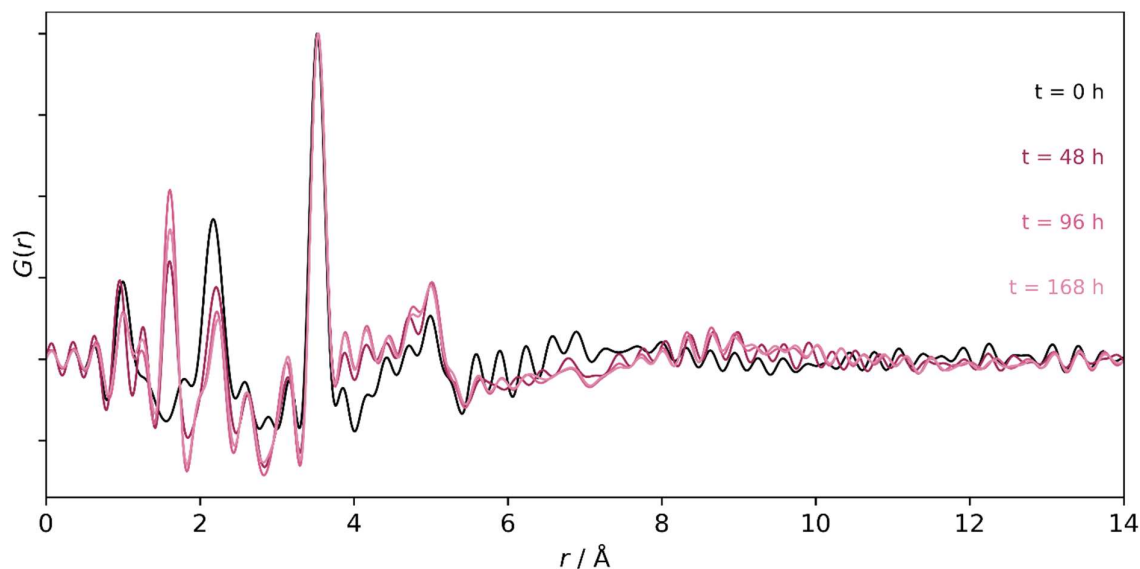


Figure 5.14. Comparison of normalised XPDF datasets for HfCl_4 in DFW 65:25:10 (room temperature) at different times after synthesis.

These changes are particularly visible around 1.9 and 4 Å, distances associated with hydrogen bonding and solvent structuring. Occurring in both Hf-free and Hf-containing solutions, these changes are likely due to the DMF hydrolysis and equilibration of the solvent mixing, rather than being specific to cluster-induced solvent structuring.

From these XPDF experiments on the Hf-containing sample, the cluster composition also appears to be changing. The unheated sample of HfCl_4 in DFW 65:25:10 shows a clear change in the XPDF during post-synthetic ageing [Figure 5.14]. Refinements performed

against the XPDF datasets suggest that the cluster composition in solution is indeed changing over time [Table 5.I]. The amount of tetramer in the solution decreases and the amount of single cluster increases during ageing. These refinements did not suggest the presence of any higher-nuclearity clusters, nor were any peaks at higher internuclear distances present in the XPDF to suggest that larger clusters form.²⁵⁵ This is in keeping with studies showing that cluster aggregation occurs in these ageing times,²⁵² but also shows that higher temperatures are required for aggregation to form the double cluster.

Table 5.I. Cluster ratios following refinement of the datasets of HfCl₄ in DFW 65:25:10 at a range of time intervals after synthesis. Due to rounding, ratios may not add up to 100.

Time after synthesis / hours	tetramer·H₂O : single cluster ratio
0	50.7 : 49.3
48	56.5 : 43.5
96	46.1 : 53.9
168	41.2 : 58.8

Ageing the sample of Hf in DFW 65:25:10 results in changes to the cluster composition. ¹H solution NMR also shows changes to the cluster-related environments over time, in all of the different solvent compositions [Figure 5.15]. While the cluster peaks change very little in terms of chemical shift, all the peaks become more intense over time, which suggests that more clusters are forming (rather than just the cluster composition/ratio changing). This is in keeping with other work in which the equilibrium amount of cluster in solution took more than 24 hours to form.²⁰¹

None of the cluster peaks in these ¹H NMR spectra resemble those found in the post-heating sample containing the double cluster [Figure 4.22]. This corroborates the evidence from the XPDF analysis of HfCl₄ in DFW 65:25:10 that the sample is unlikely to contain any clusters larger than the single cluster.

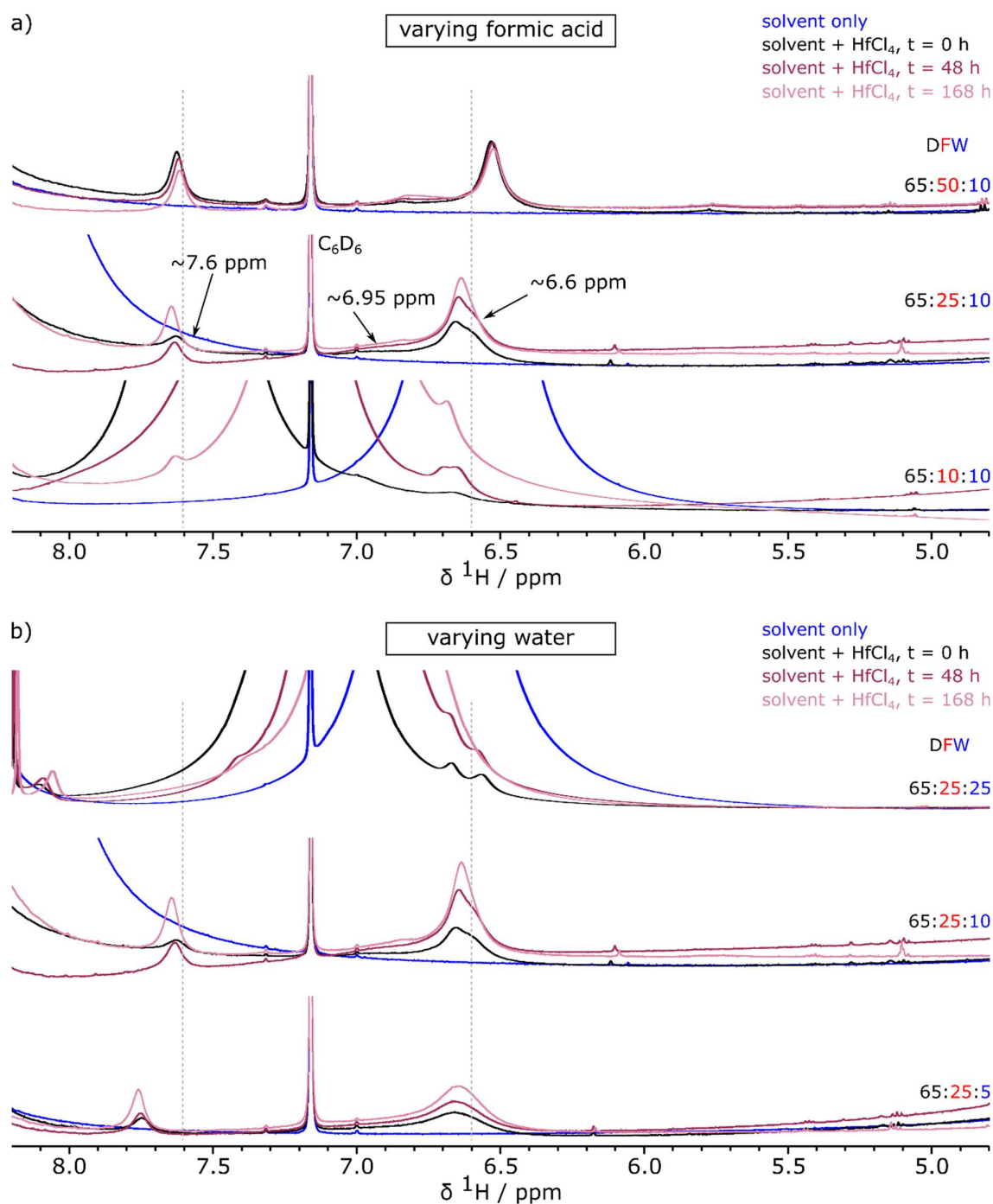


Figure 5.15 ^1H NMR of HfCl_4 in different solvents, room temperature, measured at different time intervals after synthesis, expanded view to show the cluster-related peaks: a) varying formic acid; b) varying water. Guide lines (grey, dashed) are given at 6.6 ppm and 7.6 ppm.

Samples with low concentrations of water and formic acid show only very weak cluster peaks, suggesting that little cluster material forms even after time for equilibration.

However, even the sample in DFW 65:10:10 which contained little cluster material at time $t=0$ appears also to form cluster material over ageing.

Earlier analysis suggested that the sample in DFW 65:50:10 might contain predominantly single cluster at time $t=0$ [Figure 5.4]. Since ageing favours the formation of the single cluster, that the cluster-related peaks in the ^1H NMR spectrum [Figure 5.15 a)] change little over time supports the suggestion that this sample contains little tetramer, and that the environments on the single cluster do not change significantly either.

In contrast with this high-formic-acid sample, the ^1H NMR spectra of solutions of HfCl_4 with varying amounts of water do show increases in sharpness and intensity of the cluster-related peaks over time [Figure 5.15 b)]. Complementary XPDF analysis and refinement of the high-water solution (HfCl_4 in DFW 65:25:25, or 1 : 0.79 : 1.65 molar ratio DMF : formic acid : water) show a change in cluster composition of this sample over time [Figure 5.16]: the amount of tetramer decreases (although not in the first 48 hours, as is also observed with the sample in DFW 65:25:10, perhaps due to the initial equilibrium stability of the tetramer in aqueous solutions) until the single cluster is the only species present [Table 5.II]. This is similar to the change in composition of HfCl_4 in DFW 65:25:10 but in this high-water case complete conversion from tetramer to single cluster is reached by $t = 168$ h, whereas in DFW 65:25:10 complete conversion is not reached over the ageing timescale. This is in keeping with the earlier result in which the increase in water appeared to favour the single cluster over the tetramer [Figure 5.3], and again confirms the importance of water in the formation of the single cluster.

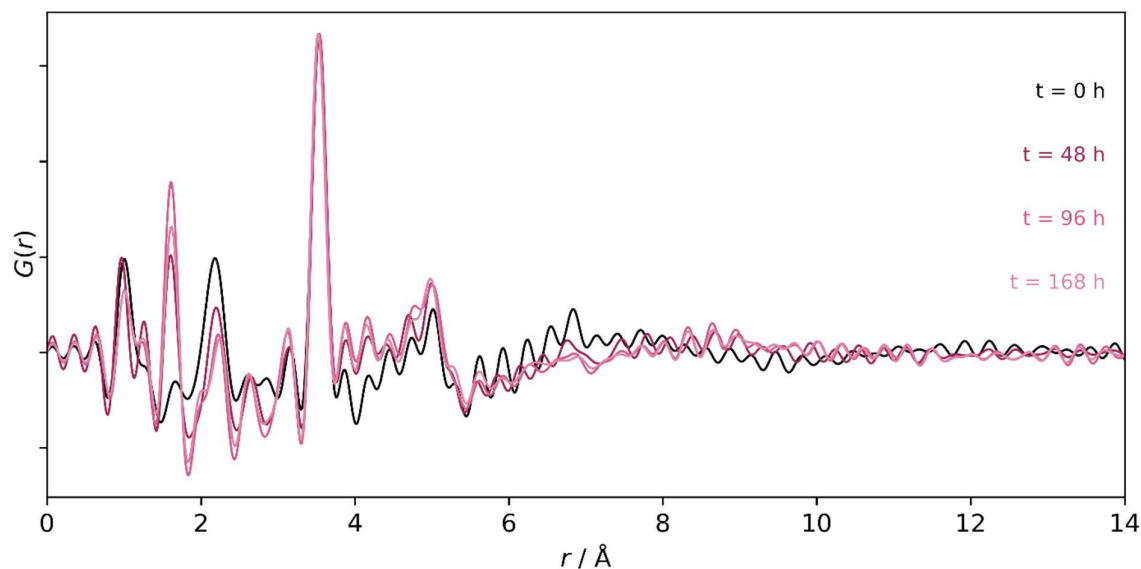


Figure 5.16. Comparison of normalised XPDF datasets for HfCl_4 in DFW 65:25:25 (room temperature) at different times after synthesis.

Table 5.II. Cluster ratios following refinement of the datasets of HfCl₄ in DFW 65:25:25 at a range of time intervals after synthesis.

Time after synthesis / hours	tetramer·H ₂ O : single cluster ratio
0	45.2 : 54.8
48	50.7 : 49.3
96	26.6 : 73.4
168	0 : 100

Heated Solutions

The effect of ageing upon samples which had been heated at 150°C for 24 hours was also investigated. Since a heated sample of HfCl₄ in DFW 65:25:10 is known to contain the double cluster at time t=0 after synthesis [see Figure 4.20], the behaviour of this sample over time was examined first. XPDF analysis was used to determine any changes to the cluster composition or core structure.

At all ageing times refinement against the XPDF datasets gives the best fit with the double cluster with no significant contribution from any other cluster species [Figure 5.17].

However, a loss of definition in the structure can be seen, especially in the peaks characteristic of the double cluster between 8 and 10 Å as well as the Hf-O peak at 2.1 Å (see Chapter 3).

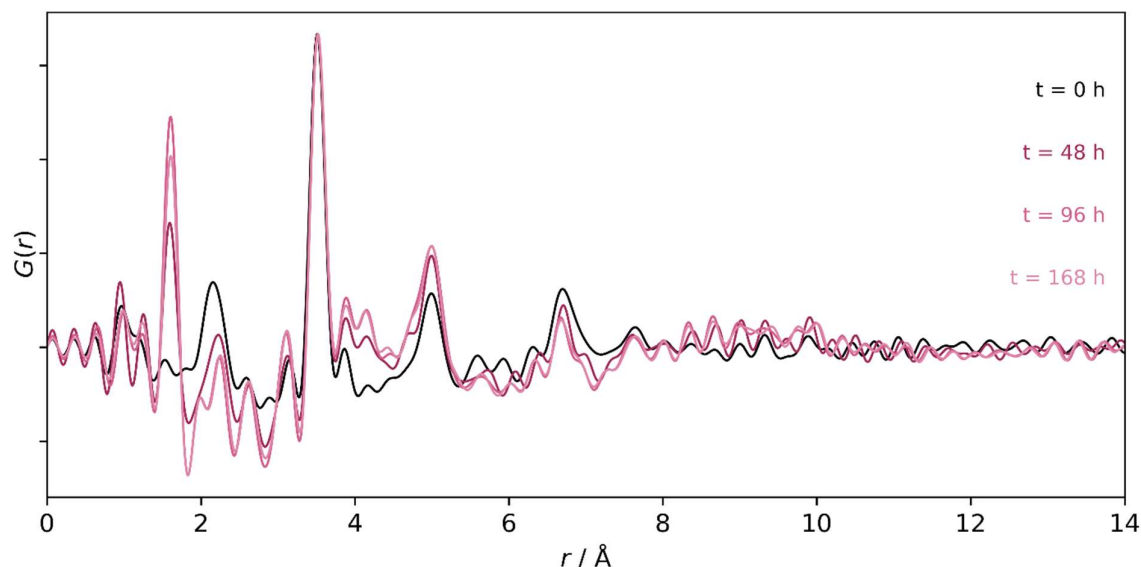


Figure 5.17. Comparison of normalised XPDF datasets for HfCl₄ in DFW 65:25:10 (reacted at 150°C for 24 hours) at different times after synthesis.

An increase in intensity is observed at ~4 Å. This is also seen in the XPDF of the post-heating Hf-free solvent as it ages [Figure 5.18], as well as the XPDF of both Hf-free and Hf-

containing unheated solutions [Figure 5.13, Figure 5.14], and is likely to result from changes in the solvent, such as hydrogen-bonding, as it equilibrates over time.²⁵⁵

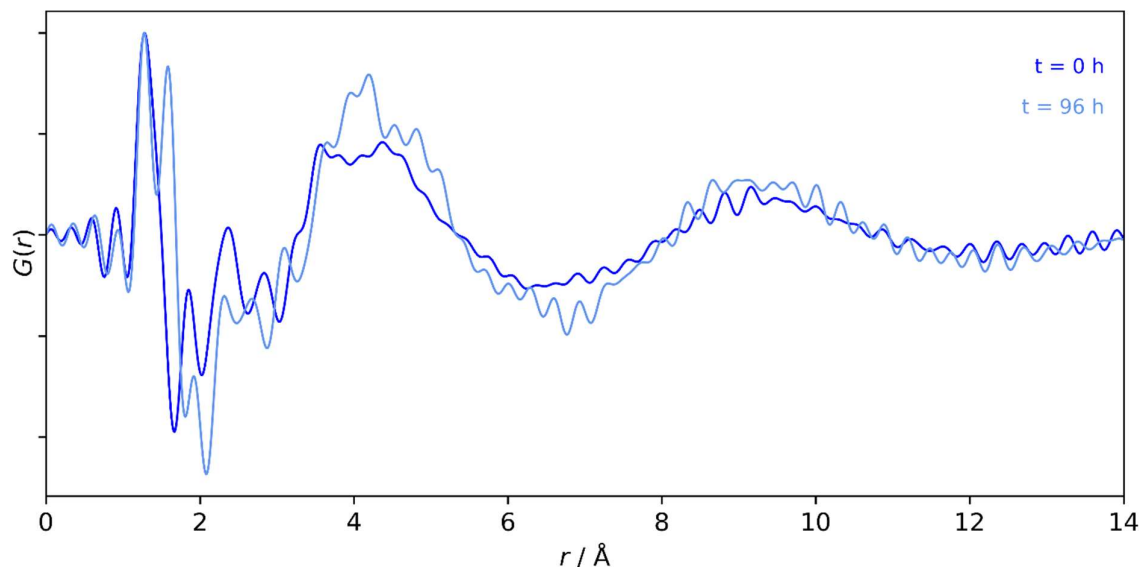


Figure 5.18. Comparison of normalised XPDF datasets for Hf-free DFW 65:25:10 (after heating at 150°C for 24 hours) at different times after synthesis.

Changes in the solvent are also visible in the ^1H NMR spectra [Figure 5.19]; similar patterns in the ‘bulk’ solution peaks are observed to those in the unheated solutions. However, unlike the unheated samples, in which changes are evident over the whole time range considered, the ‘bulk’ solvent peaks in the heated samples do not change in shift after 48 hours—even the H_3O^+ peak, which usually displays large changes in shift. This suggests that the solution processes occurring during ageing are accelerated due to the heating and so the final equilibrium state is reached sooner.

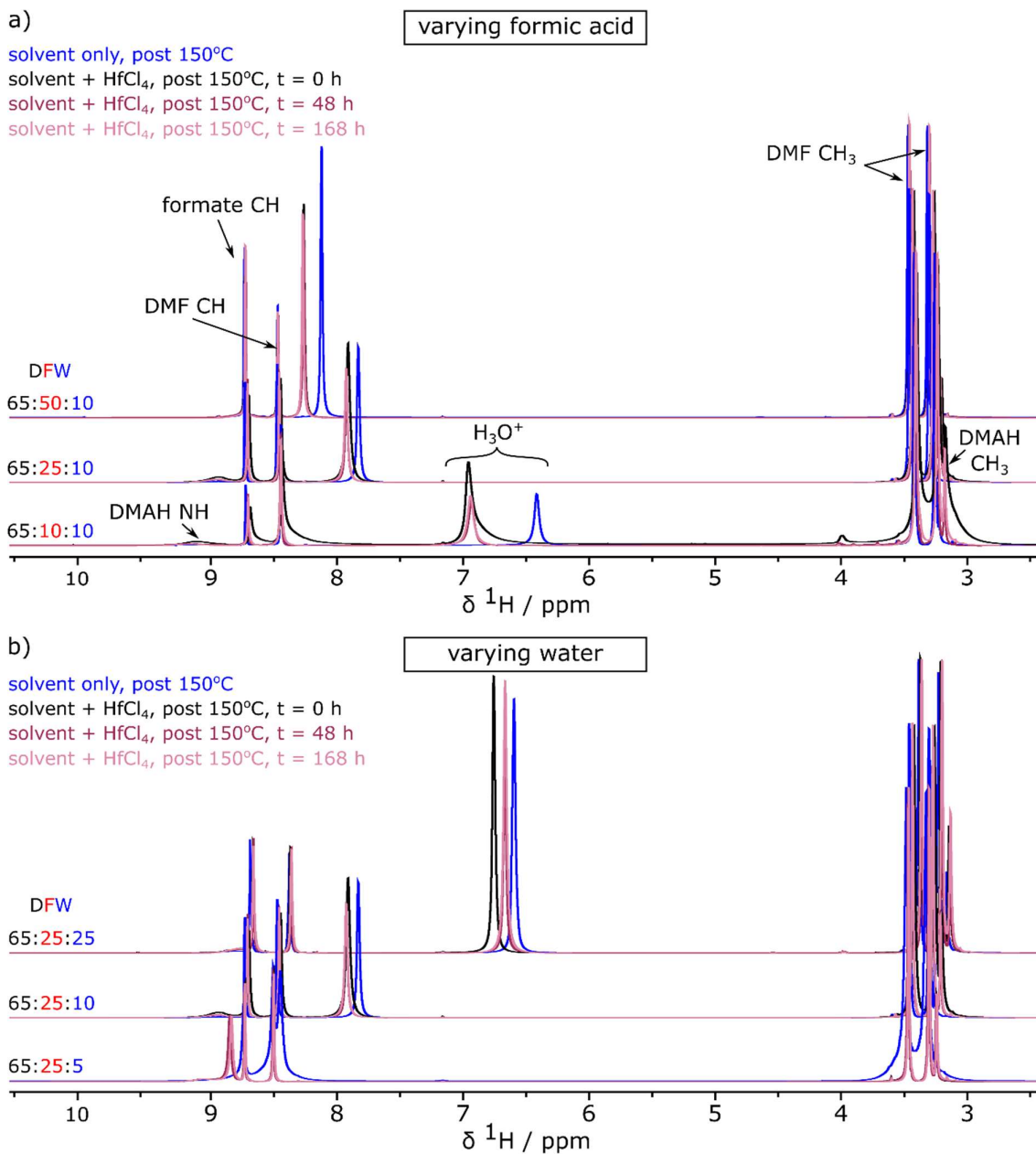


Figure 5.19. ¹H NMR of HfCl₄ in different solvents, measured at different time intervals after synthesis (heating at 150°C for 24 hours; a) varying formic acid; b) varying water.

The cluster-related peaks in the ¹H NMR spectra of HfCl₄ in DFW 65:25:10 corroborate the interpretation of the XPDF data that the double clusters degrade after heating [Figure 5.20]. These cluster-related peaks become weaker over time, in contrast to the cluster peaks in the unheated samples which increased in intensity [Figure 5.15]. This degradation is in keeping with the earlier observations of the stability of MOFs containing this cluster. The degradation products are not identifiable from either XPDF or ¹H NMR, but they are unlikely to include the single cluster or tetramer (as these would be identifiable).

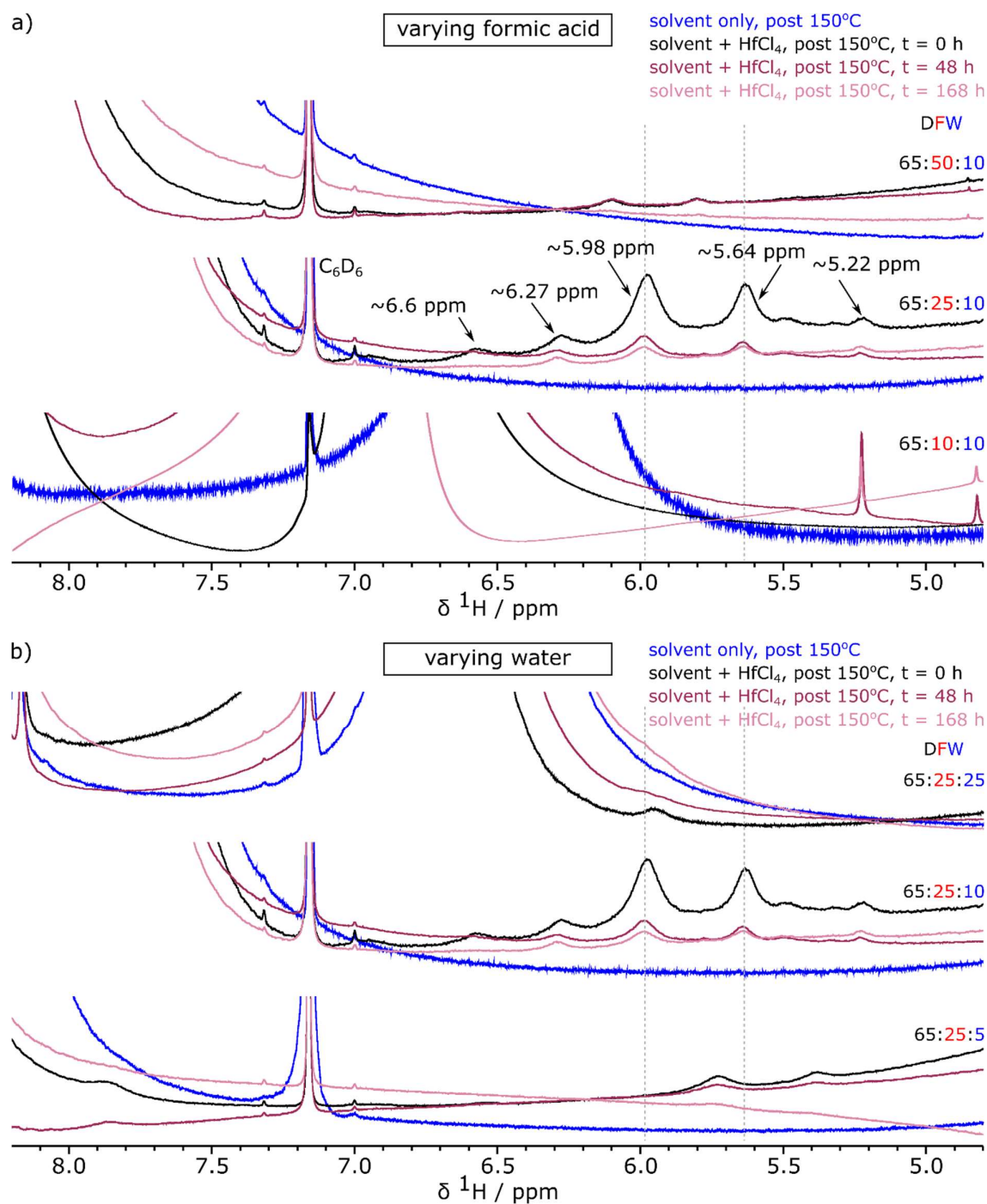


Figure 5.20. ¹H NMR of HfCl₄ in different solvents, measured at different time intervals after synthesis (heating at 150°C for 24 hours, expanded to show the region where cluster-related peaks occur: a) varying formic acid; b) varying water. Guide lines (grey, dashed) are given at 5.64 and 5.98 ppm.

The decrease in intensity is observed for the cluster peaks in all solutions, both with different amounts of formic acid and with different amounts of water. As with the bulk solvent peaks, the cluster peaks barely change in chemical shift over time, nor do there appear to be any new peaks appearing, suggesting that no new clusters form but instead that the existing

clusters degrade. Furthermore, none of the peaks appear to decrease in intensity before, or more significantly than, others, suggesting that these changes are not due merely to an alteration or exchange of coordinating ligands over time.

Post-heating HfCl_4 in DFW 65:10:10 solvent (i.e., low formic acid) appeared to contain some poorly-structured Hf complex at time $t=0$, based on XPDF analysis [Figure 5.11]. As with the clusters in DFW 65:25:10, this material degrades over time to give a pattern closely resembling the solvent only [Figure 5.21] rather than any cluster; even the Hf-Hf nearest neighbour peak at 3.5 \AA in the XPDF is lost.

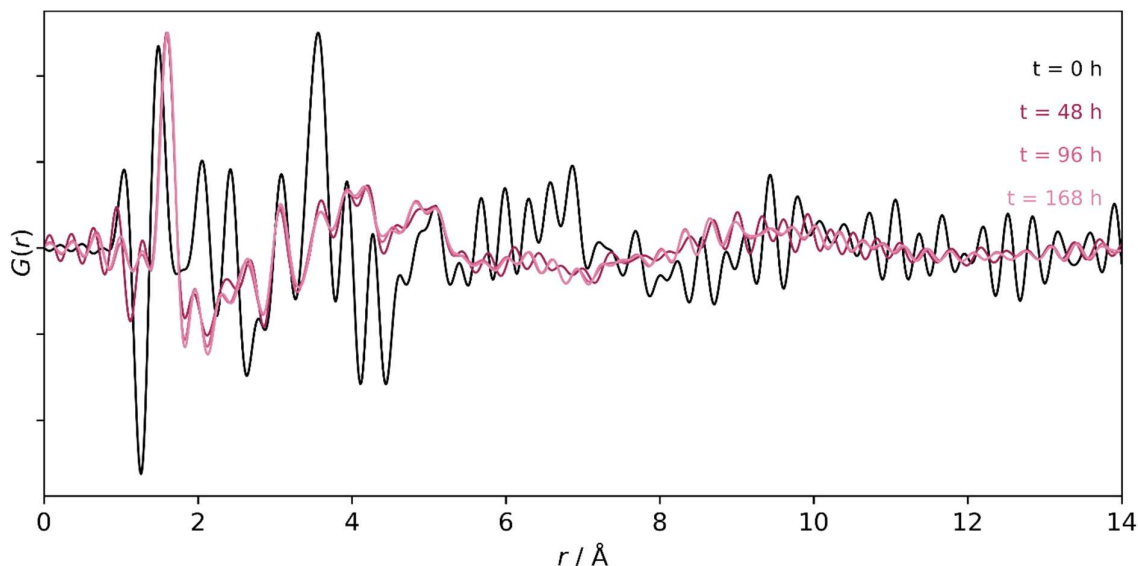


Figure 5.21. Comparison of normalised XPDF datasets for HfCl_4 in DFW 65:10:10 (reacted at 150°C for 24 hours) at different times after synthesis.

5.3 Discussion

From the outcomes of the combined NMR and XPDF experiments in this work, the presence of both water and acid are crucial to the formation of the single cluster: at low concentrations of either water or formic acid the cluster-related peaks are very weak. While in these solutions the tetramer and single cluster are found to coexist, at high concentrations of water the amount of single cluster relative to tetramer increases, again confirming the importance of water to the formation of the single cluster.

Higher overall concentrations of hafnium also favour the higher-nuclearity single cluster over the tetramer; in the previous *in situ* XPDF work, the DFW 65:25:10 solution with a lower concentration of Hf (1 : 232 : 183 : 153 Hf : DMF : formic acid : water) gave a tetramer : single cluster ratio of 1 : 0.72. In a high-Hf system, where there is more competition for coordinating groups, the formation of single clusters might be favoured due to their lower coordination requirements for water/hydroxide per cluster (up to 4 water/hydroxide directly coordinated per Hf), as opposed to tetramers which require more water coordination per cluster (6 water/hydroxide directly coordinated per Hf). The single cluster can also reduce its coordination requirement for water/hydroxide through coordinating formate ligands.

Acid is clearly important in the formation of the single cluster from the tetramer, but this reaction is not specific to formic acid alone. In solutions of acetic acid and water, increasing the amount of acetic acid relative to metal ions has been found to increase the proportion of single cluster and decrease the proportion of tetramer; this has also been observed for HCl.^{201,294} A similar behaviour could be occurring in the solutions in this work.

In all of the unheated samples in DFW solvents, the single cluster is present. In addition, upon ageing the solutions, the amount of single cluster relative to tetramer increases over time. These observations suggest that the single cluster is stable in a wide range of conditions, and that in these solutions the single cluster is thermodynamically more favourable. This goes some way to explain why this cluster motif is so common in MOF structures, despite the variety of synthesis conditions used.

In heated cluster-containing solutions, the double cluster forms. However, elevated temperature alone does not guarantee the formation of the double cluster: the amounts of formic acid and water present also have a significant effect. The range of conditions in which

the double cluster is formed is much more limited than for the single cluster or tetramer, which may explain why this cluster motif is not commonly observed.^{191,291} No—or weak—double cluster peaks are seen in the ¹H NMR spectra of solutions with either high or low amounts of formic acid and water: it seems that, for the double cluster to form, the *relative* amounts of formic acid and water are critical.

The presence of water in the solvent increases the likelihood of hydrolysis which is likely to disfavour cluster aggregation (for reasons previously discussed), so it may seem counterintuitive that low amounts of water in the solution also disfavours the formation of the double cluster. Although in unheated solutions the single cluster is favoured with higher amounts of water, the low-water solvent composition also allows for the formation of the tetramer/single cluster (albeit in low quantities) even though these species both require the presence of water to form. However, it appears that upon heating the single cluster does not (fully) aggregate to form the double cluster; in the heated solutions with low amounts of water the single cluster is observed alongside the double cluster.

The double cluster needs the presence of water to form, as there need to be enough water/hydroxide groups on the single clusters to form the μ_2 -OH bridging groups during cluster condensation. The condensation of the double cluster releases both coordinated and coordination-shell water into the 'bulk' solution²⁵⁵ but this process is likely to be insufficient on its own to enable complete, bulk double-cluster condensation, especially if water is being lost due to hydrolysis. Therefore the amount of water added in the synthesis needs to balance between too little (and therefore less likelihood of cluster condensation) and too much (which will favour hydrolysis and therefore the high pH which disfavours the aggregation of higher-nuclearity clusters).

Too high formic acid relative to the amount of water in the solvent, whilst favouring the formation of the single cluster at room temperature, also disfavours the formation of the double cluster in heated solution. This is potentially due to competition as a ligand on the single cluster, as insufficient water/hydroxide ligands will make it harder for the cluster condensation to occur.

That no identifiable clusters form in a heated solution with low formic acid is key to understanding this system: one of the functions of formic acid in the heated solutions is to

oppose the equilibrium process of hydrolysis of DMF, as well as preventing the pH from rising as significantly upon the production of dimethylamine (dimethylammonium, if protonated). It can therefore be inferred that in the low-formic-acid case the solution is likely to become more basic during the heating reaction, especially if formic acid is also lost to decomposition. Heating of acidic solutions is known to increase the amount of bridging μ_2 -OH between metal centres, and also encourages their conversion to μ_3 -O and μ_3 -OH groups.^{130,190,218} At higher pH, however, a variety of mostly mononuclear species is known to exist.^{197,218} Even though at room temperature the single cluster or tetramer might exist, if the solution is heated without sufficient formic acid to oppose the hydrolysis and lower the pH then the aggregation of the clusters will be disfavoured in comparison to lower-nuclearity species.¹⁹⁷ Supporting this suggestion, the solution with low formic acid only shows a peak in the XPDF pattern at 3.5 Å, corresponding to the nearest-neighbour Hf-Hf distance in a metal-oxo cluster; no higher-separation peaks are visible, suggesting that whatever species is present is of low nuclearity.

Not only does the double cluster have a smaller range of favourable reaction conditions, but it also appears to be less stable than the single cluster. The unheated samples show a change in composition over time towards greater proportions of the single cluster. Ageing of the DFW solutions allows hydrolysis of DMF to occur, even without heating, so the increase in the single cluster suggests that the single cluster species is not only thermodynamically stable but that its formation is not as hindered by the changes in the solution (including change in pH) due to the DMF hydrolysis. In contrast, for the post-heating solutions, every sample for which cluster-related ^1H NMR peaks are observed—including the sample known to contain the double cluster—appears to degrade over time. No other cluster species are observed to appear upon refinement against XPDF datasets, even at long ageing times. Structural degradation can, however, be observed. This is most significant in clusters observed in the low-formic-acid solution in which even the nearest-neighbour Hf-Hf distances which indicate metal-oxo structures are lost. Potentially, over time, more monomeric Hf complexes are preferentially formed as the pH rises due to increased hydrolysis.¹⁹⁷

5.4 Conclusions

The understanding gained from this work about the nature and behaviour of these metal clusters in DMF : formic acid : water solutions gives clues regarding the synthesis of Hf and Zr MOFs in similar solutions.

The amount of water present has been shown to be crucial to the identity of the cluster formed, which in turn determines the MOF structure. The reaction temperature is similarly important.¹² However, while the identity and concentration of the acid present has long been known to be critical to the MOF framework,^{12,141,175,251} this work provides insights into the underlying reasons. Hf and Zr MOFs are commonly synthesised with acidic modulators,^{137,210,382} allowing their properties to be tuned, as well as introducing defects.^{12,99,141,142} The exact nature of the modulator, however, could determine whether MOFs containing the double cluster will form. This work shows that the double cluster is far more sensitive than the single cluster, both to synthesis conditions and to ageing. Without sufficient acid present in the reaction, the pH of the solution would rise, disfavours the cluster aggregation.

Out of the carboxylic acids commonly used in modulated synthesis, formic acid is one of the most acidic. Other acidic modulators will not be as effective in maintaining a low reaction pH, and also, unlike formic acid, will not oppose the DMF hydrolysis equilibrium, and so may not be as effective if used in an attempt to synthesise a MOF with these high-nuclearity clusters in DMF solution. Additionally, in order for the MOF framework to coordinate, the linkers must be deprotonated. In lower-acid systems, as the temperature rises, the increase in pH could favour the deprotonation of the linkers and hence coordination to clusters before the reaction has reached the temperatures and timescales required for double cluster formation—that is, coordination to single clusters would occur first.

Excessive use of acid (especially relative to the amount of water present), however, not only disfavours the formation of the double cluster but would also interfere with the linker deprotonation, meaning that the clusters might coordinate poorly with the linkers. If the acid is also able to coordinate to the clusters (as in the case of monocarboxylic acid modulators) then high amounts of acid would cause competition for coordination,

potentially leading to not only high-defectivity MOFs¹⁴¹ but even lower-dimensional MOF structures due to the loss of connectivity.¹⁵

Thus, when designing a solvothermal MOF synthesis, all of these identified factors should be taken into account when deciding on the exact synthesis conditions and components of the reaction solution, in order to produce by design a MOF with the desired cluster nuclearity and connectivity. Furthermore, from the work in this thesis it appears that the exact ratio of clusters in these systems are a result of a complex balance of different factors including the relative concentrations of water and hafnium, and that these systems require further investigation in order to understand them.

Chapter 6. Conclusions and Future Work

The principal objective of this thesis was to explore the application of defect-engineering on hafnium metal-organic frameworks. Building upon recent discoveries of new phases and defectivities of UiO family MOFs, this work aimed firstly to systematically explore the synthesis conditions leading to these MOF structures in order to identify conditions for the synthesis of new MOF phases. This thesis then sought to investigate the formation routes of these MOFs, including their cluster intermediates: without understanding how MOFs and their intermediates form in relation to different synthesis conditions, it will not be possible to work towards the truly rational design of syntheses for new hafnium MOFs and hence to fully exploit the wealth of potential of these materials for real-world applications.

This thesis has also explored different techniques for understanding the structures and formation routes of MOFs. These techniques, when applied to other hafnium MOFs—and then to MOFs comprising different metals—can pave the way for a greater understanding of the synthesis routes of these important materials. Powder X-ray diffraction is a powerful tool, but assignment of structures must be performed carefully in order to distinguish between crystallographically-related frameworks, and to detect correlated disorder. However, it is limited in being able to characterise frameworks with greater disorder or those which are non-crystalline; pair distribution function analysis is then a valuable tool. Alongside thermogravimetric analysis and solution ^1H nuclear magnetic resonance spectroscopy of digested MOFs, the defectivities of MOFs can be calculated and characterised.

As discussed in the Introduction, UiO family metal-organic frameworks are suitable model systems for investigating the relationship between different defect types and concentrations and the resultant change in the MOF properties, as they can incorporate significant quantities of defects. Modulated synthesis—the inclusion of a monocarboxylic acid in the reaction mixture—was a particularly effective method of defect-engineering these MOFs due to the ease of tuning the incorporation of defects through adjusting the synthesis conditions. Prior to this work, it had been found that modulated solvothermal synthesis of UiO family MOFs with formic acid as a modulator can be used to obtain new defect-mediated MOF phases, nano-**reo** UiO-66(Hf) and **hcp** UiO-67(Hf).

Chapter 2 of this work builds on this discovery, investigating the effect of formic acid and of water in the modulated synthesis of UiO family MOFs on the phase produced. It shows that, by controlling the amounts of water and formic acid in the reaction, the **hcp** and **hns** phases of UiO-67(Hf) and UiO-66(Hf)(F4BDC) and the **hcp** phase of UiO-66(Hf) can be produced, with high phase-purity and crystallinity. This discovery shows that these defect-engineering principles can be applied not just to one specific MOF but to multiple different MOF analogues, to discover new phases related to the existing MOFs.

All **hcp** and **hns** phases contain the $\{[\text{Hf}_6\text{O}_4(\text{OH})_4]_2(\text{OH})_6\}^{18+}$ double cluster, which can be viewed as a condensation of two of the archetypal **fcu** UiO-66(Hf) $[\text{Hf}_6\text{O}_4(\text{OH})_4]^{12+}$ single clusters *via* bridging μ_2 -OH groups. Water and formic acid are clearly instrumental in determining the cluster formation, allowing the **hcp** and **hns** phases to be synthesised instead of the **fcu** phase. However, water and formic acid also create missing-linker defects in **hcp** UiO-66 alongside determining the phase, suggesting that they act in competition with the linker to coordinate to the metal clusters. That water and formic acid compete with the linker is further supported by the formation of different members of the isorecticular **hcp** series, with different linker species but the same cluster, requiring different amounts of acid and water to form. Acid and water affect the crystallinity of the resulting framework; high amounts of water in the reaction mixture decrease the crystallinity of **hcp** UiO-66(Hf) while increasing formic acid alongside the water regains framework crystallinity. Formic acid and water also are involved in postsynthetic ligand exchange of **hcp** UiO-66(Hf), both as cluster-terminating ligands preferentially exchanged and also as trace solvent increasing the response of the framework to the postsynthetic treatments. This contribution of formic acid and water to the postsynthetic response of **hcp** UiO-66(Hf) suggests that water and modulating acid play multiple roles in the formation of these defect-mediated phases, as an influence on the cluster aggregation, in their effect on the interactions within the solution, and as coordinating ligands in competition with the framework linkers both during and after synthesis.

The first of these potential roles of water and modulating acid is related to the cluster growth and aggregation. The reticular model of metal-organic frameworks emphasises the importance of the metal cluster on the topology of the MOF; in order to understand how the

hcp frameworks form, the growth of the metal clusters both on their own and as part of the framework must be understood. *In situ* pair distribution function analysis, which allows the structures of non-crystalline materials such as MOF precursors to be determined, was used in Chapter 3 to examine the solution formation of both **hcp** UiO-66(Hf) and the Hf₁₂ molecular clusters. This investigation showed that in the solvothermal synthesis the metal clusters evolve from a mixture of a tetramer and the Hf₆ single cluster at room temperature, to the single cluster and then to the Hf₁₂ double cluster as the heated reaction proceeds. The single clusters do not appear to break down and reform into the double clusters. The proposed formation mechanism of the double clusters instead involves the joining together of single clusters, with coordinating hydroxides on each single cluster forming a 'belt' of six μ_2 -OH, and with water molecules surplus to coordination requirements being released into the solution. When considered along with the *ex situ* syntheses in Chapter 2, especially that of **hcp** UiO-66(Hf) which required higher concentrations of water to form than the **fcu** phase, this indicates that water in the synthesis is necessary for the double clusters to form, which permits the formation of the **hcp** and **hns** phases.

The *in situ* XPDF experiment—supported by the NMR and XPDF studies in Chapters 4 and 5—also showed that the Hf₁₂ clusters form in solution prior to linking up into the MOF framework, confirming their key role in determining the topology of the resultant MOF. Additionally, despite the single clusters forming before the double cluster, no MOF containing the single cluster (i.e., **fcu** or nano-**reo** UiO-66) was observed. Based on the synthesis conditions, the clusters could be coordinated by water/hydroxide, formate or linkers; that no **fcu** framework forms suggests that the single clusters do not coordinate substantially to the linkers before condensing to produce the double clusters, perhaps due to dynamic exchange with water/hydroxide and formate ligands, and therefore that the formation of the double clusters occurs before cluster interlinking. The potential importance of this solution exchange on the resultant framework returns to the questions posed by Chapter 2: what are the effects of water and modulating acid on the interactions within the reaction solution, in particular on the metal clusters, and how are the interactions altered if the reaction composition is changed?

Chapters 4 and 5 explored the use of ^1H solution NMR, sensitive to the solvent species and ligands, to investigate the interactions between the metal clusters and the solvent. Under conditions related to the *in situ* MOF syntheses, solutions of molecular clusters (i.e., without linker) were made, varying the amounts of formic acid and water to determine their effects. The solvent systems are inherently complex, due to exchange and different strengths of hydrogen-bonding; upon heating, some of the solvent components react and the intermolecular interactions change. DMF hydrolyses to give formic acid and dimethylammonium, and formic acid decomposes, thus upon heating the amount of water in solution decreases and the pH increases. This means that the reaction conditions for clusters (and MOFs) are extremely sensitive to changes in the initial concentrations of water and formic acid, and that the effects of these components on the solvent composition are interconnected.

In these complex systems, the metal clusters form. The single clusters, forming alongside the tetramer at room temperature, are coordinated mostly by water/hydroxide along with some formate, and are likely surrounded by a coordination shell of water with which the ligands exchange rapidly. Upon heating, the tetramer is disfavoured and the cluster-surface groups on the single cluster appear to rearrange. The variable-temperature experiment also suggests that the single clusters have a preference for coordination by water/hydroxide even to higher temperatures. This local environment can enable the condensation of single clusters to form double clusters *via* μ_2 -OH bridges.

It is much more favourable for formate to coordinate to the double cluster compared to the single cluster and tetramer, although water/hydroxide groups are also coordinated. In different solvent compositions, the single cluster appears to form readily, but the double cluster does not form to a high degree in solvents with too high or too low amounts of formic acid or water; the relative amounts of formic acid and water are important. This is potentially due to the hydrolysis reaction and decomposition of formic acid affecting the cluster aggregation. With too little formic acid, or too much water, the hydrolysis of DMF could be significant, which raises the pH of the system and disfavours cluster aggregation (too little formic acid also disfavours the formation of the single clusters); too little water, or

too much formic acid, and there will be too few water/hydroxide groups on the clusters for the condensation to happen.

The **hcp** MOFs in this work require higher amounts of water and formic acid to form than their **fcu** analogues. This contrasts with the formation of the clusters, where the single cluster can form with high amounts of water and formic acid, but upon heating either the double cluster forms (with a narrower range of solvent compositions) or no/very little cluster is observed (outside of these conditions). Therefore the effects of changing the solvent composition on the formation of the full MOF, and on the incorporation of defects, are not only related to the formation of the clusters themselves but also to their coordinating ligands.

Both the single and double molecular clusters show coordinates to water/hydroxide and formate, although the coordination preferences vary. In the MOFs based on these clusters, these coordination groups are also observed as defects. Chapter 2 indicates that **hcp** samples synthesised with high amounts of water and lower amounts of formic acid have poorer crystallinity than samples synthesised with high amounts of both water and formic acid. This observation suggests that water may play a dominant role not just as the main coordination species on the single cluster, crucial to the formation of the double cluster, but also in the initial formation of defects in the MOF structure. Exploiting these defects, postsynthetic experiments on **hcp** UiO-66(Hf) suggest that, where clusters are initially coordinated (and so defects are initially compensated) by water/hydroxide, these terminating ligands are then replaced by formate where available: in the postsynthetic ligand exchange the water/hydroxide terminating groups on the double cluster are replaced by PyDC to a higher degree than the formate terminating groups.

In the *in situ* experiments in Chapter 3, the clusters link together to form the **hcp** MOF after the double clusters have formed, suggesting that the linkers coordinate less readily than the formate ligands (potentially due to poor solubility in DMF¹² or slow deprotonation in acidic solvent). The slower, two-step growth of the **hcp** framework at lower temperatures also has implications related to the difference in coordination between linkers and defect-compensating ligands. If cluster aggregation is slowed or disfavoured, either due to lower temperature or solvent composition, then the double clusters might not form (or form

slowly relative to linker coordination), resulting in a different framework coordination. In reactions such as the formation of the nano-**reo** phase of UiO-66(Hf), which have (relative to the amount of linker) high quantities of formic acid and low quantities of water, and where the domain structure of the MOF appears to indicate the concomitant, competitive formation of the **reo** structure (high defect : linker ratio) next to the **fcu** structure (lower defect: linker ratio),¹⁷⁵ the limited amount of water present may disfavour the formation of the double cluster and so allow the formate groups to coordinate competitively with the linkers to give the nano-**reo** domains.

Modulated synthesis, often used to incorporate missing-linker defects, has showed great potential for the future of controlling defects in MOFs. This thesis has shown that defect-engineering can be used as a starting point for the creation of hafnium MOFs with new cluster species and new topologies. However, the relationship between the solvent composition and reaction temperature and the cluster formation and subsequent framework coordination is extremely important and cannot be overlooked when considering alterations to the synthesis conditions.

This thesis has focussed on one family of MOFs, and a limited range of conditions. While members of the UiO family of MOFs are particularly ideal for exploitation due to their ease of forming defects and their stability in real-world conditions, and so were good candidates for exploration of formation routes, many other MOFs are still to be examined in this manner. Formic acid and water in particular are notable for their influence on the MOF structure *via* correlated defects; however, the formation in this work of **hcp** UiO-66(Hf) (F₄BDC), using acetic acid as a modulator, indicates that other solvents and modulating acids have the potential for exciting effects on the MOF synthesis such as the creation of new phases and defect structures. This work has also shown that temperature is an important factor in the formation of UiO family MOFs; further systematic studies on these frameworks over a range of temperatures would therefore complement the discoveries in this thesis.

By using the insights in this work, the syntheses of other hafnium MOFs, and their zirconium analogues, can be explored with the aim of producing new structures, including through the use of defect-engineering. While the M₆ and M₁₂ clusters are dominant in these DMF : formic acid : water systems, by controlling the connectivity of these clusters new

MOF topologies can be obtained. Furthermore, if Hf and Zr clusters of other nuclearities can be accessed under MOF synthesis conditions, the wealth of known cluster species can be applied to the creation of new Hf and Zr MOFs. Moving even further, there is the potential for creating MOFs with previously-undiscovered cluster species. For example, if M_6 clusters can condense together to form M_{12} double clusters, and 1D clusters comparable to 'infinite' chains of M_6 clusters are already known, it should be possible to synthesise clusters of intermediate sizes (with selected numbers of M_6 'repeat units'). Mixed-cluster MOFs could also be obtained; by considering the timing of the cluster coordination, it is also possible that MOF syntheses could be 'seeded' with pre-synthesised clusters to obtain a desired structure. This could be used to grow MOFs with epitaxial layers or core-shell forms⁷⁸ with directional stabilities and guest-binding properties, which have potential as drug delivery systems.^{401,402}

The process of defect-engineering used in this thesis has also enabled the creation of stable Hf MOF-based nanosheets, such as **hns** UiO-67(Hf), with good reproducibility. This method opens up avenues for the synthesis of other stable MOF nanomaterials. If cluster condensation can be controlled to achieve a selected number of 'repeat units' as mentioned in the last paragraph, this could not only give anisotropic MOF frameworks—ideal for applications such as separating membranes⁴¹—but also allow precise control over the layer, and hence the nanosheet, thickness.⁴ Postsynthetic treatment, exploiting the chemical anisotropy of 3-D frameworks with non-isotropic clusters, could also be used to create MOF nanomaterials. Observing the anisotropic response of **hcp** UiO-66 and **hcp** UiO-67 to postsynthetic exchange reveals the potential for deliberate delamination of these materials; furthermore, linkers with new functionalities¹²⁸ could be introduced selectively within the MOF framework, for example only within the *ab*-plane, creating even greater chemical anisotropy. Future work could also explore the possibility of postsynthetic treatment to functionalise the missing-linker sites on the clusters in defective MOFs, for example for catalysis,⁹⁶ or to react with functional groups on the linkers and introduce new properties.

This thesis has further emphasised the importance of understanding the formation routes of MOFs, using techniques such as NMR on reaction solutions and *in situ* pair distribution function analysis. Solution NMR experiments have shown the complexity of the dynamics and exchange behaviours in these solutions, both between cluster environments and with

the reaction solution: this motivates further study, including simulations, to explore the subtleties of these systems. Additionally, this thesis focussed on exploring the interactions of molecular clusters with ^1H NMR, but the additional effect of adding linker species to the reaction remains to be explored *via* this technique. This thesis has only shown a glimpse of the possibilities for the future of these techniques; in particular, since insights into the processes occurring during MOF reactions are key to the future of rational design of MOF syntheses, *in situ* techniques are particularly ripe for innovation. Combinations of *in situ* NMR and XPDF, with their different sensitivities, enable tracking of changes in the reaction solution, in MOF cluster precursors and in crystallisation processes.^{273,278,294} Owing to the fast reactions of some MOF species, and potential issues with signal-to-noise ratios, it can be difficult to observe fine detail in traditional experimental setups. Future experiments investigating the formation of MOFs and their precursors could take inspiration from *in situ* techniques such as microfluidics and continuous sampling methods,⁴⁰³ time-resolved flow hydrothermal cells^{ss} and flow NMR,³¹⁹ which are already being developed to understand reactions in fields ranging from biology to batteries.

Overall, this thesis has demonstrated the importance of understanding the formation routes of metal-organic frameworks. Without full knowledge of the relationship between the reaction conditions and the cluster growth and framework coordination, the ideal of *rational design* of new MOF structures remains far off. In solvothermal synthesis, which is the predominant method of MOF creation, interactions between the MOF components and the reaction solution are non-trivial and therefore the choice of solvent must be carefully made, with full consideration of additional factors such as temperature and side-reactions. This thesis demonstrates that approaching the formation of MOFs from the perspective of defect-engineering is advantageous in understanding the relationships between different MOF

^{ss} From the website of I15-1, Diamond Light Source, September 2021:

“XPDF is also commissioning two new in-situ environments focussed on time-resolved measurements in reacting solutions. Both environments allow for steady state measurements to be taken at time increments after two precursor solutions are passively mixed. The first cell is aimed at longer duration reactions, consisting of eight measurement positions. Here the first measurement is available for reaction times greater than ca. 0.5 seconds. The second cell is targeted at much faster reactions where data can be collected at times greater than ca. 0.05 seconds after mixing. It will be possible to run both cells at elevated temperature, to a maximum of 250°C.”⁴⁰⁷

structures. This further inspires the exploration of MOF precursors in order to understand the connection between the pre-crystallisation coordination species, the formation of defects, and the resultant MOF structures. Applying the techniques used in this thesis to other MOF families, with hafnium clusters and with other metals, will enable the creation of new MOF materials *via* understanding of their fundamental reaction chemistries, and further open up the wealth of these exciting materials for real-world applications.

Bibliography

- (1) O'Keeffe, M.; Yaghi, O. M. Deconstructing the Crystal Structures of Metal–Organic Frameworks and Related Materials into Their Underlying Nets. *Chem. Rev.* **2012**, *112* (2), 675–702. <https://doi.org/10.1021/cr200205j>.
- (2) O'Keeffe, M.; Peskov, M. A.; Ramsden, S. J.; Yaghi, O. M. The Reticular Chemistry Structure Resource (RCSR) Database of, and Symbols for, Crystal Nets. *Acc. Chem. Res.* **2008**, *41* (12), 1782–1789. <https://doi.org/10.1021/ar800124u>.
- (3) Yaghi, O. M.; Kalmutzki, M. J.; Diercks, C. S. Emergence of Metal-Organic Frameworks. In *Introduction to Reticular Chemistry*; Wiley, 2019; pp 1–27. <https://doi.org/10.1002/9783527821099.ch1>.
- (4) Furukawa, H.; Cordova, K. E.; O'Keeffe, M.; Yaghi, O. M. The Chemistry and Applications of Metal-Organic Frameworks. *Science (80-.)*. **2013**, *341* (6149), 1230444. <https://doi.org/10.1126/science.1230444>.
- (5) Batten, S. R.; Champness, N. R.; Chen, X.-M.; Garcia-Martinez, J.; Kitagawa, S.; Öhrström, L.; O'Keeffe, M.; Paik Suh, M.; Reedijk, J. Terminology of Metal–Organic Frameworks and Coordination Polymers (IUPAC Recommendations 2013). *Pure Appl. Chem.* **2013**, *85* (8), 1715–1724. <https://doi.org/10.1351/PAC-REC-12-11-20>.
- (6) Batten, S. R.; Champness, N. R.; Chen, X. M.; Garcia-Martinez, J.; Kitagawa, S.; Öhrström, L.; O'Keeffe, M.; Suh, M. P.; Reedijk, J. Coordination Polymers, Metal-Organic Frameworks and the Need for Terminology Guidelines. *CrystEngComm* **2012**, *14* (9), 3001–3004. <https://doi.org/10.1039/c2ce06488j>.
- (7) Yaghi, O. M.; Li, H. Hydrothermal Synthesis of a Metal-Organic Framework Containing Large Rectangular Channels. *J. Am. Chem. Soc.* **1995**, *117* (41), 10401–10402. <https://doi.org/10.1021/ja00146a033>.
- (8) Moghadam, P. Z.; Li, A.; Wiggin, S. B.; Tao, A.; Maloney, A. G. P.; Wood, P. A.; Ward, S. C.; Fairen-Jimenez, D. Development of a Cambridge Structural Database Subset: A Collection of Metal-Organic Frameworks for Past, Present, and Future. *Chemistry of Materials*. American Chemical Society April 11, 2017, pp 2618–2625.

<https://doi.org/10.1021/acs.chemmater.7b00441>.

- (9) Moosavi, S. M.; Nandy, A.; Jablonka, K. M.; Ongari, D.; Janet, J. P.; Boyd, P. G.; Lee, Y.; Smit, B.; Kulik, H. J. Understanding the Diversity of the Metal-Organic Framework Ecosystem. *Nat. Commun.* **2020**, *11* (1), 4068. <https://doi.org/10.1038/s41467-020-17755-8>.
- (10) Miner, E. M.; Dincă, M. Metal-Organic Frameworks: Evolved Oxygen Evolution Catalysts. *Nat. Energy* **2016**, *1* (12), 16186. <https://doi.org/10.1038/nenergy.2016.186>.
- (11) Zhao, Y.; Song, Z.; Li, X.; Sun, Q.; Cheng, N.; Lawes, S.; Sun, X. Metal Organic Frameworks for Energy Storage and Conversion. *Energy Storage Mater.* **2016**, *2*, 35–62. <https://doi.org/10.1016/j.ensm.2015.11.005>.
- (12) Cliffe, M. J.; Castillo-Martínez, E.; Wu, Y.; Lee, J.; Forse, A. C.; Firth, F. C. N.; Moghadam, P. Z.; Fairen-Jimenez, D.; Gaultois, M. W.; Hill, J. A.; Magdysyuk, O. V.; Slater, B.; Goodwin, A. L.; Grey, C. P. Metal–Organic Nanosheets Formed via Defect-Mediated Transformation of a Hafnium Metal–Organic Framework. *J. Am. Chem. Soc.* **2017**, *139* (15), 5397–5404. <https://doi.org/10.1021/jacs.7b00106>.
- (13) Pullen, S.; Fei, H.; Orthaber, A.; Cohen, S. M.; Ott, S. Enhanced Photochemical Hydrogen Production by a Molecular Diiron Catalyst Incorporated into a Metal–Organic Framework. *J. Am. Chem. Soc.* **2013**, *135* (45), 16997–17003. <https://doi.org/10.1021/ja407176p>.
- (14) Katz, M. J.; Brown, Z. J.; Colón, Y. J.; Siu, P. W.; Scheidt, K. a; Snurr, R. Q.; Hupp, J. T.; Farha, O. K. A Facile Synthesis of UiO-66, UiO-67 and Their Derivatives. *Chem. Commun.* **2013**, *49* (82), 9449. <https://doi.org/10.1039/c3cc46105j>.
- (15) Shearer, G. C.; Chavan, S.; Bordiga, S.; Svelle, S.; Olsbye, U.; Lillerud, K. P. Defect Engineering: Tuning the Porosity and Composition of the Metal–Organic Framework UiO-66 via Modulated Synthesis. *Chem. Mater.* **2016**, *28* (11), 3749–3761. <https://doi.org/10.1021/acs.chemmater.6b00602>.
- (16) Horike, S.; Kitagawa, S. Design of Porous Coordination Polymers/Metal – Organic Frameworks: Past , Present and Future. In *Metal-Organic Frameworks: Applications from*

- Catalysis to Gas Storage*; Farrusseng, D., Ed.; Wiley-VCH Verlag GmbH & Co. KGaA, 2011; pp 3–21.
- (17) Zhang, X.; Chen, Z.; Liu, X.; Hanna, S. L.; Wang, X.; Taheri-Ledari, R.; Maleki, A.; Li, P.; Farha, O. K. A Historical Overview of the Activation and Porosity of Metal-Organic Frameworks. *Chem. Soc. Rev.* **2020**, *49* (20), 7406–7427. <https://doi.org/10.1039/d0cs00997k>.
- (18) Sharmin, E.; Zafar, F. Introductory Chapter: Metal Organic Frameworks (MOFs). In *Metal-Organic Frameworks*; InTech, 2016. <https://doi.org/10.5772/64797>.
- (19) Stock, N.; Biswas, S. Synthesis of Metal-Organic Frameworks (MOFs): Routes to Various MOF Topologies, Morphologies, and Composites. *Chem. Rev.* **2012**, *112* (2), 933–969. <https://doi.org/10.1021/cr200304e>.
- (20) Zhou, H.-C.; Long, J. R.; Yaghi, O. M. Introduction to Metal–Organic Frameworks. *Chem. Rev.* **2012**, *112* (2), 673–674. <https://doi.org/10.1021/cr300014x>.
- (21) Tuffnell, J. M.; Ashling, C. W.; Hou, J.; Li, S.; Longley, L.; Ríos Gómez, M. L.; Bennett, T. D. Novel Metal-Organic Framework Materials: Blends, Liquids, Glasses and Crystal-Glass Composites. *Chem. Commun.* **2019**, *55* (60), 8705–8715. <https://doi.org/10.1039/c9cc01468c>.
- (22) Bennett, T. D.; Coudert, F. X.; James, S. L.; Cooper, A. I. The Changing State of Porous Materials. *Nat. Mater.* **2021**, *20* (9), 1179–1187. <https://doi.org/10.1038/s41563-021-00957-w>.
- (23) Sapnik, A. F.; Bechis, I.; Collins, S. M.; Johnstone, D. N.; Divitini, G.; Smith, A. J.; Chater, P. A.; Addicoat, M. A.; Johnson, T.; Keen, D. A.; Jelfs, K. E.; Bennett, T. D. Mixed Hierarchical Local Structure in a Disordered Metal–Organic Framework. *Nat. Commun.* **2021**, *12* (1), 2062. <https://doi.org/10.1038/s41467-021-22218-9>.
- (24) Yaghi, O. M.; O’Keeffe, M.; Ockwig, N. W.; Chae, H. K.; Eddaoudi, M.; Kim, J. Reticular Synthesis and the Design of New Materials. *Nature* **2003**, *423* (6941), 705–714. <https://doi.org/10.1038/nature01650>.
- (25) O’Keeffe, M. Nets, Tiles, and Metal-Organic Frameworks. *APL Mater.* **2014**, *2* (12),

124106. <https://doi.org/10.1063/1.4901292>.

- (26) Li, M.; Li, D.; O’Keeffe, M.; Yaghi, O. M. Topological Analysis of Metal–Organic Frameworks with Polytopic Linkers and/or Multiple Building Units and the Minimal Transitivity Principle. *Chem. Rev.* **2014**, *114* (2), 1343–1370. <https://doi.org/10.1021/cr400392k>.
- (27) Kim, D.; Liu, X.; Lah, M. S. Topology Analysis of Metal–Organic Frameworks Based on Metal–Organic Polyhedra as Secondary or Tertiary Building Units. *Inorg. Chem. Front.* **2015**, *2* (4), 336–360. <https://doi.org/10.1039/C4QI00236A>.
- (28) Schoedel, A.; Ji, Z.; Yaghi, O. M. The Role of Metal–Organic Frameworks in a Carbon-Neutral Energy Cycle. *Nat. Energy* **2016**, *1* (4), 16034. <https://doi.org/10.1038/nenergy.2016.34>.
- (29) Ke, F.-S.; Wu, Y.-S.; Deng, H. Metal-Organic Frameworks for Lithium Ion Batteries and Supercapacitors. *J. Solid State Chem.* **2015**, *223*, 109–121. <https://doi.org/10.1016/j.jssc.2014.07.008>.
- (30) Xia, W.; Mahmood, A.; Zou, R.; Xu, Q. Metal–Organic Frameworks and Their Derived Nanostructures for Electrochemical Energy Storage and Conversion. *Energy Environ. Sci.* **2015**, *8* (7), 1837–1866. <https://doi.org/10.1039/C5EE00762C>.
- (31) He, L.; Duan, F.; Song, Y.; Guo, C.; Zhao, H.; Tian, J.-Y.; Zhang, Z.; Liu, C.-S.; Zhang, X.; Wang, P.; Du, M.; Fang, S.-M. 2D Zirconium-Based Metal-Organic Framework Nanosheets for Highly Sensitive Detection of Mucin 1: Consistency between Electrochemical and Surface Plasmon Resonance Methods. *2D Mater.* **2017**, *4* (2), 025098. <https://doi.org/10.1088/2053-1583/aa6fc6>.
- (32) He, T.; Xu, X.; Ni, B.; Wang, H.; Long, Y.; Hu, W.; Wang, X. Fast and Scalable Synthesis of Uniform Zirconium-, Hafnium-Based Metal–Organic Framework Nanocrystals. *Nanoscale* **2017**, *9* (48), 19209–19215. <https://doi.org/10.1039/C7NR06274E>.
- (33) Zhao, M.; Lu, Q.; Ma, Q.; Zhang, H. Two-Dimensional Metal-Organic Framework Nanosheets. *Small Methods* **2017**, *1* (1–2), 1600030.

<https://doi.org/10.1002/smt.201600030>.

- (34) Boyle, T. J.; Yonemoto, D. T.; Doan, T. Q.; Alam, T. M. Synthesis and Structural Characterization of Group 4 Metal Carboxylates for Nanowire Production. *Inorg. Chem.* **2014**, *53* (23), 12449–12458. <https://doi.org/10.1021/ic501904m>.
- (35) Yamanoi, Y.; Sendo, J.; Kobayashi, T.; Maeda, H.; Yabusaki, Y.; Miyachi, M.; Sakamoto, R.; Nishihara, H. A New Method To Generate Arene-Terminated Si(111) and Ge(111) Surfaces via a Palladium-Catalyzed Arylation Reaction. *J. Am. Chem. Soc.* **2012**, *134* (50), 20433–20439. <https://doi.org/10.1021/ja308606t>.
- (36) Peng, Y.; Li, Y.; Ban, Y.; Yang, W. Two-Dimensional Metal–Organic Framework Nanosheets for Membrane-Based Gas Separation. *Angew. Chemie Int. Ed.* **2017**, *56* (33), 9757–9761. <https://doi.org/10.1002/anie.201703959>.
- (37) Wang, X.; Chi, C.; Zhang, K.; Qian, Y.; Gupta, K. M.; Kang, Z.; Jiang, J.; Zhao, D. Reversed Thermo-Switchable Molecular Sieving Membranes Composed of Two-Dimensional Metal-Organic Nanosheets for Gas Separation. *Nat. Commun.* **2017**, *8* (1), 14460. <https://doi.org/10.1038/ncomms14460>.
- (38) Sun, H.; Tang, B.; Wu, P. Rational Design of S-UiO-66@GO Hybrid Nanosheets for Proton Exchange Membranes with Significantly Enhanced Transport Performance. *ACS Appl. Mater. Interfaces* **2017**, *9* (31), 26077–26087. <https://doi.org/10.1021/acsami.7b07651>.
- (39) Tang, J.; Huang, M.; Liang, Z.; Yang, Y.; Wen, Y.; Zhu, Q. L.; Wu, X. T. Water-Stable Two-Dimensional Metal-Organic Framework Nanostructures for Fe³⁺ Ions Detection. *Cryst. Growth Des.* **2021**, *21* (9), 5275–5282. <https://doi.org/10.1021/acs.cgd.1c00606>.
- (40) Zhang, S.; Wang, J.; Zhang, Y.; Ma, J.; Huang, L.; Yu, S.; Chen, L.; Song, G.; Qiu, M.; Wang, X. Applications of Water-Stable Metal-Organic Frameworks in the Removal of Water Pollutants: A Review. *Environ. Pollut.* **2021**, *291*, 118076. <https://doi.org/10.1016/j.envpol.2021.118076>.
- (41) Li, S.; Lin, J.; Ding, Y.; Xu, P.; Guo, X.; Xiong, W.; Wu, D.-Y.; Dong, Q.; Chen, J.; Zhang, L. Defects Engineering of Lightweight Metal–Organic Frameworks-Based

- Electrocatalytic Membrane for High-Loading Lithium–Sulfur Batteries. *ACS Nano* **2021**, *15* (8), 13803–13813. <https://doi.org/10.1021/acsnano.1c05585>.
- (42) Denny, M. S.; Moreton, J. C.; Benz, L.; Cohen, S. M. Metal–Organic Frameworks for Membrane-Based Separations. *Nat. Rev. Mater.* **2016**, *1* (12), 16078. <https://doi.org/10.1038/natrevmats2016.78>.
- (43) Bai, S.; Liu, X.; Zhu, K.; Wu, S.; Zhou, H. Metal–Organic Framework-Based Separator for Lithium–Sulfur Batteries. *Nat. Energy* **2016**, *1* (7), 16094. <https://doi.org/10.1038/nenergy.2016.94>.
- (44) James, S. L. Metal-Organic Frameworks. *Chem. Soc. Rev.* **2003**, *32* (5), 276. <https://doi.org/10.1039/b200393g>.
- (45) Lu, W.; Wei, Z.; Gu, Z.-Y.; Liu, T.-F.; Park, J.; Park, J.; Tian, J.; Zhang, M.; Zhang, Q.; Gentle III, T.; Bosch, M.; Zhou, H.-C. Tuning the Structure and Function of Metal–Organic Frameworks via Linker Design. *Chem. Soc. Rev.* **2014**, *43* (16), 5561–5593. <https://doi.org/10.1039/C4CS00003J>.
- (46) Yuan, S.; Qin, J.-S.; Li, J.; Huang, L.; Feng, L.; Fang, Y.; Lollar, C.; Pang, J.; Zhang, L.; Sun, D.; Alsalme, A.; Cagin, T.; Zhou, H.-C. Retrosynthesis of Multi-Component Metal–organic Frameworks. *Nat. Commun.* **2018**, *9* (1), 808. <https://doi.org/10.1038/s41467-018-03102-5>.
- (47) Rowsell, J. L. C.; Yaghi, O. M. Metal–Organic Frameworks: A New Class of Porous Materials. *Microporous Mesoporous Mater.* **2004**, *73* (1–2), 3–14. <https://doi.org/10.1016/j.micromeso.2004.03.034>.
- (48) Kim, J.; Nam, D.; Kitagawa, H.; Lim, D. W.; Choe, W. Discovery of Zr-Based Metal–Organic Polygon: Unveiling New Design Opportunities in Reticular Chemistry. *Nano Res.* **2021**, *14* (2), 392–397. <https://doi.org/10.1007/s12274-020-2830-9>.
- (49) Fu, H.-R.; Wang, F.; Zhang, J. The Photoluminescence and Gas Sorption Properties of Three Cd(II) MOFs Based on 1,3,5-Benzenetricarboxate with –NH₂ or –OH Groups. *Dalt. Trans.* **2014**, *43* (12), 4668. <https://doi.org/10.1039/c3dt52940a>.
- (50) Cavka, J. H.; Jakobsen, S.; Olsbye, U.; Guillou, N.; Lamberti, C.; Bordiga, S.; Lillerud,

- K. P. A New Zirconium Inorganic Building Brick Forming Metal Organic Frameworks with Exceptional Stability. *J. Am. Chem. Soc.* **2008**, *130* (42), 13850–13851.
<https://doi.org/10.1021/ja8057953>.
- (51) Smith, G. L.; Eyley, J. E.; Han, X.; Zhang, X.; Li, J.; Jacques, N. M.; Godfrey, H. G. W.; Argent, S. P.; McCormick McPherson, L. J.; Teat, S. J.; Cheng, Y.; Frogley, M. D.; Cinque, G.; Day, S. J.; Tang, C. C.; Easun, T. L.; Rudić, S.; Ramirez-Cuesta, A. J.; Yang, S.; Schröder, M. Reversible Coordinative Binding and Separation of Sulfur Dioxide in a Robust Metal–Organic Framework with Open Copper Sites. *Nat. Mater.* **2019**, *18* (12), 1358–1365. <https://doi.org/10.1038/s41563-019-0495-0>.
- (52) Vahabi, A. H.; Norouzi, F.; Sheibani, E.; Rahimi-Nasrabadi, M. Functionalized Zr–UiO-67 Metal–Organic Frameworks: Structural Landscape and Application. *Coord. Chem. Rev.* **2021**, *445*, 214050. <https://doi.org/10.1016/j.ccr.2021.214050>.
- (53) Ayala, S.; Zhang, Z.; Cohen, S. M. Hierarchical Structure and Porosity in UiO-66 PolyMOFs. *Chem. Commun.* **2017**, *53* (21), 3058–3061.
<https://doi.org/10.1039/C6CC10225E>.
- (54) Ji, P.; Drake, T.; Murakami, A.; Oliveres, P.; Skone, J. H.; Lin, W. Tuning Lewis Acidity of Metal–Organic Frameworks via Perfluorination of Bridging Ligands: Spectroscopic, Theoretical, and Catalytic Studies. *J. Am. Chem. Soc.* **2018**, *140* (33), 10553–10561.
<https://doi.org/10.1021/jacs.8b05765>.
- (55) Eddaoudi, M.; Moler, D. B.; Li, H.; Chen, B.; Reineke, T. M.; O’Keeffe, M.; Yaghi, O. M. Modular Chemistry: Secondary Building Units as a Basis for the Design of Highly Porous and Robust Metal–Organic Carboxylate Frameworks. *Acc. Chem. Res.* **2001**, *34* (4), 319–330. <https://doi.org/10.1021/ar000034b>.
- (56) Easun, T. L.; Nevin, A. C. Metal Nodes and Metal Sites in Metal–Organic Frameworks. In *Organometallic Chemistry*; Patmore, N. J., Elliott, P. I. ., Eds.; The Royal Society of Chemistry, 2018; Vol. 42, pp 54–79. <https://doi.org/10.1039/9781788010672-00054>.
- (57) Kalmutzki, M. J.; Hanikel, N.; Yaghi, O. M. Secondary Building Units as the Turning Point in the Development of the Reticular Chemistry of MOFs. *Sci. Adv.* **2018**, *4* (10),

- aat9180. <https://doi.org/10.1126/sciadv.aat9180>.
- (58) Guillermin, V.; Eddaoudi, M. The Importance of Highly Connected Building Units in Reticular Chemistry: Thoughtful Design of Metal-Organic Frameworks. *Acc. Chem. Res.* **2021**, *54* (17), 3298–3312. <https://doi.org/10.1021/acs.accounts.1c00214>.
- (59) Reinsch, H.; Fröhlich, D.; Waitschat, S.; Chavan, S.; Lillerud, K.-P.; Henninger, S.; Stock, N. Optimisation of Synthesis Conditions for UiO-66-CO₂H towards Scale-up and Its Vapour Sorption Properties. *React. Chem. Eng.* **2018**, *3* (3), 365–370. <https://doi.org/10.1039/C7RE00214A>.
- (60) Hermer, N.; Wharmby, M. T.; Stock, N. Re-Determination of the Crystal Structure of MIL-91(Al). *Zeitschrift für Anorg. und Allg. Chemie* **2017**, *643* (2), 137–140. <https://doi.org/10.1002/zaac.201600358>.
- (61) Bosch, M.; Yuan, S.; Zhou, H.-C. Group 4 Metals as Secondary Building Units: Ti, Zr, and Hf-Based MOFs. In *The Chemistry of Metal-Organic Frameworks: Synthesis, Characterization, and Applications*; Kaskel, S., Ed.; Wiley-VCH Verlag GmbH & Co. KGaA: Weinheim, Germany, 2016; pp 137–170. <https://doi.org/10.1002/9783527693078.ch6>.
- (62) Planas, N.; Mondloch, J. E.; Tussupbayev, S.; Borycz, J.; Gagliardi, L.; Hupp, J. T.; Farha, O. K.; Cramer, C. J. Defining the Proton Topology of the Zr 6 -Based Metal–Organic Framework NU-1000. *J. Phys. Chem. Lett.* **2014**, *5* (21), 3716–3723. <https://doi.org/10.1021/jz501899j>.
- (63) Xiao, Y.; Han, L.; Zhang, L.; Gates, B. C.; Yang, D. Pair Sites on Nodes of Metal–Organic Framework Hcp UiO-66 Catalyze Tert -Butyl Alcohol Dehydration. *J. Phys. Chem. Lett.* **2021**, *12* (26), 6085–6089. <https://doi.org/10.1021/acs.jpcclett.1c01574>.
- (64) Yang, D.; Babucci, M.; Casey, W. H.; Gates, B. C. The Surface Chemistry of Metal Oxide Clusters: From Metal–Organic Frameworks to Minerals. *ACS Cent. Sci.* **2020**, *6* (9), 1523–1533. <https://doi.org/10.1021/acscentsci.0c00803>.
- (65) Trickett, C. A.; Osborn Popp, T. M.; Su, J.; Yan, C.; Weisberg, J.; Huq, A.; Urban, P.; Jiang, J.; Kalmutzki, M. J.; Liu, Q.; Baek, J.; Head-Gordon, M. P.; Somorjai, G. A.;

- Reimer, J. A.; Yaghi, O. M. Identification of the Strong Brønsted Acid Site in a Metal–Organic Framework Solid Acid Catalyst. *Nat. Chem.* **2019**, *11* (2), 170–176.
<https://doi.org/10.1038/s41557-018-0171-z>.
- (66) Nandy, A.; Forse, A. C.; Witherspoon, V. J.; Reimer, J. A. NMR Spectroscopy Reveals Adsorbate Binding Sites in the Metal–Organic Framework UiO-66(Zr). *J. Phys. Chem. C* **2018**, *122* (15), 8295–8305. <https://doi.org/10.1021/acs.jpcc.7b12628>.
- (67) Kalaji, A.; Soderholm, L. Aqueous Hafnium Sulfate Chemistry: Structures of Crystalline Precipitates. *Inorg. Chem.* **2014**, *53* (20), 11252–11260.
<https://doi.org/10.1021/ic501841e>.
- (68) Bai, Y.; Dou, Y.; Xie, L.-H.; Rutledge, W.; Li, J.-R.; Zhou, H.-C. Zr-Based Metal–Organic Frameworks: Design, Synthesis, Structure, and Applications. *Chem. Soc. Rev.* **2016**, *45* (8), 2327–2367. <https://doi.org/10.1039/C5CS00837A>.
- (69) Whitesides, G. M.; Boncheva, M. Beyond Molecules: Self-Assembly of Mesoscopic and Macroscopic Components. *Proc. Natl. Acad. Sci.* **2002**, *99* (8), 4769–4774.
<https://doi.org/10.1073/pnas.082065899>.
- (70) Guillermin, V.; Gross, S.; Serre, C.; Devic, T.; Bauer, M.; Férey, G. A Zirconium Methacrylate Oxocluster as Precursor for the Low-Temperature Synthesis of Porous Zirconium(IV) Dicarboxylates. *Chem. Commun.* **2010**, *46* (5), 767–769.
<https://doi.org/10.1039/B914919H>.
- (71) Wang, S.; Reinsch, H.; Heymans, N.; Wahiduzzaman, M.; Martineau-Corcós, C.; De Weireld, G.; Maurin, G.; Serre, C. Toward a Rational Design of Titanium Metal–Organic Frameworks. *Matter* **2020**, *2* (2), 440–450.
<https://doi.org/10.1016/j.matt.2019.11.002>.
- (72) Walther, P.; Puchberger, M.; Kogler, F. R.; Schwarz, K.; Schubert, U. Ligand Dynamics on the Surface of Zirconium Oxo Clusters. *Phys. Chem. Chem. Phys.* **2009**, *11* (19), 3640.
<https://doi.org/10.1039/b820731c>.
- (73) Laybourn, A.; Katrib, J.; Ferrari-John, R. S.; Morris, C. G.; Yang, S.; Udoudo, O.; Easun, T. L.; Dodds, C.; Champness, N. R.; Kingman, S. W.; Schröder, M. Metal–Organic

- Frameworks in Seconds via Selective Microwave Heating. *J. Mater. Chem. A* **2017**, *5* (16), 7333–7338. <https://doi.org/10.1039/C7TA01493G>.
- (74) Griffin, S. L.; Briuglia, M. L.; ter Horst, J. H.; Forgan, R. S. Assessing Crystallisation Kinetics of Zr Metal–Organic Frameworks through Turbidity Measurements to Inform Rapid Microwave-Assisted Synthesis. *Chem. – A Eur. J.* **2020**, *26* (30), 6910–6918. <https://doi.org/10.1002/chem.202000993>.
- (75) M. V., V.; Nageswaran, G. Review—Direct Electrochemical Synthesis of Metal Organic Frameworks. *J. Electrochem. Soc.* **2020**, *167* (15), 155527. <https://doi.org/10.1149/1945-7111/abc6c6>.
- (76) Campagnol, N.; Van Assche, T. R. C.; Li, M.; Stappers, L.; Dincă, M.; Denayer, J. F. M.; Binnemans, K.; De Vos, D. E.; Fransaer, J. On the Electrochemical Deposition of Metal–Organic Frameworks. *J. Mater. Chem. A* **2016**, *4* (10), 3914–3925. <https://doi.org/10.1039/C5TA10782B>.
- (77) Cheong, V. F.; Moh, P. Y. Recent Advancement in Metal–Organic Framework: Synthesis, Activation, Functionalisation, and Bulk Production. *Mater. Sci. Technol.* **2018**, *34* (9), 1025–1045. <https://doi.org/10.1080/02670836.2018.1468653>.
- (78) Lee, J.; Kwak, J. H.; Choe, W. Evolution of Form in Metal–Organic Frameworks. *Nat. Commun.* **2017**, *8* (1), 14070. <https://doi.org/10.1038/ncomms14070>.
- (79) Cheetham, A. K.; Mellot, C. F. In Situ Studies of the Sol–Gel Synthesis of Materials. *Chem. Mater.* **1997**, *9* (11), 2269–2279. <https://doi.org/10.1021/cm970497k>.
- (80) Hou, J.; Sapnik, A. F.; Bennett, T. D. Metal–Organic Framework Gels and Monoliths. *Chem. Sci.* **2020**, *11* (2), 310–323. <https://doi.org/10.1039/C9SC04961D>.
- (81) Fidelli, A. M.; Karadeniz, B.; Howarth, A. J.; Huskić, I.; Germann, L. S.; Halasz, I.; Etter, M.; Moon, S.-Y.; Dinnebier, R. E.; Stilinović, V.; Farha, O. K.; Friščić, T.; Užarević, K. Green and Rapid Mechanochemical Synthesis of High-Porosity NU- and UiO-Type Metal–Organic Frameworks. *Chem. Commun.* **2018**, *54* (51), 6999–7002. <https://doi.org/10.1039/C8CC03189D>.
- (82) Friščić, T. Metal–Organic Frameworks: Mechanochemical Synthesis Strategies. In

Encyclopedia of Inorganic and Bioinorganic Chemistry; John Wiley & Sons, Ltd:
Chichester, UK, 2014; pp 1–19. <https://doi.org/10.1002/9781119951438.eibc2202>.

- (83) Užarević, K.; Wang, T. C.; Moon, S.-Y.; Fidelli, A. M.; Hupp, J. T.; Farha, O. K.; Friščić, T. Mechanochemical and Solvent-Free Assembly of Zirconium-Based Metal–Organic Frameworks. *Chem. Commun.* **2016**, 52 (10), 2133–2136.
<https://doi.org/10.1039/C5CC08972G>.
- (84) Lausund, K. B.; Nilsen, O. All-Gas-Phase Synthesis of UiO-66 through Modulated Atomic Layer Deposition. *Nat. Commun.* **2016**, 7 (1), 13578.
<https://doi.org/10.1038/ncomms13578>.
- (85) Gallington, L. C.; Kim, I. S.; Liu, W.-G.; Yakovenko, A. A.; Platero-Prats, A. E.; Li, Z.; Wang, T. C.; Hupp, J. T.; Farha, O. K.; Truhlar, D. G.; Martinson, A. B. F.; Chapman, K. W. Regioselective Atomic Layer Deposition in Metal–Organic Frameworks Directed by Dispersion Interactions. *J. Am. Chem. Soc.* **2016**, 138 (41), 13513–13516.
<https://doi.org/10.1021/jacs.6b08711>.
- (86) Bauer, S.; Serre, C.; Devic, T.; Horcajada, P.; Marrot, J.; Férey, G.; Stock, N. High-Throughput Assisted Rationalization of the Formation of Metal Organic Frameworks in the Iron(III) Aminoterephthalate Solvothermal System. *Inorg. Chem.* **2008**, 47 (17), 7568–7576. <https://doi.org/10.1021/ic800538r>.
- (87) Kelty, M. L.; Morris, W.; Gallagher, A. T.; Anderson, J. S.; Brown, K. A.; Mirkin, C. A.; Harris, T. D. High-Throughput Synthesis and Characterization of Nanocrystalline Porphyrinic Zirconium Metal–Organic Frameworks. *Chem. Commun.* **2016**, 52 (50), 7854–7857. <https://doi.org/10.1039/C6CC03264H>.
- (88) Banerjee, R.; Phan, A.; Wang, B.; Knobler, C.; Furukawa, H.; O’Keeffe, M.; Yaghi, O. M. High-Throughput Synthesis of Zeolitic Imidazolate Frameworks and Application to CO₂ Capture. *Science (80-.)*. **2008**, 319 (5865), 939–943.
<https://doi.org/10.1126/science.1152516>.
- (89) National Research Council. *Mathematical Research in Materials Science*; National Academies Press: Washington, D.C., 1993. <https://doi.org/10.17226/2206>.

- (90) Spitaler, J.; Estreicher, S. K. Perspectives on the Theory of Defects. *Front. Mater.* **2018**, *5*, 70. <https://doi.org/10.3389/fmats.2018.00070>.
- (91) Newman, R. C. Defects in Silicon. *Reports Prog. Phys.* **1982**, *45* (10), 1163–1210. <https://doi.org/10.1088/0034-4885/45/10/003>.
- (92) Li, X.; Lu, K. Playing with Defects in Metals. *Nat. Mater.* **2017**, *16* (7), 700–701. <https://doi.org/10.1038/nmat4929>.
- (93) Averill, B. A.; Eldredge, P. *Chemistry: Principles, Patterns and Applications*; Flat World Knowledge, 2011.
- (94) Deng, Y.; Eames, C.; Chotard, J.-N.; Lalère, F.; Seznec, V.; Emge, S.; Pecher, O.; Grey, C. P.; Masquelier, C.; Islam, M. S. Structural and Mechanistic Insights into Fast Lithium-Ion Conduction in Li₄SiO₄–Li₃PO₄ Solid Electrolytes. *J. Am. Chem. Soc.* **2015**, *137* (28), 9136–9145. <https://doi.org/10.1021/jacs.5b04444>.
- (95) Cairns, A. B.; Goodwin, A. L. Structural Disorder in Molecular Framework Materials. *Chem. Soc. Rev.* **2013**, *42* (12), 4881–4893. <https://doi.org/10.1039/c3cs35524a>.
- (96) Chen, X.; Lyu, Y.; Wang, Z.; Qiao, X.; Gates, B. C.; Yang, D. Tuning Zr₁₂O₂₂ Node Defects as Catalytic Sites in the Metal-Organic Framework Hcp UiO-66. *ACS Catal.* **2020**, *10* (5), 2906–2914. <https://doi.org/10.1021/acscatal.9b04905>.
- (97) Feng, Y.; Chen, Q.; Jiang, M.; Yao, J. Tailoring the Properties of UiO-66 through Defect Engineering: A Review. *Ind. Eng. Chem. Res.* **2019**, *58* (38), 17646–17659. <https://doi.org/10.1021/acs.iecr.9b03188>.
- (98) Wu, H.; Chua, Y. S.; Krungleviciute, V.; Tyagi, M.; Chen, P.; Yildirim, T.; Zhou, W. Unusual and Highly Tunable Missing-Linker Defects in Zirconium Metal–Organic Framework UiO-66 and Their Important Effects on Gas Adsorption. *J. Am. Chem. Soc.* **2013**, *135* (28), 10525–10532. <https://doi.org/10.1021/ja404514r>.
- (99) Fang, Z.; Bueken, B.; De Vos, D. E.; Fischer, R. A. Defect-Engineered Metal-Organic Frameworks. *Angew. Chemie Int. Ed.* **2015**, *54* (25), 7234–7254. <https://doi.org/10.1002/anie.201411540>.
- (100) Shoaee, M.; Anderson, M. W.; Attfield, M. P. Crystal Growth of the Nanoporous

- Metal-Organic Framework HKUST-1 Revealed by In Situ Atomic Force Microscopy. *Angew. Chemie Int. Ed.* **2008**, *47* (44), 8525–8528. <https://doi.org/10.1002/anie.200803460>.
- (101) Vandichel, M.; Hajek, J.; Vermoortele, F.; Waroquier, M.; De Vos, D. E.; Van Speybroeck, V. Active Site Engineering in UiO-66 Type Metal–Organic Frameworks by Intentional Creation of Defects: A Theoretical Rationalization. *CrystEngComm* **2015**, *17* (2), 395–406. <https://doi.org/10.1039/C4CE01672F>.
- (102) Treacy, M. M. J.; Gibson, J. M.; Fan, L.; Paterson, D. J.; McNulty, I. Fluctuation Microscopy: A Probe of Medium Range Order. *Reports Prog. Phys.* **2005**, *68* (12), 2899–2944. <https://doi.org/10.1088/0034-4885/68/12/R06>.
- (103) Hauffe, K. Lattice Defect Phenomena and Diffusion Processes in Ionic, Covalent and Metallic Crystals. In *Oxidation of Metals*; Springer US: Boston, MA, 1995; pp 8–78. <https://doi.org/10.1007/978-1-4684-8920-0>.
- (104) Chen, J.; Feng, D. Crystallographic Shear Planes and Stacking Disorders in Perovskites KNbO₃ and NaNbO₃. *Phys. Status Solidi* **1989**, *116* (1), 231–235. <https://doi.org/10.1002/pssa.2211160121>.
- (105) Shearer, G. C.; Vitillo, J. G.; Bordiga, S.; Svelle, S.; Olsbye, U.; Lillerud, K. P. Functionalizing the Defects: Postsynthetic Ligand Exchange in the Metal Organic Framework UiO-66. *Chem. Mater.* **2016**, *28* (20), 7190–7193. <https://doi.org/10.1021/acs.chemmater.6b02749>.
- (106) Koschnick, C.; Stäglich, R.; Scholz, T.; Terban, M. W.; von Mankowski, A.; Savasci, G.; Binder, F.; Schökel, A.; Etter, M.; Nuss, J.; Siegel, R.; Germann, L. S.; Ochsenfeld, C.; Dinnebier, R. E.; Senker, J.; Lotsch, B. V. Understanding Disorder and Linker Deficiency in Porphyrinic Zirconium-Based Metal–Organic Frameworks by Resolving the Zr₈O₆ Cluster Conundrum in PCN-221. *Nat. Commun.* **2021**, *12* (1), 3099. <https://doi.org/10.1038/s41467-021-23348-w>.
- (107) Dissegna, S.; Epp, K.; Heinz, W. R.; Kieslich, G.; Fischer, R. A. Defective Metal–Organic Frameworks. *Adv. Mater.* **2018**, *30* (37), 1704501. <https://doi.org/10.1002/adma.201704501>.

- (108) Yin, C.; Liu, Q.; Chen, R.; Liu, J.; Yu, J.; Song, D.; Wang, J. Defect-Induced Method for Preparing Hierarchical Porous Zr–MOF Materials for Ultrafast and Large-Scale Extraction of Uranium from Modified Artificial Seawater. *Ind. Eng. Chem. Res.* **2019**, *58* (3), 1159–1166. <https://doi.org/10.1021/acs.iecr.8b04034>.
- (109) Furukawa, H.; Müller, U.; Yaghi, O. M. “Heterogeneity within Order” in Metal–Organic Frameworks. *Angew. Chemie Int. Ed.* **2015**, *54* (11), 3417–3430. <https://doi.org/10.1002/anie.201410252>.
- (110) Guan, Y.; Li, Y.; Zhou, J.; Zhang, T.; Ding, J.; Xie, Z.; Wang, L. Defect Engineering of Nanoscale Hf-Based Metal–Organic Frameworks for Highly Efficient Iodine Capture. *Inorg. Chem.* **2021**, *60* (13), 9848–9856. <https://doi.org/10.1021/acs.inorgchem.1c01120>.
- (111) Taddei, M.; Wakeham, R. J.; Koutsianos, A.; Andreoli, E.; Barron, A. R. Post-Synthetic Ligand Exchange in Zirconium-Based Metal–Organic Frameworks: Beware of The Defects! *Angew. Chemie Int. Ed.* **2018**, *57* (36), 11706–11710. <https://doi.org/10.1002/anie.201806910>.
- (112) Kim, M.; Cahill, J. F.; Fei, H.; Prather, K. A.; Cohen, S. M. Postsynthetic Ligand and Cation Exchange in Robust Metal–Organic Frameworks. *J. Am. Chem. Soc.* **2012**, *134* (43), 18082–18088. <https://doi.org/10.1021/ja3079219>.
- (113) Idrees, K. B.; Chen, Z.; Zhang, X.; Mian, M. R.; Drout, R. J.; Islamoglu, T.; Farha, O. K. Tailoring Pore Aperture and Structural Defects in Zirconium-Based Metal–Organic Frameworks for Krypton/Xenon Separation. *Chem. Mater.* **2020**, *32* (9), 3776–3782. <https://doi.org/10.1021/acs.chemmater.9b05048>.
- (114) Cheetham, A. K.; Bennett, T. D.; Coudert, F.-X.; Goodwin, A. L. Defects and Disorder in Metal Organic Frameworks. *Dalt. Trans.* **2016**, *45* (10), 4113–4126. <https://doi.org/10.1039/C5DT04392A>.
- (115) Feng, X.; Hajek, J.; Jena, H. S.; Wang, G.; Veerapandian, S. K. P.; Morent, R.; De Geyter, N.; Leyssens, K.; Hoffman, A. E. J.; Meynen, V.; Marquez, C.; De Vos, D. E.; Van Speybroeck, V.; Leus, K.; Van Der Voort, P. Engineering a Highly Defective Stable UiO-66 with Tunable Lewis- Brønsted Acidity: The Role of the Hemilabile Linker. *J. Am. Chem. Soc.* **2020**, *142* (6), 3174–3183. <https://doi.org/10.1021/jacs.9b13070>.

- (116) Abednatanzi, S.; Gohari Derakhshandeh, P.; Depauw, H.; Coudert, F.-X.; Vrielinck, H.; Van Der Voort, P.; Leus, K. Mixed-Metal Metal–Organic Frameworks. *Chem. Soc. Rev.* **2019**, *48* (9), 2535–2565. <https://doi.org/10.1039/C8CS00337H>.
- (117) Ha, J.; Lee, J. H.; Moon, H. R. Alterations to Secondary Building Units of Metal–Organic Frameworks for the Development of New Functions. *Inorg. Chem. Front.* **2020**, *7* (1), 12–27. <https://doi.org/10.1039/C9QI01119F>.
- (118) Peters, A. W.; Otake, K.; Platero-Prats, A. E.; Li, Z.; DeStefano, M. R.; Chapman, K. W.; Farha, O. K.; Hupp, J. T. Site-Directed Synthesis of Cobalt Oxide Clusters in a Metal–Organic Framework. *ACS Appl. Mater. Interfaces* **2018**, *10* (17), 15073–15078. <https://doi.org/10.1021/acsami.8b02825>.
- (119) DeStefano, M. R.; Islamoglu, T.; Garibay, S. J.; Hupp, J. T.; Farha, O. K. Room-Temperature Synthesis of UiO-66 and Thermal Modulation of Densities of Defect Sites. *Chem. Mater.* **2017**, *29* (3), 1357–1361. <https://doi.org/10.1021/acs.chemmater.6b05115>.
- (120) Caratelli, C.; Hajek, J.; Cirujano, F. G.; Waroquier, M.; Llabrés i Xamena, F. X.; Van Speybroeck, V. Nature of Active Sites on UiO-66 and Beneficial Influence of Water in the Catalysis of Fischer Esterification. *J. Catal.* **2017**, *352*, 401–414. <https://doi.org/10.1016/j.jcat.2017.06.014>.
- (121) Canivet, J.; Vandichel, M.; Farrusseng, D. Origin of Highly Active Metal–Organic Framework Catalysts: Defects? Defects! *Dalt. Trans.* **2016**, *45* (10), 4090–4099. <https://doi.org/10.1039/C5DT03522H>.
- (122) Øien, S.; Wragg, D.; Reinsch, H.; Svelle, S.; Bordiga, S.; Lamberti, C.; Lillerud, K. P. Detailed Structure Analysis of Atomic Positions and Defects in Zirconium Metal–Organic Frameworks. *Cryst. Growth Des.* **2014**, *14* (11), 5370–5372. <https://doi.org/10.1021/cg501386j>.
- (123) Vandichel, M.; Hajek, J.; Ghysels, A.; De Vos, A.; Waroquier, M.; Van Speybroeck, V. Water Coordination and Dehydration Processes in Defective UiO-66 Type Metal–Organic Frameworks. *CrystEngComm* **2016**, *18* (37), 7056–7069. <https://doi.org/10.1039/C6CE01027J>.

- (124) Yang, D.; Bernales, V.; Islamoglu, T.; Farha, O. K.; Hupp, J. T.; Cramer, C. J.; Gagliardi, L.; Gates, B. C. Tuning the Surface Chemistry of Metal Organic Framework Nodes: Proton Topology of the Metal-Oxide-Like Zr₆ Nodes of UiO-66 and NU-1000. *J. Am. Chem. Soc.* **2016**, *138* (46), 15189–15196. <https://doi.org/10.1021/jacs.6b08273>.
- (125) Jiang, J.; Yaghi, O. M. Brønsted Acidity in Metal–Organic Frameworks. *Chem. Rev.* **2015**, *115* (14), 6966–6997. <https://doi.org/10.1021/acs.chemrev.5b00221>.
- (126) Hernandez, A. F.; Impastato, R. K.; Hossain, M. I.; Rabideau, B. D.; Glover, T. G. Water Bridges Substitute for Defects in Amine-Functionalized UiO-66, Boosting CO₂ Adsorption. *Langmuir* **2021**, *37* (35), 10439–10449. <https://doi.org/10.1021/acs.langmuir.1c01149>.
- (127) Shearer, G. C.; Chavan, S.; Ethiraj, J.; Vitillo, J. G.; Svelle, S.; Olsbye, U.; Lamberti, C.; Bordiga, S.; Lillerud, K. P. Tuned to Perfection: Ironing Out the Defects in Metal–Organic Framework UiO-66. *Chem. Mater.* **2014**, *26* (14), 4068–4071. <https://doi.org/10.1021/cm501859p>.
- (128) Bunck, D. N.; Dichtel, W. R. Mixed Linker Strategies for Organic Framework Functionalization. *Chem. - A Eur. J.* **2013**, *19* (3), 818–827. <https://doi.org/10.1002/chem.201203145>.
- (129) Gutov, O. V.; Hevia, M. G.; Escudero-Adán, E. C.; Shafir, A. Metal–Organic Framework (MOF) Defects under Control: Insights into the Missing Linker Sites and Their Implication in the Reactivity of Zirconium-Based Frameworks. *Inorg. Chem.* **2015**, *54* (17), 8396–8400. <https://doi.org/10.1021/acs.inorgchem.5b01053>.
- (130) Solovkin, A. S.; Tsvetkova, Z. N. THE CHEMISTRY OF AQUEOUS SOLUTIONS OF ZIRCONIUM SALTS (DOES THE ZIRCONYL ION EXIST?). *Russ. Chem. Rev.* **1962**, *31* (11), 655–669. <https://doi.org/10.1070/RC1962v031n11ABEH001326>.
- (131) Lister, B. A. J.; McDonald, L. A. Some Aspects of the Solution Chemistry of Zirconium. *J. Chem. Soc.* **1952**, 4315. <https://doi.org/10.1039/jr9520004315>.
- (132) Intorre, B. I.; Martell, A. E. Zirconium Complexes in Aqueous Solution. I. Reaction with Multidentate Ligands. *J. Am. Chem. Soc.* **1960**, *82* (2), 358–364.

<https://doi.org/10.1021/ja01487a027>.

- (133) Kanazhevskii, V. V.; Novgorodov, B. N.; Shmachkova, V. P.; Kotsarenko, N. S.; Kriventsov, V. V.; Kochubey, D. I. Structure of Zirconium Complexes in Aqueous Solutions. *Mendeleev Commun.* **2001**, *11* (6), 211–212.
<https://doi.org/10.1070/MC2001v011n06ABEH001509>.
- (134) Saku, Y.; Sakai, Y.; Shinohara, A.; Hayashi, K.; Yoshida, S.; Kato, C. N.; Yoza, K.; Nomiya, K. Sandwich-Type Hf IV and Zr IV Complexes Composed of Tri-Lacunary Keggin Polyoxometalates: Structure of $[M_3(\mu-OH)_3(A-\alpha-PW_9O_{34})_2]_9^-$ (M = Hf and Zr). *Dalt. Trans.* **2009**, *3* (5), 805–813. <https://doi.org/10.1039/B813710M>.
- (135) KOBAYASHI, T.; SASAKI, T.; TAKAGI, I.; MORIYAMA, H. Zirconium Solubility in Ternary Aqueous System of Zr(IV)-OH-Carboxylates. *J. Nucl. Sci. Technol.* **2009**, *46* (2), 142–148. <https://doi.org/10.1080/18811248.2007.9711515>.
- (136) Morris, W.; Wang, S.; Cho, D.; Auyeung, E.; Li, P.; Farha, O. K.; Mirkin, C. A. Role of Modulators in Controlling the Colloidal Stability and Polydispersity of the UiO-66 Metal–Organic Framework. *ACS Appl. Mater. Interfaces* **2017**, *9* (39), 33413–33418.
<https://doi.org/10.1021/acsami.7b01040>.
- (137) Wißmann, G.; Schaate, A.; Lilienthal, S.; Bremer, I.; Schneider, A. M.; Behrens, P. Modulated Synthesis of Zr-Fumarate MOF. *Microporous Mesoporous Mater.* **2012**, *152*, 64–70. <https://doi.org/10.1016/j.micromeso.2011.12.010>.
- (138) Schaate, A.; Roy, P.; Godt, A.; Lippke, J.; Waltz, F.; Wiebcke, M.; Behrens, P. Modulated Synthesis of Zr-Based Metal-Organic Frameworks: From Nano to Single Crystals. *Chem. - A Eur. J.* **2011**, *17* (24), 6643–6651.
<https://doi.org/10.1002/chem.201003211>.
- (139) Ravon, U.; Savonnet, M.; Aguado, S.; Domine, M. E.; Janneau, E.; Farrusseng, D. Engineering of Coordination Polymers for Shape Selective Alkylation of Large Aromatics and the Role of Defects. *Microporous Mesoporous Mater.* **2010**, *129* (3), 319–329. <https://doi.org/10.1016/j.micromeso.2009.06.008>.
- (140) Øien-Ødegaard, S.; Bouchevreau, B.; Hylland, K.; Wu, L.; Blom, R.; Grande, C.;

- Olsbye, U.; Tilset, M.; Lillerud, K. P. UiO-67-Type Metal–Organic Frameworks with Enhanced Water Stability and Methane Adsorption Capacity. *Inorg. Chem.* **2016**, *55* (5), 1986–1991. <https://doi.org/10.1021/acs.inorgchem.5b02257>.
- (141) Cliffe, M. J.; Wan, W.; Zou, X.; Chater, P. A.; Kleppe, A. K.; Tucker, M. G.; Wilhelm, H.; Funnell, N. P.; Coudert, F.-X.; Goodwin, A. L. Correlated Defect Nanoregions in a Metal–Organic Framework. *Nat. Commun.* **2014**, *5* (1), 4176. <https://doi.org/10.1038/ncomms5176>.
- (142) Cai, G.; Jiang, H.-L. A Modulator-Induced Defect-Formation Strategy to Hierarchically Porous Metal–Organic Frameworks with High Stability. *Angew. Chemie Int. Ed.* **2017**, *56* (2), 563–567. <https://doi.org/10.1002/anie.201610914>.
- (143) Abánades Lázaro, I.; Almora-Barrios, N.; Tatay, S.; Popescu, C.; Martí-Gastaldo, C. Linker Depletion for Missing Cluster Defects in Non-UiO Metal–Organic Frameworks. *Chem. Sci.* **2021**, *12* (35), 11839–11844. <https://doi.org/10.1039/D1SC02408F>.
- (144) Winarta, J.; Shan, B.; Mcintyre, S. M.; Ye, L.; Wang, C.; Liu, J.; Mu, B. A Decade of UiO-66 Research: A Historic Review of Dynamic Structure, Synthesis Mechanisms, and Characterization Techniques of an Archetypal Metal–Organic Framework. *Cryst. Growth Des.* **2020**, *20* (2), 1347–1362. <https://doi.org/10.1021/acs.cgd.9b00955>.
- (145) Furukawa, H.; Gándara, F.; Zhang, Y.-B.; Jiang, J.; Queen, W. L.; Hudson, M. R.; Yaghi, O. M. Water Adsorption in Porous Metal–Organic Frameworks and Related Materials. *J. Am. Chem. Soc.* **2014**, *136* (11), 4369–4381. <https://doi.org/10.1021/ja500330a>.
- (146) Jiang, H.-L.; Feng, D.; Liu, T.-F.; Li, J.-R.; Zhou, H.-C. Pore Surface Engineering with Controlled Loadings of Functional Groups via Click Chemistry in Highly Stable Metal–Organic Frameworks. *J. Am. Chem. Soc.* **2012**, *134* (36), 14690–14693. <https://doi.org/10.1021/ja3063919>.
- (147) Liu, T.-F.; Feng, D.; Chen, Y.-P.; Zou, L.; Bosch, M.; Yuan, S.; Wei, Z.; Fordham, S.; Wang, K.; Zhou, H.-C. Topology-Guided Design and Syntheses of Highly Stable Mesoporous Porphyrinic Zirconium Metal–Organic Frameworks with High Surface

- Area. *J. Am. Chem. Soc.* **2015**, *137* (1), 413–419. <https://doi.org/10.1021/ja5111317>.
- (148) Mondloch, J. E.; Bury, W.; Fairen-Jimenez, D.; Kwon, S.; DeMarco, E. J.; Weston, M. H.; Sarjeant, A. A.; Nguyen, S. T.; Stair, P. C.; Snurr, R. Q.; Farha, O. K.; Hupp, J. T. Vapor-Phase Metalation by Atomic Layer Deposition in a Metal–Organic Framework. *J. Am. Chem. Soc.* **2013**, *135* (28), 10294–10297. <https://doi.org/10.1021/ja4050828>.
- (149) Bon, V.; Senkowska, I.; Baburin, I. A.; Kaskel, S. Zr- and Hf-Based Metal–Organic Frameworks: Tracking Down the Polymorphism. *Cryst. Growth Des.* **2013**, *13* (3), 1231–1237. <https://doi.org/10.1021/cg301691d>.
- (150) Ji, P.; Manna, K.; Lin, Z.; Feng, X.; Urban, A.; Song, Y.; Lin, W. Single-Site Cobalt Catalysts at New Zr₁₂(M₃-O)₈(M₃-OH)₈(M₂-OH)₆ Metal–Organic Framework Nodes for Highly Active Hydrogenation of Nitroarenes, Nitriles, and Isocyanides. *J. Am. Chem. Soc.* **2017**, *139* (20), 7004–7011. <https://doi.org/10.1021/jacs.7b02394>.
- (151) Waitschat, S.; Reinsch, H.; Stock, N. Water-Based Synthesis and Characterisation of a New Zr-MOF with a Unique Inorganic Building Unit. *Chem. Commun.* **2016**, *52* (86), 12698–12701. <https://doi.org/10.1039/C6CC06287C>.
- (152) Leubner, S.; Zhao, H.; Van Velthoven, N.; Henrion, M.; Reinsch, H.; De Vos, D. E.; Kolb, U.; Stock, N. Expanding the Variety of Zirconium-based Inorganic Building Units for Metal–Organic Frameworks. *Angew. Chemie* **2019**, *131* (32), 11111–11116. <https://doi.org/10.1002/ange.201905456>.
- (153) Guillerm, V.; Ragon, F.; Dan-Hardi, M.; Devic, T.; Vishnuvarthan, M.; Campo, B.; Vimont, A.; Clet, G.; Yang, Q.; Maurin, G.; Férey, G.; Vittadini, A.; Gross, S.; Serre, C. A Series of Isorecticular, Highly Stable, Porous Zirconium Oxide Based Metal–Organic Frameworks. *Angew. Chemie Int. Ed.* **2012**, *51* (37), 9267–9271. <https://doi.org/10.1002/anie.201204806>.
- (154) Mouchaham, G.; Cooper, L.; Guillou, N.; Martineau, C.; Elkaïm, E.; Bourrelly, S.; Llewellyn, P. L.; Allain, C.; Clavier, G.; Serre, C.; Devic, T. A Robust Infinite Zirconium Phenolate Building Unit to Enhance the Chemical Stability of Zr MOFs. *Angew. Chemie Int. Ed.* **2015**, *54* (45), 13297–13301. <https://doi.org/10.1002/anie.201507058>.

- (155) Cooper, L.; Guillou, N.; Martineau, C.; Elkaim, E.; Taulelle, F.; Serre, C.; Devic, T. Zr IV Coordination Polymers Based on a Naturally Occurring Phenolic Derivative. *Eur. J. Inorg. Chem.* **2014**, 2014 (36), 6281–6289. <https://doi.org/10.1002/ejic.201402891>.
- (156) Lammert, M.; Reinsch, H.; Murray, C. A.; Wharmby, M. T.; Terraschke, H.; Stock, N. Synthesis and Structure of Zr(IV)- and Ce(IV)-Based CAU-24 with 1,2,4,5-Tetrakis(4-Carboxyphenyl)Benzene. *Dalt. Trans.* **2016**, 45 (47), 18822–18826. <https://doi.org/10.1039/c6dt03852b>.
- (157) Falaise, C.; Volkringer, C.; Vigier, J.-F.; Henry, N.; Beaurain, A.; Loiseau, T. Three-Dimensional MOF-Type Architectures with Tetravalent Uranium Hexanuclear Motifs (U₆O₈). *Chem. - A Eur. J.* **2013**, 19 (17), 5324–5331. <https://doi.org/10.1002/chem.201203914>.
- (158) Falaise, C.; Volkringer, C.; Loiseau, T. Mixed Formate-Dicarboxylate Coordination Polymers with Tetravalent Uranium: Occurrence of Tetranuclear {U₄O₄} and Hexanuclear {U₆O₄(OH)₄} Motifs. *Cryst. Growth Des.* **2013**, 13 (7), 3225–3231. <https://doi.org/10.1021/cg400643g>.
- (159) Jacobsen, J.; Gosch, J.; Stock, N. Synthesis, Structure, and Characterization of Defect-Free [Hf₆(M₃-O)₄(M₃-OH)₄(C₄H₂O₄)₆] (Hf-UiO-66-Fum). *Zeitschrift für Anorg. und Allg. Chemie* **2018**, 644 (24), 1771–1776. <https://doi.org/10.1002/zaac.201800338>.
- (160) Poschmann, M. P. M.; Waitschat, S.; Reinsch, H.; Stock, N. Synthesis of Two New Hf-MOFs with UiO-66 and CAU-22 Structure Employing 2,5-pyrazinedicarboxylic Acid as Linker Molecule. *Zeitschrift für Anorg. und Allg. Chemie* **2021**, zaac.202100184. <https://doi.org/10.1002/zaac.202100184>.
- (161) Dalapati, R.; Sakthivel, B.; Ghosalya, M. K.; Dhakshinamoorthy, A.; Biswas, S. A Cerium-Based Metal–Organic Framework Having Inherent Oxidase-like Activity Applicable for Colorimetric Sensing of Biothiols and Aerobic Oxidation of Thiols. *CrystEngComm* **2017**, 19 (39), 5915–5925. <https://doi.org/10.1039/C7CE01053B>.
- (162) Lammert, M.; Glißmann, C.; Reinsch, H.; Stock, N. Synthesis and Characterization of New Ce(IV)-MOFs Exhibiting Various Framework Topologies. *Cryst. Growth Des.* **2017**, 17 (3), 1125–1131. <https://doi.org/10.1021/acs.cgd.6b01512>.

- (163) Falaise, C.; Charles, J.-S.; Volkringer, C.; Loiseau, T. Thorium Terephthalates Coordination Polymers Synthesized in Solvothermal DMF/H₂O System. *Inorg. Chem.* **2015**, *54* (5), 2235–2242. <https://doi.org/10.1021/ic502725y>.
- (164) Jakobsen, S.; Gianolio, D.; Wragg, D. S.; Nilsen, M. H.; Emerich, H.; Bordiga, S.; Lamberti, C.; Olsbye, U.; Tilset, M.; Lillerud, K. P. Structural Determination of a Highly Stable Metal–Organic Framework with Possible Application to Interim Radioactive Waste Scavenging: Hf–UiO-66. *Phys. Rev. B* **2012**, *86* (12), 125429. <https://doi.org/10.1103/PhysRevB.86.125429>.
- (165) Cliffe, M. J.; Hill, J. A.; Murray, C. A.; Coudert, F.-X.; Goodwin, A. L. Defect-Dependent Colossal Negative Thermal Expansion in UiO-66(Hf) Metal–Organic Framework. *Phys. Chem. Chem. Phys.* **2015**, *17* (17), 11586–11592. <https://doi.org/10.1039/C5CP01307K>.
- (166) Luu, C. L.; Nguyen, T. T. Van; Nguyen, T.; Hoang, T. C. Synthesis, Characterization and Adsorption Ability of UiO-66-NH₂. *Adv. Nat. Sci. Nanosci. Nanotechnol.* **2015**, *6* (2), 025004. <https://doi.org/10.1088/2043-6262/6/2/025004>.
- (167) Liang, W.; Coghlan, C. J.; Ragon, F.; Rubio-Martinez, M.; D’Alessandro, D. M.; Babarao, R. Defect Engineering of UiO-66 for CO₂ and H₂O Uptake – a Combined Experimental and Simulation Study. *Dalt. Trans.* **2016**, *45* (11), 4496–4500. <https://doi.org/10.1039/C6DT00189K>.
- (168) Usman, M.; Helal, A.; Abdelnaby, M. M.; Alloush, A. M.; Zeama, M.; Yamani, Z. H. Trends and Prospects in UiO-66 Metal–Organic Framework for CO₂ Capture, Separation, and Conversion. *Chem. Rec.* **2021**, *21* (7), 1771–1791. <https://doi.org/10.1002/tcr.202100030>.
- (169) Xydias, P.; Spanopoulos, I.; Klontzas, E.; Froudakis, G. E.; Trikalitis, P. N. Drastic Enhancement of the CO₂ Adsorption Properties in Sulfone-Functionalized Zr- and Hf–UiO-67 MOFs with Hierarchical Mesopores. *Inorg. Chem.* **2014**, *53* (2), 679–681. <https://doi.org/10.1021/ic402430n>.
- (170) Vermoortele, F.; Bueken, B.; Le Bars, G.; Van de Voorde, B.; Vandichel, M.; Houthoofd, K.; Vimont, A.; Daturi, M.; Waroquier, M.; Van Speybroeck, V.;

- Kirschhock, C.; De Vos, D. E. Synthesis Modulation as a Tool To Increase the Catalytic Activity of Metal–Organic Frameworks: The Unique Case of UiO-66(Zr). *J. Am. Chem. Soc.* **2013**, *135* (31), 11465–11468. <https://doi.org/10.1021/ja405078u>.
- (171) Su, F.; Zhang, S.; Ji, H.; Zhao, H.; Tian, J.-Y.; Liu, C.-S.; Zhang, Z.; Fang, S.; Zhu, X.; Du, M. Two-Dimensional Zirconium-Based Metal–Organic Framework Nanosheet Composites Embedded with Au Nanoclusters: A Highly Sensitive Electrochemical Aptasensor toward Detecting Cocaine. *ACS Sensors* **2017**, *2* (7), 998–1005. <https://doi.org/10.1021/acssensors.7b00268>.
- (172) Rimoldi, M.; Howarth, A. J.; DeStefano, M. R.; Lin, L.; Goswami, S.; Li, P.; Hupp, J. T.; Farha, O. K. Catalytic Zirconium/Hafnium-Based Metal–Organic Frameworks. *ACS Catal.* **2017**, *7* (2), 997–1014. <https://doi.org/10.1021/acscatal.6b02923>.
- (173) Wei, J.-Z.; Gong, F.-X.; Sun, X.-J.; Li, Y.; Zhang, T.; Zhao, X.-J.; Zhang, F.-M. Rapid and Low-Cost Electrochemical Synthesis of UiO-66-NH₂ with Enhanced Fluorescence Detection Performance. *Inorg. Chem.* **2019**, *58* (10), 6742–6747. <https://doi.org/10.1021/acs.inorgchem.9b00157>.
- (174) Naseri, A. M.; Zarei, M.; Alizadeh, S.; Babaei, S.; Zolfigol, M. A.; Nematollahi, D.; Arjomandi, J.; Shi, H. Synthesis and Application of [Zr-UiO-66-PDC-SO₃H]Cl MOFs to the Preparation of Dicyanomethylene Pyridines via Chemical and Electrochemical Methods. *Sci. Rep.* **2021**, *11* (1), 16817. <https://doi.org/10.1038/s41598-021-96001-7>.
- (175) Johnstone, D. N.; Firth, F. C. N.; Grey, C. P.; Midgley, P. A.; Cliffe, M. J.; Collins, S. M. Direct Imaging of Correlated Defect Nanodomains in a Metal–Organic Framework. *J. Am. Chem. Soc.* **2020**, *142* (30), 13081–13089. <https://doi.org/10.1021/jacs.0c04468>.
- (176) Goodenough, J. B. Influence of Atomic Vacancies on the Properties of Transition-Metal Oxides. I. TiO_x and VO_x. *Phys. Rev. B* **1972**, *5* (8), 2764–2774. <https://doi.org/10.1103/PhysRevB.5.2764>.
- (177) Burdett, J. K.; Mitchell, J. F. Nonstoichiometry in Early Transition Metal Compounds with the Rocksalt Structure. *Prog. Solid State Chem.* **1995**, *23* (2), 131–170. [https://doi.org/10.1016/0079-6786\(95\)00001-B](https://doi.org/10.1016/0079-6786(95)00001-B).

- (178) Liu, L.; Chen, Z.; Wang, J.; Zhang, D.; Zhu, Y.; Ling, S.; Huang, K.-W.; Belmabkhout, Y.; Adil, K.; Zhang, Y.; Slater, B.; Eddaoudi, M.; Han, Y. Imaging Defects and Their Evolution in a Metal–Organic Framework at Sub-Unit-Cell Resolution. *Nat. Chem.* **2019**, *11* (7), 622–628. <https://doi.org/10.1038/s41557-019-0263-4>.
- (179) Zhu, L.; Zhang, D.; Xue, M.; Li, H.; Qiu, S. Direct Observations of the MOF (UiO-66) Structure by Transmission Electron Microscopy. *CrystEngComm* **2013**, *15* (45), 9356. <https://doi.org/10.1039/c3ce41122b>.
- (180) Kalidindi, S. B.; Nayak, S.; Briggs, M. E.; Jansat, S.; Katsoulidis, A. P.; Miller, G. J.; Warren, J. E.; Antypov, D.; Corà, F.; Slater, B.; Prestly, M. R.; Martí-Gastaldo, C.; Rosseinsky, M. J. Chemical and Structural Stability of Zirconium-based Metal–Organic Frameworks with Large Three-Dimensional Pores by Linker Engineering. *Angew. Chemie Int. Ed.* **2015**, *54* (1), 221–226. <https://doi.org/10.1002/anie.201406501>.
- (181) DeCoste, J. B.; Peterson, G. W.; Jasuja, H.; Glover, T. G.; Huang, Y.; Walton, K. S. Stability and Degradation Mechanisms of Metal–Organic Frameworks Containing the $Zr_6O_4(OH)_4$ Secondary Building Unit. *J. Mater. Chem. A* **2013**, *1* (18), 5642. <https://doi.org/10.1039/c3ta10662d>.
- (182) Klet, R. C.; Liu, Y.; Wang, T. C.; Hupp, J. T.; Farha, O. K. Evaluation of Brønsted Acidity and Proton Topology in Zr- and Hf-Based Metal–Organic Frameworks Using Potentiometric Acid–Base Titration. *J. Mater. Chem. A* **2016**, *4* (4), 1479–1485. <https://doi.org/10.1039/C5TA07687K>.
- (183) McHugh, L. N.; McPherson, M. J.; McCormick, L. J.; Morris, S. A.; Wheatley, P. S.; Teat, S. J.; McKay, D.; Dawson, D. M.; Sansome, C. E. F.; Ashbrook, S. E.; Stone, C. A.; Smith, M. W.; Morris, R. E. Hydrolytic Stability in Hemilabile Metal–Organic Frameworks. *Nat. Chem.* **2018**, *10* (11), 1096–1102. <https://doi.org/10.1038/s41557-018-0104-x>.
- (184) Ashworth, D. J.; Foster, J. A. Metal–Organic Framework Nanosheets (MONs): A New Dimension in Materials Chemistry. *J. Mater. Chem. A* **2018**, *6* (34), 16292–16307. <https://doi.org/10.1039/C8TA03159B>.
- (185) Ongari, D.; Tiana, D.; Stoneburner, S. J.; Gagliardi, L.; Smit, B. Origin of the Strong

- Interaction between Polar Molecules and Copper(II) Paddle-Wheels in Metal Organic Frameworks. *J. Phys. Chem. C* **2017**, *121* (28), 15135–15144.
<https://doi.org/10.1021/acs.jpcc.7b02302>.
- (186) Spijksma, G.; Blank, D. H.; Bouwmeester, H. J.; Kessler, V. Modification of Different Zirconium Propoxide Precursors by Diethanolamine. Is There a Shelf Stability Issue for Sol-Gel Applications? *Int. J. Mol. Sci.* **2009**, *10* (11), 4977–4989.
<https://doi.org/10.3390/ijms10114977>.
- (187) Feng, D.; Jiang, H.-L.; Chen, Y.-P.; Gu, Z.-Y.; Wei, Z.; Zhou, H.-C. Metal–Organic Frameworks Based on Previously Unknown Zr₈/Hf₈ Cubic Clusters. *Inorg. Chem.* **2013**, *52* (21), 12661–12667. <https://doi.org/10.1021/ic4018536>.
- (188) CCDC. CSD web interface – intuitive, cross-platform, web-based access to CSD data. Cambridge Crystallographic Data Centre, 12 Union Road, Cambridge, UK.
- (189) Chen, Z.; Chen, Z.; Farha, O. K.; Chapman, K. W. Mechanistic Insights into Nanoparticle Formation from Bimetallic Metal–Organic Frameworks. *J. Am. Chem. Soc.* **2021**, *143* (24), 8976–8980. <https://doi.org/10.1021/jacs.1c04269>.
- (190) Artner, C.; Czakler, M.; Schubert, U. New Zirconium and Zirconium–Titanium Oxo Cluster Types by Expansion or Metal Substitution of the Octahedral Zr₆O₈ Structural Motif. *Inorganica Chim. Acta* **2015**, *432*, 208–212.
<https://doi.org/10.1016/j.ica.2015.04.013>.
- (191) Malaestean, I. L.; Alici, M. K.; Besson, C.; Ellern, A.; Kögerler, P. Solid-State Coexistence of {Zr₁₂} and {Zr₆} Zirconium Oxocarboxylate Clusters. *CrystEngComm* **2014**, *16* (1), 43–46. <https://doi.org/10.1039/C3CE41829D>.
- (192) Smith, J. A.; Singh-Wilmot, M. A.; Carter, K. P.; Cahill, C. L.; Lough, A. J.; Knee, C. S. Eight Rare Earth Metal Organic Frameworks and Coordination Polymers from 2-Nitroterephthalate: Syntheses, Structures, Solid-State Luminescence and an Unprecedented Topology. *New J. Chem.* **2016**, *40* (9), 7338–7349.
<https://doi.org/10.1039/C6NJ00822D>.
- (193) Kickelbick, G.; Schubert, U. Hydroxy Carboxylate Substituted Oxozirconium Clusters.

- J. Chem. Soc. Dalt. Trans.* **1999**, No. 8, 1301–1306. <https://doi.org/10.1039/a807939k>.
- (194) Jiang, H.; Zhang, W.; Kang, X.; Cao, Z.; Chen, X.; Liu, Y.; Cui, Y. Topology-Based Functionalization of Robust Chiral Zr-Based Metal–Organic Frameworks for Catalytic Enantioselective Hydrogenation. *J. Am. Chem. Soc.* **2020**, *142* (21), jacs.0c00637. <https://doi.org/10.1021/jacs.0c00637>.
- (195) Kickelbick, G.; Holzinger, D.; Brick, C.; Trimmel, G.; Moons, E. Hybrid Inorganic–Organic Core–Shell Nanoparticles from Surface-Functionalized Titanium, Zirconium, and Vanadium Oxo Clusters. *Chem. Mater.* **2002**, *14* (10), 4382–4389. <https://doi.org/10.1021/cm021216y>.
- (196) Mak, T. C. W. Refinement of the Crystal Structure of Zirconyl Chloride Octahydrate. *Can. J. Chem.* **1968**, *46* (22), 3491–3497. <https://doi.org/10.1139/v68-579>.
- (197) Ekberg, C.; Källvenius, G.; Albinsson, Y.; Brown, P. L. Studies on the Hydrolytic Behavior of Zirconium(IV). *J. Solution Chem.* **2004**, *33* (1), 47–79. <https://doi.org/10.1023/B:JOSL.0000026645.41309.d3>.
- (198) Hu, Z.; Nalaparaju, A.; Peng, Y.; Jiang, J.; Zhao, D. Modulated Hydrothermal Synthesis of UiO-66(Hf)-Type Metal–Organic Frameworks for Optimal Carbon Dioxide Separation. *Inorg. Chem.* **2016**, *55* (3), 1134–1141. <https://doi.org/10.1021/acs.inorgchem.5b02312>.
- (199) Gross, S.; Kickelbick, G.; Puchberger, M.; Schubert, U. Mono-, Di-, and Trimetallic Methacrylate-Substituted Metal Oxide Clusters Derived from Hafnium Butoxide. *Monatshefte für Chemie / Chem. Mon.* **2003**, *134* (8), 1053–1063. <https://doi.org/10.1007/s00706-003-0031-3>.
- (200) Clearfield, A.; Vaughan, P. A. The Crystal Structure of Zirconyl Chloride Octahydrate and Zirconyl Bromide Octahydrate. *Acta Crystallogr.* **1956**, *9* (7), 555–558. <https://doi.org/10.1107/s0365110x56001558>.
- (201) Hennig, C.; Weiss, S.; Kraus, W.; Kretzschmar, J.; Scheinost, A. C. Solution Species and Crystal Structure of Zr(IV) Acetate. *Inorg. Chem.* **2017**, *56* (5), 2473–2480. <https://doi.org/10.1021/acs.inorgchem.6b01624>.

- (202) Åberg, M. An X-Ray Investigation of Some Aqueous Zirconium(IV) Halide, a Hafnium(IV) Chloride, and Some Zirconium(IV) Perchlorate Solutions. *Acta Chem. Scand.* **1977**, *31a*, 171–181. <https://doi.org/10.3891/acta.chem.scand.31a-0171>.
- (203) Muha, G. M.; Vaughan, P. A. Structure of the Complex Ion in Aqueous Solutions of Zirconyl and Hafnium Oxyhalides. *J. Chem. Phys.* **1960**, *33* (1), 194–199. <https://doi.org/10.1063/1.1731077>.
- (204) Hagfeldt, C.; Kessler, V.; Persson, I. Structure of the Hydrated, Hydrolysed and Solvated Zirconium(Zr^{IV}) and Hafnium(Hf^{IV}) Ions in Water and Aprotic Oxygen Donor Solvents. A Crystallographic, EXAFS Spectroscopic and Large Angle X-Ray Scattering Study. *Dalt. Trans.* **2004**, No. 14, 2142–2151. <https://doi.org/10.1039/B402804J>.
- (205) Zobel, M.; Neder, R. B.; Kimber, S. A. J. Universal Solvent Restructuring Induced by Colloidal Nanoparticles. *Science (80-.)*. **2015**, *347* (6219), 292–294. <https://doi.org/10.1126/science.1261412>.
- (206) Boyle, T. J.; Ottley, L. A. M.; Hoppe, S. M.; Campana, C. F. Series of Comparable Dinuclear Group 4 Neo-Pentoxide Precursors for Production of PH Dependent Group 4 Nanoceramic Morphologies. *Inorg. Chem.* **2010**, *49* (23), 10798–10808. <https://doi.org/10.1021/ic101205d>.
- (207) Rao, N.; Holerca, M. N.; Klein, M. L.; Pophristic, V. Computational Study of the Zr 4+ Tetranuclear Polymer, $[\text{Zr}_4(\text{OH})_8(\text{H}_2\text{O})_{16}]^{8+}$. *J. Phys. Chem. A* **2007**, *111* (45), 11395–11399. <https://doi.org/10.1021/jp0734880>.
- (208) Goberna-Ferrón, S.; Park, D. H.; Amador, J. M.; Keszler, D. A.; Nyman, M. Amphoteric Aqueous Hafnium Cluster Chemistry. *Angew. Chemie - Int. Ed.* **2016**, *55* (21), 6221–6224. <https://doi.org/10.1002/anie.201601134>.
- (209) Tosan, J. L.; Durand, B.; Roubin, M.; Chassagneux, F.; Bertin, F. Coupled Raman and Infrared Spectroscopic Study of Acetic or Formic Zirconyl Chloride Aqueous Solutions. *J. Non. Cryst. Solids* **1994**, *168* (1–2), 23–32. [https://doi.org/10.1016/0022-3093\(94\)90116-3](https://doi.org/10.1016/0022-3093(94)90116-3).

- (210) Bumstead, A. M.; Cordes, D. B.; Dawson, D. M.; Chakarova, K. K.; Mihaylov, M. Y.; Hobday, C. L.; Düren, T.; Hadjiivanov, K. I.; Slawin, A. M. Z.; Ashbrook, S. E.; Prasad, R. R. R.; Wright, P. A. Modulator-Controlled Synthesis of Microporous STA-26, an Interpenetrated 8,3-Connected Zirconium MOF with the *t*-Topology, and Its Reversible Lattice Shift. *Chem. - A Eur. J.* **2018**, *24* (23), 6115–6126.
<https://doi.org/10.1002/chem.201705136>.
- (211) Wang, X.; Zhang, X.; Li, P.; Otake, K. I.; Cui, Y.; Lyu, J.; Krzyaniak, M. D.; Zhang, Y.; Li, Z.; Liu, J.; Buru, C. T.; Islamoglu, T.; Wasielewski, M. R.; Li, Z.; Farha, O. K. Vanadium Catalyst on Isostructural Transition Metal, Lanthanide, and Actinide Based Metal-Organic Frameworks for Alcohol Oxidation. *J. Am. Chem. Soc.* **2020**, *141* (20), 8306–8314. <https://doi.org/10.1021/jacs.9b02603>.
- (212) Devia, D. H.; Sykes, A. G. Aqueous Solution Chemistry of Zirconium(IV). 1. Kinetic Studies on Hydrogen Ion and General Acid (HX) Induced Dissociations of the Tetrameric Ion $[\text{Zr}_4(\text{OH})_8(\text{H}_2\text{O})_{16}]^{8+}$. *Inorg. Chem.* **1981**, *20* (3), 910–913.
<https://doi.org/10.1021/ic50217a054>.
- (213) Kickelbick, G.; Feth, M. P.; Bertagnolli, H.; Puchberger, M.; Holzinger, D.; Gross, S. Formation of Organically Surface-Modified Metal Oxo Clusters from Carboxylic Acids and Metal Alkoxides: A Mechanistic Study. *J. Chem. Soc. Dalt. Trans.* **2002**, No. 20, 3892–3898. <https://doi.org/10.1039/b207994a>.
- (214) *Metal-Organic Frameworks in Biomedical and Environmental Field*; Horcajada Cortés, P., Rojas Macías, S., Eds.; Springer International Publishing: Cham, 2021.
<https://doi.org/10.1007/978-3-030-63380-6>.
- (215) Kickelbick, G.; Wiede, P.; Schubert, U. Variations in Capping the $\text{Zr}_6\text{O}_4(\text{OH})_4$ Cluster Core: X-Ray Structure Analyses of $[\text{Zr}_6(\text{OH})_4\text{O}_4(\text{OOC}-\text{CH}=\text{CH}_2)_4]^{2+}$ (μ -OOC-CH=CH₂)₄ and $\text{Zr}_6(\text{OH})_4\text{O}_4(\text{OOCR})_{12}(\text{PrOH})$ (R = Ph, CMe = CH₂). *Inorganica Chim. Acta* **1999**, *284* (1), 1–7. [https://doi.org/10.1016/S0020-1693\(98\)00251-5](https://doi.org/10.1016/S0020-1693(98)00251-5).
- (216) Kogler, F. R.; Jupa, M.; Puchberger, M.; Schubert, U. Control of the Ratio of Functional and Non-Functional Ligands in Clusters of the Type $\text{Zr}_6\text{O}_4(\text{OH})_4(\text{Carboxylate})_{12}$ for Their Use as Building Blocks for Inorganic–Organic Hybrid Polymers. *J. Mater.*

- Chem.* **2004**, *14* (21), 3133–3138. <https://doi.org/10.1039/B405769D>.
- (217) Fric, H.; Puchberger, M.; Schubert, U. Contributions to the Structural Chemistry of 2-Amino Alcoholate Derivatives of Titanium and Zirconium Alkoxides and Their Partial Hydrolysis Products. *Eur. J. Inorg. Chem.* **2008**, *2008* (9), 1452–1461. <https://doi.org/10.1002/ejic.200701163>.
- (218) Singhal, A.; Toth, L. M.; Lin, J. S.; Affholter, K. Zirconium(IV) Tetramer/Octamer Hydrolysis Equilibrium in Aqueous Hydrochloric Acid Solution. *J. Am. Chem. Soc.* **1996**, *118* (46), 11529–11534. <https://doi.org/10.1021/ja9602399>.
- (219) Zheng, C.; Greer, H. F.; Chiang, C.-Y.; Zhou, W. Microstructural Study of the Formation Mechanism of Metal–Organic Framework MOF-5. *CrystEngComm* **2014**, *16* (6), 1064–1070. <https://doi.org/10.1039/C3CE41291A>.
- (220) Sun, Q.; Liu, C.; Zhang, G.; Zhang, J.; Tung, C. H.; Wang, Y. Aqueous Isolation of 17-Nuclear Zr/Hf Oxide Clusters during the Hydrothermal Synthesis of ZrO₂/HfO₂. *Chem. - A Eur. J.* **2018**, *24* (55), 14701–14706. <https://doi.org/10.1002/chem.201801267>.
- (221) Hu, Y. J.; Knope, K. E.; Skanthakumar, S.; Kanatzidis, M. G.; Mitchell, J. F.; Soderholm, L. Understanding the Role of Aqueous Solution Speciation and Its Application to the Directed Syntheses of Complex Oxidic Zr Chlorides and Sulfates. *J. Am. Chem. Soc.* **2013**, *135* (38), 14240–14248. <https://doi.org/10.1021/ja405555h>.
- (222) Pakamoré, I.; Rousseau, J.; Rousseau, C.; Monflier, E.; Szilágyi, P. Á. An Ambient-Temperature Aqueous Synthesis of Zirconium-Based Metal–Organic Frameworks. *Green Chem.* **2018**, *20* (23), 5292–5298. <https://doi.org/10.1039/C8GC02312C>.
- (223) D'Amato, R.; Donnadio, A.; Carta, M.; Sangregorio, C.; Tiana, D.; Vivani, R.; Taddei, M.; Costantino, F. Water-Based Synthesis and Enhanced CO₂ Capture Performance of Perfluorinated Cerium-Based Metal–Organic Frameworks with UiO-66 and MIL-140 Topology. *ACS Sustain. Chem. Eng.* **2019**, *7* (1), 394–402. <https://doi.org/10.1021/acssuschemeng.8b03765>.
- (224) Bon, V.; Senkovskyy, V.; Senkovska, I.; Kaskel, S. Zr(IV) and Hf(IV) Based Metal–Organic Frameworks with Reo-Topology. *Chem. Commun.* **2012**, *48* (67), 8407–8409.

<https://doi.org/10.1039/c2cc34246d>.

- (225) Zhang, C.; Ren, Z.; Liu, L.; Yin, Z. Modelling Hydrogen Bonds in N,N-Dimethylformamide. *Mol. Simul.* **2013**, *39* (11), 875–881.
<https://doi.org/10.1080/08927022.2013.775438>.
- (226) Jedlovsky, P.; Bakó, I.; Pálinkás, G.; Dore, J. C. Structural Investigation of Liquid Formic Acid X-Ray and Neutron Diffraction, and Reverse Monte Carlo Study. *Mol. Phys.* **1995**, *86* (1), 87–105. <https://doi.org/10.1080/00268979500101861>.
- (227) Cordeiro, J. M. M.; Freitas, L. C. G. Study of Water and Dimethylformamide Interaction by Computer Simulation. *Zeitschrift fur Naturforsch. - Sect. A J. Phys. Sci.* **1999**, *54* (2), 110–116. <https://doi.org/10.1515/zna-1999-0204>.
- (228) Basma, N.; Cullen, P. L.; Clancy, A. J.; Shaffer, M. S. P.; Skipper, N. T.; Headen, T. F.; Howard, C. A. The Liquid Structure of the Solvents Dimethylformamide (DMF) and Dimethylacetamide (DMA). *Mol. Phys.* **2019**, *117* (22), 3353–3363.
<https://doi.org/10.1080/00268976.2019.1649494>.
- (229) Jedlovsky, P.; Turi, L. A New Five-Site Pair Potential for Formic Acid in Liquid Simulations. *J. Phys. Chem. A* **1997**, *101* (14), 2662–2665.
<https://doi.org/10.1021/jp961891t>.
- (230) Lei, Y.; Li, H.; Pan, H.; Han, S. Structures and Hydrogen Bonding Analysis of N,N-Dimethylformamide and N,N-Dimethylformamide-Water Mixtures by Molecular Dynamics Simulations. *J. Phys. Chem. A* **2003**, *107* (10), 1574–1583.
<https://doi.org/10.1021/jp026638+>.
- (231) Ludwig, R. Water: From Clusters to the Bulk. *Angewandte Chemie - International Edition*. Wiley-VCH Verlag May 18, 2001, pp 1808–1827. [https://doi.org/10.1002/1521-3773\(20010518\)40:10<1808::AID-ANIE1808>3.0.CO;2-1](https://doi.org/10.1002/1521-3773(20010518)40:10<1808::AID-ANIE1808>3.0.CO;2-1).
- (232) Narten, A. H.; Levy, H. A. Observed Diffraction Pattern and Proposed Models of Liquid Water. *Science (80-.)*. **1969**, *165* (3892), 447–454.
<https://doi.org/10.1126/science.165.3892.447>.
- (233) Skinner, L. B.; Huang, C.; Schlesinger, D.; Pettersson, L. G. M.; Nilsson, A.; Benmore,

- C. J. Benchmark Oxygen-Oxygen Pair-Distribution Function of Ambient Water from x-Ray Diffraction Measurements with a Wide Q-Range. *J. Chem. Phys.* **2013**, *138* (7), 074506. <https://doi.org/10.1063/1.4790861>.
- (234) Yang, B.; Lang, H.; Liu, Z.; Wang, S.; Men, Z.; Sun, C. Three Stages of Hydrogen Bonding Network in DMF-Water Binary Solution. *J. Mol. Liq.* **2021**, *324*, 114996. <https://doi.org/10.1016/j.molliq.2020.114996>.
- (235) Tomar, D.; Rana, B.; Jena, K. C. The Structure of Water-DMF Binary Mixtures Probed by Linear and Nonlinear Vibrational Spectroscopy. *J. Chem. Phys.* **2020**, *152* (11), 114707. <https://doi.org/10.1063/1.5141757>.
- (236) Jadzyn, J.; Świergiel, J. On Similarity of Hydrogen-Bonded Networks in Liquid Formamide and Water as Revealed in the Static Dielectric Studies. *Phys. Chem. Chem. Phys.* **2012**, *14* (9), 3170–3175. <https://doi.org/10.1039/c2cp23960d>.
- (237) Hippler, M. Proton Relaxation and Intermolecular Structure of Liquid Formic Acid: A Nuclear Magnetic Resonance Study. *Phys. Chem. Chem. Phys.* **2002**, *4* (8), 1457–1463. <https://doi.org/10.1039/b110358j>.
- (238) Pająk, Z.; Szcześniak, E. Structure and Microdynamic Behaviour of Liquid Formic Acid. *Chem. Phys. Lett.* **1977**, *49* (2), 269–272. [https://doi.org/10.1016/0009-2614\(77\)80584-8](https://doi.org/10.1016/0009-2614(77)80584-8).
- (239) Gupta, R.; Chandra, A. Single Particle and Pair Dynamics in Water-Formic Acid Mixtures Containing Ionic and Neutral Solutes: Nonideality in Dynamical Properties. *J. Chem. Phys.* **2008**, *128* (18), 184506. <https://doi.org/10.1063/1.2913058>.
- (240) Soffientini, S.; Bernasconi, L.; Imberti, S. The Hydration of Formic Acid and Acetic Acid. *J. Mol. Liq.* **2015**, *205*, 85–92. <https://doi.org/10.1016/j.molliq.2014.11.030>.
- (241) Dingley, A. J.; Cordier, F.; Grzesiek, S. An Introduction to Hydrogen Bond Scalar Couplings. *Concepts Magn. Reson.* **2001**, *13* (2), 103–127. [https://doi.org/10.1002/1099-0534\(2001\)13:2<103::AID-CMR1001>3.0.CO;2-M](https://doi.org/10.1002/1099-0534(2001)13:2<103::AID-CMR1001>3.0.CO;2-M).
- (242) Ohtaki, H. Effects of Temperature and Pressure on Hydrogen Bonds in Water and in Formamide. *J. Mol. Liq.* **2003**, *103–104* (SPEC.), 3–13. <https://doi.org/10.1016/S0167->

7322(02)00124-1.

- (243) Biswas, S.; Mallik, B. S. Effects of Temperature on the Structure and Dynamics of Aqueous Mixtures of N,N-Dimethylformamide. *J. Chem. Eng. Data* **2014**, *59* (10), 3250–3257. <https://doi.org/10.1021/je5002544>.
- (244) Heravi, M. M.; Ghavidel, M.; Mohammadkhani, L. Beyond a Solvent: Triple Roles of Dimethylformamide in Organic Chemistry. *RSC Adv.* **2018**, *8* (49), 27832–27862. <https://doi.org/10.1039/C8RA04985H>.
- (245) Noel, N. K.; Congiu, M.; Ramadan, A. J.; Fearn, S.; McMeekin, D. P.; Patel, J. B.; Johnston, M. B.; Wenger, B.; Snaith, H. J. Unveiling the Influence of PH on the Crystallization of Hybrid Perovskites, Delivering Low Voltage Loss Photovoltaics. *Joule* **2017**, *1* (2), 328–343. <https://doi.org/10.1016/j.joule.2017.09.009>.
- (246) Nelson, W. L.; Engelder, C. J. The Thermal Decomposition of Formic Acid. *J. Phys. Chem.* **1926**, *30* (4), 470–475. <https://doi.org/10.1021/j150262a003>.
- (247) Ida, T.; Nishida, M.; Hori, Y. Revisiting Formic Acid Decomposition by a Graph-Theoretical Approach. *J. Phys. Chem. A* **2019**, *123* (44), 9579–9586. <https://doi.org/10.1021/acs.jpca.9b05994>.
- (248) Barham, H. N.; Clark, L. W. The Decomposition of Formic Acid at Low Temperatures. *J. Am. Chem. Soc.* **1951**, *73* (10), 4638–4640. <https://doi.org/10.1021/ja01154a042>.
- (249) Fenwick, A. Q.; Luca, O. R. The Formation of CO by Thermal Decomposition of Formic Acid under Electrochemical Conditions of CO₂ Reduction. *J. Photochem. Photobiol. B Biol.* **2014**, *152*, 43–46. <https://doi.org/10.1016/j.jphotobiol.2015.04.003>.
- (250) Yu, J.; Savage, P. E. Decomposition of Formic Acid under Hydrothermal Conditions. *Ind. Eng. Chem. Res.* **1998**, *37* (1), 2–10. <https://doi.org/10.1021/ie970182e>.
- (251) Firth, F. C. N.; Cliffe, M. J.; Vulpe, D.; Aragonés-Anglada, M.; Moghadam, P. Z.; Fairen-Jimenez, D.; Slater, B.; Grey, C. P. Engineering New Defective Phases of UiO Family Metal–Organic Frameworks with Water. *J. Mater. Chem. A* **2019**, *7* (13), 7459–7469. <https://doi.org/10.1039/C8TA10682G>.
- (252) Taddei, M.; Van Bokhoven, J. A.; Ranocchiari, M. Influence of Water in the Synthesis

- of the Zirconium-Based Metal–Organic Framework UiO-66: Isolation and Reactivity of $[\text{ZrCl}(\text{OH})_2(\text{DMF})_2]\text{Cl}$. *Inorg. Chem.* **2020**, *16* (11), 7860–7868.
<https://doi.org/10.1021/acs.inorgchem.0c00991>.
- (253) Butova, V. V.; Budnyk, A. P.; Charykov, K. M.; Vetlitsyna-Novikova, K. S.; Lamberti, C.; Soldatov, A. V. Water as a Structure-Driving Agent between the UiO-66 and MIL-140A Metal-Organic Frameworks. *Chem. Commun.* **2019**, *55* (7), 901–904.
<https://doi.org/10.1039/c8cc07709f>.
- (254) Zhou, Z.; Shi, Y.; Zhou, X. Theoretical Studies on the Hydrogen Bonding Interaction of Complexes of Formic Acid with Water. *J. Phys. Chem. A* **2004**, *108* (5), 813–822.
<https://doi.org/10.1021/jp030642j>.
- (255) Firth, F. C. N.; Gaultois, M. W.; Wu, Y.; Stratford, J. M.; Keeble, D. S.; Grey, C. P.; Cliffe, M. J. Exploring the Role of Cluster Formation in UiO Family Hf Metal–Organic Frameworks with in Situ X-Ray Pair Distribution Function Analysis. *J. Am. Chem. Soc.* **2021**, *143* (47), 19668–19683. <https://doi.org/10.1021/jacs.1c06990>.
- (256) Yuan, S.; Qin, J. S.; Zou, L.; Chen, Y. P.; Wang, X.; Zhang, Q.; Zhou, H. C. Thermodynamically Guided Synthesis of Mixed-Linker Zr-MOFs with Enhanced Tunability. *J. Am. Chem. Soc.* **2016**, *138* (20), 6636–6642.
<https://doi.org/10.1021/jacs.6b03263>.
- (257) Goesten, M. G.; De Lange, M. F.; Olivos-Suarez, A. I.; Bavykina, A. V.; Serra-Crespo, P.; Krywka, C.; Bickelhaupt, F. M.; Kapteijn, F.; Gascon, J. Evidence for a Chemical Clock in Oscillatory Formation of UiO-66. *Nat. Commun.* **2016**, *7* (1), 1–8.
<https://doi.org/10.1038/ncomms11832>.
- (258) Garcia-Garfido, J. M.; Enríquez, J.; Chi-Durán, I.; Jara, I.; Vivas, L.; Hernández, F. J.; Herrera, F.; Singh, D. P. Millimeter-Scale $\text{Zn}(3\text{-Ptz})_2$ metal-Organic Framework Single Crystals: Self-Assembly Mechanism and Growth Kinetics. *ACS Omega* **2021**, *6* (27), 17289–17298. <https://doi.org/10.1021/acsomega.1c01272>.
- (259) Sommer, S.; Gjerlevsen Nielsen, I.; Brummerstedt Iversen, B. Group 13 Precursor Structures and Their Effect on Oxide Nanocrystal Formation. *Chem. - A Eur. J.* **2020**, *26* (5), 1022–1026. <https://doi.org/10.1002/chem.201904422>.

- (260) Christensen, R. S.; Kløve, M.; Roelsgaard, M.; Sommer, S.; Iversen, B. B. Unravelling the Complex Formation Mechanism of HfO₂ Nanocrystals Using in Situ Pair Distribution Function Analysis. *Nanoscale* **2021**, *13* (29), 12711–12719. <https://doi.org/10.1039/D1NR03044B>.
- (261) Mi, J. L.; Jensen, K. M. Ø.; Tyrsted, C.; Bremholm, M.; Iversen, B. B. In Situ Total X-Ray Scattering Study of the Formation Mechanism and Structural Defects in Anatase TiO₂ Nanoparticles under Hydrothermal Conditions. *CrystEngComm* **2015**, *17* (36), 6868–6877. <https://doi.org/10.1039/c5ce00544b>.
- (262) Tyrsted, C.; Becker, J.; Hald, P.; Bremholm, M.; Pedersen, J. S.; Chevallier, J.; Cerenius, Y.; Iversen, S. B.; Iversen, B. B. In-Situ Synchrotron Radiation Study of Formation and Growth of Crystalline CexZr1-XO₂ Nanoparticles Synthesized in Supercritical Water. *Chem. Mater.* **2010**, *22* (5), 1814–1820. <https://doi.org/10.1021/cm903316s>.
- (263) Tyrsted, C.; Lock, N.; Jensen, K. M. Ø.; Christensen, M.; Bøjesen, E. D.; Emerich, H.; Vaughan, G.; Billinge, S. J. L.; Iversen, B. B. Evolution of Atomic Structure during Nanoparticle Formation. *IUCrJ* **2014**, *1* (3), 165–171. <https://doi.org/10.1107/S2052252514006538>.
- (264) Foltin, M.; Stueber, G. J.; Bernstein, E. R. Investigation of the Structure, Stability, and Ionization Dynamics of Zirconium Oxide Clusters. *J. Chem. Phys.* **2001**, *114* (20), 8971–8989. <https://doi.org/10.1063/1.1359177>.
- (265) Li, R.; Chawla, A.; Linares, N.; Sutjianto, J. G.; Chapman, K. W.; Martínez, J. G.; Rimer, J. D. Diverse Physical States of Amorphous Precursors in Zeolite Sol Gel Syntheses. *Ind. Eng. Chem. Res.* **2018**, *57* (25), 8460–8471. <https://doi.org/10.1021/acs.iecr.8b01695>.
- (266) Nenoff, T. M.; Karena W. Chapman, Peter J. Chupas, Haiyan Zhao, Kevin A. Beyer, S. H. L. In-Situ Study of Nanoparticle Formation in Zeolites. In *Pacificchem 2020*; 2020.
- (267) Castillo-Blas, C.; Moreno, J. M.; Romero-Muñiz, I.; Platero-Prats, A. E. Applications of Pair Distribution Function Analyses to the Emerging Field of Non-Ideal Metal–Organic Framework Materials. *Nanoscale* **2020**, *12* (29), 15577–15587. <https://doi.org/10.1039/D0NR01673J>.

- (268) Platero-Prats, A. E.; Mavrandonakis, A.; Gallington, L. C.; Liu, Y.; Hupp, J. T.; Farha, O. K.; Cramer, C. J.; Chapman, K. W. Structural Transitions of the Metal-Oxide Nodes within Metal-Organic Frameworks: On the Local Structures of NU-1000 and UiO-66. *J. Am. Chem. Soc.* **2016**, *138* (12), 4178–4185. <https://doi.org/10.1021/jacs.6b00069>.
- (269) Zhang, J.; Longley, L.; Liu, H.; Ashling, C. W.; Chater, P. A.; Beyer, K. A.; Chapman, K. W.; Tao, H.; Keen, D. A.; Bennett, T. D.; Yue, Y. Structural Evolution in a Melt-Quenched Zeolitic Imidazolate Framework Glass during Heat-Treatment. *Chem. Commun.* **2019**, *55* (17), 2521–2524. <https://doi.org/10.1039/c8cc09574d>.
- (270) Easun, T. L.; Moreau, F.; Yan, Y.; Yang, S.; Schröder, M. Structural and Dynamic Studies of Substrate Binding in Porous Metal–Organic Frameworks. *Chem. Soc. Rev.* **2017**, *46* (1), 239–274. <https://doi.org/10.1039/C6CS00603E>.
- (271) Krause, S.; Reuter, F. S.; Ehrling, S.; Bon, V.; Senkovska, I.; Kaskel, S.; Brunner, E. Impact of Defects and Crystal Size on Negative Gas Adsorption in DUT-49 Analyzed by in Situ ¹²⁹Xe NMR Spectroscopy. *Chem. Mater.* **2020**, *32* (11), 4641–4650. <https://doi.org/10.1021/acs.chemmater.0c01059>.
- (272) Baumgartner, B.; Ikigaki, K.; Okada, K.; Takahashi, M. Infrared Crystallography for Framework and Linker Orientation in Metal-Organic Framework Films. *Chem. Sci.* **2021**, *12* (27), 9298–9308. <https://doi.org/10.1039/d1sc02370e>.
- (273) Terban, M. W.; Banerjee, D.; Ghose, S.; Medasani, B.; Shukla, A.; Legg, B. A.; Zhou, Y.; Zhu, Z.; Sushko, M. L.; De Yoreo, J. J.; Liu, J.; Thallapally, P. K.; Billinge, S. J. L. Early Stage Structural Development of Prototypical Zeolitic Imidazolate Framework (ZIF) in Solution. *Nanoscale* **2018**, *10* (9), 4291–4300. <https://doi.org/10.1039/c7nr07949d>.
- (274) Stavitski, E.; Goesten, M.; Juan-Alcañiz, J.; Martinez-Joaristi, A.; Serra-Crespo, P.; Petukhov, A. V.; Gascon, J.; Kapteijn, F. Kinetic Control of Metal-Organic Framework Crystallization Investigated by Time-Resolved in Situ X-Ray Scattering. *Angew. Chemie - Int. Ed.* **2011**, *50* (41), 9624–9628. <https://doi.org/10.1002/anie.201101757>.
- (275) Shearan, S. J. I.; Jacobsen, J.; Costantino, F.; D’Amato, R.; Novikov, D.; Stock, N.; Andreoli, E.; Taddei, M. In Situ X-Ray Diffraction Investigation of the Crystallisation of Perfluorinated CeIV-Based Metal–Organic Frameworks with UiO-66 and MIL-140

- Architectures. *Chem. – A Eur. J.* **2021**, *27* (21), 6579–6592.
<https://doi.org/doi.org/10.1002/chem.202005085>.
- (276) Yeung, H. H. M.; Sapnik, A. F.; Massingberd-Mundy, F.; Gaultois, M. W.; Wu, Y.; Fraser, D. A. X.; Henke, S.; Pallach, R.; Heidenreich, N.; Magdysyuk, O. V.; Vo, N. T.; Goodwin, A. L. Control of Metal–Organic Framework Crystallization by Metastable Intermediate Pre-Equilibrium Species. *Angew. Chemie - Int. Ed.* **2019**, *58* (2), 566–571.
<https://doi.org/10.1002/anie.201810039>.
- (277) Godfrey, H. G. W.; Briggs, L.; Han, X.; Trenholme, W. J. F.; Morris, C. G.; Savage, M.; Kimberley, L.; Magdysyuk, O. V.; Drakopoulos, M.; Murray, C. A.; Tang, C. C.; Frogley, M. D.; Cinque, G.; Yang, S.; Schröder, M. Analysis by Synchrotron X-Ray Scattering of the Kinetics of Formation of an Fe-Based Metal-Organic Framework with High CO₂ Adsorption. *APL Mater.* **2019**, *7* (11), 111104.
<https://doi.org/10.1063/1.5121644>.
- (278) Jones, C. L.; Hughes, C. E.; Yeung, H. H. M.; Paul, A.; Harris, K. D. M.; Easun, T. L. Exploiting in Situ NMR to Monitor the Formation of a Metal-Organic Framework. *Chem. Sci.* **2021**, *12* (4), 1486–1494. <https://doi.org/10.1039/d0sc04892e>.
- (279) Taddei, M.; Casati, N.; Steitz, D. A.; Dümbgen, K. C.; Van Bokhoven, J. A.; Ranocchiari, M. In Situ High-Resolution Powder X-Ray Diffraction Study of UiO-66 under Synthesis Conditions in a Continuous-Flow Microwave Reactor. *CrystEngComm* **2017**, *19* (23), 3206–3214. <https://doi.org/10.1039/c7ce00867h>.
- (280) Ragon, F.; Horcajada, P.; Chevreau, H.; Hwang, Y. K.; Lee, U. H.; Miller, S. R.; Devic, T.; Chang, J. S.; Serre, C. In Situ Energy-Dispersive x-Ray Diffraction for the Synthesis Optimization and Scale-up of the Porous Zirconium Terephthalate UiO-66. *Inorg. Chem.* **2014**, *53* (5), 2491–2500. <https://doi.org/10.1021/ic402514n>.
- (281) Zhu, H.; Huang, Y.; Ren, J.; Zhang, B.; Ke, Y.; Jen, A. K. -Y.; Zhang, Q.; Wang, X. L.; Liu, Q. Bridging Structural Inhomogeneity to Functionality: Pair Distribution Function Methods for Functional Materials Development. *Advanced Science*. John Wiley and Sons Inc March 22, 2021, p 2003534. <https://doi.org/10.1002/advs.202003534>.
- (282) Eckert, M. Disputed Discovery: The Beginnings of X-Ray Diffraction in Crystals in

- 1912 and Its Repercussions. *Acta Crystallogr. Sect. A Found. Crystallogr.* **2012**, 68 (1), 30–39. <https://doi.org/10.1107/S0108767311039985>.
- (283) Cheetham, A. K.; Goodwin, A. L. Crystallography with Powders. *Nat. Mater.* **2014**, 13 (8), 760–762. <https://doi.org/10.1038/nmat4044>.
- (284) Sivia, D. S. S. *Elementary Scattering Theory for X-Ray and Neutron Users*, 1st ed.; Oxford University Press, 2011.
- (285) Hammond, C. *The Basics of Crystallography and Diffraction*, 4th ed.; Oxford University Press, 2015. <https://doi.org/10.1093/acprof:oso/9780198738671.001.0001>.
- (286) Dove, M. T. *Structure and Dynamics: An Atomic View of Materials*; Oxford University Press, 2002.
- (287) Pawley, G. S. Unit-Cell Refinement from Powder Diffraction Scans. *J. Appl. Crystallogr.* **1981**, 14 (6), 357–361. <https://doi.org/10.1107/S0021889881009618>.
- (288) Rietveld, H. M. A Profile Refinement Method for Nuclear and Magnetic Structures. *J. Appl. Crystallogr.* **1969**, 2 (2), 65–71. <https://doi.org/10.1107/S0021889869006558>.
- (289) *The Rietveld Method*; Young, R. A., Ed.; Oxford University Press, 1993.
- (290) Warren, B. E. X-Ray Diffraction in Random Layer Lattices. *Phys. Rev.* **1941**, 59 (9), 693–698. <https://doi.org/10.1103/PhysRev.59.693>.
- (291) Puchberger, M.; Kogler, F. R.; Jupa, M.; Gross, S.; Fric, H.; Kickelbick, G.; Schubert, U. Can the Clusters $Zr_6O_4(OH)_4(OOCR)_2$ and $[Zr_6O_4(OH)_4(OOCR)_2]_2$ Be Converted into Each Other? *Eur. J. Inorg. Chem.* **2006**, 2006 (16), 3283–3293. <https://doi.org/10.1002/ejic.200600348>.
- (292) Åberg, M.; Glaser, J. ^{17}O and 1H NMR Study of the Tetranuclear Hydroxo Zirconium Complex in Aqueous Solution. *Inorganica Chim. Acta* **1993**, 206 (1), 53–61. [https://doi.org/10.1016/S0020-1693\(00\)89259-2](https://doi.org/10.1016/S0020-1693(00)89259-2).
- (293) Tanaka, Y.; Steffen, R. M.; Shera, E. B.; Reuter, W.; Hoehn, M. V.; Zumbro, J. D. Systematics of Ground-State Quadrupole Moments of Odd-A Deformed Nuclei Determined with Muonic $M \times$ Rays. *Phys. Rev. C* **1984**, 29 (5), 1830–1838.

<https://doi.org/10.1103/PhysRevC.29.1830>.

- (294) Xu, H.; Sommer, S.; Broge, N. L. N.; Gao, J.; Iversen, B. B. The Chemistry of Nucleation: In Situ Pair Distribution Function Analysis of Secondary Building Units During UiO-66 MOF Formation. *Chem. - A Eur. J.* **2019**, *25* (8), 2051–2058. <https://doi.org/10.1002/chem.201805024>.
- (295) Van Vleet, M. J.; Weng, T.; Li, X.; Schmidt, J. R. In Situ, Time-Resolved, and Mechanistic Studies of Metal–Organic Framework Nucleation and Growth. *Chem. Rev.* **2018**, *118* (7), 3681–3721. <https://doi.org/10.1021/acs.chemrev.7b00582>.
- (296) Yeung, H. H.-M.; Wu, Y.; Henke, S.; Cheetham, A. K.; O'Hare, D.; Walton, R. I. In Situ Observation of Successive Crystallizations and Metastable Intermediates in the Formation of Metal-Organic Frameworks. *Angew. Chemie* **2016**, *128* (6), 2052–2056. <https://doi.org/10.1002/ange.201508763>.
- (297) Anker, A. S.; Christiansen, T. L.; Weber, M.; Schmiele, M.; Brok, E.; Kjær, E. T. S.; Juhás, P.; Thomas, R.; Mehring, M.; Jensen, K. M. Ø. Structural Changes during the Growth of Atomically Precise Metal Oxido Nanoclusters from Combined Pair Distribution Function and Small-Angle X-Ray Scattering Analysis. *Angew. Chemie - Int. Ed.* **2021**, *60* (37), 20407–20416. <https://doi.org/10.1002/anie.202103641>.
- (298) Billinge, S. J. L. The Rise of the X-Ray Atomic Pair Distribution Function Method: A Series of Fortunate Events. *Philos. Trans. R. Soc. A Math. Phys. Eng. Sci.* **2019**, *377* (2147), 20180413. <https://doi.org/10.1098/rsta.2018.0413>.
- (299) Billinge, S. Local Structure from Total Scattering and Atomic Pair Distribution Function (PDF) Analysis. In *Powder Diffraction*; Dinnebier, R. E., Billinge, S. J. L., Eds.; Royal Society of Chemistry: Cambridge, 2008; pp 464–493. <https://doi.org/10.1039/9781847558237-00464>.
- (300) Farrow, C. L.; Billinge, S. J. L. Relationship between the Atomic Pair Distribution Function and Small-Angle Scattering : Implications for Modeling of Nanoparticles. *Acta Crystallogr. Sect. A Found. Crystallogr.* **2009**, *65* (3), 232–239. <https://doi.org/10.1107/S0108767309009714>.

- (301) Fitch, A. N. Synchrotron Methods. In *Comprehensive Coordination Chemistry III*; Elsevier, 2021; pp 160–182. <https://doi.org/10.1016/B978-0-12-409547-2.14660-8>.
- (302) Egami, T.; Billinge, S. J. L. *Underneath the Bragg Peaks: Structural Analysis of Complex Materials*; Elsevier, 2003.
- (303) Keen, D. A. A Comparison of Various Commonly Used Correlation Functions for Describing Total Scattering. *J. Appl. Crystallogr.* **2001**, *34* (2), 172–177. <https://doi.org/10.1107/S0021889800019993>.
- (304) Tucker, M. G.; Keen, D. A.; Dove, M. T.; Goodwin, A. L.; Hui, Q. RMCProfile: Reverse Monte Carlo for Polycrystalline Materials. *J. Phys. Condens. Matter* **2007**, *19* (33), 335218. <https://doi.org/10.1088/0953-8984/19/33/335218>.
- (305) Juhás, P.; Davis, T.; Farrow, C. L.; Billinge, S. J. L. PDFgetX3: A Rapid and Highly Automatable Program for Processing Powder Diffraction Data into Total Scattering Pair Distribution Functions. *J. Appl. Crystallogr.* **2013**, *46* (2), 560–566. <https://doi.org/10.1107/S0021889813005190>.
- (306) Toby, B. H.; Egami, T. Accuracy of Pair Distribution Function Analysis Applied to Crystalline and Non-crystalline Materials. *Acta Crystallogr. Sect. A* **1992**, *48* (3), 336–346. <https://doi.org/10.1107/S0108767391011327>.
- (307) Compton, A. H. A Quantum Theory of the Scattering of X-Rays by Light Elements. *Phys. Rev.* **1923**, *21* (5), 483–502. <https://doi.org/10.1103/PhysRev.21.483>.
- (308) Skinner, L. B.; Benmore, C. J.; Parise, J. B. Area Detector Corrections for High Quality Synchrotron X-Ray Structure Factor Measurements. *Nucl. Instruments Methods Phys. Res. Sect. A Accel. Spectrometers, Detect. Assoc. Equip.* **2012**, *662* (1), 61–70. <https://doi.org/10.1016/j.nima.2011.09.031>.
- (309) Juhás, P.; Farrow, C. L.; Yang, X.; Knox, K. R.; Billinge, S. J. L. Complex Modeling: A Strategy and Software Program for Combining Multiple Information Sources to Solve Ill Posed Structure and Nanostructure Inverse Problems. *Acta Crystallogr. Sect. A Found. Adv.* **2015**, *71* (6), 562–568. <https://doi.org/10.1107/S2053273315014473>.
- (310) Yan, Z.; Kirby, C. W.; Huang, Y. Directly Probing the Metal Center Environment in

- Layered Zirconium Phosphates by Solid-State ^{91}Zr NMR. *J. Phys. Chem. C* **2008**, *112* (23), 8575–8586. <https://doi.org/10.1021/jp711137c>.
- (311) Salassa, G.; Bürgi, T. NMR Spectroscopy: A Potent Tool for Studying Monolayer-Protected Metal Nanoclusters. *Nanoscale Horizons* **2018**, *3* (5), 457–463. <https://doi.org/10.1039/C8NH00058A>.
- (312) Zhang, R. F.; Li, C. P.; Wang, Q. F.; Ma, C. L. Ligand-Assisted Assembly of Polyoxozirconium Clusters: Syntheses and Characterizations of Tri- and Tetranuclear Half-Zirconocene Complexes. *J. Coord. Chem.* **2010**, *63* (12), 2105–2112. <https://doi.org/10.1080/00958972.2010.497838>.
- (313) Aime, S.; Gobetto, R. Solid State ^{13}C NMR Spectra of Metal Carbonyl Clusters. *J. Clust. Sci.* **1993**, *4* (1), 1–8. <https://doi.org/10.1007/BF01028380>.
- (314) Ohlin, C. A.; Casey, W. H. ^{17}O NMR as a Tool in Discrete Metal Oxide Cluster Chemistry. In *Annual Reports on NMR Spectroscopy*; Academic Press Inc., 2018; Vol. 94, pp 187–248. <https://doi.org/10.1016/bs.arnmr.2018.01.001>.
- (315) Chu, P. J.; Ziebarth, R. P.; Corbett, J. D.; Gerstein, B. C. Characterization of Interstitial Hydrogen within Metal Clusters in $\text{Zr}_6\text{Cl}_{12}\text{H}$ and ZrClO_xH_y , by Solid-State Nuclear Magnetic Resonance. *J. Am. Chem. Soc.* **1988**, *110* (16), 5324–5329. <https://doi.org/10.1021/ja00224a016>.
- (316) Labouriau, A.; Panjabi, G.; Enderle, B.; Pietrass, T.; Gates, B. C.; Earl, W. L.; Ott, K. C. ^{129}Xe NMR Spectroscopy of Metal Carbonyl Clusters and Metal Clusters in Zeolite NaY. *J. Am. Chem. Soc.* **1999**, *121* (33), 7674–7681. <https://doi.org/10.1021/ja990532j>.
- (317) Harris, K. D. M.; Hughes, C. E.; Williams, P. A.; Edwards-Gau, G. R. ‘NMR Crystallization’: In-Situ NMR Techniques for Time-Resolved Monitoring of Crystallization Processes. *Acta Crystallogr. Sect. C Struct. Chem.* **2017**, *73* (3), 137–148. <https://doi.org/10.1107/S2053229616019811>.
- (318) Gunnarsdóttir, A. B.; Amanchukwu, C. V.; Menkin, S.; Grey, C. P. Noninvasive in Situ NMR Study of “Dead Lithium” Formation and Lithium Corrosion in Full-Cell Lithium Metal Batteries. *J. Am. Chem. Soc.* **2020**, *142* (49), 20814–20827.

<https://doi.org/10.1021/jacs.0c10258>.

- (319) Zhao, E. W.; Liu, T.; Jónsson, E.; Lee, J.; Temprano, I.; Jethwa, R. B.; Wang, A.; Smith, H.; Carretero-González, J.; Song, Q.; Grey, C. P. In Situ NMR Metrology Reveals Reaction Mechanisms in Redox Flow Batteries. *Nature* **2020**, *579* (7798), 224–228. <https://doi.org/10.1038/s41586-020-2081-7>.
- (320) Hughes, C. E.; Williams, P. A.; Kariuki, B. M.; Harris, K. D. M. Establishing the Transitory Existence of Amorphous Phases in Crystallization Pathways by the CLASSIC NMR Technique. *ChemPhysChem* **2018**, *19* (24), 3341–3345. <https://doi.org/10.1002/cphc.201800976>.
- (321) Hughes, C. E.; Williams, P. A.; Harris, K. D. M. “CLASSIC NMR”: An In-Situ NMR Strategy for Mapping the Time-Evolution of Crystallization Processes by Combined Liquid-State and Solid-State Measurements. *Angew. Chemie* **2014**, *126* (34), 9085–9089. <https://doi.org/10.1002/ange.201404266>.
- (322) Lucier, B. E. G.; Huang, Y. A Review of ⁹¹Zr Solid-State Nuclear Magnetic Resonance Spectroscopy. *Annu. Reports NMR Spectrosc.* **2015**, *84*, 233–289. <https://doi.org/10.1016/bs.arnmr.2014.10.005>.
- (323) Carnevale, D.; Mouchaham, G.; Wang, S.; Baudin, M.; Serre, C.; Bodenhausen, G.; Abergel, D. Natural Abundance Oxygen-17 Solid-State NMR of Metal Organic Frameworks Enhanced by Dynamic Nuclear Polarization. *Phys. Chem. Chem. Phys.* **2021**, *23* (3), 2245–2251. <https://doi.org/10.1039/d0cp06064j>.
- (324) Moraru, B.; Gross, S.; Kickelbick, G.; Trimmel, G.; Schubert, U. A New Type of Methacrylate-Substituted Oxozirconium Clusters: [Zr₃O(OR)₅(OMc)₅]₂ and [Zr₃O(OR)₃(OMc)₇]₂. *Monatshefte für Chemie* **2001**, *132* (9), 993–999. <https://doi.org/10.1007/s007060170039>.
- (325) Trimmel, G.; Gross, S.; Kickelbick, G.; Schubert*, U. Swelling Behavior and Thermal Stability of Poly(Methylmethacrylate) Crosslinked by the Oxozirconium Cluster Zr₄O₂(Methacrylate)₁₂. *Appl. Organomet. Chem.* **2001**, *15* (5), 401–406. <https://doi.org/10.1002/aoc.161>.

- (326) Gao, Y.; Kogler, F. R.; Peterlik, H.; Schubert, U. Ring-Opening Metathesis Polymerizations with Norbornene Carboxylate-Substituted Metal Oxo Clusters. *J. Mater. Chem.* **2006**, *16* (32), 3268–3276. <https://doi.org/10.1039/b518277h>.
- (327) Shaikh, S. M.; Usov, P. M.; Zhu, J.; Cai, M.; Alatis, J.; Morris, A. J. Synthesis and Defect Characterization of Phase-Pure Zr-MOFs Based on Meso-Tetracarboxyphenylporphyrin. *Inorg. Chem.* **2019**, *58*, 5145–5153. <https://doi.org/10.1021/acs.inorgchem.9b00200>.
- (328) Mukherjee, A.; Sen, T. K.; Baskaran, S.; Sivasankar, C.; Mandal, S. K. Slow Hydrolysis of an Organozirconium Complex: The First Polyoxometallic Heptanuclear Zirconium Oxide. *J. Organomet. Chem.* **2015**, *775*, 76–79. <https://doi.org/10.1016/j.jorganchem.2014.10.022>.
- (329) Bono, D.; Hartig, J.; Huber, M.; Schnöckel, H.; De Jongh, L. J. ²⁷Al NMR Study of the Metal Cluster Compound Al₅O₁₂H₁₈. *J. Clust. Sci.* **2007**, *18* (1), 319–331. <https://doi.org/10.1007/s10876-007-0111-3>.
- (330) Chen, L.; Cotton, F. A.; Wojtczak, W. A. Zirconium Clusters from the Reaction of ZrCl₄ with HSnBu₃ Followed by Addition of Phosphines: Zr₆Cl₁₄H₄(PR₃)₄ Compounds. *Inorg. Chem.* **1996**, *35* (10), 2988–2994. <https://doi.org/10.1021/ic951256m>.
- (331) Kickelbick, G.; Schubert, U. Oxozirconium Methacrylate Clusters: Zr₆(OH)₄O₄(OMc)₁₂ and Zr₄O₂(OMc)₁₂ (OMc = Methacrylate). *Chem. Ber.* **1997**, *130* (4), 473–478. <https://doi.org/10.1002/cber.19971300406>.
- (332) Faccini, F.; Fric, H.; Schubert, U.; Wendel, E.; Tsetsgee, O.; Müller, K.; Bertagnolli, H.; Venzo, A.; Gross, S. ω-Mercapto-Functionalized Hafnium- and Zirconium-Oxoclusters as Nanosized Building Blocks for Inorganic-Organic Hybrid Materials: Synthesis, Characterization and Photothiol-Ene Polymerization. *J. Mater. Chem.* **2007**, *17* (31), 3297–3307. <https://doi.org/10.1039/b702714a>.
- (333) Keeler, J. *Understanding NMR Spectroscopy*, 2nd ed.; Wiley, 2010.
- (334) Sanders, J. K. M.; Hunter, B. K. *Modern NMR Spectroscopy: A Guide for Chemists*, 2nd ed.; Oxford University Press, 1993.

- (335) Abraham, R. J.; Fisher, J.; Loftus, P. *Introduction to NMR Spectroscopy*; John Wiley & Sons, 1988. <https://doi.org/https://www.wiley.com/en-us/Introduction+to+NMR+Spectroscopy-p-9780471918943>.
- (336) Neuhaus, D. Nuclear Overhauser Effect. In *Encyclopedia of Magnetic Resonance*; John Wiley & Sons, Ltd: Chichester, UK, 2011. <https://doi.org/10.1002/9780470034590.emrstm0350.pub2>.
- (337) Shearer, G. C.; Forselv, S.; Chavan, S.; Bordiga, S.; Mathisen, K.; Bjørgen, M.; Svelle, S.; Lillerud, K. P. In Situ Infrared Spectroscopic and Gravimetric Characterisation of the Solvent Removal and Dehydroxylation of the Metal Organic Frameworks UiO-66 and UiO-67. *Top. Catal.* **2013**, *56* (9–10), 770–782. <https://doi.org/10.1007/s11244-013-0027-0>.
- (338) Abánades Lázaro, I. A Comprehensive Thermogravimetric Analysis Multifaceted Method for the Exact Determination of the Composition of Multifunctional Metal-Organic Framework Materials. *Eur. J. Inorg. Chem.* **2020**, *2020* (45), 4284–4294. <https://doi.org/10.1002/ejic.202000656>.
- (339) Al-Terkawi, A.-A.; Scholz, G.; Emmerling, F.; Kemnitz, E. Mechanochemical Synthesis, Characterization, and Structure Determination of New Alkaline Earth Metal-Tetrafluoroterephthalate Frameworks: Ca(PBDC-F4)·4H₂O, Sr(PBDC-F4)·4H₂O, and Ba(PBDC-F4). *Cryst. Growth Des.* **2016**, *16* (4), 1923–1933. <https://doi.org/10.1021/acs.cgd.5b01457>.
- (340) Waitschat, S.; Fröhlich, D.; Reinsch, H.; Terraschke, H.; Lomachenko, K. A.; Lamberti, C.; Kummer, H.; Helling, T.; Baumgartner, M.; Henninger, S.; Stock, N. Synthesis of M-UiO-66 (M = Zr, Ce or Hf) Employing 2,5-Pyridinedicarboxylic Acid as a Linker: Defect Chemistry, Framework Hydrophilisation and Sorption Properties. *Dalt. Trans.* **2018**, *47* (4), 1062–1070. <https://doi.org/10.1039/c7dt03641h>.
- (341) Liang, W.; Babarao, R.; Murphy, M. J.; D’Alessandro, D. M. The First Example of a Zirconium-Oxide Based Metal–Organic Framework Constructed from Monocarboxylate Ligands. *Dalt. Trans.* **2015**, *44* (4), 1516–1519. <https://doi.org/10.1039/C4DT03183K>.
- (342) Ling, S.; Slater, B. Dynamic Acidity in Defective UiO-66. *Chem. Sci.* **2016**, *7* (7), 4706–

4712. <https://doi.org/10.1039/C5SC04953A>.
- (343) Valenzano, L.; Civalieri, B.; Chavan, S.; Bordiga, S.; Nilsen, M. H.; Jakobsen, S.; Lillerud, K. P.; Lamberti, C. Disclosing the Complex Structure of UiO-66 Metal Organic Framework: A Synergic Combination of Experiment and Theory. *Chem. Mater.* **2011**, *23* (7), 1700–1718. <https://doi.org/10.1021/cm1022882>.
- (344) Ghosh, P.; Colón, Y. J.; Snurr, R. Q. Water Adsorption in UiO-66 : The Importance of Defects. *Chem Commun* **2014**, *50* (77), 11329–11331. <https://doi.org/10.1039/C4CC04945D>.
- (345) Singh, T. I.; Rajeshkhanna, G.; Pan, U. N.; Kshetri, T.; Lin, H.; Kim, N. H.; Lee, J. H. Alkaline Water Splitting Enhancement by MOF-Derived Fe–Co–Oxide/Co@NC-MNS Heterostructure: Boosting OER and HER through Defect Engineering and In Situ Oxidation. *Small* **2021**, *17* (29), 2101312. <https://doi.org/10.1002/sml.202101312>.
- (346) Hu, Z.; Peng, Y.; Kang, Z.; Qian, Y.; Zhao, D. A Modulated Hydrothermal (MHT) Approach for the Facile Synthesis of UiO-66-Type MOFs. *Inorg. Chem.* **2015**, *54* (10), 4862–4868. <https://doi.org/10.1021/acs.inorgchem.5b00435>.
- (347) Coelho, A. A. TOPAS and TOPAS-Academic: An Optimization Program Integrating Computer Algebra and Crystallographic Objects Written in C++. *J. Appl. Crystallogr.* **2018**, *51* (1), 210–218. <https://doi.org/10.1107/S1600576718000183>.
- (348) Macrae, C. F.; Bruno, I. J.; Chisholm, J. A.; Edgington, P. R.; McCabe, P.; Pidcock, E.; Rodriguez-Monge, L.; Taylor, R.; Van De Streek, J.; Wood, P. A. Mercury CSD 2.0 - New Features for the Visualization and Investigation of Crystal Structures. *J. Appl. Crystallogr.* **2008**, *41* (2), 466–470. <https://doi.org/10.1107/S0021889807067908>.
- (349) Momma, K.; Izumi, F. VESTA 3 for Three-Dimensional Visualization of Crystal, Volumetric and Morphology Data. *J. Appl. Crystallogr.* **2011**, *44*, 1272–1276.
- (350) Dubbeldam, D.; Calero, S.; Ellis, D. E.; Snurr, R. Q. RASPA: Molecular Simulation Software for Adsorption and Diffusion in Flexible Nanoporous Materials. *Mol. Simul.* **2015**, *42* (2), 81–101. <https://doi.org/10.1080/08927022.2015.1010082>.
- (351) Potoff, J. J.; Siepmann, J. I. Vapor–Liquid Equilibria of Mixtures Containing Alkanes,

- Carbon Dioxide, and Nitrogen. *AIChE J.* **2001**, *47* (7), 1676–1682.
<https://doi.org/10.1002/aic.690470719>.
- (352) Rappé, A. K.; Casewit, C. J.; Colwell, K. S.; Goddard III, W. A.; Skiff, W. M. UFF, a Full Periodic Table Force Field for Molecular Mechanics and Molecular Dynamics Simulations. *J. Am. Chem. Soc.* **1992**, *114* (25), 10024–10035.
<https://doi.org/10.1021/ja00051a040>.
- (353) Lorentz, H. A. Ueber Die Anwendung Des Satzes Vom Virial in Der Kinetischen Theorie Der Gase. *Ann. Phys.* **1881**, *248* (1), 127–136.
<https://doi.org/10.1002/andp.18812480110>.
- (354) Berthelot, D. Sur Le Melange Des Gaz. *C. R. Hebd. Seances Acad. Sci.* **1898**, *126*, 1703–1855.
- (355) Nickerl, G.; Leistner, M.; Helten, S.; Bon, V.; Senkovska, I.; Kaskel, S. Integration of Accessible Secondary Metal Sites into MOFs for H₂S Removal. *Inorg. Chem. Front.* **2014**, *1* (4), 325–330. <https://doi.org/10.1039/c3qi00093a>.
- (356) Trickett, C. A.; Gagnon, K. J.; Lee, S.; Gándara, F.; Bürgi, H.-B.; Yaghi, O. M. Definitive Molecular Level Characterization of Defects in UiO-66 Crystals. *Angew. Chemie* **2015**, *127* (38), 11314–11319. <https://doi.org/10.1002/ange.201505461>.
- (357) Lawrence, M. C.; Schneider, C.; Katz, M. J. Determining the Structural Stability of UiO-67 with Respect to Time: A Solid-State NMR Investigation. *Chem. Commun.* **2016**, *52* (28), 4971–4974. <https://doi.org/10.1039/c5cc09919f>.
- (358) Ermer, M.; Mehler, J.; Kriesten, M.; Avadhut, Y.; Schulz, P. S.; Hartmann, M. Synthesis of the Novel MOF Hcp UiO-66 Employing Ionic Liquids as Linker Precursors. *Dalt. Trans.* **2018**, *47*, 14426–14430. <https://doi.org/10.1039/C8DT02999G>.
- (359) Momeni, M. R.; Cramer, C. J. Structural Characterization of Pristine and Defective [Zr₁₂(M₃-O)₈(M₃-OH)₈(M₂-OH)₆]₁₈₊ Double-Node Metal-Organic Framework and Predicted Applications for Single-Site Catalytic Hydrolysis of Sarin. *Chem. Mater.* **2018**, *30* (13), 4432–4439. <https://doi.org/10.1021/acs.chemmater.8b01913>.
- (360) Brunauer, S.; Emmett, P. H.; Teller, E. Adsorption of Gases in Multimolecular Layers.

- J. Am. Chem. Soc.* **1938**, *60* (2), 309–319. <https://doi.org/10.1021/ja01269a023>.
- (361) Andersson, S.; Sundholm, A.; Magnéli, A. A Homologous Series of Mixed Titanium Chromium Oxides $Ti_{(n-2)}Cr_2O_{(2n-1)}$ Isomorphous with the Series $Ti_{(n)}O_{(2n-1)}$ and $V_{(n)}O_{(2n-1)}$. *Acta Chem. Scand.* **1959**, *13*, 989–997.
- (362) Fairen-Jimenez, D.; Galvelis, R.; Torrisi, A.; Gellan, A. D.; Wharmby, M. T.; Wright, P. A.; Mellot-Draznieks, C.; Düren, T. Flexibility and Swing Effect on the Adsorption of Energy-Related Gases on ZIF-8: Combined Experimental and Simulation Study. *Dalt. Trans.* **2012**, *41* (35), 10752–10762. <https://doi.org/10.1039/c2dt30774j>.
- (363) Lowell, S.; Shields, J. E. Adsorption Isotherms. In *Powder Surface Area and Porosity*; Springer, Dordrecht, 1984; pp 11–13.
- (364) Schneider, P. Adsorption Isotherms of Microporous-Mesoporous Solids Revisited. *Appl. Catal. A, Gen.* **1995**, *129* (2), 157–165. [https://doi.org/10.1016/0926-860X\(95\)00110-7](https://doi.org/10.1016/0926-860X(95)00110-7).
- (365) Li, B.; Zhu, X.; Hu, K.; Li, Y.; Feng, J.; Shi, J.; Gu, J. Defect Creation in Metal-Organic Frameworks for Rapid and Controllable Decontamination of Roxarsone from Aqueous Solution. *J. Hazard. Mater.* **2016**, *302*, 57–64. <https://doi.org/10.1016/j.jhazmat.2015.09.040>.
- (366) Peterson, G. W.; Moon, S.-Y.; Wagner, G. W.; Hall, M. G.; Decoste, J. B.; Hupp, J. T.; Farha, O. K. Tailoring the Pore Size and Functionality of UiO-Type Metal – Organic Frameworks for Optimal Nerve Agent Destruction. *Inorg. Chem.* **2015**, *54* (20), 9684–9686. <https://doi.org/10.1021/acs.inorgchem.5b01867>.
- (367) Horvath, G.; Kawazoe, K. Method for the Calculation of Effective Pore Size Distribution in Molecular Sieve Carbon. *J. Chem. Eng. Japan* **1983**, *16* (6), 470–475.
- (368) Dombrowski, R. J.; Lastoskie, C. M.; Hyduke, D. R. The Horvath – Kawazoe Method Revisited. *Colloids Surfaces A Physicochem. Eng. Asp.* **2001**, *187–188*, 23–39.
- (369) Barrett, E. P.; Joyner, L. G.; Halenda, P. P. The Determination of Pore Volume and Area Distributions in Porous Substances. I. Computations from Nitrogen Isotherms. *J. Am. Chem. Soc.* **1951**, *73* (1), 373–380. <https://doi.org/10.1021/ja01145a126>.

- (370) Cheng, L. S.; Yang, R. T. Improved Horvath-Kawazoe Equations Including Spherical Pore Models for Calculating Micropore Size Distribution. *Chem. Eng. Sci.* **1994**, *49* (16), 2599–2609.
- (371) Saito, A.; Foley, H. C. Curvature and Parametric Sensitivity in Models for Adsorption in Micropores. *AIChE J.* **1991**, *37* (3), 429–436.
- (372) Basham, M.; Filik, J.; Wharmby, M. T.; Chang, P. C. Y.; El Kassaby, B.; Gerring, M.; Aishima, J.; Levik, K.; Pulford, B. C. A.; Sikharulidze, I.; Sneddon, D.; Webber, M.; Dhesi, S. S.; Maccherozzi, F.; Svensson, O.; Brockhauser, S.; Náray, G.; Ashton, A. W. Data Analysis Workbench (DAWN). *J. Synchrotron Radiat.* **2015**, *22* (3), 853–858.
<https://doi.org/10.1107/S1600577515002283>.
- (373) Harris, C. R.; Millman, K. J.; van der Walt, S. J.; Gommers, R.; Virtanen, P.; Cournapeau, D.; Wieser, E.; Taylor, J.; Berg, S.; Smith, N. J.; Kern, R.; Picus, M.; Hoyer, S.; van Kerkwijk, M. H.; Brett, M.; Haldane, A.; del Río, J. F.; Wiebe, M.; Peterson, P.; Gérard-Marchant, P.; Sheppard, K.; Reddy, T.; Weckesser, W.; Abbasi, H.; Gohlke, C.; Oliphant, T. E. Array Programming with NumPy. *Nature* **2020**, *585* (7825), 357–362.
<https://doi.org/10.1038/s41586-020-2649-2>.
- (374) Virtanen, P.; Gommers, R.; Oliphant, T. E.; Haberland, M.; Reddy, T.; Cournapeau, D.; Burovski, E.; Peterson, P.; Weckesser, W.; Bright, J.; van der Walt, S. J.; Brett, M.; Wilson, J.; Millman, K. J.; Mayorov, N.; Nelson, A. R. J.; Jones, E.; Kern, R.; Larson, E.; Carey, C. J.; Polat, İ.; Feng, Y.; Moore, E. W.; VanderPlas, J.; Laxalde, D.; Perktold, J.; Cimrman, R.; Henriksen, I.; Quintero, E. A.; Harris, C. R.; Archibald, A. M.; Ribeiro, A. H.; Pedregosa, F.; van Mulbregt, P.; Vijaykumar, A.; Bardelli, A. Pietro; Rothberg, A.; Hilboll, A.; Kloeckner, A.; Scopatz, A.; Lee, A.; Rokem, A.; Woods, C. N.; Fulton, C.; Masson, C.; Häggström, C.; Fitzgerald, C.; Nicholson, D. A.; Hagen, D. R.; Pasechnik, D. V.; Olivetti, E.; Martin, E.; Wieser, E.; Silva, F.; Lenders, F.; Wilhelm, F.; Young, G.; Price, G. A.; Ingold, G. L.; Allen, G. E.; Lee, G. R.; Audren, H.; Probst, I.; Dietrich, J. P.; Silterra, J.; Webber, J. T.; Slavič, J.; Nothman, J.; Buchner, J.; Kulick, J.; Schönberger, J. L.; de Miranda Cardoso, J. V.; Reimer, J.; Harrington, J.; Rodríguez, J. L. C.; Nunez-Iglesias, J.; Kuczynski, J.; Tritz, K.; Thoma, M.; Newville, M.; Kümmerer, M.; Bolingbroke, M.; Tartre, M.; Pak, M.; Smith, N. J.; Nowaczyk, N.; Shebanov, N.;

- Pavlyk, O.; Brodtkorb, P. A.; Lee, P.; McGibbon, R. T.; Feldbauer, R.; Lewis, S.; Tygier, S.; Sievert, S.; Vigna, S.; Peterson, S.; More, S.; Pudlik, T.; Oshima, T.; Pingel, T. J.; Robitaille, T. P.; Spura, T.; Jones, T. R.; Cera, T.; Leslie, T.; Zito, T.; Krauss, T.; Upadhyay, U.; Halchenko, Y. O.; Vázquez-Baeza, Y. SciPy 1.0: Fundamental Algorithms for Scientific Computing in Python. *Nat. Methods* **2020**, *17* (3), 261–272. <https://doi.org/10.1038/s41592-019-0686-2>.
- (375) Daigle, M.; Bi, W.; Légaré, M. A.; Morin, J. F.; Fontaine, F. G. Synthesis of Carboxylate Cp*Zr(IV) Species: Toward the Formation of Novel Metallocavitands. *Inorg. Chem.* **2015**, *54* (11), 5547–5555. <https://doi.org/10.1021/acs.inorgchem.5b00634>.
- (376) Fitzgerald, M.; Pappas, I.; Zheng, C.; Xie, Z. L.; Huang, X. Y.; Tao, S.; Pan, L. First Hexanuclear Zirconium Macrocycle Sustained in a Chair-like Conformation by Glycolic Acids. *J. Chem. Soc. Dalt. Trans.* **2009**, No. 32, 6289–6291. <https://doi.org/10.1039/b912160a>.
- (377) Bai, G.; Ma, Q.; Roesky, H. W.; Vidovic, D.; Herbst-Irmer, R. New Synthetic Route for Organic Polyoxometallic Clusters: Synthetic and Structural Investigations on the First Dumb-Bell Shaped Polyoxozirconium Hydroxide with the [Zr₉(M₅-O)₂(M₃-O)₄(μ-O)₄(μ-OH)₈] Core Structure. *Chem. Commun.* **2003**, 3 (7), 898–899. <https://doi.org/10.1039/b212281b>.
- (378) Kalaji, A.; Soderholm, L. A Novel Nonanuclear Hafnium Oxide–Hydroxide–Sulphate Cluster Crystallised from Aqueous Solution. *Chem. Commun.* **2014**, 50 (8), 997–999. <https://doi.org/10.1039/c3cc48167k>.
- (379) Kang, X. M.; Hu, H. S.; Wu, Z. L.; Wang, J. Q.; Cheng, P.; Li, J.; Zhao, B. An Ultrastable Matryoshka [Hf₁₃] Nanocluster as a Luminescent Sensor for Concentrated Alkali and Acid. *Angew. Chemie - Int. Ed.* **2019**, *58* (46), 16610–16616. <https://doi.org/10.1002/anie.201907557>.
- (380) Xu, T.; Hou, X.; Wang, Y.; Zhang, J.; Zhang, J.; Liu, B. A Gigantic Polyoxozirconate with Visible Photoactivity. *Dalt. Trans.* **2017**, 46 (31), 10185–10188. <https://doi.org/10.1039/c7dt02013a>.
- (381) Platero-Prats, A. E.; League, A. B.; Bernales, V.; Ye, J.; Gallington, L. C.; Vjunov, A.;

- Schweitzer, N. M.; Li, Z.; Zheng, J.; Mehdi, B. L.; Stevens, A. J.; Dohnalkova, A.; Balasubramanian, M.; Farha, O. K.; Hupp, J. T.; Browning, N. D.; Fulton, J. L.; Camaioni, D. M.; Lercher, J. A.; Truhlar, D. G.; Gagliardi, L.; Cramer, C. J.; Chapman, K. W. Bridging Zirconia Nodes within a Metal-Organic Framework via Catalytic Ni-Hydroxo Clusters to Form Heterobimetallic Nanowires. *J. Am. Chem. Soc.* **2017**, *139* (30), 10410–10418. <https://doi.org/10.1021/jacs.7b04997>.
- (382) Bon, V.; Senkovska, I.; Weiss, M. S.; Kaskel, S. Tailoring of Network Dimensionality and Porosity Adjustment in Zr- and Hf-Based MOFs. *CrystEngComm* **2013**, *15* (45), 9572–9577. <https://doi.org/10.1039/c3ce41121d>.
- (383) Piszczek, P.; Radtke, A.; Grodzicki, A.; Wojtczak, A.; Chojnacki, J. The New Type of [Zr₆(M₃-O)₄(M₃-OH)₄] Cluster Core: Crystal Structure and Spectral Characterization of [Zr₆O₄(OH)₄(OOCR)₁₂] (R=But, C(CH₃)₂Et). *Polyhedron* **2007**, *26* (3), 679–685. <https://doi.org/10.1016/j.poly.2006.08.025>.
- (384) Piszczek, P.; Radtke, A.; Wojtczak, A.; Muzioł, T.; Chojnacki, J. Synthesis, Structure Characterization and Thermal Properties of [Zr₆(M₃-O)₄(M₃-OH)₄(OOCCH₂tBu)₉(M₂-OH)₃]₂. *Polyhedron* **2009**, *28* (2), 279–285. <https://doi.org/10.1016/j.poly.2008.10.034>.
- (385) Salomon, W.; Roch-Marchal, C.; Mialane, P.; Rouschmeyer, P.; Serre, C.; Haouas, M.; Taulelle, F.; Yang, S.; Ruhlmann, L.; Dolbecq, A. Immobilization of Polyoxometalates in the Zr-Based Metal Organic Framework UiO-67. *Chem. Commun.* **2015**, *51* (14), 2972–2975. <https://doi.org/10.1039/c4cc09986a>.
- (386) Siskos, M. G.; Tzakos, A. G.; Gerothanassis, I. P. Accurate Ab Initio Calculations of O-H...O and O-H...-O Proton Chemical Shifts: Towards Elucidation of the Nature of the Hydrogen Bond and Prediction of Hydrogen Bond Distances. *Org. Biomol. Chem.* **2015**, *13* (33), 8852–8868. <https://doi.org/10.1039/c5ob00920k>.
- (387) Konrat, R.; Tollinger, M.; Kontaxis, G.; Kräutler, B. NMR Techniques to Study Hydrogen Bonding in Aqueous Solution. *Monatshefte für Chemie / Chem. Mon.* **1999**, *130* (8), 961–982. <https://doi.org/10.1007/PL00010281>.
- (388) Zarycz, M. N. C.; Fonseca Guerra, C. NMR ¹H-Shielding Constants of Hydrogen-

- Bond Donor Reflect Manifestation of the Pauli Principle. *J. Phys. Chem. Lett.* **2018**, *9* (13), 3720–3724. <https://doi.org/10.1021/acs.jpcllett.8b01502>.
- (389) Charisiadis, P.; Kontogianni, V. G.; Tsiafoulis, C. G.; Tzakos, A. G.; Siskos, M.; Gerothanassis, I. P. ¹H-NMR as a Structural and Analytical Tool of Intra- and Intermolecular Hydrogen Bonds of Phenol-Containing Natural Products and Model Compounds. *Molecules*. MDPI AG September 2, 2014, pp 13643–13682. <https://doi.org/10.3390/molecules190913643>.
- (390) Fulmer, G. R.; Miller, A. J. M.; Sherden, N. H.; Gottlieb, H. E.; Nudelman, A.; Stoltz, B. M.; Bercaw, J. E.; Goldberg, K. I. NMR Chemical Shifts of Trace Impurities: Common Laboratory Solvents, Organics, and Gases in Deuterated Solvents Relevant to the Organometallic Chemist. *Organometallics* **2010**, *29* (9), 2176–2179. <https://doi.org/10.1021/om100106e>.
- (391) Moret, S.; Dyson, P. J.; Laurency, G. Direct, in Situ Determination of PH and Solute Concentrations in Formic Acid Dehydrogenation and CO₂ Hydrogenation in Pressurised Aqueous Solutions Using ¹H and ¹³C NMR Spectroscopy. *Dalt. Trans.* **2013**, *42* (13), 4353–4356. <https://doi.org/10.1039/c3dt00081h>.
- (392) Rondinini, S. PH Measurements in Non-Aqueous and Aqueous-Organic Solvents - Definition of Standard Procedures. *Anal. Bioanal. Chem.* **2002**, *374* (5), 813–816. <https://doi.org/10.1007/s00216-002-1455-z>.
- (393) Limbach, H.-H.; Tolstoy, P. M.; Pérez-Hernández, N.; Guo, J.; Shenderovich, I. G.; Denisov, G. S. OHO Hydrogen Bond Geometries and NMR Chemical Shifts: From Equilibrium Structures to Geometric H/D Isotope Effects, with Applications for Water, Protonated Water, and Compressed Ice. *Isr. J. Chem.* **2009**, *49* (2), 199–216. <https://doi.org/10.1560/ijc.49.2.199>.
- (394) Solomon, I. Relaxation Processes in a System of Two Spins. *Phys. Rev.* **1955**, *99* (2), 559–565. <https://doi.org/10.1103/PhysRev.99.559>.
- (395) Macura, S.; Ernst, R. R. Elucidation of Cross Relaxation in Liquids by Two-Dimensional N.M.R. Spectroscopy. *Mol. Phys.* **1980**, *41* (1), 95–117. <https://doi.org/10.1080/00268978000102601>.

- (396) Jeener, J.; Meier, B. H.; Bachmann, P.; Ernst, R. R. Investigation of Exchange Processes by Two-Dimensional NMR Spectroscopy. *J. Chem. Phys.* **1979**, *71* (11), 4546–4553.
<https://doi.org/10.1063/1.438208>.
- (397) Anet, F. A. L.; Bourn, A. J. R. Nuclear Magnetic Resonance Spectral Assignments from Nuclear Overhauser Effects. *J. Am. Chem. Soc.* **1965**, *87* (22), 5250–5251.
<https://doi.org/10.1021/ja00950a048>.
- (398) Boros, S.; Gáspári, Z.; Batta, G. Accurate NMR Determinations of Proton–Proton Distances. *Annu. Reports NMR Spectrosc.* **2018**, *94*, 1–39.
<https://doi.org/10.1016/bs.arnmr.2017.12.002>.
- (399) Hulushe, S. T.; Hosten, E. C.; Watkins, G. M. Dimethylammonium 2,4,5-Tricarboxybenzoate: An Example of the Decarbonylation of N,N-Dimethylformamide in the Presence of a Metal and a Benzenepolycarboxylic Acid. Is Zirconium(IV) the Tsotsi? *Acta Crystallogr. Sect. E Crystallogr. Commun.* **2016**, *72* (Pt 11), 1521–1525.
<https://doi.org/10.1107/S2056989016014948>.
- (400) Walther, C.; Rothe, J.; Fuss, M.; Büchner, S.; Koltsov, S.; Bergmann, T. Investigation of Polynuclear Zr(IV) Hydroxide Complexes by Nanoelectrospray Mass-Spectrometry Combined with XAFS. *Anal. Bioanal. Chem.* **2007**, *388* (2), 409–431.
<https://doi.org/10.1007/s00216-007-1223-1>.
- (401) Haddad, S.; Abánades Lázaro, I.; Fantham, M.; Mishra, A.; Silvestre-Albero, J.; Osterrieth, J. W. M.; Kaminski Schierle, G. S.; Kaminski, C. F.; Forgan, R. S.; Fairen-Jimenez, D. Design of a Functionalized Metal-Organic Framework System for Enhanced Targeted Delivery to Mitochondria. *J. Am. Chem. Soc.* **2020**, *142* (14), 6661–6674. <https://doi.org/10.1021/jacs.0c00188>.
- (402) Gao, X.; Hai, X.; Baigude, H.; Guan, W.; Liu, Z. Fabrication of Functional Hollow Microspheres Constructed from MOF Shells: Promising Drug Delivery Systems with High Loading Capacity and Targeted Transport. *Sci. Rep.* **2016**, *6* (1), 37705.
<https://doi.org/10.1038/srep37705>.
- (403) Cahill, J. F.; Khalid, M.; Retterer, S. T.; Walton, C. L.; Kertesz, V. In Situ Chemical Monitoring and Imaging of Contents within Microfluidic Devices Having a Porous

Membrane Wall Using Liquid Microjunction Surface Sampling Probe Mass Spectrometry. *J. Am. Soc. Mass Spectrom.* **2020**, *31* (4), 832–839.
<https://doi.org/10.1021/jasms.9b00093>.

- (404) Schneemann, A.; Bon, V.; Schwedler, I.; Senkovska, I.; Kaskel, S.; Fischer, R. A. Flexible Metal–Organic Frameworks. *Chem. Soc. Rev.* **2014**, *43* (16), 6062–6096.
<https://doi.org/10.1039/C4CS00101J>.
- (405) Carrington, E. J.; Dodsworth, S. F.; van Meurs, S.; Warren, M. R.; Brammer, L. Post-Synthetic Modification Unlocks a 2D-to-3D Switch in MOF Breathing Response: A Single-Crystal-Diffraction Mapping Study. *Angew. Chemie - Int. Ed.* **2021**, *60* (33), 17920–17924. <https://doi.org/10.1002/anie.202105272>.
- (406) Carrington, E. J.; McAnally, C. A.; Fletcher, A. J.; Thompson, S. P.; Warren, M.; Brammer, L. Solvent-Switchable Continuous-Breathing Behaviour in a Diamondoid Metal-Organic Framework and Its Influence on CO₂ versus CH₄ Selectivity. *Nat. Chem.* **2017**, *9* (9), 882–889. <https://doi.org/10.1038/nchem.2747>.
- (407) Diamond Light Source. I15-1 Sample Environments
<https://www.diamond.ac.uk/Instruments/Crystallography/I15-1/sample-environments.html> (accessed Sep 16, 2021).

Appendices

Appendix A: Calculation used for TGA curves of hcp UiO-66

When analysing a sample of hcp UiO-66 MOF, containing BDC linkers and defect-compensating hydroxide/water and monocarboxylate formate anions, if the TGA curve is normalised so that the final mass observed is equal to 1, and relating quantities to the Hf₁₂ double cluster,

$$composition_{final} = 12(HfO_2)$$

$$m_{final} = 12m_{HfO_2} = 12m_{Hf} + 24m_O \equiv 1$$

Prior to the final decomposition step, the MOF will have an intact framework, but with the clusters dehydroxylated and with any (formate) monocarboxylate anions replaced by hydroxide/water,

$$cluster_{dehyd} = [Hf_6O_6]_2(OH)_6$$

$$m_{cluster_{dehyd}} = 12m_{Hf} + 18m_O + 6m_H$$

$$MOF_{dehyd} = cluster_{dehyd}(BDC_{1/2})_x(OH)_{z+y}$$

$$\begin{aligned} m_{MOF_{dehyd}} &= m_{cluster_{dehyd}} + \frac{1}{2}x(m_{BDC}) + (z+y)(m_O + m_H) \\ &= 12m_{Hf} + (18+z+y)m_O + (6+z+y)m_H + \frac{1}{2}x(m_{BDC}) \end{aligned}$$

Therefore, the mass lost in the final decomposition will be given by

$$m_{loss} = m_{MOF_{dehyd}} - m_{final} = (z+y-6)m_O + (6+z+y)m_H + \frac{1}{2}x(m_{BDC})$$

Each Hf₁₂ cluster has 18 bidentate coordination sites,

$$18 = x + y + z$$

Giving

$$m_{loss} = (12-x)m_O + (24-x)m_H + \frac{1}{2}x(m_{BDC})$$

Which can be solved from the TGA data, and thus the formula of the dehydroxylated MOF.

In the pre-dehydroxylation MOF, the MOF formula is given by



$$m_{\text{MOF}} = 12m_{\text{Hf}} + (22 + 3z)m_{\text{O}} + (14 + 5z)m_{\text{H}} + \frac{1}{2}x(m_{\text{BDC}}) + y(m_{\text{FcOH}})$$

The ratio of x to y can be found using ^1H NMR.

This then enables calculation of the expected mass of the pre-dehydroxylation MOF, as well as the ratio of BDC : formate : hydroxide/water ligands in the framework, and thus the defectivity.

Appendix B: *in situ* hydrothermal cell for XPDF measurements

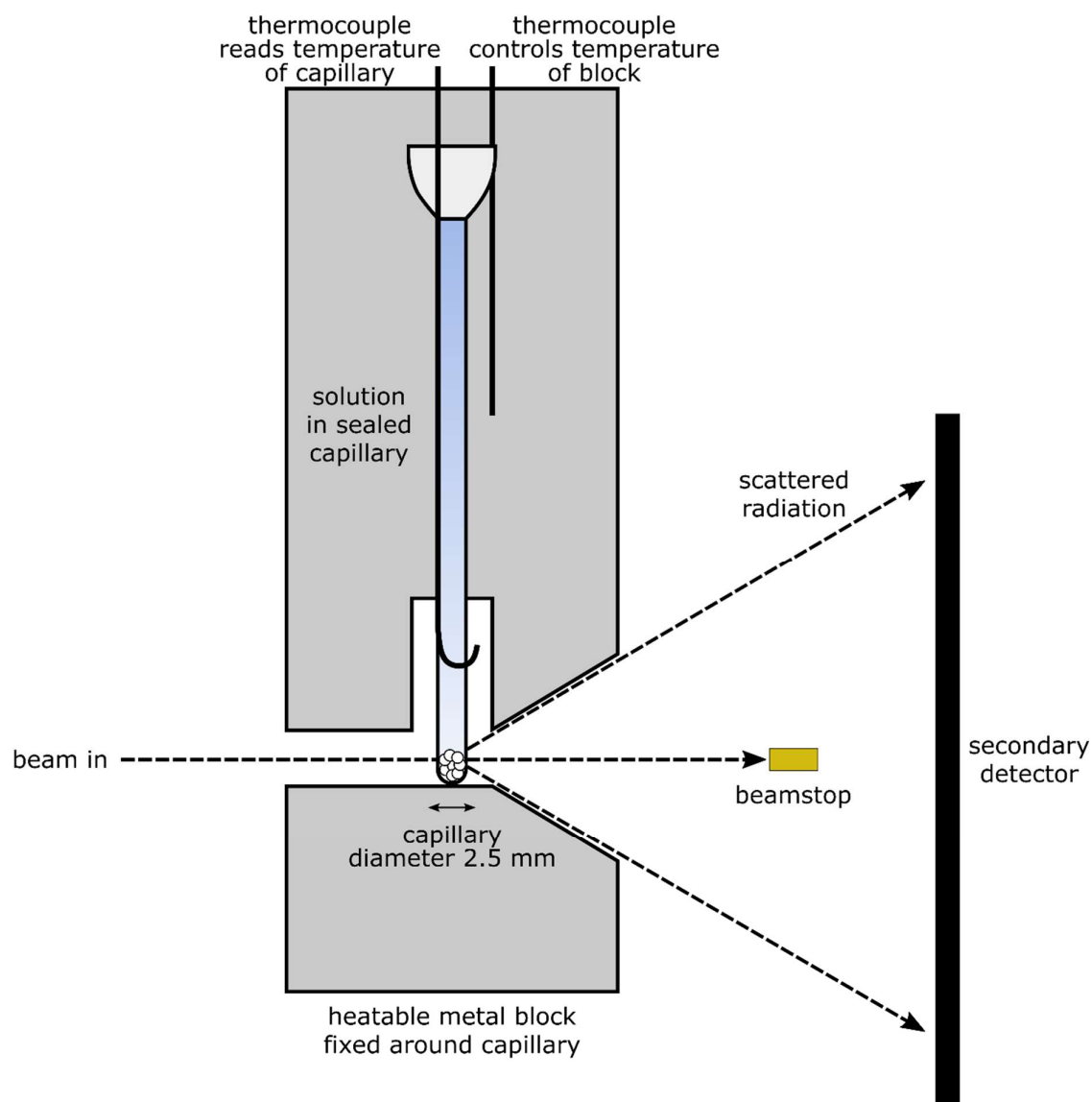


Figure B 1. Schematic of *in situ* experimental setup at the beamline

Appendix C: selective one-dimensional NOESY spectra

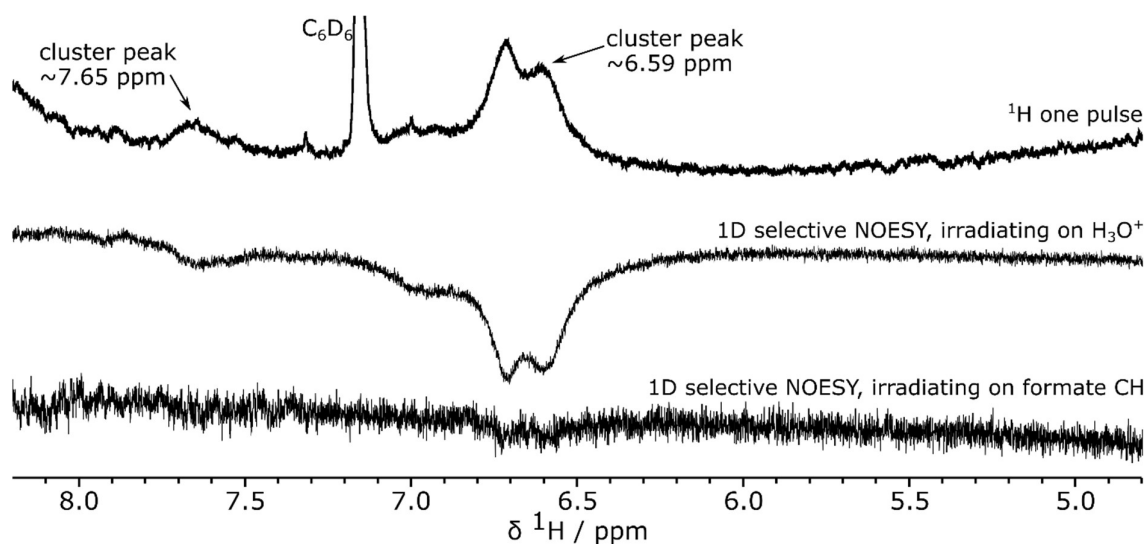


Figure C 1. ^1H NMR and 1-dimensional selective NOESY spectra taken at 278 K of the unheated sample of HfCl_4 in DFW 65:25:10, expanded to view the cluster environments. The H_3O^+ peak at 9.07 ppm and the formate CH peak at 8.71 ppm were irradiated in separate experiments to investigate correlations from these environments to the cluster environments. The selective NOESY spectra are phased so that the irradiated peak is negative; the negative cluster peaks therefore have the same phase.

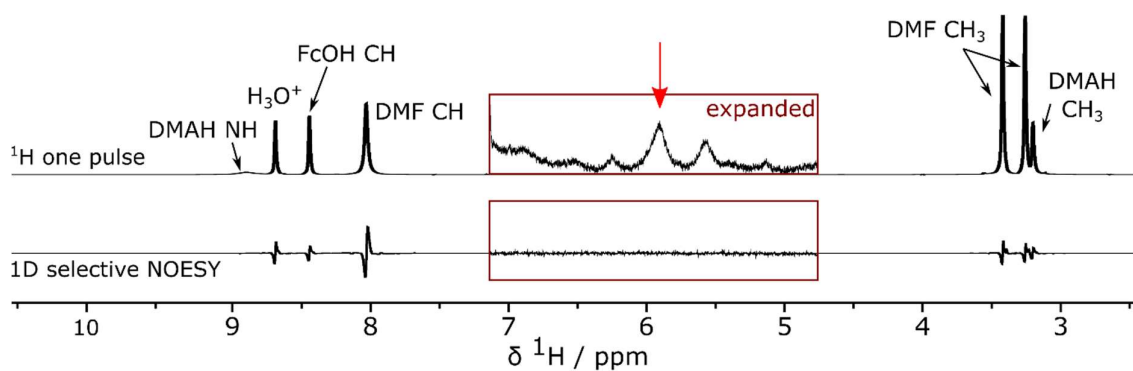


Figure C 2. ^1H NMR and 1-dimensional selective NOESY spectra taken at room temperature of the sample of HfCl_4 in DFW 65:25:10 heated at 150°C , investigating correlation both between the cluster environments and from the cluster environments to the solvent. The irradiated peak at 5.92 ppm is indicated by the red arrow. expanded to view the cluster environments.

Appendix D: ^{13}C NMR of DFW 65:25:10 solutions

^{13}C spectra were recorded on a Bruker AVIII HD Smart Probe ($\omega_{\text{1H}} = 500$ MHz) spectrometer, using a zgpg30 single pulse sequence with a 30° pulse length of $10 \mu\text{s}$, a recycle delay of 3 s and 64 scans.

Solutions were loaded into medium-wall (0.77 mm wall thickness, 3.43 mm internal diameter) Wilmad NMR tubes.

Spectra were referenced to C_6D_6 at 128.39 ppm ($\delta^{13}\text{C}$), loaded inside a sealed capillary in the NMR tube in order to reduce unwanted additional solvent interactions in the samples.

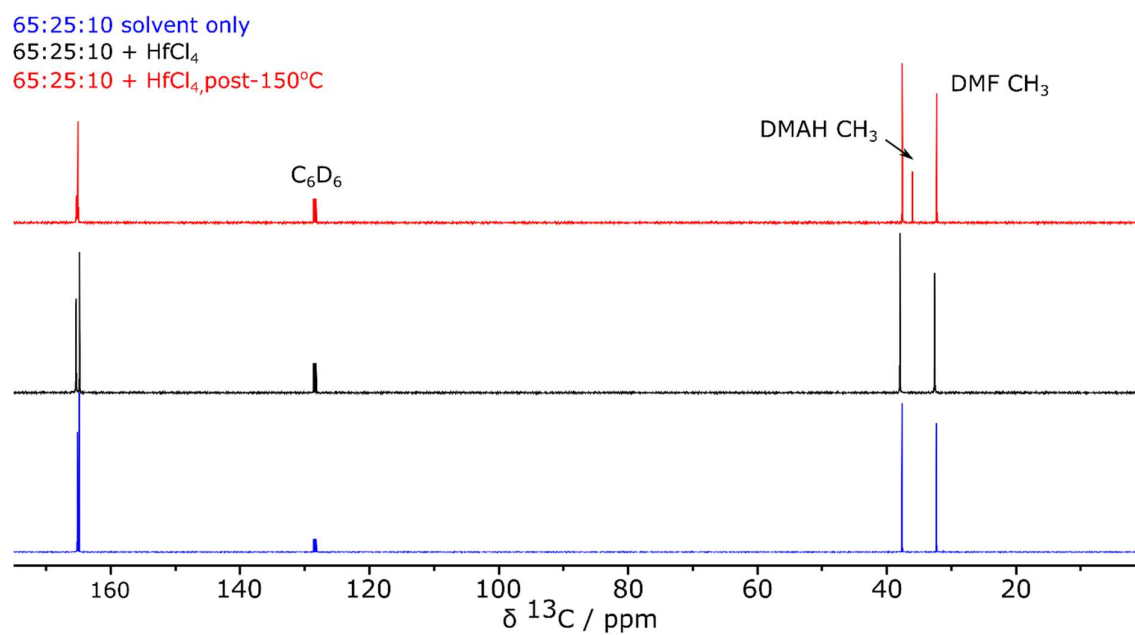


Figure D 1. ^{13}C NMR spectra of solutions of DMF : formic acid : water, both with and without HfCl_4 , and with and without heating.

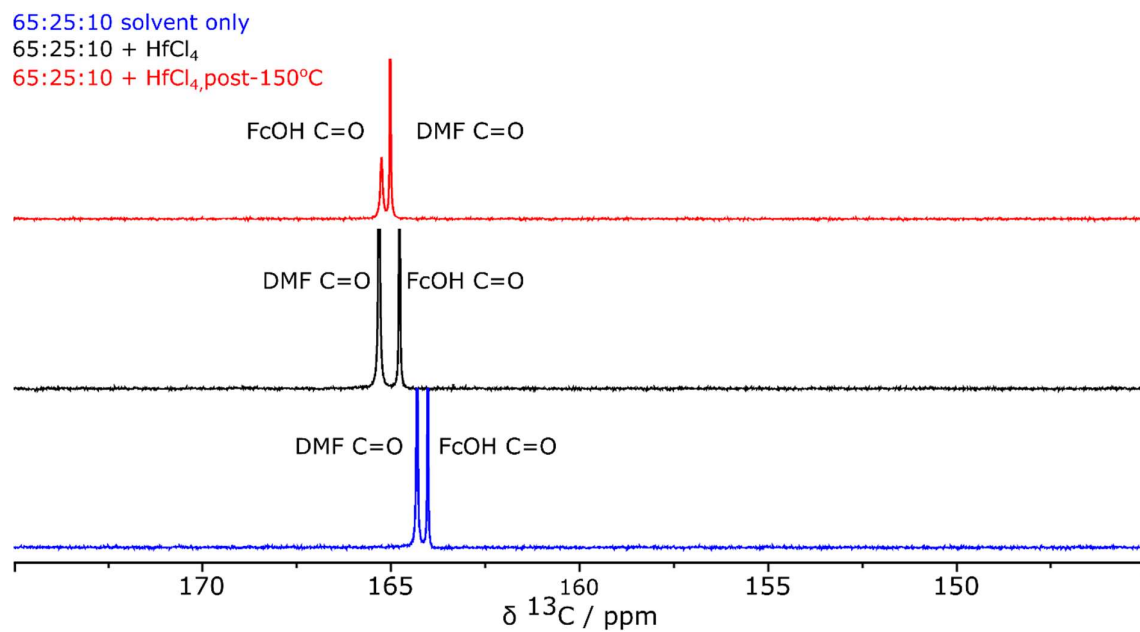


Figure D 2. ¹³C NMR spectra of solutions of DMF : formic acid : water, both with and without HfCl₄, and with and without heating, expanded to show the carbonyl signals.